Single and Double Polarization Observables in the Electrodisintegration of the Deuteron from BLAST

by

Adam DeGrush

Submitted to the Department of Physics
in partial fulfillment of the requirements for the degree of

Doctor of Philosophy

at the

MASSACHUSETTS INSTITUTE OF TECHNOLOGY

March 2010

Author .....
Department of Physics
March, 2010

Certified by .....
Robert Redwine
Professor
Thesis Supervisor

Accepted by .....
Krishna Rajagopal
Associate Department Head for Education

Single and Double Polarization Observables in the Electrodisintegration of the Deuteron from BLAST

by

Adam DeGrush

Submitted to the Department of Physics
on March, 2010, in partial fulfillment of the
requirements for the degree of
Doctor of Philosophy

Abstract

Understanding the underlying mechanisms involved in the interactions between nucleons is one of the fundamental problems in nuclear physics. Over roughly the last 70 years, this question has been approached on many different fronts. We believe that the theory underlying the interaction between nucleons is that between quarks and gluons described by Quantum Chromodynamics; however, a complete solution to the nucleon-nucleon interaction within this framework has yet to emerge.

In parallel, the advent of polarization experiments involving both polarized beams and targets has provided new experimental avenues to test our understanding the reaction mechanisms involved in the nucleon-nucleon interaction. One important example is the electrodisintegration of the deuteron, ${}^2\overleftrightarrow{H}(\vec{e},e'p)n$, in particular the measurement of the beam-vector asymmetry, A_{ed}^V, and the tensor asymmetry, A_d^T. Both of these asymmetries are sensitive to the d-wave components of the deuteron and are thus measurements of the effects of the tensor force in the nucleon-nucleon interaction.

This work reports on measurements of A_{ed}^V and A_d^T in the electrodisintegration of the deuteron that were performed by the BLAST collaboration at the Bates Linear Accelerator Center involving two data runs during 2004 and 2005. The measurements consisted of cross sections and asymmetries vs. missing momentum for a Q^2 range of $0.1(GeV/c)^2 < Q^2 < 0.5(GeV/c)^2$. Comparisons between Monte Carlo simulations based on a particular theoretical framework are made, and conclusions are drawn.

Thesis Supervisor: Robert Redwine
Title: Professor

Acknowledgments

Most importantly, I would like to thank my thesis advisor, Professor Robert Redwine, and my supervising research scientist, Dr. Douglas Hasell both for showing an infinite amount of patience throughout my work as a Ph.D. student. Specifically, I would like to thank Prof. Redwine for his never-ending–but always useful–comments and corrections to my thesis. I am certain he spent countless hours perusing the pages of my work to find the path towards improvement. As he stated regarding his corrections,"this will never end". To Dr. Hasell, I cherished his useful insights on my research and on my thesis. His ability to explain complicated problems simply yet thoroughly is truly a gift that few possess. His organization of both mind and work is something to be admired and imitated.

I would also like to thank those graduate students who worked on the BLAST project. Their support and hard work had made the inevitably difficult times bearable and the experiment possible. In particular, I would like to thank Nikolas Meitanis for joining me in long walks and conversation over a wide range of topics: politics, art, history, and literature. I learned a great deal from his opinions on these subjects and I hope the same was true for him. In addition, I am deeply grateful for the work of Aaron Maschinot which was the foundation on which this work was built. He provided an excellent starting point for the continuation of this analysis.

On a more personal note, I would like to thank those people who supported me in friendship at various stages during my research; it's completion would not have been possible without their companionship. Chris Van Wert, a dear friend, had stood by me from beginning to its end as few were able. His longstanding friendship has been valuable throughout the years and, hopefully, will continue in a similar vein in the future. Also, I am grateful to those whom I have been close to during my time here. They include Watjana Lilaonitkul, Yuko Ishii, Valeriya Gadiyak, Claudia Abonia, Rachel Mcpherson, Aayeesha Siddiqui, Jason Seeley and my father, Richard DeGrush. Secondly, I would like to thank those who supported me in my personal growth during this phase of my life: Prof. Robert Scanlan, Dominique Stassart,

Marcia Yousik, and Adam Conklin.

Finally, I would like to thank the additional members of my thesis advising committee, Prof. Richard Milner and Dr. William T. Donnelly, for their useful insights, and again, patience, in the completion of this work.

Dedicated to the memory of my grandmother Elizabeth Martis.

Contents

List of Figures

Chapter 1

Introduction

1.1 History of Nuclear Physics

Understanding the constituents of the nucleon and their interactions have been major foci in nuclear physics since the discovery of the proton by Ernest Rutherford in 1919 [1] and the neutron by James Chadwick in 1932 [2]. A complete description of the problem, however, remains elusive primarily because of its inherent complexity: at the confinement scale, the energy scale of ordinary matter, the nucleon is a complex system of quarks and gluons and this gives rise to a complicated residual force between nucleons. While the theory underlying the strong interaction between quarks is governed by QCD, its predictive power at the scale of nuclear physics ($Q^2 \leq 1$ GeV/c^2) is limited when compared with the theory of Quantum Electrodynamics (QED) which governs the interaction of charged particles. QED's strong predictive power stems from its weak coupling constant; this effectively limits the number of virtual photon exchanges in perturbative QED calculations necessary to adequately predict phenomena.

The first theory of the nuclear force was proposed by Yukawa in 1935 [3]. In it, it was necessary for the force be carried by a massive particle to account for its finite range and for the mediating particle to interact strongly as to couple to nucleons. From Heisenberg's uncertainty principle and the known size of the nucleus, Yukawa predicted the meson to have a mass of around 100 MeV/c^2. The first particle

attributed to Yukawa's meson was the muon, However, it was eventually correctly classified as a lepton and a strongly interacting meson with the right mass, the pion, was discovered by Powell, Lattes and Occhialini in 1947 [4]. This gave substantial credence to the pion exchange model of the nuclear force, so that the idea of pionic or at least mesonic exchange as a suitable picture of the interaction mechanism at low four-momentum transfer (Q^2) has remained a lasting presence in the field of nuclear physics with many modern models containing this concept. The model closest to the spirit of Yukawa's theory, for example, is the Bonn Potential [5] whose underlying contributions may be viewed as a modern continuation of Yukawa's concept, *i.e.* each piece in the nucleon-nucleon potential is directly related to a particular meson exchange [1]. The potentials are used within the context of a formalism to generate scattering observables to compare with data. One such example of a class of observables and the major thrust of BLAST is measurement of the electromagnetic form factors of the nucleon and the deuteron using polarization observables of both target and beam. The expansion and development of the modeling of nuclear matter still continues; a particular interesting example is a revival and further development of work done since the 1970's using a Vector Dominance Model with Dispersion Relations to describe the photon coupling to the nucleon. This has been able to account for the electromagnetic form factors of the protons and neutron very well, as well as the size of the deviation from unity of the scaled form factor ratio, $\mu_p \frac{G_E^p}{G_E^n}$, vs Q^2. More on this subject will be discussed below.

1.2 Quark Model and QCD

The quark model of the nucleon began with the discovery of parton distributions from deep-inelastic scattering experiments at high momentum transfers preformed by Friedman, Kendall, and Taylor at the Stanford Linear Accelerator [6] These exper-

[1] NB: these potentials are entirely non-relativistic and inadequate in giving a full description of nuclear systems and scattering since the nucleons within light nuclei have relativistic components. In the context of the non-relativistic formalism (non-relativistic potentials) used in the analysis of the data in this thesis, one handles relativistic effects separately as corrections.

iments led to the static picture of the nucleon where the proton and neutron each consist of three quarks, uud and ddu, respectively. As QCD progressed and more scattering data became available, a dynamical picture of the nucleon emerged. The nucleon is described by a system of strongly interacting quarks and gluons whose interaction is described by a Yang Mills theory based on an internal color symmetry. A major feature of this theory is the variable coupling strength that grows with decreasing Q^2, so at high Q^2, one essentially scatters from free point-like objects; the system is said to have the property of asymptotic freedom. In this regime of weak coupling, perturbative QCD has strong predictive power providing evidence for QCD as the underlying theory governing all strongly interacting particles. Difficulties arise, however, in QCD's tractability in handling interactions at low momentum transfers due to the property of confinement. At low energies the renormalized coupling grows large, making it impossible to truncate calculations in a perturbative way; quarks are no longer free but are strongly coupled together by gluons. Therefore at these low energies a complicated physical picture of the nucleon develops where, in addition to the three valence quarks, there is the existence of the quark sea. It is these sea quarks that are represented as mesons and form the long-range structure of the nucleon [7].

Currently QCD based calculations at the low Q^2 regime that typically defines nuclear physics is limited. Since the problem is intractable using straightforward perturbative techniques, attempts to use alternative QCD-based methods to handle low energy nuclear physics, such as Lattice QCD [8] and Chiral Perturbation Theory [9], have had some success and are expected to have further success in the future.

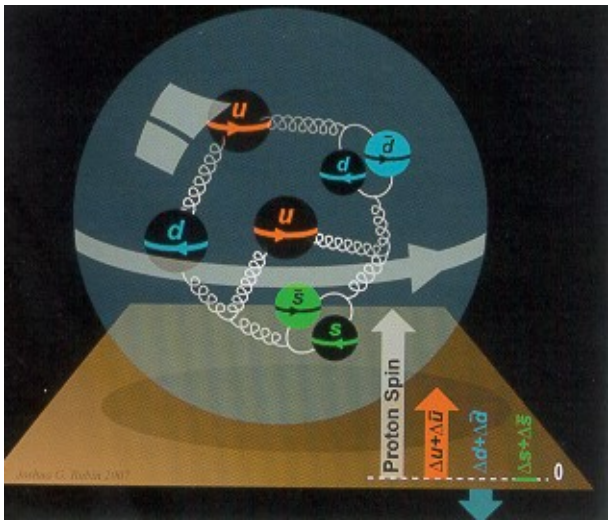

(a) Simplified schematic of the quark model of the nucleon and how the nucleon's spin is distributed amongst its quark contents.

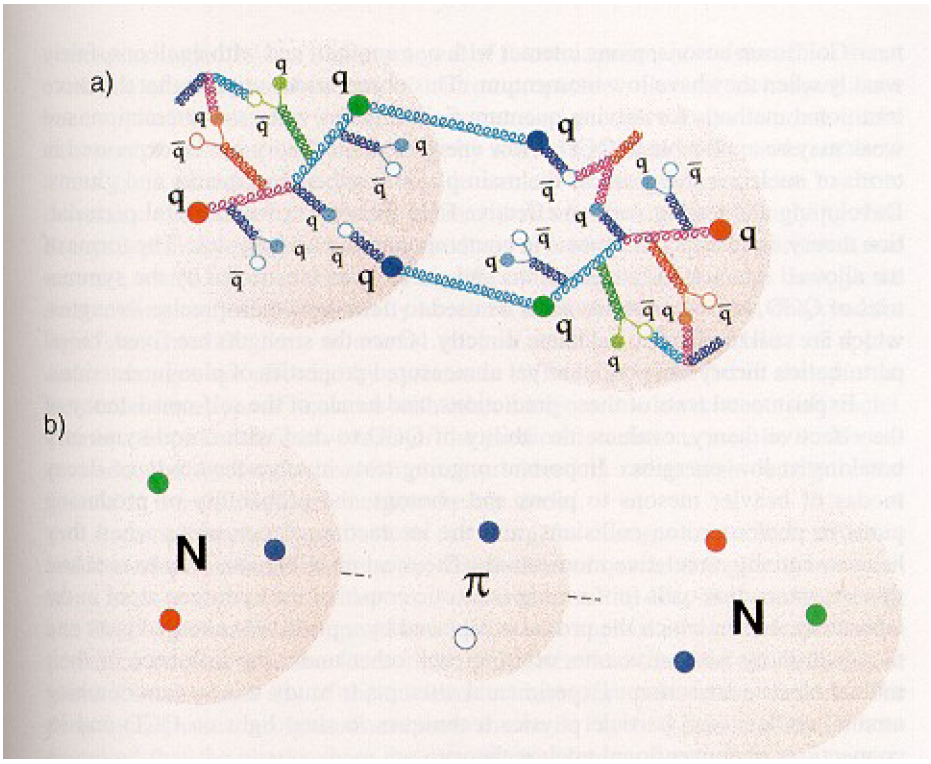

(b) Simplified schematic showing two paradigmatic representations of the nuclear force. Picture (a) shows the force at the QCD level while Picture (b) shows the nuclear force as the exchange of mesons.

Figure 1-1: Schematics showing two representations of the interactions between nucleons

1.3 Electron Scattering From Nuclei

Experimentally, a large amount of work has been devoted to understanding the electromagnetic structure of light nuclei by the scattering of electrons since the benefits of using the electron as a probe of the nucleus are numerous [7]. The electron is a point-like particle and its lack of structure allows one to write the exact form of its electromagnetic current. Also, as previously stated, the fine structure constant is small enough so that only the one-photon exchange (OPE) process is often required with, higher-order Feynman diagrams being roughly suppressed by a factor of α^2_{QED}. Finally, experimentally it is easy to achieve high-intensity, beams that are also polarized; using polarized beams in conjunction with polarized targets or final state polarization measurements have provided new ways to experimentally access the electromagnetic structure of nuclei and nucleons.

If one limits electron-nuclei scattering to the OPE reaction, the Feynman diagram is shown here in its most general form in Figure 1-2. The left side is purely QED so that the electromagnetic current for the electron with initial four momentum K and final four momentum K' is well known and given by

$$J_e(K, K')_\mu = -\frac{em_e^2}{EE'}\bar{u}_e(K')\gamma_u u_e(K), \tag{1.1}$$

where m_e is the mass of the electron, E and E' are the electron's initial and final state energies, respectively, $\bar{u}_e$ and u_e are the Dirac spinors and γ_μ is the μ^{th} component of the gamma vector. For the hadronic side, only the initial and possibly final (for the exclusive channel) states are known. Because the actual coupling mechanism of the photon to the nucleus is uncertain, the typical procedure for the hadronic side is to write the most generalized electromagnetic form for the current limited only by symmetry principles.

Traditionally, the extraction of the nucleon and the deuteron form factors have been obtained from analyzing the cross section of unpolarized scattering of electrons from nucleons and light nuclei. The hadronic current used to obtain the cross section is traditionally treated non-relativistically and the process is limited to one photon

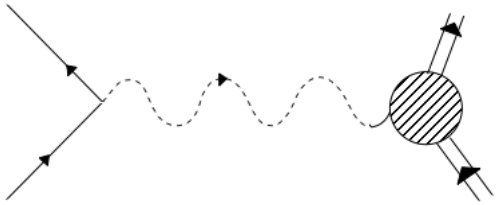

Figure 1-2: Feynman diagram for one photon exchange process where the electron scatters off an arbitrary nucleus; the electron's four momentum is measured in the final state while that of the nucleus is not

exchange, i.e. either the Plane Wave Impulse Approximation for the the bare nucleon or the properly symmeterized Plane Wave Born Approximation for nucleon knock-out of the deuteron or ^{3}He where photon coupling to either nucleon can occur. Higher-order photon exchange processes are difficult to include because one must account for all possible intermediate states, *e.g.* N*, the Δ, ρ, *etc.* as allowed by kinematics.

For interactions with a bare nucleon, Lorentz invariance, charge conservation and spatial symmetries restrict the nucleon current to the general form,

$$J^\mu = -ie\left[F_1(Q^2)\gamma^\mu + \frac{\kappa_N}{2M_N}F_2(Q^2)i\sigma^{\mu\nu}q_\nu\right], \tag{1.2}$$

where e is the electric charge, $F_1(Q^2)$ and $F_2(Q^2)$ are the Dirac and Pauli form factors, respectively, with F_1 denoting the helicity-non-flipping Dirac form factor and F_2 is the helicity flipping piece, γ^μ is the gamma four-vector component, $\sigma^{\mu\nu}$ is the antisymmetric tensor, q_ν is the μ^{th} component of the four-vector, and finally κ_N is the anomalous magnetic moment for the nucleon (N= n or p). F_1 and F_2 are typically rewritten to form the Sachs electric, $G_E(Q^2)$, and magnetic, $G_M(Q^2)$, form factors [2]. These quantities are related to the charge and magnetization currents in the Breit frame where the energy transfer, ω, is zero so that the magnitude of the three momentum transfer, $\vec{q}$, is equal to the four momentum transfer, *i.e.*, $|\vec{q}\cdot\vec{q}|=$

[2]If parity violating electron scattering is included then one must allow for strangeness in the nucleon and therefore the inclusion of the strange form factors, $G_E^s(Q^2)$ and $G_M^s(Q^2)$, and in addition, the axial form factors, . These quantities are small and are not the focus of this thesis or the BLAST project.

Q^2 [3]. F_1 and F_2 are related to $G_E(Q^2)$ and $G_M(Q^2)$ by the expressions

$$G_E(Q^2) = F_1(Q^2) - \tau_N F_2(Q^2) \tag{1.3}$$

and

$$G_M(Q^2) = F_1(Q^2) + \kappa_N F_2(Q^2), \tag{1.4}$$

with $\tau_N \equiv \frac{Q^2}{2M_N^2}$. The equation for the cross section in the one photon approximation then becomes

$$\frac{d\sigma}{d\Omega} = \frac{E'}{E}\sigma_{Mott}\left[\frac{G_E^2 + G_M^2}{1+\tau_N} + 2\tau_N G_M^2 \tan^2\frac{\theta}{2}\right], \tag{1.5}$$

where Q^2 is the 4-momentum transfer, E and E' are the initial and final electron energies respectively, θ_e is the scattered electron angle, and σ_{Mott} is the Mott cross section describing scattering from point-like fermions. To determine the two form factors, a Rosenbluth separation is performed. This process typically consists of forming the reduced cross section by taking the true cross section and dividing it by the factor $\frac{\epsilon(1+\tau_N)E}{\sigma_{Mott}}$,

$$\sigma_R = \tau_N G_M^2(Q^2) + \epsilon G_E^2(Q^2). \tag{1.6}$$

By examining data at fixed Q^2, and plotting the reduced cross section as a function of $\epsilon = f(\theta_e, E)$. The slope of the line gives $G_E(Q^2)$ while the y-intercept gives $G_M(Q^2)$.

There are significant limitations to this method of extracting nucleon form factors using unpolarized scattering. Only the proton is stable against decay and therefore make acceptable targets. The bare neutron, on the other hand, decays with a mean lifetime of roughly 886 seconds. Therefore, one must rely on knock-out scattering in the quasi-elastic regime from light nuclei such as deuterons or ^{3}He and subtract off any model effects due to interaction between nucleons. The model dependence can have significant contributions; for example, there is a theoretical uncertainty band of nearly 50% for $G_E^n(Q^2)$ measurements at low Q^2 as a result of model dependence from unpolarized measurements. Secondly, while a Rosenbluth separation works well for

[3]Note that the typical convention for four momentum transfer used in nuclear physics is followed, i.e.$Q \equiv q$ where q is the standard four momentum transfer used in particle physics, $\omega^2 - \vec{q}\cdot\vec{q}$

the proton at low Q^2, at high Q^2, $G_M^p(Q^2)$ dominates over $G_E^p(Q^2)$ making it difficult to extract $G_E^p(Q^2)$. In fact at high Q^2, $G_E^p(Q^2)$ contributes only few percent level relative to the contribution from $G_M^p(Q^2)$. To extract $G_E^p(Q^2)$ in this range where its contribution is very small, it is believed that higher photon exchange processes than the OPE approximation are needed.

Results from these methods scale at low Q^2 to a reasonable degree of accuracy according to a dipole formula given by $G_D \equiv (1 + Q^2/0.71)^{-2}$ as,

$$G_E^p(Q^2) \sim G_M^p(Q^2)/\mu_p \sim G_M^n(Q^2)/\mu_n \sim G_D. \tag{1.7}$$

However, high Q^2 ($Q^2 > 2$ (GeV/c)^2) polarization data has shown strong deviations from unity for the scaled form factor ratio primarily due to deviations from the dipole form for $G_E^p(Q^2)$; this has been confirmed by ratio measurements using polarization observables.

1.4 Polarized Scattering

With the development of highly polarized intense electron beams and the ability to polarize the target or measure the polarization state of the final state particle(s), a broad avenue of nuclear physics has opened. To summarize generally: measurements of polarization observables have provided access to certain structure functions often masked by larger ones, have given less model-dependent ways to access certain structure functions, and, finally, have provided more sensitive tests of how theoretical formalisms account for various subnuclear effects and relativistic corrections. The major thrust of the BLAST project has been investigation of the electromagnetic structure of nucleons and light nuclei from electron scattering using polarization observables where the beam and the target had the ability to be polarized.

A specific example of the benefits of using polarization has been the investigation of the form factor ratio for the proton. In e-p elastic scattering with BLAST, the target and beam were both polarized. Here, the differential cross section takes the

following form,

$$\frac{d\sigma}{d\Omega}(E,\theta_e,\theta^*,\phi^*) = \frac{d\sigma}{d\Omega}(E,\theta_e)\Big[1 + \vec{p}_e\vec{p}_T \cdot \vec{A}(\tau,\epsilon;\theta^*,\phi^*)\Big], \tag{1.8}$$

where the form factor $G_E^p(Q^2)$ is in a sense magnified by $G_M^p(Q^2)$ for high Q^2 in the product of the target polarization and the asymmetry $\vec{A}$,

$$\vec{p}_T \cdot \vec{A} \sim \sqrt{2}G_E^p(\tau)G_M^p(\tau)\sin\theta^*\cos\phi^* + \sqrt{\tau(1+\epsilon)}(G_M^p(\tau))^2\cos\theta^*. \tag{1.9}$$

The BLAST target polarization direction was such that data collected from opposite sectors of the detector corresponded to different kinematic directions between the q vector and the target polarization of either roughly parallel kinematics ($\theta^* = 0$) or perpendicular kinematics ($\theta^* = \frac{\pi}{2},\ \phi^* = 0\ or\ \pi$) . By taking the ratio of the formed asymmetries from separate kinematical regions, one gains access to the ratio of the form factors directly,

$$\sqrt{\frac{\tau(1+\epsilon)}{2\epsilon}} \cdot \frac{A_\parallel}{A_\perp} = \frac{G_E^p(\tau)}{G_M^p(\tau)}. \tag{1.10}$$

Besides this combination of polarization observables being a direct measurement of the ratio, it is also expected to have less dependence on higher photon exchange corrections to the electric form factor ratio. This is because the first term in Eq. 1.10 has a factor of $G_M^p(\tau)$ as well. This "magnifies" the term so that the ratio is less sensitive to G_E^p corrections. Figure 1-3(a) shows the most recent collection for the scaled form factor ratio including those recently published by BLAST. Higher Q^2 data clearly shows a large falloff as Q^2 increases especially for $Q^2 > 2$ GeV/c^2 leading to new investigations on the nature of this non-dipole characteristic for the form factor ratio.

A very promising model for nucleon-nucleon coupling recently revived and modernized uses vector meson and dispersive effects through coupling to $\pi\pi$, $\rho\pi$, and $\kappa\bar{\kappa}$ continua, the Vector Meson Dominance plus Dispersion Relation based models (VMD+DR) [10]. The most recent versions of these models incorporate elements that provide the correct asymptotic behavior as $Q^2 \to \infty$.

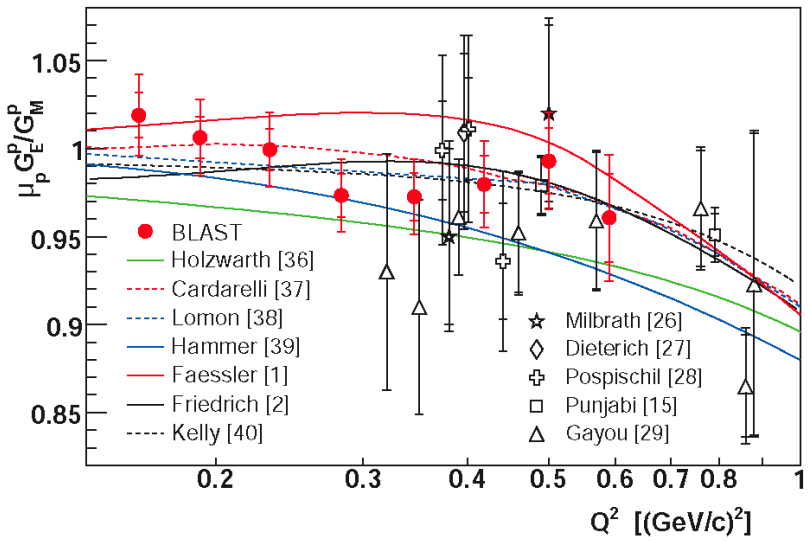

(a) BLAST G_E^n vs Q^2 measurement. Recently published BLAST data on the measurement of the neutron's electric form factor. Included are other published measurements using polarization observables. The curve is a parameterized fit to the data with a one sigma error band.

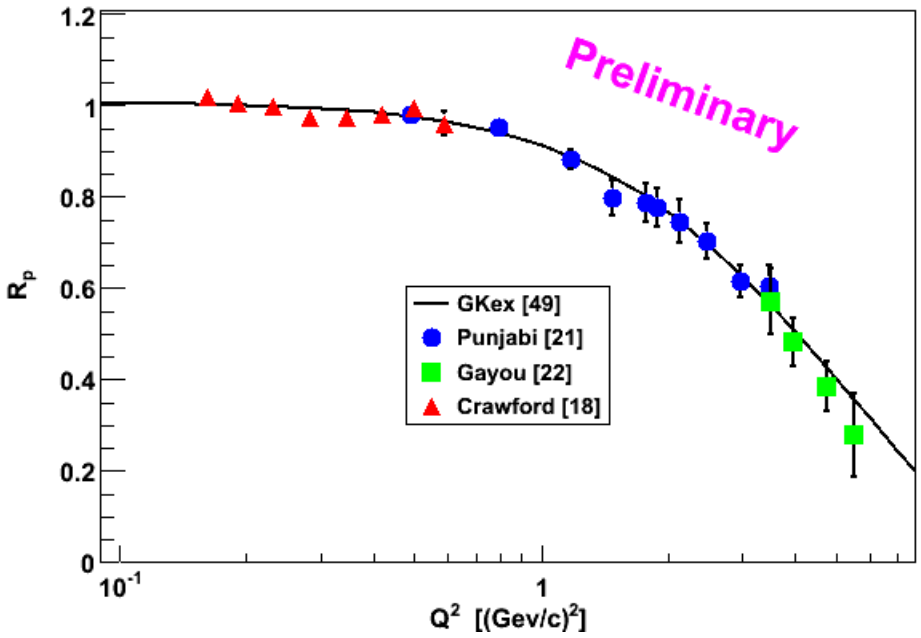

(b) Results showing the predictive power of the GKex model for the neutron form factor. BLAST data along with recently published data is included. These results are preliminary but are expected to be published soon

Figure 1-3: Electric Form Factor of the Neutron from the BLAST Experiment (Figure 1-6(a)) and various measurements along with a curve predicted by the GKex Model (Figure 1-6(b))

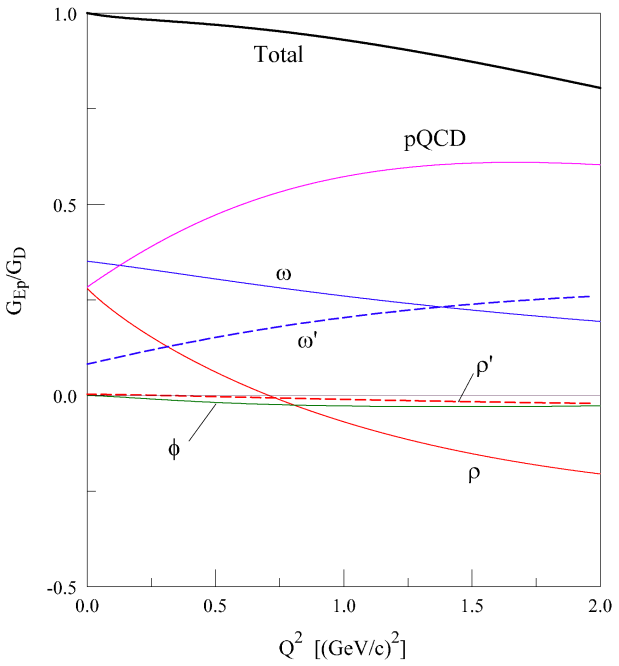

(a) Results from the GKex model showing various contributions to the scaled electric form factor for the proton.

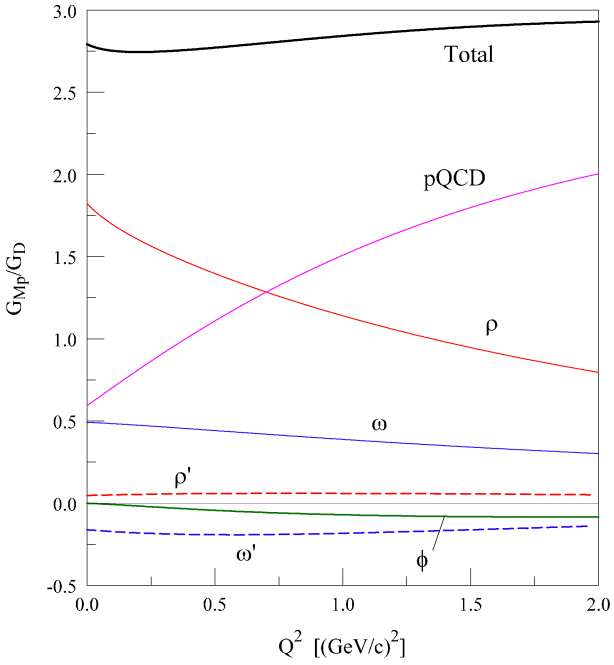

(b) Results from the GKex model showing various contributions to the scaled magnetic form factor for the proton.

Figure 1-4: Results from the GKex model for the scaled electric and magnetic form factor for the proton

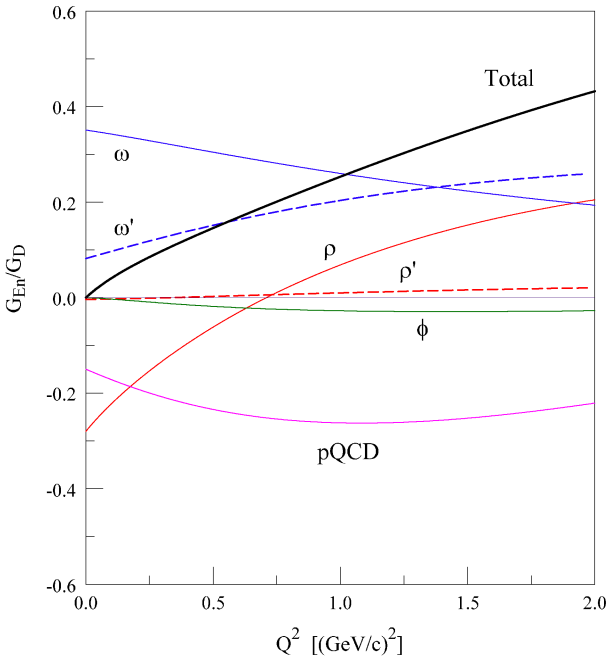

(a) Results from the GKex model showing various contributions to the scaled electric form factor for the neutron.

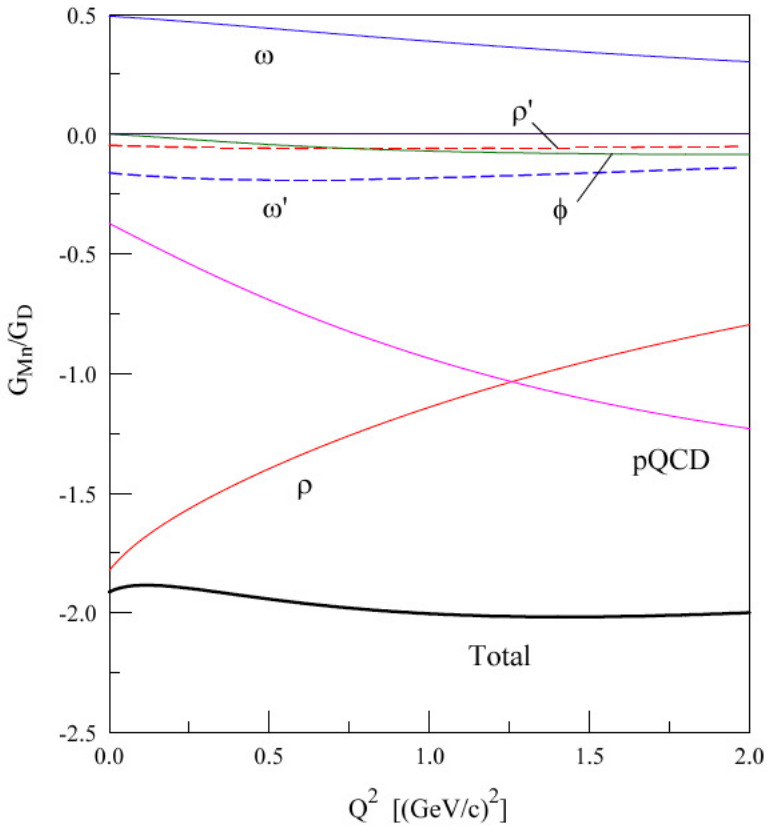

(b) Results from the GKex model showing various contributions to the scaled magnetic form factor for the neutron.

Figure 1-5: Results from the GKex model showing various contributions to the scaled magnetic form factor for the neutron.

The work shows that the dipole-like Q^2 dependence on the magnetic form factors are the result of delicate cancellations of vector meson contributions. For example Figures 1-5(a) and 1-5(b) show the relative contributions to the electromagnetic form factor relative to either the dipole form factor (for the electric) or form factor multiplied by the appropriate magnetic moment (for magnetic) vs Q^2 from 0(GeV/c)^2 to 2 (GeV/c)^2 . This has led to some interesting insights into the relative roles of each vector meson contribution and the asymptotic behavior term. The ϕ and ρ' do not contributed significantly to any of the four results shown. Also, ω' has an important contribution to the electric form factors but plays a minimal role in the magnetic. However, ω, ρ and the pQCD contribute significantly to the four form factors. In the case of the electric form factors, ω plus ω' contribute, when added, to a roughly flat contribution of 50% over the entire Q^2 range. On other hand, for the proton's electric form factor at low Q^2, the pQCD and the ρ term contribute roughly a constant value of 50% providing the nearly dipole range at low Q^2. However, the ρ term falls slightly faster than the pQCD term, resulting in a falling off from unity up to about 20% at $Q^2 = 2$ (GeV/c)^2. The cancellation between ρ term and the pQCD cancellation is even more uneven for the neutron's electric form factor. Here again, ω+ω' contribute a flat value of $\sim 22\%$ over the entire Q^2 range while the rising behavior of G_E^n is primarily due to the asymmetric cancellation between the pQCD and the ρ term with the ρ falling much faster than the rising pQCD term. In the context of the form factor ratio measurements, this model supports the idea that the deviations of the form factors from their dipole counterparts primarily arise from the nucleons electric moment and not magnetic.

In this range, a comparison of this model to data can be made, including the recent BLAST data published here [10] where G_n^E was measured by from the reaction ${}^2\overleftrightarrow{H}(\vec{e}, e'n)$ with the initial electron beam was polarized with polarization P_e and the target polarized with polarization P_z for vector polarization and P_{zz} for tensor polarization. In this case the total differential cross section can be written in terms

of the each of the cross section contributions as,

$$\frac{d\sigma}{d\Omega_e d\Omega_{pq} d\omega} = \sigma_{unp}(1 + \Sigma + P_e\Delta), \tag{1.11}$$

where σ_{unp} is the unpolarized differential cross section, Σ is the differential cross section that depends only on the target polarization and Δ depends on both the beam and target polarizations. The polarization dependent cross sections are

$$\Sigma = \sqrt{\frac{3}{2}} P_z A_d^V + \sqrt{\frac{1}{2}} P_{zz} A_d^T \tag{1.12}$$

and

$$\Delta = A_e + \sqrt{\frac{3}{2}} P_z A_{ed}^V + \sqrt{\frac{1}{2}} P_{zz} A_{ed}^T, \tag{1.13}$$

where A_e is the beam asymmetry, A_d^V is the vector asymmetry, A_d^T is the tensor asymmetry, $A_e^V d$ is the beam-vector asymmetry, and $A_e^T d$, is the beam-tensor asymmetry.

By limiting to data where only the vector polarization is analyzed the beam-vector asymmetry is formed by taking the following combination of yields for different sets of polarization states,

$$P_e P_z \cdot A_{ed}^V = \sqrt{\frac{3}{2}} \cdot \frac{Y_{++} + Y_{--} + Y_{+-} + Y_{-+}}{Y_{Tot}}, \tag{1.14}$$

where the first '$\pm$' in the yields corresponds to the beam helicity and the second '$\pm$' is the target spin state. This combination of experimental yields is equal to approximately

$$A_{ed}^V \approx a \cos\theta^* + b \frac{G_E^n(Q^2)}{G_M^n(Q^2)} \sin\theta^* \cos\theta^*. \tag{1.15}$$

where a and b are known kinematical factors, and θ^* and $\phi*$ are the target angles with respect to the q vector. By choosing data with roughly perpendicular kinematics ($\theta^* \approx \pi/2$) the first term becomes negligible and one has nearly direct access to the the form factor ratio. This method of measuring this double polarization observable is relatively independent of subnuclear effects like final state interactions (FSI), meson exchange currents (MEC), Isobar currents (IC) or relativistic correction (RC)

although it was necessary to include their effects in especially at high Q^2.

The final extraction done by measuring the ratio of the two form factors and using a parameterizing of G_M^n that was in good agreement with current data. Figure 1-6(a) is the extracted BLAST data along with other recent polarization measurements. It does not show the pronounced bump structure as previously seen. The next graph(Figure 1-6(b) is a set of similar data including the BLAST work along with the GKex model for the G_E^n. It demonstrates the good agreement between the model and polarization data.

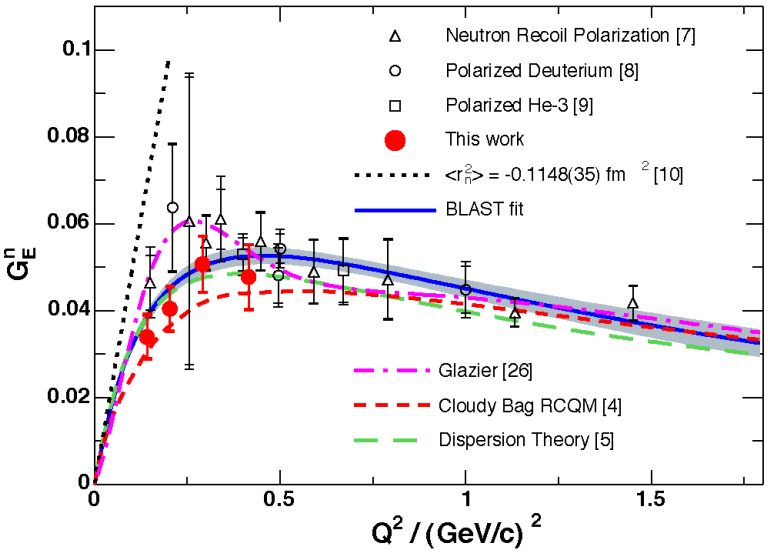

(a) BLAST G_E^n vs Q^2 measurement. Recently published BLAST data on the measurement of the neutron's electric form factor. Included are other published measurements using polarization observables. The curve is a parameterized fit to the data with a one sigma error band.

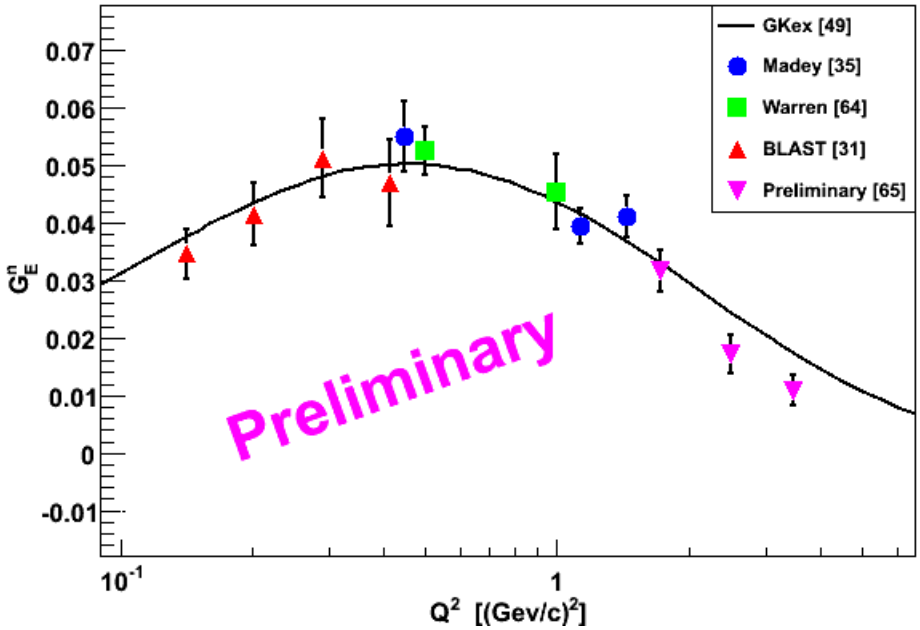

(b) Results showing the predictability of the GKex model for the neutron form factor. BLAST data along with recently published data is included. These results are preliminary but are expected to be published soon

Figure 1-6: Electric Form Factor of the Neutron from the BLAST Experiment (Figure 1-6(a)) and various measurements along with a curve predicted by the GKex Model (Figure 1-6(b))

1.5 A_{ed}^V and A_d^T in the reaction ${}^2\overleftrightarrow{H}(\vec{e}, e'p')n$

Since the free proton is stable and easily polarizable, protons provide the most model independent source to measure their electromagnetic form factors, G_E^p and G_M^p when used in electron scattering experiments . However, light nuclei such as the deuteron or ^{3}He when the proton is detected in the final state and in the kinematic regime where the proton is considered quasi-free provides a good test to how well the formalism takes into account the subnuclear effects already mentioned. Although it can also be used to measure the form factor ratio when one limits the missing momentum to the smallest sensible value so that in theory one scatters elastically from an essentially free nucleus. One must properly symmetrize the Feynman diagrams since it is not certain to which nucleon the photon couples even in this restricted set of kinematics. However, in general the diagram including only photon-proton coupling, the Plan Wave Impulse Approximation (PWIA) dominates over the symmeterized, Plane Wave Born Approximation (PWBA) for the low Q^2 values of BLAST. How correctly this approximates a free proton is still uncertain since it can have high velocity components within the nucleus as well.

The subject of this thesis is the measurement of the beam-vector and tensor asymmetries in the double-polarization experiments ${}^2\overleftrightarrow{H}(\vec{e}, e'p')n$. These particular symmetries were chosen because of their significant size and their sensitivity to D-state and subnuclear effects in the kinematic regime of this experiment. With a wide range of Q^2 and missing momentum available due to the BLAST experiment, a large amount of data was collected from two separate runs of different target spin angles of nominally 32° and 47°. The first purpose to the choice of target angles was that protons scattered into the left detector corresponded to roughly parallel kinematics ($\theta^* \approx 0, \phi^* \approx 0$) and those scattered into the right sector had approximately perpendicular kinematics ($\theta^* \approx \frac{\pi}{2}, \phi^* \approx 0$). This allowed for the selecting out certain terms by choosing the appropriate kinematics.

The formalism incorporated into the BLAST Monte Carlo was developed by Arenhoevel *et al.* [11], where the nucleons are treated non-relativistically and subnuclear

and relativistic effects are included separately. The general polarization observables are written in Arenhoevel's framework as combinations of the beam and target polarizations multiplied by an an experimentally measurable asymmetry:

$$P_X = A_0(X) + P_1^d A_d^V(X) + P_2^d A^T(X) + h\big[A_e(X) + P_1^d A_{ed}^V(X) + P_2 d A_{ed}^T(X)\big]. \quad (1.16)$$

Each asymmetry contains virtual photon matrix density elements multiplied by structure functions. The structure functions contain information on the electromagnetic structure of the proton, as well as the virtual coupling to the neutron and subnuclear effects.

In addition, because the beam-vector asymmetry as the missing momentum goes to zero is substantially independent of model choice and subnuclear or relativistic effects, it was used to extract the product of the beam and vector polarization, i.e. hP_z to high degree of accuracy. This value was used for all experiments involving the deuteron as the polarized target where double polarization measurements were done.

1.6 NIKHEF Results

The first and only previous measurement of the beam-vector and tensor asymmetries with the proton measured in the final state was performed at NIKHEF using a polarized internal target at the Amsterdam Pulse Stretcher storage ring [12, 13]. The outgoing electron and proton were detected with the BigBite magnetic spectrometer which was limited by its θ acceptance to a solid angle of 96 msr; the central Q^2 value was 0.21 $(\mathrm{GeV/c})^2$. The results were compared to Monte Carlo simulations that incorporated the model developed by Arenhoevel for the Bonn potential as well as other NN potentials including subnuclear effects; this model was similar to one incorporated into BLAST. The results showed that for the beam-vector asymmetry there was little dependence on subnuclear effects in the low missing momentum region while within the framework used by Arenhoevel where the D-state is a suitable component of the ground state, an increase and switching of sign of the measurement as missing mo-

mentum increases was a clear sign of the effect of the D-state. The measurement also showed that mainly isobar configurations are required for the agreement of data with theory. In the limit that the Plane Wave Impulse Approximation (PWIA) is valid, the tensor asymmetry is a direct measurement of combinations of the S-state and D-state wave functions in momentum space in the relative neutron-proton system. Also, since A_D^T vs $\cos\theta_M$ is proportional to $d^2(0,0) = \frac{3}{2}\cos^2\theta_M - \frac{1}{2}$ in the PWIA, a measured deviation from the zero crossings provided a good test to the extent which this approximation is valid. The measurement also provided a further test of how well sub-nuclear effects are understood. It was found that other potentials affected the results by only a small percentage ($\sim 1\%$) below 150 MeV/c in missing momentum, and that relativistic effects accounted for only a 2% correction [13]. These results from BLAST provide an important complement to the NIKHEF data, in addition to BLAST covering a wider kinematic range.

This thesis is an analysis of the sets of data with nominal target spin angles of 32° and 47° taken in the years 2004 and 2005, respectively. A previous analysis of the 32° data set was performed by Maschinot [14], while a reanalysis was necessary due to various improvements in the detector software [15]. First, the position of the wire chambers was corrected on the order of 12 mm, leading to a better absolute momentum precision. This improvement of the absolute in momentum precision from 50 MeV/c to 8 MeV/c led to a smaller kinematic correction with uncertainty was therefore smaller. Third, an improved timing calibration for the TOF and neutron detectors led to better timing cuts and subsequently a decrease in pion contamination, which produced a better understanding of the Q^2 dependence in hP_z. Results comparing different theoretical results using different nucleon-nucleon potentials and subnuclear and relativistic corrections compared with $A_e^V d$ and A_d^T for Q^2 values in four bins varying from 0.1-0.5 (GeV/c)^2 and missing momentum in five bins varying from 0.0-0.5 (GeV/c). Other asymmetries were predicted and found to be negligible due to symmetry arguments.

Chapter 2

Theoretical Motivation

2.1 Introduction

The deuteron has played a crucial role in the study of nuclear physics since its discovery by Urey and collaborators in 1932 [16]. Being the simplest bound nuclear system, it has served and continues to serve as a primary testing ground for nuclear theories. Static properties such as its binding energy, magnetic dipole and charge quadrupole moments, asymptotic D/S ratio as well as scattering observables have placed strong constraints on any theory or effective model that tries to explain the interaction between nucleons.

Yet our understanding of this, even the simplest system, is still incomplete. Although we believe that underlying the nuclear force is the strong force between quarks and massless gluons described by the theory of QCD, a satisfying description of this force between nucleons has yet to emerge. The main impediment to our understanding is that the strong coupling constant α_s is large at the low energy regime where nucleons exist. A complementary picture, Yukawa's theory of the pion, one that predated Quantum Chromodynamics, set the ground work for meson-based field theories, where the interaction between nucleons is described predominately by the exchange of mesons. Expanding and further elucidating the nature of these models has been a major drive for the study of nuclear physics for the last 40 years, while work on a QCD calculations continue.

Recently, a significant amount of effort has been placed on the study of the spin structure of the deuteron through scattering experiments using polarization observables [17, 18, 19, 20, 21, 22, 23, 24, 13]. The use of polarization allows access to small amplitudes often masked by larger ones. For example, in elastic scattering of polarized electrons from the deuteron, a measurement of T_{20} gives access to the otherwise largely hidden quadrupole form factor, $G_Q(Q^2)$. Complementary information is obtained by electrodisintegration of the deuteron where in the quasielastic regime and in the Plane Wave Impulse Approximation (PWIA), one obtains access to information on the momentum densities of the D-state. The D-state is important in that its source is due to a tensor component in the nucleon-nucleon potential. The subject of this thesis is the measurement of the beam vector (A_{ed}^V) and tensor asymmetries (A_d^T) from the electrodisintegration of the deuteron with polarized electrons and a polarized target with the proton detected in the final state. This is an important test of how well the models and formalism handle the tensor component as well as contributions from subnuclear degrees of freedom.

In this chapter, motivations for the measurement of beam-vector and tensor asymmetries are described. First, a brief historical overview of the D-state of the deuteron, along with Yukawa's attempt to apply a field theory to the nuclear force, are discussed. Then, after a description of some key features of modern nucleon-nucleon potentials, the ground state for the deuteron is described in both position-space and momentum-space with particular attention to the D-state relative to the S-state. An overview of theory and recent results of elastic electrodisintegration of the deuteron is shown to provide another way of measuring the D-state contribution. Finally, electrodisintegration of the deuteron is described with special emphasis on the theoretical framework our experiment is testing.

Throughout this chapter and well as throughout this thesis, references are made to the D-state of deuteron. However, it is important to keep in mind that the percentage of D-state, P_D once thought to be the quiddity of the description of the D-state is in fact not a measurable quantity. By applying an arbitrary unitary transformation (U_E) of arbitrary strength and arbitrary, finite range, P_D can be changed with equal

arbitrariness rendering the quantity meaningless [25]. Therefore, any discussion of the D-state properties should be qualified by the particular framework (unitary transformation) in which they are calculated. For this thesis U_E will be taken as the one that minimizes meson-exchange currents while maximizing P_D. There do exist quantities, referred to as "outside" quantities, that are calculated outside the range of the nuclear force and hence unaffected by such transformations. In particular, the S/D asymptotic ratio, η is an absolute true outside quantity and is therefore measurable.

2.2 Early History

The first evidence for an L=2 component in the ground state of the deuteron was the measurement of a non-zero quadrupole moment by Kellog, *et al.* [26] in 1938 from the comparison of magnetic resonance measurements between H_2 and D_2 molecules. They found the D_2 molecule's J=1 and I=1 state had, instead of a single peak, a peak with 6 well-spread resonances. The central peak was due to the magnetic moment of the deuteron; however the large spread in the secondary resonances could only be explained by the deuteron possessing a quadrupole moment. The results were quite striking, since a non-zero quadrupole moment meant that the nuclear force had a non-central component.

The quadrupole moment operator is a spherical tensor of rank 2 and can be written in terms of spherical harmonics as

$$\hat{\mathbf{Q}} = \frac{16\pi}{5} e r^2 Y_{20}(\theta, \phi), \tag{2.1}$$

the expectation value of which is

$$Q = \langle J, M = J \mid \hat{\mathbf{Q}} \mid J, M = J \rangle. \tag{2.2}$$

Since this quantity vanishes for $J < 1$, the quadrupole moment provided the first evidence of the D state component in the ground state of the nucleus. Since the percentage of D-state in the ground state is a poorly defined quantity, the asymptotic

ratio of D-state to S-state is more certain with a value between 0.0260-0.0275 [27]. Around the same time, Yukawa asserted his meson theory of the nuclear force which was the first attempt to describe it by applying a quantum field theory [3]. Similar to the later-developed Quantum Electrodynamics where the force is mediated by massless photons, Yukawa attempted to explain the short-range nature of the nuclear force by postulating that the particle mediating the force had mass. In this theory, if the nucleons are assumed to be infinitely heavy the Klein Gordon equation becomes, in the static limit with a point source of strength g,

$$\nabla^2\phi(\mathbf{r}) = \frac{m^2c^2}{\hbar^2}\phi(r) = g\delta(r), \tag{2.3}$$

the solution of which is the "Yukawa Potential"

$$\phi(\mathbf{r}) = \frac{g}{4\pi r}e^{mcr/\hbar}. \tag{2.4}$$

The range is therefore set by the mass mediating the interaction. With a known range of the nuclear force at the time of around 2 fm, this placed the mass at roughly 100 MeV/c^2. Originally thought to be the muon, ten years later it was shown that the muon did not interact strongly with nuclei. Fortunately, this was the same year the pion, with a mass $140MeV/c^2$, was discovered by Occhialini [28]. As more data became available and more information on the structure of the nucleon-nucleon potential became known, pion exchange became identified with the long-range part of the nuclear force [29], [30].

2.3 Modern Approach to Non-relativistic Nucleon-Nucleon Potential

Since there are many competing versions of the modern nucleon-nucleon potential, the reader is advised to refer to the original sources for each: Reid [31], Paris [32], Bonn [5], Urbana [33], and ArgonneV18 [34]. The summary given here is only a brief

outline of some key features and how they directly affect the qualitative structure of the deuteron ground state.

In the non-relativistic quantum mechanical approach, the hamiltonian for the proton-neutron system is written as

$$H = \frac{-\hbar^2}{2\mu}\nabla^2 + V_{12}(r), \tag{2.5}$$

where μ is the reduced mass, $V_{12}(r)$ is the two-nucleon potential, and r is the relative coordinate of the proton-neutron system. Once a potential is specified, a solution to the two-body problem is solved largely by numerical techniques. Figure 2-1 shows a

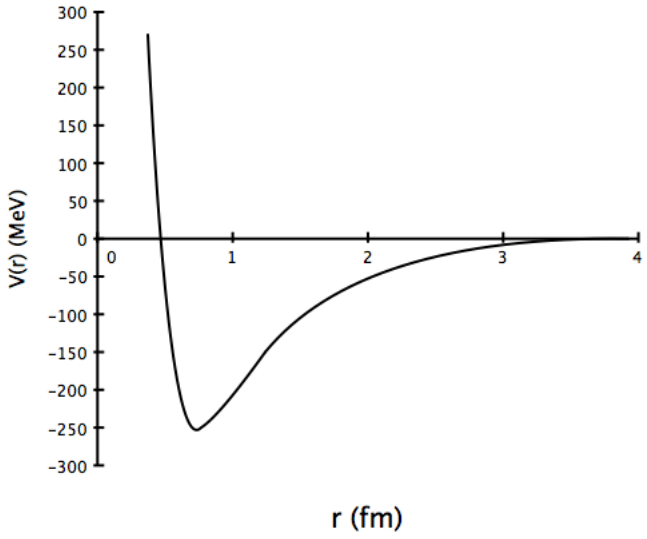

Figure 2-1: Schematic graph of nucleon-nucleon potential

graph of a typical nucleon-nucleon potential in terms of the relative separation. It is convenient to divide the potential into three regions for pedagogical purposes: the short-range repulsive core; the intermediate, attractive part; and the long range part of the potential. Different groups have attempted to explain these regions in different ways, but with similar success. One approach relies on extending the Yukawa pion exchange model to that of one boson exchange (OBE) which includes the more massive mesons and subsequently two-meson exchanges (2π, $\pi\rho$, $\pi\omega$), with the intermediate range being the exchange of heavier bosons. Multiple meson exchanges are handled

by treating the exchange meson's strength as an adjustable parameter. The other method, one that is used by the Paris group for example, is to write down the most general nucleon-nucleon potential using only symmetry properties as constraints and then apply fits to current data. There are approaches that are a mixture between the two methods where, for example, the Argonne V18 interaction handles the short range phenomenologically while intermediate ranges are done with mesons. Each potential has numerous parameters that are adjusted to fit to the available data, both static and scattering observables.

The Short-Range Repulsive Core

The repulsive hard-core was first clearly seen by studying nucleon-nucleon scattering phase shifts. By comparing the $L = 0$, 1_0^S to the $L = 2$, 1_2^D phase shifts, one sees that a negative value is obtained at around 250 MeV for the L=0 state and around 800 MeV for the L=2 state. Since a negative value implies a repulsive force and the fact that the $L = 0$ feels no centrifugal barrier, the two-nucleon system must feel a repulsive barrier at short ranges. For a value of 250 MeV this corresponds to a relative separation of 0.5 fm which can be seen in Figure 2-1. Qualitatively the hardcore repulsion can be seen as the result of the spin-spin interaction at the quark level [35]. At short ranges the two nucleons overlap and as the number of quark pairs with parallel spins increases, so does its energy. To compensate for this at least two quarks can be placed into the L=1 state, to maintain the Pauli exclusion principle. This excitation energy, however, causes an increase in energy as well. It is these two effects that can be used to explain quantitatively the repulsion at low energies, but there is yet to be a solution at the QCD level. Within the context of nucleon-nucleon models, all treat the short-range potential phenomenologically either from the start or with boson-exchange models including phenomenological form factors [36].

The Long Range Part

The long range part of the nucleon-nucleon potential is the result of pion exchange and is an important contribution to the tensor force. This term has significant consequences, since the static and dynamic quantities of the D-state are sensitive to the

coupling strength of the pion. The modern version of pion exchange is written as

$$V^{\pi} = \frac{f^2_{\pi NN}}{4\pi}\frac{M_{\pi}}{3}[Y_{\pi}(r)\sigma_i\sigma_j + T_{\pi}(r)S_{ij}\tau_i \cdot \tau_j] \tag{2.6}$$

with

$$Y_{\pi}(r) = \frac{e^{-\mu r}}{\mu r} \tag{2.7}$$

and

$$T_{\pi}(r) = [1 + \frac{3}{\mu r} + \frac{3}{\mu r}^{2}][\frac{e^{-\mu r}}{\mu r}] \tag{2.8}$$

$$S_{ij} = \frac{3}{r^2}(\sigma_i \cdot r)(\sigma_j \cdot r) - \sigma_i \cdot \sigma_j \tag{2.9}$$

where S_{ij} is the tensor operator

The spin effects are clearly seen with the inclusion of the Pauli-spin operators, which causes correlations between the spatial part (hence nucleon densities) and the spin state of the nucleons. The term including the tensor operator is responsible for generating the small admixture of D-state in the ground state, $i.e.$

$$\langle {}^3S_1 \mid S_{ij} \mid {}^3D_1\rangle \neq 0. \tag{2.10}$$

The Intermediate Attractive Part

The intermediate attractive range runs from about 0.6 to 2 fm and is described by the exchange of two pions by the Paris group [32]. In the case of the one-boson-exchange (OBE) model a scalar iso-scalar boson is invented, called the σ with a mass between 500 and 700 MeV where the mass and coupling constant are considered as free parameters. It can be shown that this represents a parameterization of the 2 pion exchanges, but is far simpler to calculate.

2.4 Ground State of the Deuteron

The nucleon-nucleon potential can be written generally in the case of the deuteron in terms of the relative coordinate $r = \frac{|r_p - r_n|}{2}$ as follows[1]:

$$V(r) = V^c(r) + V^t(r)S_{ij} + V^{ls}(r)(\mathbf{L} \cdot \mathbf{S}) + V^{l2}(r)L^2 + V^{ls2}(r)(\mathbf{L} \cdot \mathbf{S})^2, \qquad (2.11)$$

Where $V^c(r)$ is the central part and $V^t(r)S_{ij}$ is the tensor part of the potential which gives rise to the D-state.

Solutions to these potentials are

$$\Psi_J^{M_J}(\mathbf{r}) = R_0(r)\mathcal{Y}_{011}^{M_J}(\hat{r}) + R_2(r)\mathcal{Y}_{211}^{M_J}(\hat{r}), \qquad (2.12)$$

where R_0 and R_2 are the radial wave functions of the S and D states, respectively, and $\mathcal{Y}_{LJS}^{M_J}(\hat{r})$ are the spin angle functions. From Figure 2-2(a) it is apparent that the long-range potential is fairly model-independent with greater differences between the theories for $r < 2$ fm. It is instructive to examine the spin projection dependent deuteron densities as a function of interparticle distance and polar angle, $\rho_J^{M_J}(r', \theta)$ which are

$$\rho_J^0(\mathbf{r'}) = \frac{4}{\pi}[C_0(2r') - 2C_2(2r')P_2(\cos\theta)] \qquad (2.13)$$

$$\rho_J^{\pm 1}(\mathbf{r'}) = \frac{4}{\pi}[C_0(2r') + C_2(2r')P_2(\cos\theta)] \qquad (2.14)$$

and

$$C_0(r) = R_0^2(r) + R_2^2(r) \qquad (2.15)$$

$$C_2(r) = \sqrt{2}R_0^2(r)R_2^2(r) - \frac{1}{2}R_2^2(r) \qquad (2.16)$$

Figures 2-3(a) and 2-3(b) show the densities in the x'-z' plane. To generate the three-dimensional shape, the figures are rotated about the z' axis. For the $M_J = 0$ state, the maximum density occurs at roughly a distance of 1 fm, with a hole at the center. Thus, the generated distribution is a toroid with a central hole due to the

[1]It should be noted for the Paris potential the L operator is replaced by the ∇ operator

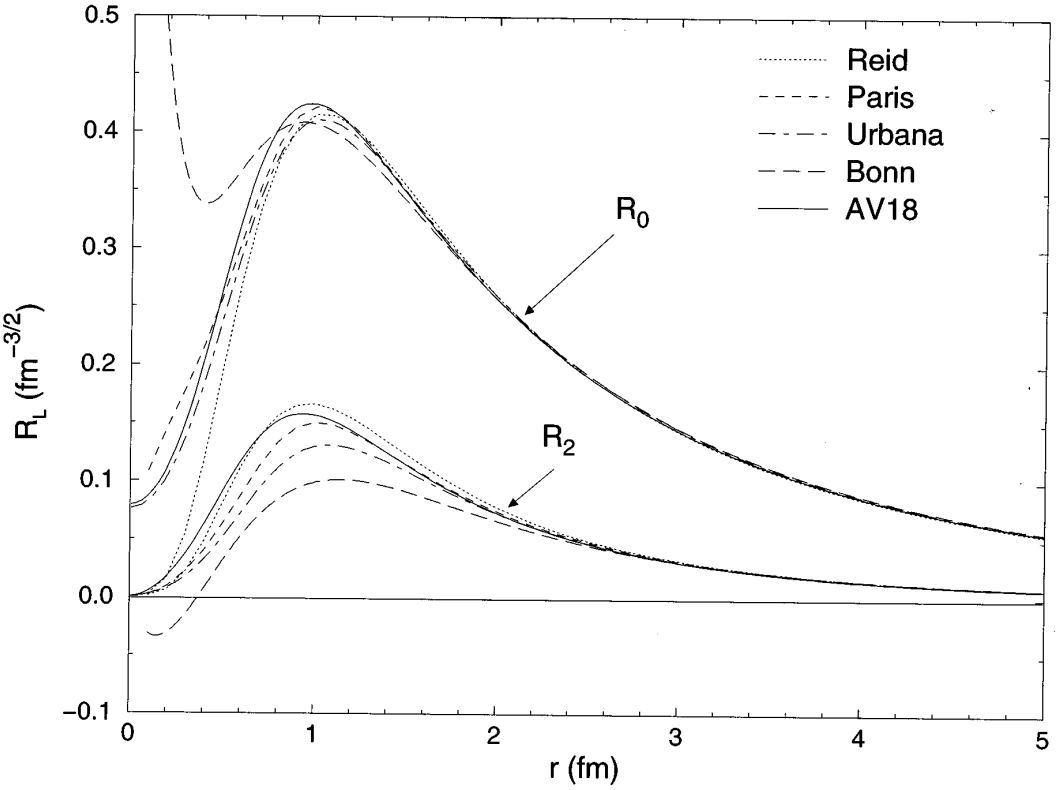

(a) Deuteron densities in the x',z' plane for the M_J=0 state (left) and $M_J = \pm 1$ (right). Results are from using the Argonne v18 potential

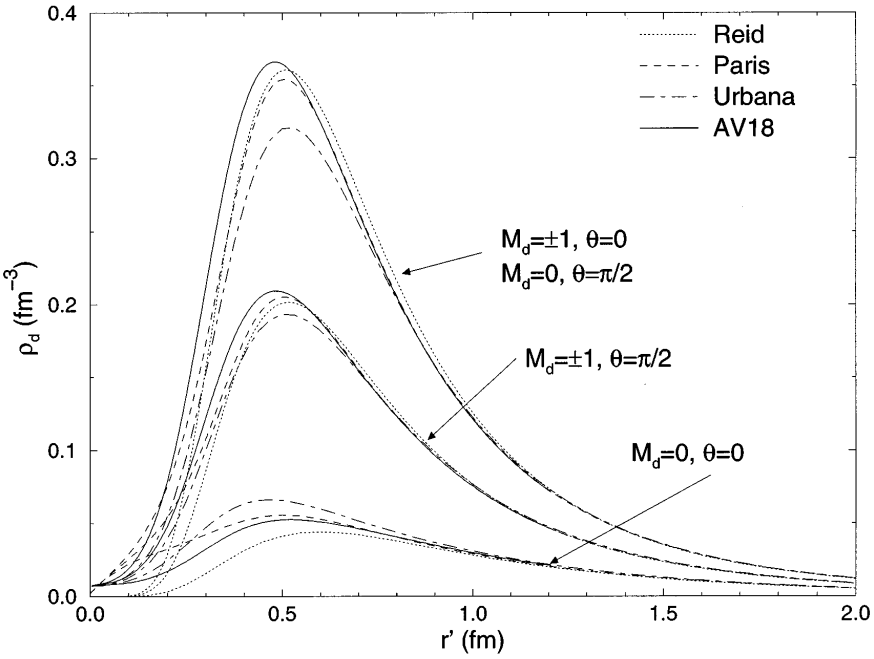

(b) Deuteron densities for various spin projections, M_J and θ

Figure 2-2: Radial wavefunctions and density distribution in r-space. Results are from using the Argonne v18 potential. [37]

repulsive core. Likewise the M_J=±1 states have a maximum density at roughly 1 fm with the shape being that of a "dumbbell" (see Figure 2-4). It is important to note that these shapes are a direct result of the tensor force. In the absence of the D-state, $R_2 = 0$ so that $C_2(r) = 0$ and the angular dependence disappears leaving

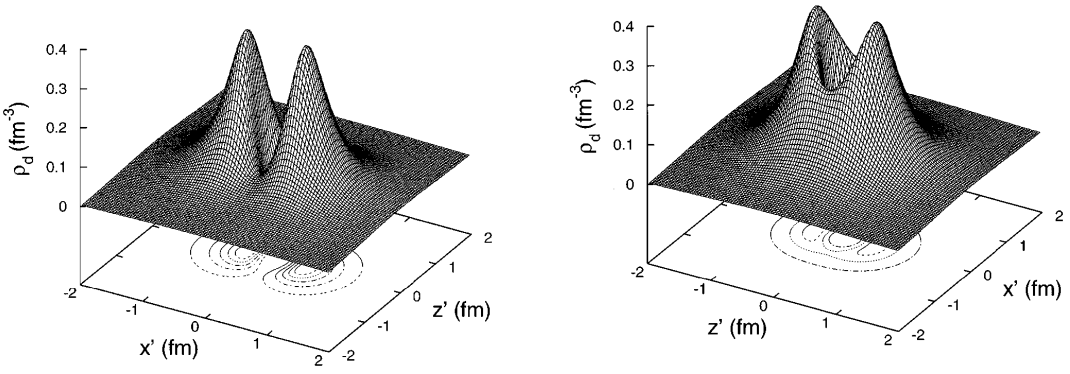

(a) $M_J = 0$ (b) $M_J = \pm 1$

Figure 2-3: Deuteron densities in the x',z' plane for the $M_J = 0$ state (left) and $M_J = \pm 1$ (right). Results are using the Argonne v18 potential. [37]

$$\rho_J^{M_J}(\mathbf{r}) = \frac{4}{\pi}(R_0^2(r) + R_2^2(r)) \tag{2.17}$$

or shells of equidensity as a function of r. On the other hand, by comparing the density distributions for $\theta = 0$ and $\theta = \frac{\pi}{2}$ (Figure 2-2(b)), one finds large differences in densities depending on how the deuteron is oriented. For example in the $M_J = 0$ state, the difference between $\theta = 0$ and $\theta = \frac{\pi}{2}$ is roughly a factor of 7 greater. It is also worthy to note that the effect is more pronounced for the $M_J = 0$ state than for the $M_J = 1$ state by a factor of 2. This implies that tensor effects are the strongest and performing scattering experiments using polarization is a fruitful way of investigating their effects.

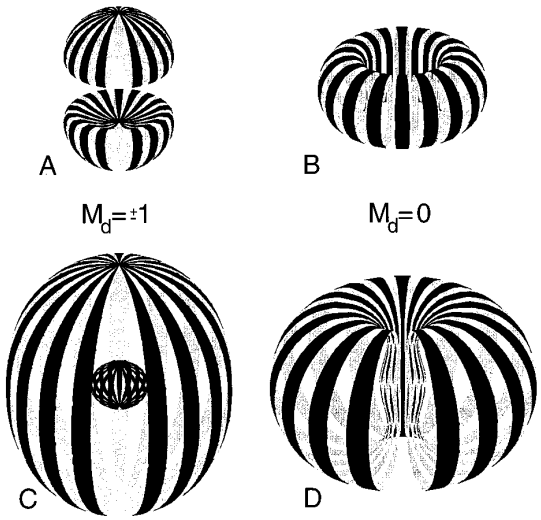

Figure 2-4: Three dimensional representations of deuteron densities for both states. Both A and B is for $\rho(\mathbf{r}') = 0.24 \cdot fm^{-3}$ showing characteristic dumbbell and toroid shapes. Figures C and D are for where $\rho(\mathbf{r}') = 0.08 \cdot fm^{-3}$ or about $r' = 1.2fm$. Note for the $M_J = 0$ state that at low r' the distribution has a small inner shell due to the repulsive core and a large outer one. [37]

2.5 Wavefunctions in Momentum Space

In the limit that the Plane Wave Impulse Approximation can be used, the spin-dependent cross-section is proportional to the spin-dependent momentum distributions. It is useful then to look at the Fourier transformations of the radial wavefunctions to obtain the spin-dependent momentum distrubutions. The Fourier transformation from r-space to p-space is given by

$$\tilde{\Psi}_J^{M_J} = (\frac{1}{2\pi})^{3/2} \int d^3\mathbf{r} e^{-\mathbf{k}\cdot\mathbf{r}} \Psi_d^{M_J}(\mathbf{r}) \tag{2.18}$$

$$= \tilde{R}_0(r)\mathcal{Y}_{011}^{M_J}(\hat{k}) + \tilde{R}_2(r)\mathcal{Y}_{211}^{M_J}(\hat{k}), \tag{2.19}$$

where the radial function for the different L states are given by

$$\tilde{R}_L(k) = i^L \sqrt{\frac{2}{\pi}} \int_0^\infty r^2 dr j_L(kr) R_L(r), \tag{2.20}$$

where $j_L(kr)$ is the spherical Bessel function of rank L. The spin-dependent momentum distributions are obtained from the product of the wavefunction with its hermi-

tian conjugate. These are written in terms of the relative momentum, $p = \frac{|p_p - p_n|}{2}$, and θ_p, the polar angle of $\mathbf{k}$,

$$\tilde{\rho}_J^0(\mathbf{r}') = \frac{4}{\pi}[\tilde{C}_0(p) - 2\tilde{C}_2(p)P_2(\cos\theta_p)] \tag{2.21}$$

and

$$\tilde{\rho}_J^{\pm 1}(\mathbf{r}') = \frac{4}{\pi}[\tilde{C}_0(p) + \tilde{C}_2(p)P_2(\cos\theta_p)], \tag{2.22}$$

with the normalization

$$\int d^3\mathbf{k}\tilde{\rho}_J^{M_J}(\mathbf{k}) = 1 \tag{2.23}$$

Figure 2-5 shows the momentum density distributions for $\theta_p = 0$ and $\pi/2$ for the three spin projections. The nodes seen for both $M_J = 1$, $\theta = 0$ and $M_J = 0$, $\theta = \pi/2$ are the result of Fourier transforming peaks as seen in figures 2-3(a) and 2-3(b); this is an approximation of the Fourier transform of two delta functions at distances $\pm d$ whose solution is $\pm d \cdot cos(kd)$. In the case $M_J = 0$, $\theta = \pi/2$, the nodes are related to the size of the the toroid. For $M_J = 1, \theta = 0$ the node is related to the "dumbbell" separation. Again similar to the result for the r-space, the average of the spin-dependent densities loses all dependence on the L=2 state and in addition dependence on θ_p.

$$\tilde{\rho}^{avg} = \frac{1}{3}(\tilde{\rho}^{M_0} + \tilde{\rho}^{M_{+1}} + \tilde{\rho}^{M_{-1}}) \tag{2.24}$$

$$= \frac{1}{3\pi}\tilde{C}_0(p) \tag{2.25}$$

and that in this limit and one must turn to polarization scattering to access the D-state in this approximation.

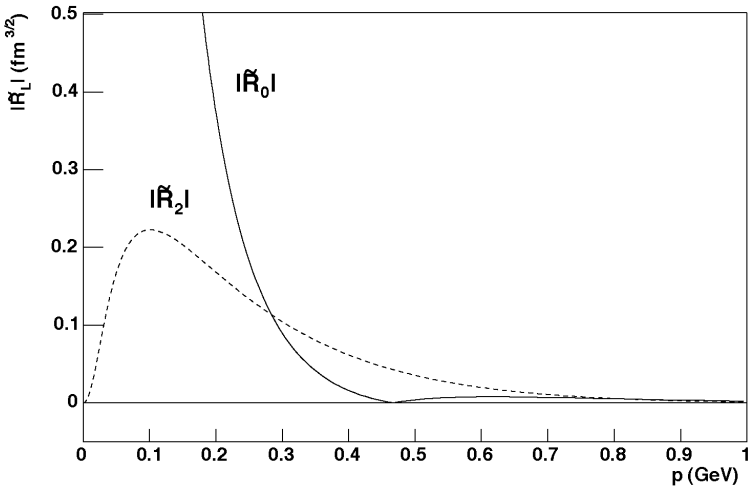

(a) Magnitudes of p-space radial wavefunctions for S-state and D-state

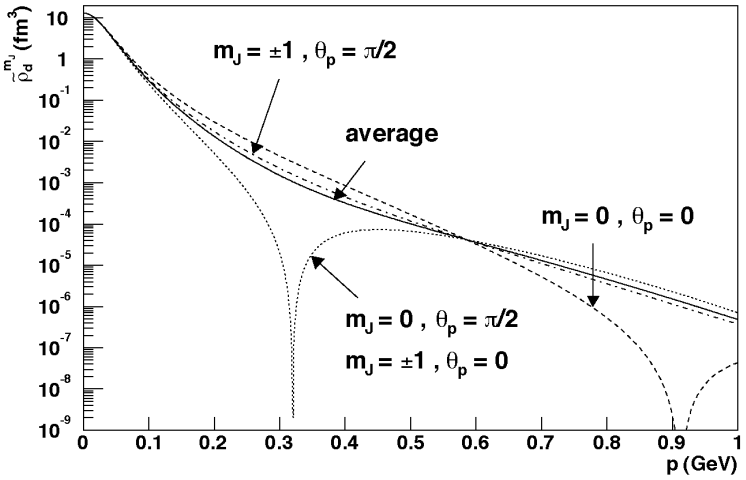

(b) P-space densities for $MJ = 0$ and $M_J = \pm 1$ for $theta_p = 0, \pi/2$

Figure 2-5: Deuteron densities in r and p-space for the S-state and D-state. Results are from using the Bonn potential. [5]

2.6 Polarized Inclusive Elastic ed Scattering

The benefits of using polarization observables can be clearly seen in the case of elastic-scattering from deuterium. There are three independent form factors that describe the system, conventionally taken as the charge, magnetic, and quadrupole form factors, G_C, G_M, and G_Q, the result of elastic electron scattering from a J=1 nucleus. Following the formalism given by Donnelly and Raskin [38], in this PWIA case, parity and time reversal require that only the three possible multipoles exist:

$$F_0(q) = \frac{1}{3}\langle 1\|\hat{M}(q)\|1>, C0 \tag{2.26}$$

$$F_1(q) = \frac{1}{3}\langle 1\|i\hat{T}_1^{MAG}(q)\|1>, M1 \tag{2.27}$$

$$F_2(q) = \frac{1}{3}\langle 1\|\hat{M}_2(q)\|1>, C2 \tag{2.28}$$

where the $\hat{M}(q)$ is the charge operator, $i\hat{T}_1^{MAG}(q)$ is the magnetic operator and $\hat{M}_2(q)$ is the charge quadrupole operator. These F form factors are related to G_C, G_M, and G_Q by

$$\sqrt{4\pi}F_0(q) = (1+\tau)G_C \tag{2.29}$$

$$\sqrt{4\pi}F_1(q) = -\frac{2}{3}\sqrt{\tau(1+\tau)}G_M \tag{2.30}$$

$$\sqrt{4\pi}F_1(q) = 2\frac{\sqrt{2}}{3}\tau(1+\tau)G_Q \tag{2.31}$$

where τ is $-Q^2/2M_d^2$. to the individual nucleons and the overall deuteron structure can be obtained by examining the reaction in the impulse approximation (IA), where it is assumed that the photon couples to an individual nucleon. In this case, the deuteron electromagnetic form factors can be written as products of nucleon form factors and the body form factor which depend on the deuteron wave functions [39].

$$G_C(Q^2) = (G_E^p + G_E^n)\int \left[u^2(r) + w^2(r)\right] j_0\left(\frac{Qr}{2}\right) dr \tag{2.32}$$

$$G_Q(Q^2) = \frac{3}{\eta\sqrt{2}}(G_E^p + G_E^n)\int w(r)\left[u(r) - \frac{w(r)}{\sqrt{8}}\right] j_2\left(\frac{Qr}{2}\right) dr \tag{2.33}$$

$$G_M(Q^2) = 2(G_M^p + G_M^n)\int \left\{ \left[u^2(r) - \frac{w^2(r)}{2} \right] j_0\left(\frac{Qr}{2}\right) + \left[\frac{u(r)w(r)}{\sqrt{2}} + \frac{w^2(r)}{2} \right] j_2\left(\frac{Qr}{2}\right) \right\} dr + \frac{3}{2}(G_E^p + G_E^n)\int w^2(r)\left[j_0\left(\frac{Qr}{2}\right) + j_2\left(\frac{Qr}{2}\right) \right] dr \tag{2.34}$$

When polarization is not used, however, the structure of the deuteron appears in the familiar structure functions $A(Q^2)$ and $B(Q^2)$ corresponding to scattering from longitudinally and tranversely polarized photons. The cross-section takes the familiar form,

$$S_0 \equiv \frac{d\sigma}{d\Omega}(0,0,0) = \left(\frac{d\sigma}{d\Omega}\right)_M \cdot \frac{1}{f}\left[A(Q^2) + B(Q^2)\tan^2\frac{\theta_e}{2} \right]. \tag{2.35}$$

A and B can be separated by performing a Rosenbluth decomposition whereby the initial energy and scattering angle are varied while the energy and momentum transferred are kept constant. Unfortunately G_C, G_Q and G_M appear in A as incoherent sums of squares and only G_M appears in B:

$$A(Q^2) \equiv G_C^2(Q^2) + \tfrac{8}{9}\eta^2 G_Q^2(Q^2) + \tfrac{2}{3}\eta G_M^2(Q^2) \tag{2.36}$$

$$B(Q^2) \equiv \tfrac{4}{3}\eta(1+\eta)G_M^2(Q^2) \tag{2.37}$$

with $\eta \equiv \frac{Q^2}{4m_d^2}$. A third observable is therefore needed to extract all three form factors. This can be accomplished by polarizing the initial deuteron target or measuring the final state polarization of the scattered deuteron while still retaining an unpolarized beam. Typically what is measured is the polarization observable T_{20}, chosen because it contains an interference term between $G_C(Q^2)$ and $G_Q(Q^2)$ and therefore the small quadrupole form factor is "magnified" by the large charge form factor,

$$T_{20} \equiv -\frac{\sqrt{2}\eta}{3\tilde{S}}\left[4G_C(Q^2)G_Q(Q^2) + \frac{4\eta}{3}G_Q(Q^2)^2 + \left(\frac{1}{2} + \epsilon\right) G_M(Q^2)^2 \right]. \tag{2.38}$$

Here $\tilde{S} \equiv A(Q^2) + B(Q^2)\tan^2\frac{\theta_e}{2}$ and $\epsilon \equiv (1+\eta)\tan^2\frac{\theta_e}{2}$.

Since T_{20} depends on both Q^2 and the angle θ_e it is customary for comparison purposes to define $\tilde{t}_{20}$ which eliminates both the magnetic form factor and the angular

dependence by defining $Y = \frac{2\eta}{3}\frac{G_Q}{G_C}$, $X = \sqrt{\frac{\eta\left[1+2(1+\eta)\tan^2\frac{\theta_e}{2}\right]}{3}}\frac{G_M}{G_C}$; and define the quantity $\tilde{t}_{20}$,

$$\tilde{t}_{20}(Q^2) = \frac{T_{20}(Q^2,\theta_e) + \frac{\delta}{2\sqrt{2}}}{1-\delta} = -\sqrt{2}\frac{Y(2+Y)}{1+2Y^2}, \quad \text{with} \quad \delta = \frac{2X^2}{1+2Y^2+2X^2}. \quad (2.39)$$

One important aspect of this quantity is the location of its node which occurs when $G_C = 0$ and $T_{20} = -1/\sqrt{2}$. This is related to the sharp drop in the p-space wave-function of the S-wave and is therefore related to the location of repulsive core.

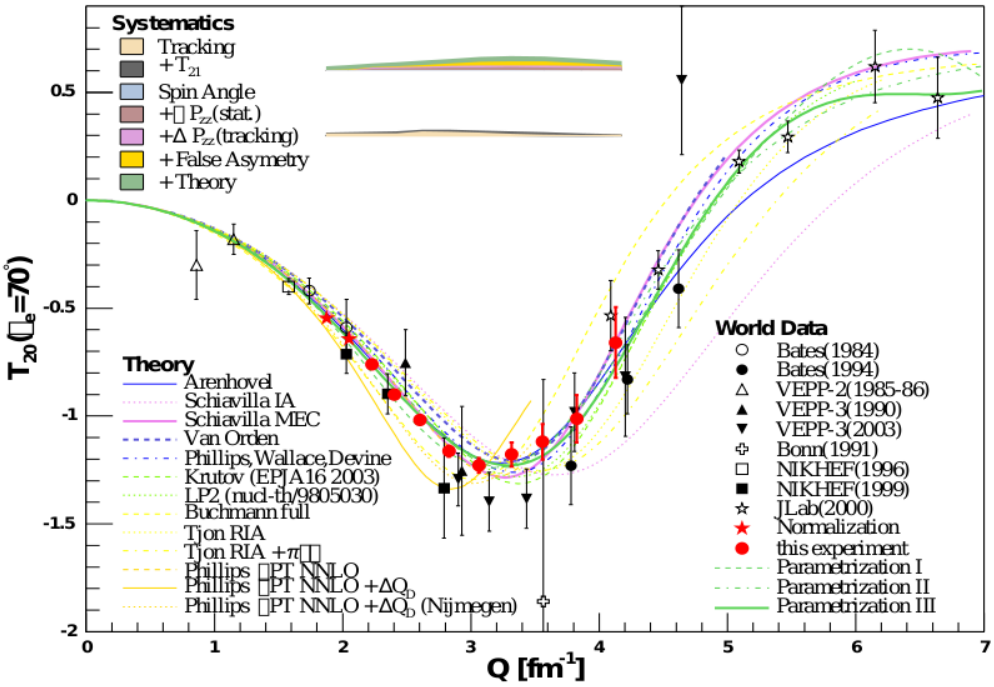

Figure 2-6: World data on T_{20} with theory including recent BLAST data [40].

With the relatively recent high polarization of targets and the ability to detect final state polarization, data for all three form factors have been determined out to a Q^2 of roughly 7 fm^{-1}. Figures 2-6, 2-7(a), 2-7(b) and 2-8 show the recent world data on both T_{20} and the three form factors G_C, G_Q, and G_M. These measurements provide a solid test of the limitations to the NRIA and over recent years this has motivated more sophisticated models in an attempt to understand the discrepancy between data and

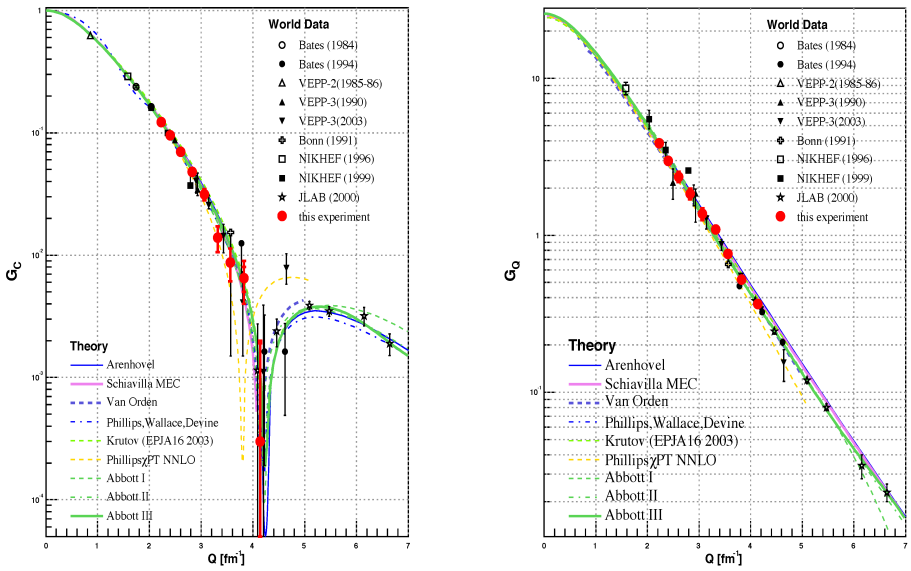

(a) GC vs Q^2 (b) GQ vs Q^2

Figure 2-7: Extracted G_C and G_Q separated with BLAST and world $A(Q^2)$ data [40].

experiment, which include: the addition of MEC and relativistic corrections to the NRIA [42, 43, 44, 37], quasipotential equations with relativistic approximations [45, 46, 47], and chiral perturbation theory [48] and fully relativistic calculation in the impulse approximation including both on and off-shell final state interactions [49]. The models explain the data relatively well; however, none is consistent with all form factors and static moment data.

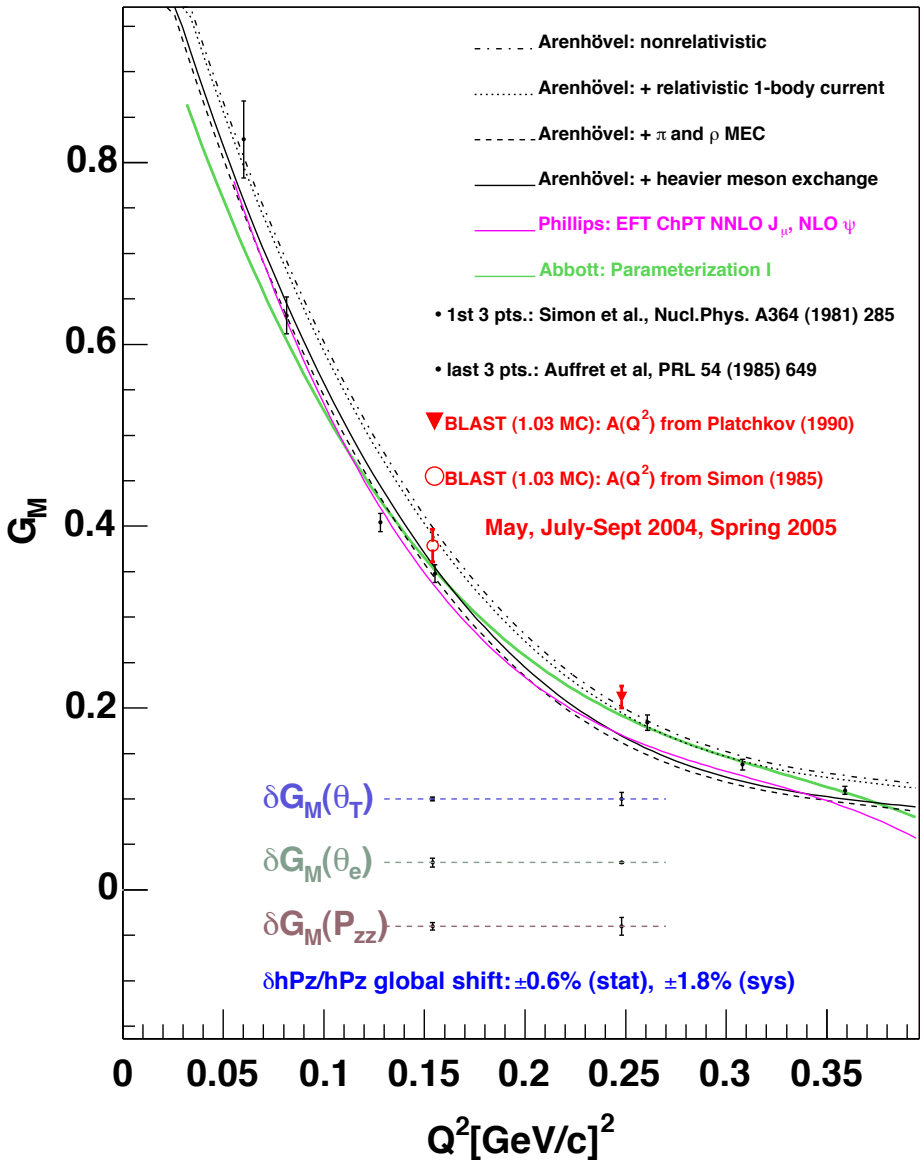

Figure 2-8: G_M including world data and recent BLAST measurements [41].

2.7 Polarized Exclusive Electrodisintegration of Deuterons

2.7.1 Kinematics

Figure 2-9 shows the geometry for the electrodisintegration of the deuteron with a polarized beam and polarized target. In the one-photon-exchange process, an electron e with four momentum in the lab of $k = (\epsilon, \vec{K}')$ and helicity h emits a virtual photon of four-momentum $q = (\omega, \vec{q})$ and the electron scatters with a final four-momentum of $\vec{K}' = (\epsilon', \vec{K}')$. The virtual photon breaks up the deuteron which is at rest in the lab, $P_d = (M_d, 0)$, resulting in a scattered proton $P_p = (E_p, P_p)$ and neutron $P_n = (E_n, p_n)$ in the final state. The three vectors, $\vec{K}$, $\vec{K}'$, and $\vec{q}$ lie in the scattering plane and are used to define the lab frame of reference where the z-axis lies along the $\hat{q}$ direction, $\hat{y}$ is perpendicular to the scattering plane or in the $\frac{\vec{K}\times\vec{K}'}{|\vec{K}\times\vec{K}'|}$ direction, and x' is defined so the three unit vectors form a right-handed coordinate system. It is in this system that the lab target angles (θ_d, ϕ_d) are defined and are used along with the q-vector to define the orientation plane.

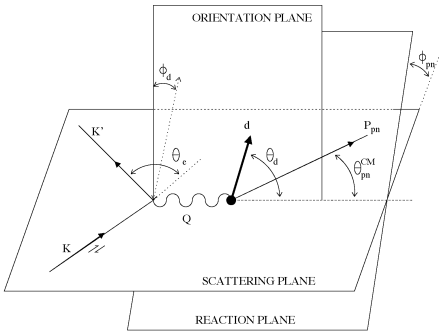

Figure 2-9: Kinematics for electrodisintegration of the deuteron

Although the lab frame is useful for experimental measurements, typically the center of mass frame (c.m.) of the final np system is chosen for theoretical calculations. The c.m. system is related to the lab frame by a boost along $\vec{q}$ characterized by the boost parameter γ. Where γ is defined as

$$\gamma = \frac{E_{np}^{LAB}}{W_{np}} \tag{2.40}$$

with E_{np}^{LAB}, the final energy of the np system, and W_{np}, the invariant mass of the final state. In terms of lab quantities, this is given by

$$W_{np} = \sqrt{(E_{np}^{LAB})^2 - (\vec{q}^{LAB})^2} \tag{2.41}$$

$$= \sqrt{M_d(M_d + 2\omega) - Q^2}. \tag{2.42}$$

In this frame the relative np momentum, $\vec{p}_{np} = \frac{\vec{p}_p - \vec{p}_n}{2}$, is $\vec{p}_{np} = (p^{c.m.}, \theta^{c.m.}, \phi)$ and along with $\vec{q}$ define the reaction plane (the superscript from ϕ angle is dropped since azimuthal angles are unaffected by boosts along the z-direction). The asymmetries are functions of the polarization angles θ_d and $\tilde{\phi}_d = \phi_{pn} - \phi_d$ as well as the three independent variables needed to characterize the structure functions. A useful variable experimentally is the "missing momentum" whose vector is defined as the difference between the measured proton momentum and the virtual photon 3-vector:

$$\vec{p}_M \equiv \vec{p'} - \vec{q} \tag{2.43}$$

In the case that only the proton that interacts with the photon, the missing momentum is equal to the bound relative momentum of the proton and in this way measuring an asymmetry as a function of this variable approximates probing shorter distances of the deuteron structure for higher p_m values. Also, to the extent that the fermi momentum of the proton can be ignored, a value of zero for p_m implies that the proton was struck "quasi-elastically". This limiting case occurs when $Q^2 = 2m_p\omega$, where m_p is the mass of the proton. In this regime one expects the Plane Wave Impulse Approximation to hold, but as p_m increases other effects such as Meson Exchange Currents (MEC), Isobar Configurations (IC), and Final State Interactions (FSI) should have a greater contribution as well as the coupling of the photon to the neutron, the Plane Wave Born Approximation (PWBA).

An important distinction between the Plane Wave Impulse Approximation and the Plane Wave Born Approximation needs to be made. The connection of the cross-section as giving direct access to the the momentum wave functions of the deuteron

can only be made in the case that coupling of the photon to the neutron can be ignored. When the interaction is described by incoming and outgoing plane waves and the bare proton is the same as that when in the deuteron, the factorized cross-section depends on the spectral function $S(E_m, p_m)$ and represents the probability of finding a proton with initial energy and momentum as E_m (limited by the deuteron's binding energy as $2.2MeV$) and p_m respectively. The factorized differential cross section is

$$\frac{d^6\sigma}{d\epsilon' d\Omega_{\epsilon'} dT_p d\Omega_p} = pE_p\sigma_{ep}S(E_m, p_m), \tag{2.44}$$

where p is the magnitude of $\vec{p}$ and E_p are the final three-momentum and energy respectively. By integrating the spectral function over missing energies in the above equation over the E_m range, the result within the PWIA framework is the momentum distribution for the deuteron,

$$\rho(P_m) = \int_{\Delta E_m} S(E_m, p_m)dE_m = u^2(p_m) + w^2(p_m). \tag{2.45}$$

2.7.2 Formalism

The total cross section can be written in terms of asymmetries diluted by various combinations of the beam helicity h, vector asymmetry $\tilde{P}_z$, and tensor polarizations $\tilde{P_{zz}}$ as follows [50]:

$$\begin{aligned} \frac{d\sigma}{d\omega d\Omega_e d\Omega_{pn}^{CM}} &\equiv S\left(h, \tilde{P}_z, \tilde{P}_{zz}\right) \\ &= S_0\left(1 + \tilde{P}_z A_d^V + \tilde{P}_{zz}A_d^T + h\left(A_e + \tilde{P}_z A_{ed}^V + \tilde{P}_{zz}A_{ed}^T\right)\right) \end{aligned} \tag{2.46}$$

Here, h is the helicity of the electron beam, and $\tilde{P}_z$ and $\tilde{P}_{zz}$ are the respective vector and tensor polarizations of the deuteron target as described above. Also, $\Omega_e \equiv (\theta_e, \phi_e)$ and $\Omega_{pn}^{CM} \equiv (\theta_{pn}^{CM}, \phi_{pn})$ are the respective scattered electron and proton-neutron spherical angles. S_0 is the totally unpolarized cross section:

$$S_0 \equiv S\left(0, 0, 0\right) = c\left(\rho_L f_L + \rho_T f_T + \rho_{LT} f_{LT}\cos\phi_{pn} + \rho_{TT} f_{TT}\cos 2\phi_{pn}\right) \tag{2.47}$$

The 41 structure functions are contained in five asymmetries: the beam asymmetry A_e, vector asymmetry, A_d^V, tensor asymmetry A_d^T, beam-vector asymmetry, A_{ed}^V, and the beam-tensor asymmetry, A_{ed}^T.

$$\begin{aligned} A_d^V = \frac{c}{S_0} \sum_{M=0}^{1} \big[\big(& \rho_L f_L^{1M} + \rho_T f_T^{1M} \\ & + \rho_{LT} f_{LT}^{1M+} \cos\phi_{pn} + \rho_{TT} f_{TT}^{1M+} \cos 2\phi_{pn} \big) \sin M\tilde{\phi} \\ & + \left(\rho_{LT} f_{LT}^{1M-} \sin\phi_{pn} + \rho_{TT} f_{TT}^{1M-} \sin 2\phi_{pn} \right) \cos M\tilde{\phi} \Big] \, d_{M0}^1(\theta_d) \end{aligned} \tag{2.48}$$

$$\begin{aligned} A_d^T = \frac{c}{S_0} \sum_{M=0}^{2} \big[\big(& \rho_L f_L^{2M} + \rho_T f_T^{2M} \\ & + \rho_{LT} f_{LT}^{2M+} \cos\phi_{pn} + \rho_{TT} f_{TT}^{2M+} \cos 2\phi_{pn} \big) \cos M\tilde{\phi} \\ & - \left(\rho_{LT} f_{LT}^{2M-} \sin\phi_{pn} + \rho_{TT} f_{TT}^{2M-} \sin 2\phi_{pn} \right) \sin M\tilde{\phi} \Big] \, d_{M0}^2(\theta_d) \end{aligned} \tag{2.49}$$

$$A_e = \frac{c}{S_0} \rho'_{LT} f'_{LT} \sin\phi_{pn} \tag{2.50}$$

$$\begin{aligned} A_{ed}^V = \frac{c}{S_0} \sum_{M=0}^{1} \Big[& \left(\rho'_T f_T^{\prime 1M} + \rho'_{LT} f_{LT}^{\prime 1M-} \cos\phi_{pn} \right) \cos M\tilde{\phi} \\ & - \rho'_{LT} f_{LT}^{\prime 1M+} \sin\phi_{pn} \sin M\tilde{\phi} \Big] \, d_{M0}^1(\theta_d) \end{aligned} \tag{2.51}$$

$$\begin{aligned} A_{ed}^T = \frac{c}{S_0} \sum_{M=0}^{2} \Big[& \left(\rho'_T f_T^{\prime 2M} + \rho'_{LT} f_{LT}^{\prime 2M-} \cos\phi_{pn} \right) \sin M\tilde{\phi} \\ & + \rho'_{LT} f_{LT}^{\prime 2M+} \sin\phi_{pn} \cos M\tilde{\phi} \Big] \, d_{M0}^2(\theta_d) \end{aligned} \tag{2.52}$$

The scattering amplitudes associated with A_d^V and A_{ed}^T are the imaginary part of the scattering amplitude. This is the result of parity and time reversal invariance. Since in the absence of final state interactions, these amplitudes can be made real and are hence zero giving negligible values when FSI is included. The beam asymmetry, A_e, is non-zero but small in the case of BLAST because it is proportional to $\sin\phi$ and since BLAST is symmetric in this angle, the integral over this angle leaves a small quantity. This leaves A_{ed}^V and A_d^T as the most experimentally viable observables for BLAST. To separate out the asymmetries one measures certain combinations of beam and

target polarization. Each asymmetry can therefore be separated out in the following manner:

$$
\begin{aligned}
S_0 &= \frac{1}{6}\Big[S(h,\tilde{P}_z,\phi\tilde{P}_{zz}) + S(-h,\tilde{P}_z,\tilde{P}_{zz}) + S(h,-\tilde{P}_z,\tilde{P}_{zz}) \\
&\quad + S(-h,-\tilde{P}_z,\tilde{P}_{zz}) + S(h,0,-2\tilde{P}_{zz}) + S(-h,0,-2\tilde{P}_{zz})\Big] \qquad (2.53)\\
A_e &= \frac{1}{6hS_0}\Big[S(h,\tilde{P}_z,\tilde{P}_{zz}) - S(-h,\tilde{P}_z,\tilde{P}_{zz}) + S(h,-\tilde{P}_z,\tilde{P}_{zz}) \\
&\quad - S(-h,-\tilde{P}_z,\tilde{P}_{zz}) + S(h,0,-2\tilde{P}_{zz}) - S(-h,0,-2\tilde{P}_{zz})\Big] \qquad (2.54)\\
A_d^V &= \frac{1}{4\tilde{P}_z S_0}\Big[S(h,\tilde{P}_z,\tilde{P}_{zz}) + S(-h,\tilde{P}_z,\tilde{P}_{zz}) \\
&\quad - S(h,-\tilde{P}_z,\tilde{P}_{zz}) - S(-h,-\tilde{P}_z,\tilde{P}_{zz})\Big] \qquad (2.55)\\
A_d^T &= \frac{1}{12\tilde{P}_{zz} S_0}\Big[S(h,\tilde{P}_z,\tilde{P}_{zz}) + S(-h,\tilde{P}_z,\tilde{P}_{zz}) + S(h,-\tilde{P}_z,\tilde{P}_{zz}) \\
&\quad + S(-h,-\tilde{P}_z,\tilde{P}_{zz}) - 2[S(h,0,-2\tilde{P}_{zz}) + S(-h,0,-2\tilde{P}_{zz})]\Big] \qquad (2.56)\\
A_{ed}^V &= \frac{1}{4h\tilde{P}_z S_0}\Big[S(h,\tilde{P}_z,\tilde{P}_{zz}) - S(-h,\tilde{P}_z,\tilde{P}_{zz}) \\
&\quad - S(h,-\tilde{P}_z,\tilde{P}_{zz}) + S(-h,-\tilde{P}_z,\tilde{P}_{zz})\Big] \qquad (2.57)\\
A_{ed}^T &= \frac{1}{12h\tilde{P}_{zz} S_0}\Big[S(h,\tilde{P}_z,\tilde{P}_{zz}) - S(-h,\tilde{P}_z,\tilde{P}_{zz}) + S(h,-\tilde{P}_z,\tilde{P}_{zz}) \\
&\quad - S(-h,-\tilde{P}_z,\tilde{P}_{zz}) - 2[S(h,0,-2\tilde{P}_{zz}) - S(-h,0,-2\tilde{P}_{zz})]\Big] \qquad (2.58)
\end{aligned}
$$

Measuring asymmetries is experimentally advantageous because the measurement depends only on the ratio of counts for various beam and target configurations. Since the total cross-section cancels out, regions of detector inefficiencies cancel to first order in the measurement.

The dynamical information on the electrodisintegration of the deuteron is contained within the structure functions, $f_{\mu\mu}^{(\prime)IM}$. Therefore, a complete measurement of the system is to separate out these functions. There is not a comprehensive method for doing this; however, below are two general cases and the reader is instructed to refer to the appendix of [50] for a complete list.

The general form of the asymmetries is

$$A(\phi, \tilde{\phi}, \theta_d) = \sum_{M=0}^{I} \alpha_{IM}(\phi, \tilde{\phi}) d^I_{MO}(\theta_d), \tag{2.59}$$

where the angles ϕ and $\tilde{\phi}$ separate in the form of

$$\alpha_{IM}(\phi, \tilde{\phi}) = c_{IM}(\phi) \cos M\tilde{\phi} + s_{IM}(\phi) \sin M\tilde{\phi} \tag{2.60}$$

and the functional form of the $c's$ or s's take on either

$$\sum_{l=0}^{l=2} a_l \cdot \cos l\phi \tag{2.61}$$

or

$$\sum_{l=0}^{l=2} a_l \cdot \sin l\phi \tag{2.62}$$

It is important to note that the coefficients, a_l's, contain products of the virtual photon density matrix elements and the structure functions. The two main cases for determining a_l, for the vector case (I=1) and the tensor case (I=2), are given below.

I=1 Case (Vector Asymmetries)

1) The vector asymmetry contains α_{10} and α_{11}. To access α_{10} a target angle of $\theta_d = 0$ is chosen such that $d^1_{00} = \cos\theta_d = 1$ and $d^1_{10} = -\frac{1}{2}\sin\theta_d = 0$. Conversely $\theta_d = \frac{\pi}{2}$ to access α_{10}.

2) To access the particular c_{1M} or s_{1M}, $\tilde{\theta}$ is chosen such to be $\tilde{\phi} = 0$ or $\frac{\pi}{2M}$ where $M \neq 0$.

3.) Finally, separation of a particular a_n or b_n is achieved by choosing an appropriate ϕ.

I=2 Case (Tensor Asymmetries)

1) For the tensor asymmetries, choosing θ_d will yield α_{20} and then $\theta_d = \pi/4$ and $\theta = \pi/2$ gives α_{21} and α_{22} and to separate these two, one chooses $\theta_d = \arccos(1/\sqrt{3})$ along with $\tilde{\phi}$ or $\tilde{\phi} + \pi$ respectively. The sum and difference of these two give α_{21} and α_{22}.

2.) To obtain C_{IM} one chooses $\tilde{\phi} = 0$ and for the S_{IM} term, $\tilde{\phi} = \pi/2M$ for

$M \neq= 0$

3.) A separation of a particular a_n or b_n is acheived by choosing an appropriate ϕ^2.

2.7.3 Calculations and Corrections to the Asymmetries

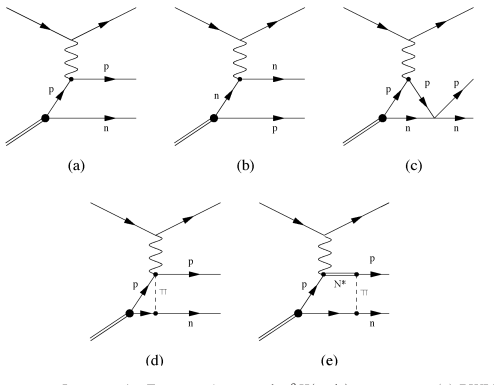

Figure 2-10: Feynman diagrams for lowest order electrodisintegration where the proton is detected in the final state i.e. ${}^2H(e,e'p)n$. (a) PWIA (b) PWIA coupling to neutron (c) final state interaction (d) meson exchange current with a π (e) N^* excited state. Symmetrization of (a) and (b) is the Plane Wave Born Approximation (PWBA)

NN-potential models

The formalism to describe the electrodisintegration of the deuteron was developed by Arenhoevel and collaborators and has incorporated a number of realistic potentials into the formalism. He has employed the Nijmegen, Paris, Bonn (r and p-space versions) and the Argonne V18 [11]. In general, observables were found to depend rather moderately on the choice of potential used. In the work here, only the Bonn p-space and the completely phenomenological Argonne V18 in r-space are shown.

MEC Corrections

In the disintegration of the deuteron, it is necessary to include two-body currents that result from the production of mesons (π, ρ, ω) in the nucleon-nucleon interaction. In the case of the Bonn potential, all mesons exchanged are put in explicitly, resulting

[2]In some cases the a_o term will contain a combination of structure functions. In this case a Rosenbluth separation is needed.

in a relatively straightforward meson exchange current. The recipe for handling the 2-body currents in the completely phenomenological, Argonne V18 was put forth by Riska [51] and Buchman [52]. They associate the isospin-central and tensor parts of the NN potential with the pion and rho-exchange like potential of corresponding meson exchange models.

Relativistic Corrections

There are three sources for relativistic effects [44]. The first effect is inherent in the deuteron itself since the nucleons have relativistic components in the rest frame of the nucleus. In this case the nucleons cannot be described by simply the non-relativistic reduction of the Dirac Current especially at higher energies and momentum transfer. The work of Arenhoevel handles this by maintaining leading order corrections of the Dirac-Pauli form factors (for p-space) or, alternatively the Sachs form factors, for r-space code. Each one body operator[3] is written as the standard form plus the next to leading order contributions.

The second contribution occurs because the calculations are done in the c.m. system, one that is boosted due to the momentum transfer of the electron. The result is that the wavefunction are no longer described purely non-relativistically. The wave function does not separate into a piece that depends on the overall motion of the deuteron described by the c.m. coordinate $\vec{P} = \vec{p}_1 + \vec{p}_2$ and a wavefunction of the relative coordinate $\vec{p} = \frac{\vec{p}_1 - \vec{p}_2}{2}$ but rather

$$|\vec{P}, \vec{p} >= |\vec{P}_{c.m.} > \otimes e^{-i\chi(\vec{P})} |\vec{p}_{int} > \tag{2.63}$$

where $\chi(\vec{P})$ is the boost generator. Keeping only the leading terms results in a non-vanishing interaction dependent part that exists only for pseudoscalar meson exchange [44]. The third contribution to relativistic corrections are attributed to the current operators themselves. They are expanded in quantities of p/M_p with only the leading

[3] In addition Arenhoevel uses on-shell form factors in the one-body operators. It is unclear whether it is justified since bound nucleons are not the same as free ones and subject to the strong force. There has been recent work where off-shell effects were investigated for deuteron photo-disintegration using a simple pion-cloud model and were shown to be negligible.

order beyond the non-relativistic limit retained[4]. Since the nucleon will have a value around the fermi-momentum $p \sim p_F \sim 55\ MeV/c$ giving a value of $\sim \frac{1}{5}$ keeping only the leading order term is justified. For a list of current operators, the reader is instructed to consult the appendix of [53].

Isobar configurations

Isobar degrees of freedom are incorporated directly into the wave functions as opposed to applying nonlocal two-body operators for the excited states. This allows the handling of real excitation of the delta when the momentum transfer exceeds pion threshold. The r-space code has included $N\Delta$, $NN(1440)$, and $\Delta\Delta$ configurations with the $N\Delta$ configuration for the p-space code [11]. The wavefunctions are obtained either by perturbative means or using the coupled channel approach. The method using the coupled channeled approach, as was used for the p-space Bonn potential, is described in [53].

2.7.4 Tensor Asymmetry

As shown by equation (2.25), one loses the ability to access the L=2 state in the PWIA approximation when performing electrodisintegration measurements without polarization. Therefore, one must turn to polarization to access the D-state in this approximation. While in the elastic channel the total nuclear current is measured, for electrodisintegration the cross section factorizes into two parts: an off-shell e-p cross section and a part containing the spin-dependent momentum distribution. The tensor asymmetry in this case is directly related to the spin densities as follows:

$$A_d^T = \sqrt{\frac{1}{2}}\frac{\sigma_{+1}(p_m) + \sigma_{-1}(p_m) - 2\sigma_0(p_m)}{\sigma_0(p_m) + \sigma_{-1}(p_m) + \sigma_{+1}(p_m)} \tag{2.64}$$

$$= \frac{\tilde{C}_2(k)}{\tilde{C}_0(k)} P_2(\cos\theta) \tag{2.65}$$

$$= -\frac{2\tilde{R}_2(p)\tilde{R}_0(p) + \frac{1}{\sqrt{2}}\tilde{R}_2^2(p)}{\tilde{R}_0(p)^2 + \tilde{R}_2(p)^2}(\frac{3}{2}\cos^2\theta_k - \frac{1}{2}) \tag{2.66}$$

[4] A fully relativistic treatment of the the $^2D(e,e'),n$ at BLAST energies has been done by Jeschonnek and Van Orden. In they apply the Gross equation to describe the deuteron ground scattering both on and off-shell treatments to the final state interactions.

Figure 2-11 shows calculations for A_d^T vs relative momentum p and $\cos\theta_p$. Since the tensor asymmetry is proportional to $\tilde{R}_2$, A_d^T vs p would be zero in the case of a purely S ground state. In the region of low momentum where $\tilde{R}_0(p) << \tilde{R}_2(p)$, or less than 0.3 GeV, the tensor asymmetry is directly related to the ratio of the D to S state probabilities.

When examining the tensor asymmetry as a function of θ_p, the shape in this approximation is proportional to $d^2_{0,0}$ and therefore well known. The zeros should occur at $\cos\theta_k = \sqrt{(1/3)}$ with deviations a strong test of non-PWIA effects, *i.e.*, including the photon coupling to the neutron, interactions in the final state, meson-exchange currents and isobar currents. Figure 2-12 shows the first measurement of A_d^T vs $\cos\theta_s$,the angle between polarization axis and p_m that was done at the NIKHEF using a polarized target in the internal AmPS electron storage ring along with detector-specific calculations as done by Arenhoevel's group. The results show fairly good agreement with the theoretical curves of the full calculation. They also investigated various potentials: the Paris, Bonn, Nijimegen and Argonne potentials and found the results differ by less than 1% for the missing momentum range of their experiment. In addition, they found that relativistic effects only need to be carried out to second order in the current operators and the boost operator term can be ignored.

2.7.5 Beam-Vector Asymmetry

Along with the tensor asymmetry, the beam-vector asymmetry provides a solid testing ground of the D-state contribution as well as the subnuclear effects and isobar configurations mentioned previously. Figure 2-13 shows a measurement of A_{ed}^V vs p_m from the experiment done at NIKHEF[12] along with theoretical curves of increasing effects incorporated into the calculation. One sees that the asymmetry is negative for low p_m and in the absence of the D-state remains nearly flat as p_m increases. When a D-state is included, the value of A_{ed}^V remains flat until the D-state begins to dominate over the S-state. In the PWIA this can be seen from the figure to be around 300 MeV. Also all subnuclear effects and effects of the PWBA disappear as

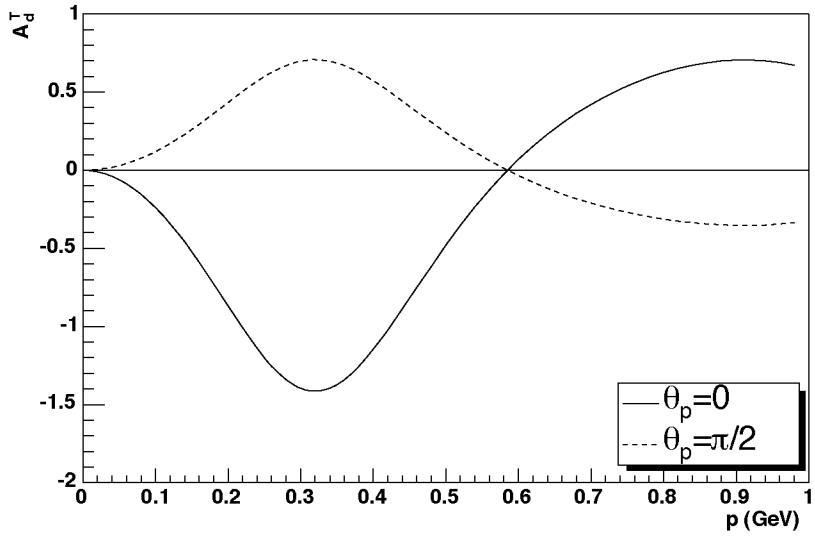

(a) A_d^T vs p

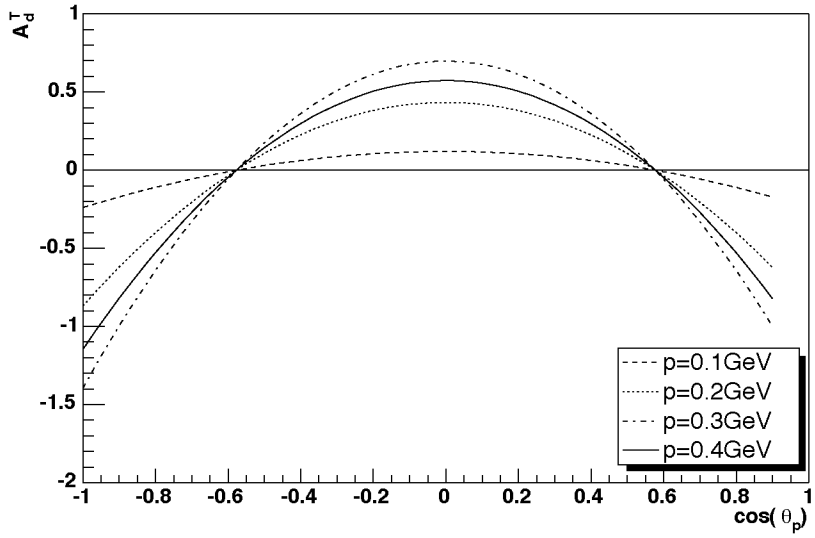

(b) A_d^T vs $\cos\theta_p$

Figure 2-11: Calculated values of A_d^T vs relative momentum, p, and $\cos\theta$. Taken from [14]

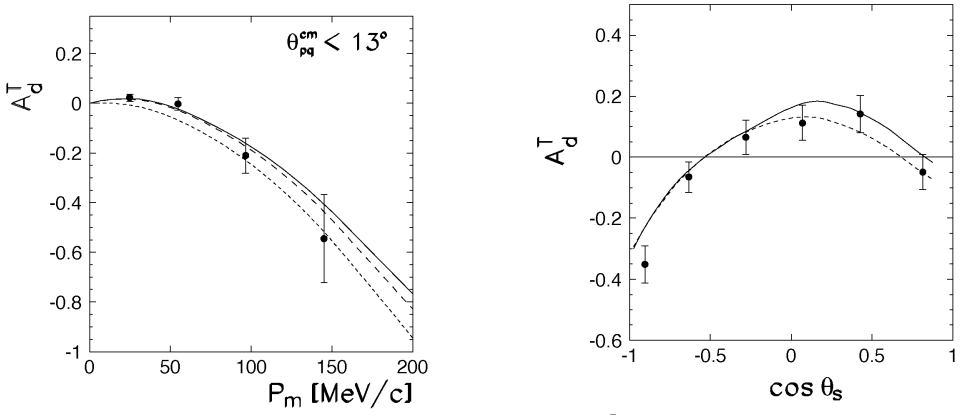

(a) A_d^T vs p_m. The dashed curve is the result for PWBA, the solid curve includes FSI, MEC, and IC contributions and relativistic corrections.

(b) A_d^T vs $\cos\theta_m$. The short-dashed curve represents PWBA, the long dashed-curve FSI are also included, and the solid curve is the full calculation.

Figure 2-12: Measurement of A_d^T vs p_m and $\cos\theta_m$ from the NIKHEF experiment using the Big Bite Spectrometer [13]

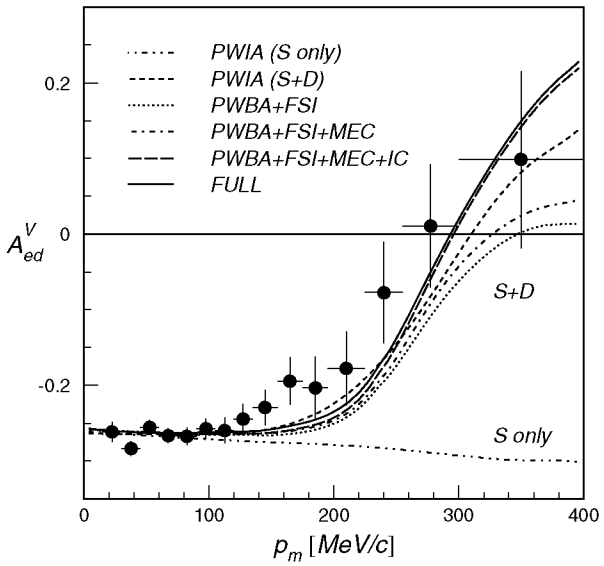

Figure 2-13: Measurment of A_{ed}^V vs p_m from the NIKHEF experiment using the Big Bite Spectrometer [13]

$p_m \to 0$, but as p_m increases, essentially the full calculation is needed for agreement between theory and data at higher values of p_m. An exception to this appears in the intermediate range of 150 MeV to 300 MeV where in [12] they attribute the source of disagreement between theory and experiment to a lack of understanding of the D-state contribution or contributions of Δ excitations. Since in the quasi-elastic limit the reaction mimics elastic electron-nucleon scattering, one can write the beam-vector asymmetry in terms of the ratio of the electric to magnetic form factor:

$$A_{ed}^{V}\left(\theta_d, \phi_d\right)_{p/n} = -\sqrt{\frac{2}{3}} \frac{1}{\left(1 + \frac{\rho_L}{\rho_T} R_{p/n}^2\right)} \left[\frac{\rho'_T}{\rho_T} \cos\theta_d + 2\frac{\rho'_{LT}}{\rho_T} \sin\theta_d \cos\phi_d R_{p/n},\right] \quad (2.67)$$

where the "p/n" subscript refers to whether the proton/neutron is detected in the final state and $R_{p/n}$ is the ratio of electric to magnetic nucleon form factors, $G_E^{p/n}/G_M^{p/n}$.

By detecting the scattered nucleon in plane with "perpendicular" kinematics where $(\theta_d, \phi_d) = (\pi/2, 0)$, one has direct access to the ratio of electric to magnetic form factors,

$$A_{ed}^{V}\left(\theta_d = \frac{\pi}{2}, \phi_d = 0\right)_{p/n} = -2\sqrt{\frac{2}{3}} \frac{\rho'_{LT}\rho_{p/n}}{\rho_T} R_{p/n}. \quad (2.68)$$

This provides a nearly model-independent way of measuring the rather uncertain G_E^n when the neutron is detected in the final state, which was a major thrust of the BLAST project [54, 55, 56]. In the case of the proton, since the value of A_{ed}^V is essentially model independent at low p_m, this provides an accurate method to measure the product of the beam and vector target polarization, $h \cdot P_z$ whose value can be used for other reactions in the experiment.

Chapter 3

Experimental Setup

3.1 MIT Bates

3.1.1 Polarized Source and Bates Linac

Polarized electrons were created by photoemission from a GaAs cathode using circularly polarized light [57] [58] [59]. The photocathode was doped with 5% Phosphorous to lower the peak polarization wavelength from 850 nm to 810 nm to match the light source, which consisted of a fiber-coupled diode array laser system operating at 808 $\pm$ 3 nm with 250 W peak power. Circularly polarized light was obtained by a system of polarizers and wave plates with a half-wave plate inserted in or out to flip the emerging electron's spin. A Wein filter was used to rotate the beam polarization to the desired orientation before injecting into the ring.

Beam polarization was monitored periodically with a 20 MeV transmission polarimeter [60]. In the transmission polarimeter the electron beam struck a Berylium Oxide target and emitted bremsstrahlung photons whose polarization was directly related to that of the beam polarization. These photons passed through a scintillator serving as a discriminator before being absorbed in a magnetic iron block. The rate of transmission is dependent on the photon polarization and that of the iron, known as roughly the fraction of unpaired electrons. In this way the transmission rate is related back to the initial electron polarization.

After emerging from the photocathode, the beam entered the Bates Linac and recirculator. The linac consisted of 190 m of RF cavities and could accelerate electrons up to 440 MeV in a single pass. To increase the energy further, the beam entered the recirculator and made a second pass in the Linac with the final beam energy up to 1 GeV [61].

3.1.2 South Hall Ring

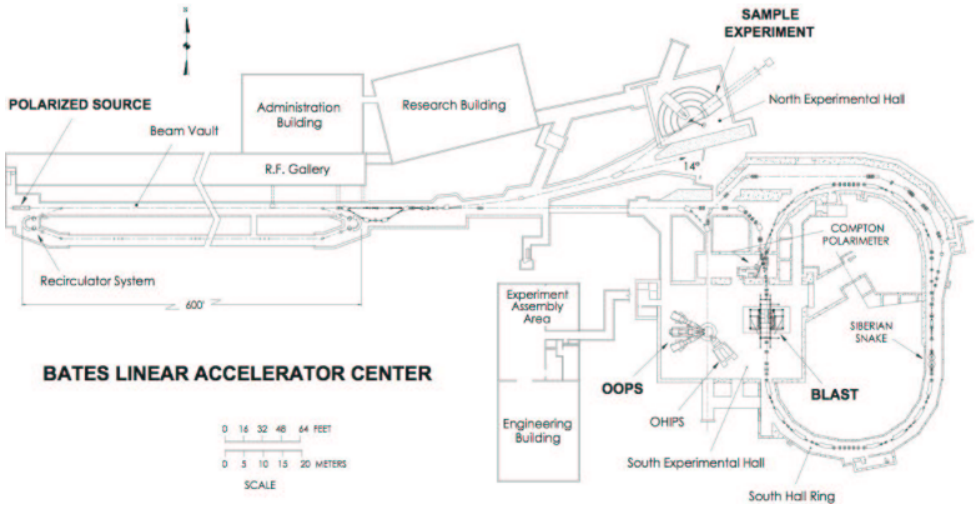

Figure 3-1: Layout of the Bates Linear Accelerator Center including various experiments: OOPS,OHIPS, SAMPLE and BLAST

Upon leaving the linac, the beam was injected into the South Hall Ring in a process that consists of stacking beam pulses "head to tail". Beam pulses left the photo-cathode at a rate of 10 Hz (based on the damping time from the south hall ring) with a peak intensity of 2 mA and a width of 1.6 μ s. This was further shortened by an energy compression system to 1.3 μ s, chosen to be the transit time for beam around the recirculator. Thus in the "head to tail" scheme, the front edge of electrons of the recirculated pulse follows immediately behind the trailing edge from the buncher. For each pulse, 4 mA was added to the ring in a way that makes it nearly continuous.

The South Hall Ring followed a race track design with two curved and two straight sections (See Figure 3-1). There were 16 dipoles to bend the beam and a single

RF cavity was used to compensate for synchrotron radiation losses. The BLAST detector was located in the western straight section near the injection point. Because of this, the beam had a strong waist and the injected beam has a cross-over to ensure the target was not stuck during beam stacking. Typically, operation consisted of stacking currents in excess of 200 mA whose lifetime was measured by a South Hall Ring's Direct Current Current Transformer. Lifetimes upwards of 45 minutes were achieved with an empty target cell, limited by quantum lifetime. For normal operation, however, lifetimes with internal targets were typically on the order 25 minutes.

A series of quality control measures were installed to ensure the beam was operated properly. Plastic scintillators, installed on all sides of the beam pipe downstream of the target cell, were used in tandem with beam scraping slits to minimize and monitor the strength and extent of the beam halo. In addition, 32 other beam position monitors and a synchrotron light monitor, which told information on the beam profile, were used for steering the beam through the target. Finally, steering correctors were needed to sustain two different beam tunes for injection and storage.

Since the spin of an electron moving in a ring will precess about the ring's plane, leaving it rotated 180 degrees from its initial direction after one-half turn, a method was needed to preserve the polarization near the target. A Siberian Snake [62] was therefore installed in the eastern straight section of the ring, across from the target. Designed in Novosibirsk, the snake consisted of two solenoids that rotated the spin 180 degrees about the beam line. In this way the spin rotation of the southern half was compensated by the rotation through the northern half providing the correct polarization at the target.

3.1.3 Compton Polarimeter

Since double polarization asymmetries are diluted by the product of beam and target polarizations, a real time measurement of the target polarization was essential. In addition, the beam polarization changed with every fill, and therefore the method needed to be fast, accurate and non-destructive, since any effects were required to be

folded into the measurement. These qualifications led to the decision to use Compton Polarimetry techniques to measure the beam polarization.

In Compton polarimetry [63] a circularly polarized photon beam scatters off polarized electrons with most of the photons scattering backwards, i.e. at 180 °, and are heavily boosted into the UV range. The resulting asymmetry of left-handed vs. right-handed photons scattered off longitudinally polarized electrons (as was the case for BLAST) is a function of the energy and dependent on the polarization of the electrons. In this way the beam polarization can be extracted with minimal effect on its properties.

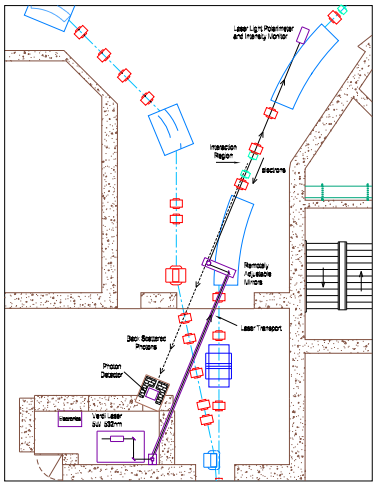

Figure 3-2: Layout of the Compton Polarimeter as Situated in the South Hall

The BLAST Compton Polarimeter was situated just upstream of the target region to minimize background effects due to bremsstrahlung (See Figure 3-2) [64]. With a design heavily influenced by the NIKHEF polarimeter [12], it consisted of a 5 Watt laser operating at 532 nm light and used a series of remote controlled mirrors to steer the laser beam at a crossing angle of less than 2 mrad. The resulting scattered photons were detected with a pure CsI calorimeter with a moveable lead collimator in front of the detector to minimize background due to beam halo. In addition high rates into the detector when operating at full beam current were attenuated by the insertion of stainless steel absorbers in front of the laser, whose attenuation response

was nearly flat across the energy spectrum and insensitive to photon polarizations.

For beam energies less than 1 GeV, the analyzing power was a few percent, making polarization extraction difficult. Furthermore, the Compton edge, where the asymmetry was largest, was low compared to the maximum Brehmstrahlung energy making separation of the signal from background another challenge. Figure 3-3 shows the raw ADC spectrum and asymmetry results for a single measurement. Figure 3-3(a) shows a signal to background of 8:1 obtained through precise beam steering and use of the lead collimator. For the asymmetry result (figure 3-3(b)), the polarization was extracted by fitting the measured result to a theoretical curve wherein the beam polarization was treated as a free parameter.

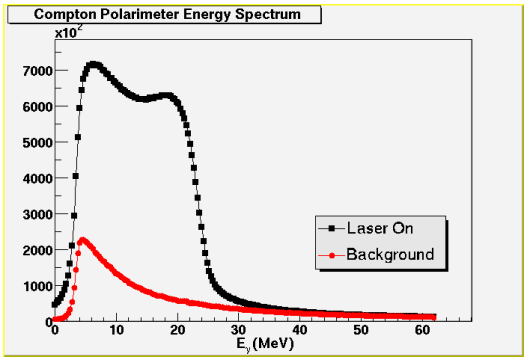

(a) Raw ADC spectrum for Compton Polarimeter

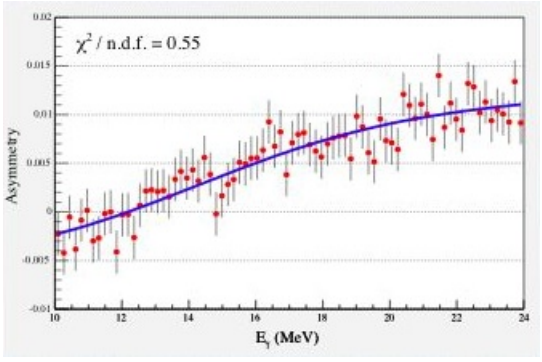

(b) Asymmetry measurement for a single fill showing theoretical fit used to extract beam polarization

Figure 3-3: Compton polarimetry data and analysis for a single beam fill

During normal operation the beam polarization direction was flipped every fill. To verify that the value was the same for each helicity state and a not systematic effect due to differences in beam tune, a spin flipper was installed in the ring [65] that rotated the beam polarization. This magnet worked by ramping the frequency of an RF dipole magnet through an RF-induced depolarizing resonance, thereby flipping the beam helicity by 180 degrees in real-time. Figure 3-4 shows measurements taken before and after using the RF flipping magnet. The beam polarization was found to be the same for both helicity states within the experimental uncertainty.

Polarization measurements over the duration of this experiment are shown in Figure 3-5. The average polarization was measured to be $P = 0.6558 \pm 0.0007(stat) \pm$

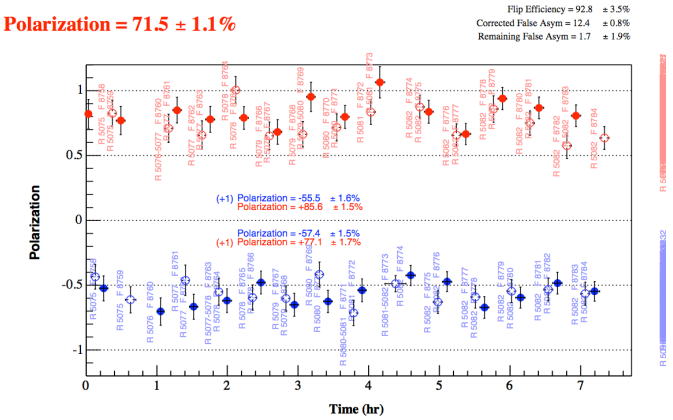

Figure 3-4: Beam polarization for both helicity states in addition to those measurements using the RF flipping magnet. The solid circles are the measurement made at the beginning of a fill, the hollow circles are after the spin flipper was used.

$0.04(sys)$ with a systematic error mainly due to uncertainty in the analyzing power and beam alignment.

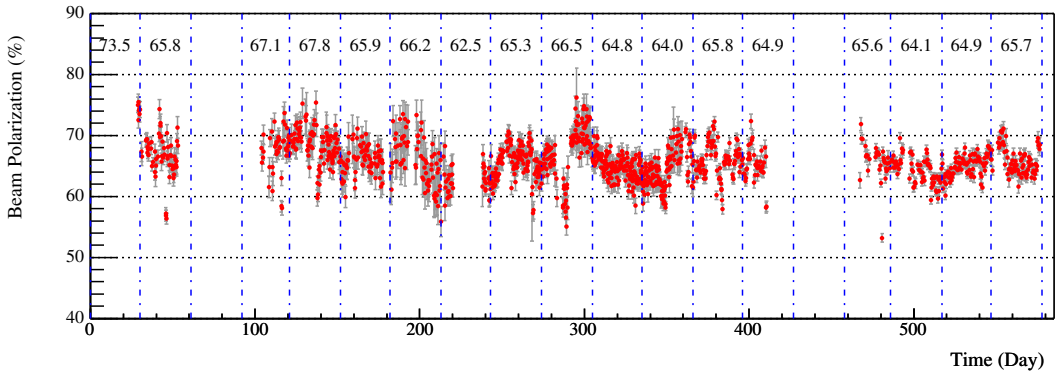

Figure 3-5: Beam polarization results over the entire running of BLAST

3.2 Atomic Beam Source

Internal targets have been used increasingly over recent years due to their many benefits. Although their densities are much lower than for solid targets, they have a high degree of polarization and are pure in species. This eliminates the need to preform complicated background subtraction and therefore removes a major source of systematic uncertainty. In addition, polarized gas targets can be rapidly switched,

both in terms of gas used and the state of polarization so that systematic effects are further minimized.

The internal targets of polarized hydrogen and deuterium were provided by an atomic beam source, ABS [66]. Based on the ABS at NIKHEF [67], the BLAST ABS had to undergo significant design changes to accommodate the small space requirements and the high residual magnetic field of BLAST.

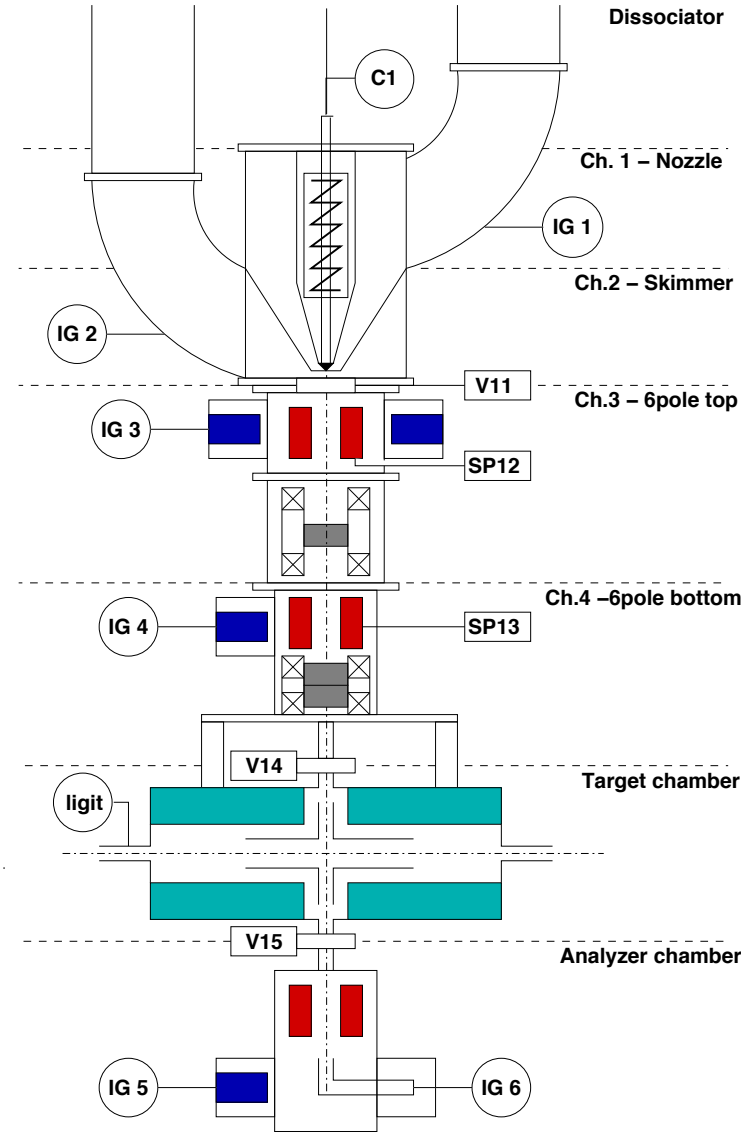

Figure 3-6: Schematic showing the layout of the ABS

Figure 3-6 shows a schematic of the BLAST ABS. Gas from a gas feed system flowed through an RF dissosciator to produced atomic hydrogen or deuterium. The gas traveled through a series of apertures, forming an atomic beam of atoms where it then passed through a series of sextupole magnets and RF transition units. By the Stern-Gerlach effect, the sextupole magnets focused those atoms with + 1/2 spin while de-focusing the rest, while the transition units caused transition between hyperfine states using RF fields. By using these apparatuses in specific combinations, individual quantum states were selected, and a beam of a pure polarized species was produced. After the beam was been formed, it entered the target storage cell where it interacted with the beam, diffusing to the ends of the cell before being pumped away. At the bottom of the storage cell there was a small aperture where gas was fed into a Breit-Rabbi polarimeter [68]. This helped in tuning and monitoring the performance of the transition units.

Figure 3-7 shows the hyperfine states for hydrogen and deuterium. For hydrogen, the beam first passed through the first sextupole magnet, leaving states 1 and 2. Next, the medium field transition unit situated between the two sextupoles, caused a transition from state 2 to state 3. Therefore after passing through the second sextupole, state 1 remained, a vector plus (V+) state. Then, by turning the weak field transition on, the transition was made from 1 to 3, or the Vector minus state (V-).

Polarized Deuterium operated in hyperfine three states: one a pure tensor minus state (T-), and the other two combinations of tensor and vector polarizations. First, the beam passed through the first sextupole, leaving states 1,2 and 3. Then for pure tensor minus, the MFT induces a transition from state 1 to state 4. This left states 2 and 3 populated after the second sextupole so that with the WFT off, the SFT causes a transition of state 3 to state 5 leaving the beam in a pure tensor minus state. For the other states, a combination of vector plus/minus (V+/V-) with T+ , the MFT unit causes a transition between 3 and 4. Then for V+ and T+, the WFT is off and the SFT causing a transition between 2 and 6, populating 1 and 6. For the V- and T+ state, the WFT causes transitions 1 to 3 and 2 to 4 leaving the final state populated

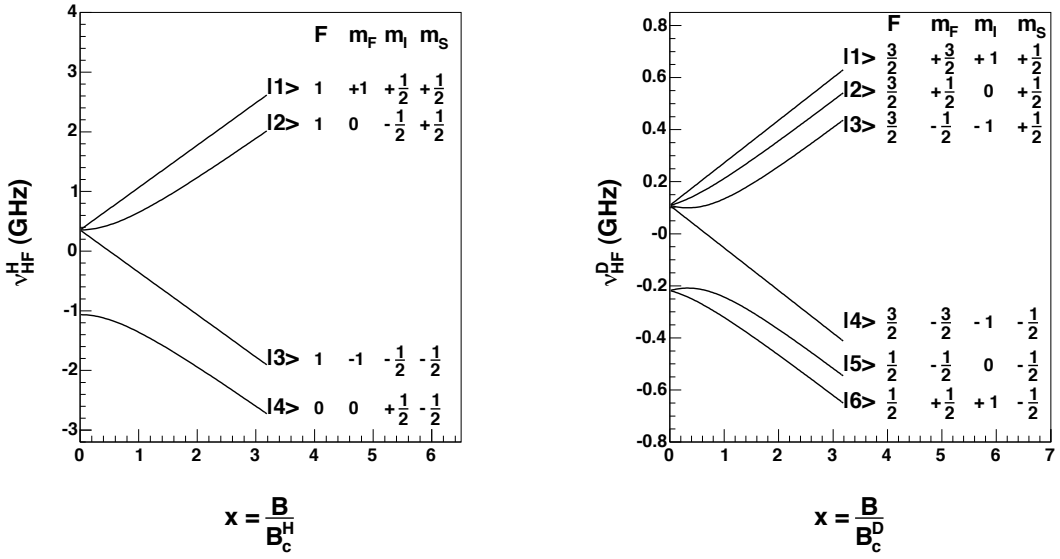

(a) Hydrogen

(b) Deuterium.

Figure 3-7: Breit Rabbi Diagram of energy levels of hydrogen and deuterium

by states 3 and 4. The results are summarized for both hydrogen and deuterium in Table 3.1

	Hydrogen		**Deuterium**		
Name	V+	V-	T-	T+,V-,	T+,V-
Sextupole	1,2	1,2	1,2,3	1,2,3,	1,2,3
MFT	1,3	1,3	2,3,4	1,2,4	1,2,4
Sextupole	1	1	2,3	1,2	1,2
WFT	off	3	off	off	3,4
SFT	off	off	3.5	1,6	off
States	1	3	3,5	1,6	3,4
P_z	+1	-1	0	-1	+1
P_{zz}	+1	-1	-2	+1	+1

Table 3.1: Hyperfine states selected by the ABS for Hydrogen and Deuterium

The atomic beam then entered the target cell which consisted of a 60 cm long, 1.5 cm diameter cylindrical aluminum tube (See Figure 3-8). By having the cell connected directly to the beam line, there were no exit or entrance windows that could create background events. Gas was injected through a feed tube at the top of the cell and diffused outward to the ends where it was pumped away. The density distribution

was therefore triangular in shape with virtually no gas extending beyond the cell ends. To prevent depolarization and recombination effects from collisions with the cell wall during this diffusion, the cell was cooled to around 100 K and coated with the hydrophobic substance, Drifilm. In addition, to protect the cell walls from beam halo and injection flash, a thick tungsten colliminator with 1 cm diameter aperature was installed just upstream from the target cell.

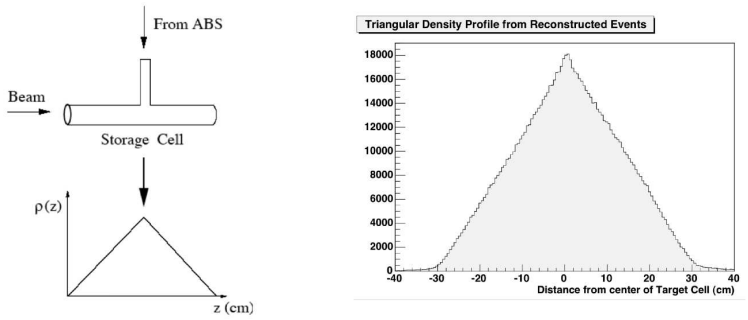

Figure 3-8: Schematic of the target storage cell. The measured density distribution as reconstructed vertex position (figure on right) is triangular as expected

To orient the target polarization of the gas within the target cell, a pair of electromagnet's were used. These consisted of two copper Helmholtz coils: one for the transverse field and one for the longitudinal one. Therefore, by the applying the appropriate currents, the target polarization was set to a specific direction within the horizontal plane. Figure 3-9 shows the spin profile measurements for 2004 and 20 05 data. The average spin angles were $31.3^\circ \pm 0.43^\circ$ for 2004 and $47.4^\circ \pm 0.45^\circ$ for 2005. These angles were chosen so that roughly the electrons scattered into the left sector were perpendicular to the beam spin and electrons scattered into the right sector were parallel. Due to the finite size of the coils and residual external fields, variations existed in the magnetic field along the beam line. A series survey measurements using hall probes and a magnetic compass developed by Jefferson Lab mapped the transverse field along the beam axis. Because all measurements yielded the same shape, a parameterized fit was preformed to the measurements leaving the average value free to be set from real physics analysis. For the case of hydrogen, this was determined by ep elastic scattering, for deuterium, by analyzing elastic e-d scattering data.

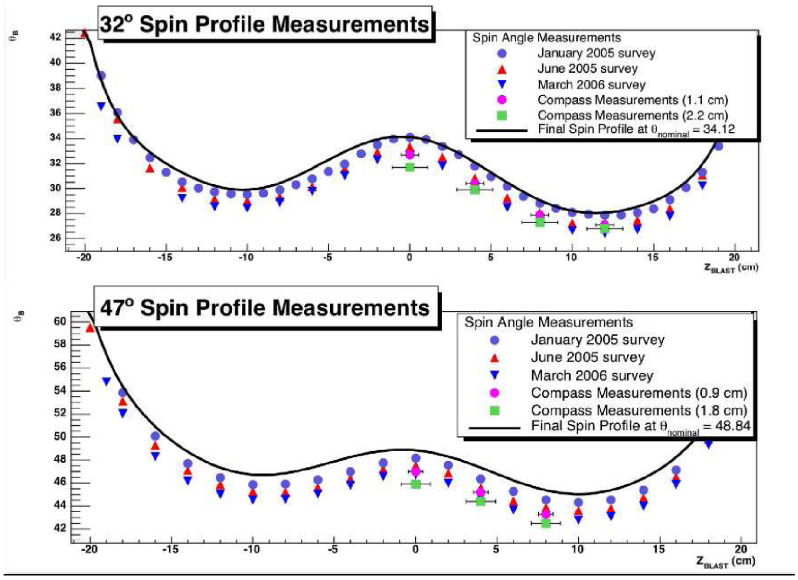

Figure 3-9: Target spin profile measurements along the beam axis for the 2004 data set (top) and the 2005 run (bottom). The different data points are made from various measuring techniques, while the curve is a fit to the data with the nominal value set by experiment

3.3 The Toroidal Magnet

The magnetic field for BLAST was provided by a toroidal magnet, a design chosen for its low field and low field gradient near the target region. The field was used to bend the trajectory of charged particles through the wire chamber to measure the sign of the charge and the particle's momentum. In addition, it reduced background events by sweeping away low energy particles before they made it through the detector.

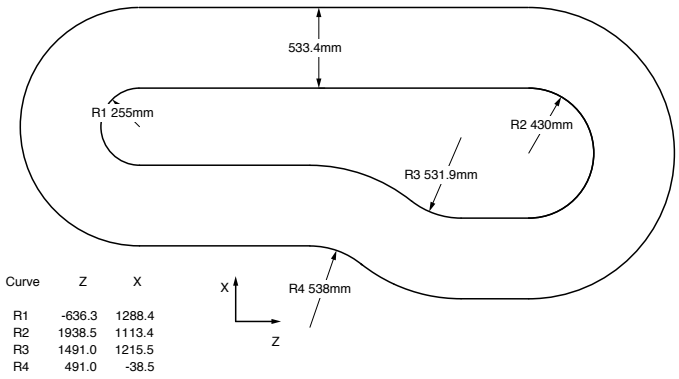

Figure 3-10: Schematic of a single BLAST toroid coil showing dimensions and position relative to target

The toroid consisted of 8 copper coils situated around the beam pipe (See Figure 3-10). Each coil contained 26 turns of hollow, 1.5 inch square copper tube. The coils were encased in G10 fiberglass sheets and epoxied to form a permanent mold. At maximum strength, the BLAST toroid had an operating current of 6730 A, producing a maximum field of approximately 3.8 kG. During operation the current was counter-clockwise, with electron (protons) bending inwards (outwards).

The two important goals during the commissioning phase of the BLAST toroid, was the minimization of the field near the target region and the mapping of the field in the shadow of the BLAST detector [69]. Since the internal target's polarization direction was set by Helmholtz coils located around the cell, it was important to have minimized any external fields near this region since an additional field would have caused a shift in the polarization vector. In addition small field and field gradients field along the beam pipe were necessary to minimize beam transport. The actual field needed to be determined as well, since the charge particles momentum was determined by swimming the particle through the BLAST detector with the velocity vector recalculated due to the magnetic field at each step.

The first step in the commissioning process was the positioning of the coils. By using the coil plane and the water inlets as alignment points, the coils were held first in the vertical and the alignment points referenced to survey targets on each coil. Then the coils were placed in their nominal position using electronic theodolites and CLASH (the SLAC intersection "laser" program). However, once in their nominal position, further adjustment was needed to minimize the field and gradients at the centerline. The six coils were thus moved radially between 2.6 and 7 mm, leaving the transverse field on the centerline at less than 10 G at full current which was sufficient for operation.

In theory, the magnetic field could have been calculated analytically from the Bio-Savart Law, however, uncertainties in the coil placement within the fiberglass mold and no direct surveying reference points left their exact positions unknown. In addition, the coils within their frames were not rigid: it was discovered that the inner edge of the coil bowed 7 mm under its own weight as compared to when the coils were

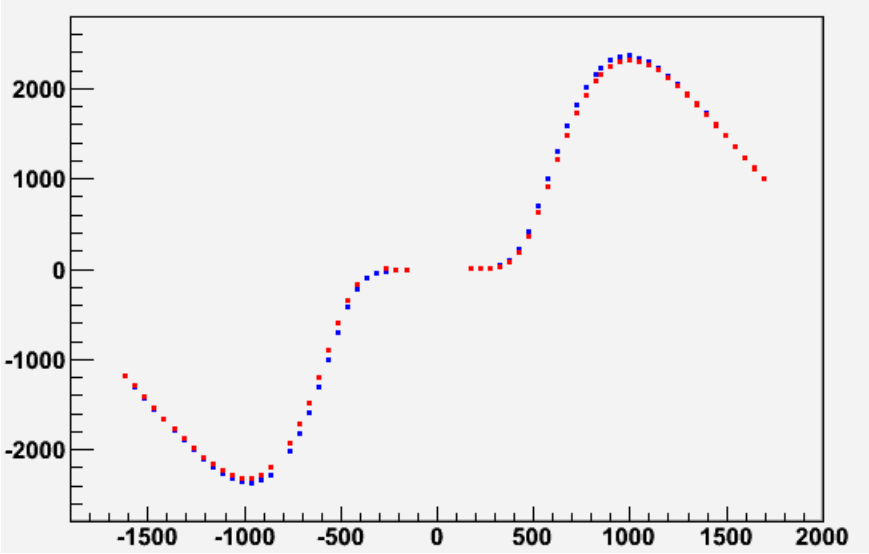

Figure 3-11: The y-component of the magnetic field in the horizontal plane of BLAST at an x value of 500 cm. The blue points are those determined from measurement; the red are calculated from Bio-Savart's Law

held vertically and the coils also had moved radially when energized. These effects and limitations necessitated a direct measurement of the fields.

The mapping setup consisted of an EPICS controlled table with a probe arm mounted on three independent axes. Hall probes were mounted on the probe arm and a sequencer program was written that would step the motor through the field region, pause until vibrations ceased at each measuring point, read and recorded the magnetic field. This was done on a 5 cm cubic grid in the table coordinate system, consisting of approximately 35,000 points.

Although the Bio-Savart calculation could not be used to obtain the true magnetic field, it was used to determine the coil displacements necessary to agree with the measured data. By letting the four coils surrounding the drift chamber to move radially, longitudinally and azimuthally, the agreement reached between measured and calculated around 1% (See Figure 3-11) was obtained. This was used to fill in those points either inaccessible to the mapping table or points the sequencer program had missed.

After the missing points were filled in, an interpolation was done to convert from the table coordinate system grid to one in beam coordinates. The differences in

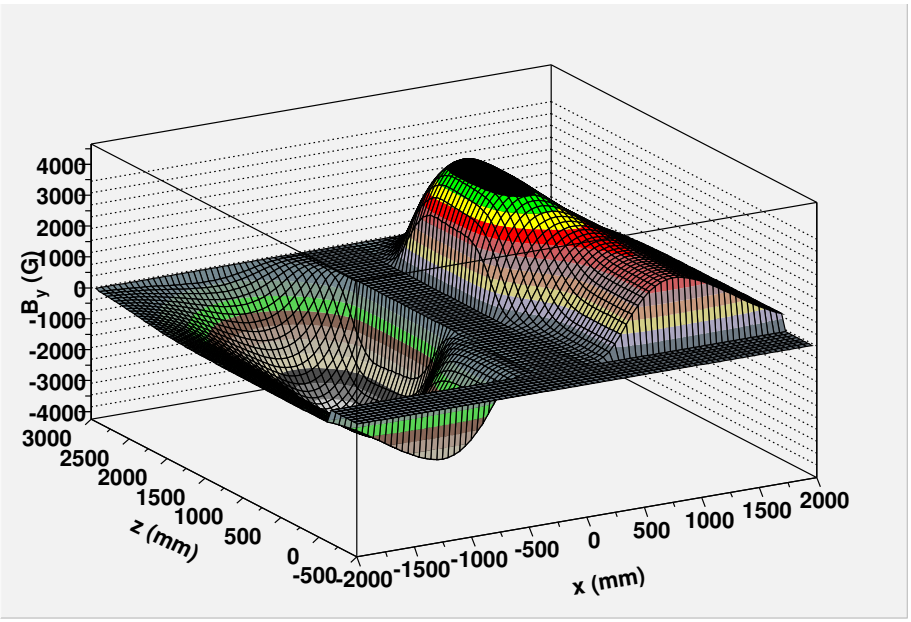

Figure 3-12: A two-dimensional plot of the y-component of the magnetic field in the horizontal plane of BLAST. Missing points were filled in by Bio-Savart Calculations

distances were small enough that only a second-order interpolation was needed. Figure 3-12 shows the magnitude of the magnetic field along dimensions for the beam coordinate grid. The uncertainty in the interpolation was typically less than 0.05%.

Uncertainties in B-field	
Probe Position * Field Gradient	$< 0.5\%$
Interpolation	$< 0.11\%$
Probe Precision	$< 0.1\%$
Bio-Savart Data	$< 2\%$

Table 3.2: Table showing sources of uncertainties in the B-field. These effects are small contributions to the momentum resolution

Table 3.2 shows the different contributions in the uncertainty in obtaining magnetic field points within the grid. The uncertainties were independent and when added in quadrature resulted in an overall uncertainty in the momentum of less than 0.25% when integrating a high momentum particle over its path. This is a minor effect when compared to the 2-3% momentum resolution dominated by multiple scattering and the uncertainty in the drift chamber wire positions.

3.4 Cerenkov Detectors

The Cerenkov detectors were used to distinguish between pions and electrons with momenta up to 700 MeV/c and with efficiency better than 90%. Cerenkovs were used because the TOF timing resolution was inadequate to provide such separation. In the theory of Cerenkov radiation [70], a charge particle passing through a medium will emit light if its velocity is greater than the velocity of light in that medium, in other words

$$v > \frac{c}{n} \tag{3.1}$$

where n is the index of refraction and c is the speed of light. The result is akin to a shockwave in sound, however, in this case light is emitted in a forward cone with a well-defined angle given by

$$cos\theta_c = \frac{1}{\beta * n} \tag{3.2}$$

Thus, Cerenkovs can be used to measure the velocity of an incoming particle by measuring the angle of the light emitted. Conversely, it can be used to perform particle identification for two particles who have characteristic separations in energies. By carefully choosing an index of refraction, particles with energies greater than

$$E > \frac{1}{\sqrt{1 - \frac{1}{n^2}}} \tag{3.3}$$

will emit light and be detected while other particles will not.

CC BOX	PMT's	n	θ	TOF Subtended	Efficiency %
Left 0	6	1.02	$20° < \theta < 35°$	0-3	0.886 ± 0.006
Left 1	8	1.03	$35° < \theta < 35°$	4-7	0.854 ± 0.009
Left 2	12	1.03	$50° < \theta < 80°$	8-11	0.911 ± 0.024
Right 0	6	1.02	$20° < \theta < 35°$	0-3	0.883 ± 0.006
Right 1	8	1.03	$35° < \theta < 50°$	4-7	0.944 ± 0.014
Right 2	12	1.03	$50° < \theta < 80°$	8-11	0.935 ± 0.028

Table 3.3: Physical Characteristics of Cerenkov's including efficiencies measured from elastic e-p scattering

Table 3.3 describes the design characteristics of the BLAST Cerenkovs. The Cerenkov's consisted of four detector's in each sector situated beyond the drift chambers. Each detector box contained 11x11x1 cm^3 layers of aerogel laid out in strips and a series of photo-multiplier tubes at each end: the forward-most box had 6 PMT's, the next had 8, while the last two had 12. The forward most detector used aerogel with an index of refraction of 1.020 while the back detectors used an index of refraction of 1.030. The inside of each box was painted with Spectraflect, a white diffusively reflective paint that had 96-98% reflectivity for wavelengths in the visible.

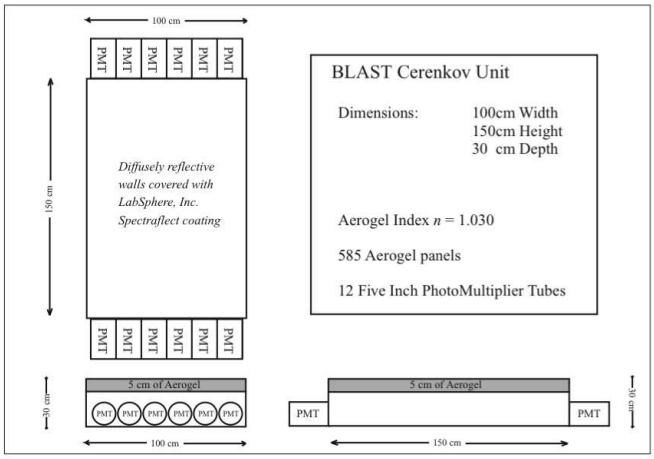

Figure 3-13: Physical layout of a Cereknov Box

The photomultiplier tubes were initially shielded with two concentric iron cylinders of 10 mm and 6 mm wall thickness with an air gap around each tube. However, measurements showed a significant residual field of 3-5 G when the toroid was energized which reduced the number of photons generated per Cerenkov hit. Therefore, extra iron plates 0.5 inch thick for the forward region and 1 inch thick for the backward region were added between the toroid and the PMT's.

To increase the efficiency of low-energy deuteron detection, the backward-most detectors were removed with the fourth box used in tandem with the Backward Angle TOF detector (BAT's). This detector was used to increase the angular coverage of elastic ep events.

To determine the efficiencies of the Cerenkovs, elastic e-p events were studied. In this case, a clean elastic e-p sample of events was obtained by placing cuts (charge,

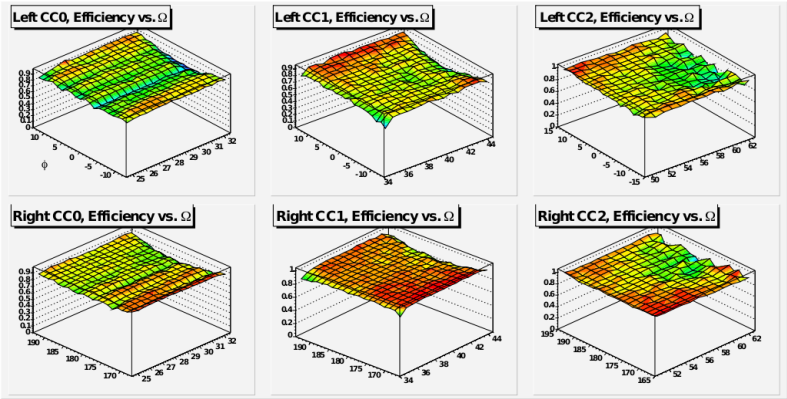

Figure 3-14: Cerenkov efficiencies vs angular acceptance from elastic ep events

coplanarity, invariant mass, etc) other than a Cerenkov cut. The efficiency was then defined as the number of events that fired a Cerenkov plus a corresponding Time of Flight Counter (See Section 3.5) divided by event with just a hit in the Time of Flight Counter. As a side note, since there were some events that missed the Cerenkov box but fired a Time of Flight Counter, only events with hits in one of the middle two TOF Bars behind a Cerenkov were counted. In this way, inefficiencies due to edge-effects are eliminated. Figure 3-14 shows the efficiencies of Cerekovs over the angular acceptance of BLAST with results showing efficiencies on the order of 90% for all boxes.

3.5 Time of Flight Counters

The BLAST time of flight detectors served three major functions: the TOFs provided the trigger for the BLAST detector, in particular the common stop for the wire chamber; they gave timing and energy information used to perform particle identification; and finally, since the signals were measured at both the top and bottom of the TOF bars by photo-multiplier tubes, coarse position information was obtained and used for co-planarity cuts.

The emission of light in a plastic scintillator is typically a multi-step process [71] First, an entering charged particle will excite a fluorescent material embedded in the plastic. The molecule de-excites, emitting in the UV range. However, to produce

light at detectable wavelengths, another light-emitting material is added which has strong absorption for the UV and emits light in the visible. Since detectors are used to provide timing information, it is important to have materials whose excited states are short-lived. In this way, the response time of a detector can be very fast, on the order of fractions of a nanosecond.

The BLAST TOFs are located behind the Cerenkovs and subtend roughly the same angles as the wire chamber, $20^\circ < \theta < 80^\circ$ polar and $\pm 15^\circ$ azimuthal. Each sector has 16 vertical scintillator bars, consisting of Bicron-BC-408 plastic scintillator whose response time is approximately 0.9 ns and attenuation length was 210 cm. PMT's were at the end of each scintillator bar to multiply and readout the signal. To minimize the effects of the BLAST magnetic field, the light guides were bent away from the target, leaving the PMT's roughly perpendicular to the field to maximize the effects of shielding.

Timing information used as a trigger was done by placing the top and bottom PMT signals into a mean timer. This signal from the closer TOFs were delayed so that the trigger could be used as a common stop for the wire chamber. The timing differnce between these two signals, on the other hand, were used to determine a rough position along the length of the TOF.

Figure 3-15 shows the coplanarity of e-p elastic events. By taking the vertical position of the TOF's, the sum of the two azimuthal angles for an elastic ep event was coplanar to within a couple of degrees. This was used to select out good ep events.

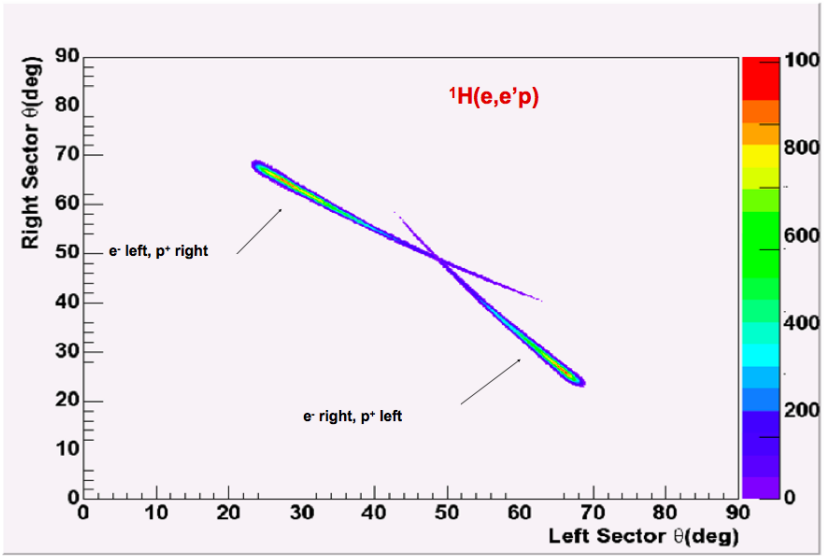

Figure 3-15: Graph showing co-planarity of ep elastic events

3.6 Trigger and Data Acquisition System

The BLAST trigger was a programmable trigger that could accept multiple physics events as was found in BLAST. Initially developed for the JLab's Hall A high resolution spectrometers, it was redesigned for the BLAST detector.

Figure 3-16 shows a layout of the BLAST trigger system. Outputs from each of the detector component were split before the trigger, with one signal going to ADC's and the other going into the trigger's discriminators. After detector hits were digitized, their timing information was obtained by sending the signal to TDC's. In addition the signal was taken as inputs to the trigger logic, the Memory Lookup Unit (MLU). The MLU was a lookup table that for a specific combination of input signals, would output a definite logic signal. In this case, a potential track, i.e. a specific combination of detector hits in a sector, will receive a specific output bit from the MLU (all detectors signals could not be entered directly into the MLU however because of its limited number of inputs leaving some of the detector signals to be OR'ed together). Finally, output signals from each sector's MLU were then sent to a "cross" MLU, or XMLU which combined information from both sectors to form a potential physics event and was assigned an output bit, a trigger. Each trigger type

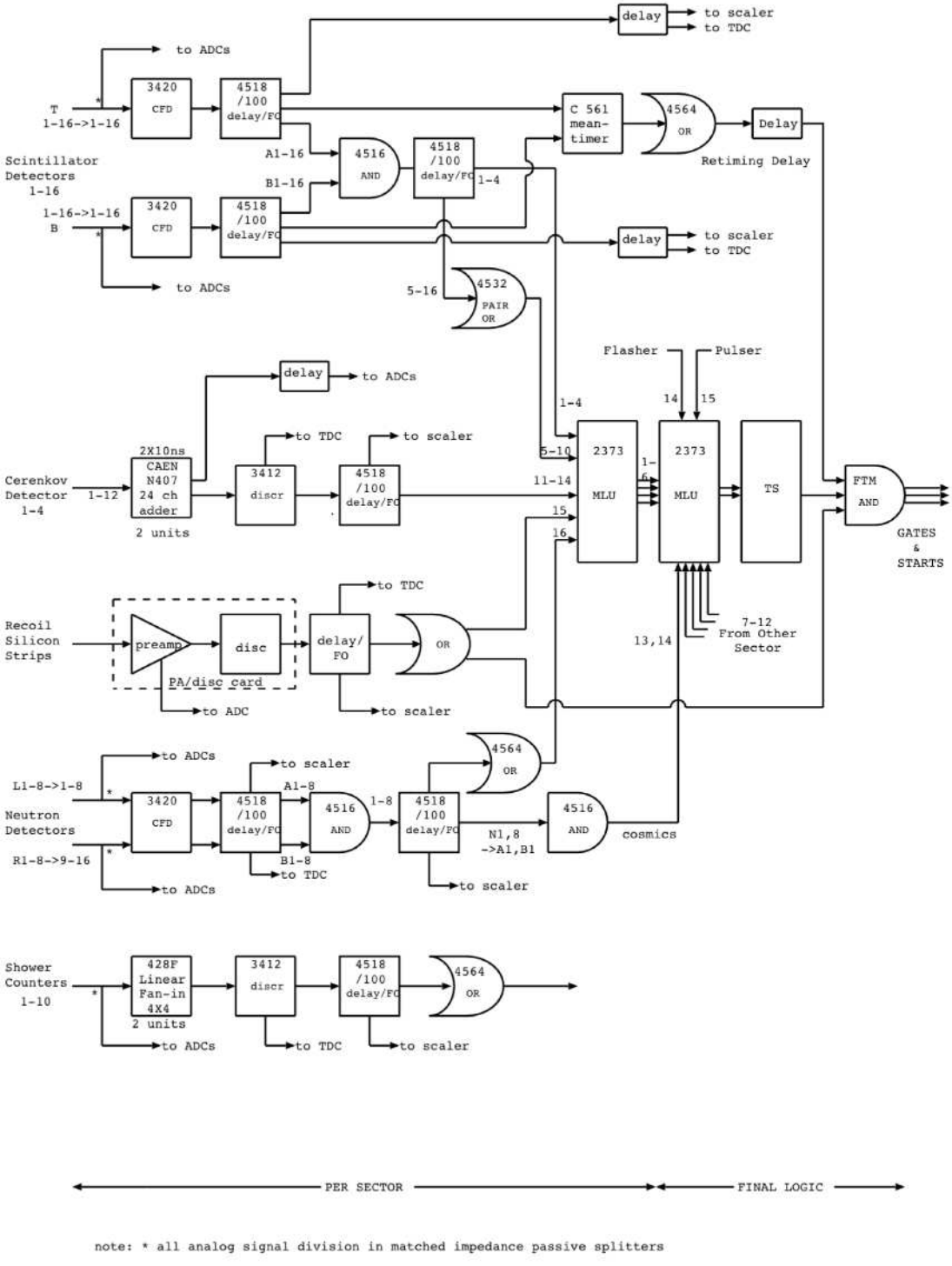

Figure 3-16: Schematic of the BLAST level 1 trigger for a single sector.

could be pre-scaled, and multiple physics events could be assigned a single trigger, however each would be given the same pre-scale factor. The total output of the XMLU for BLAST contained 8 classes of physics events. The benefit of pre-classifying events within the trigger was a lower computational overhead during the actual physics analysis.

Early in data taking it was noticed that many events made it through the trigger without drift chamber tracks. This caused a significant amount of unnecessary dead time. Therefore, a second level trigger was built which required, in addition to a physics event from the first trigger, at least one wire chamber hit in each wire chamber for every charged particle event, i.e. for a TOF hit in the same sector. This reduced the dead time required to readout a noise event since a fast clear could be performed. Consequently, a noise event took only 5 μs instead of 835 μs away from data taking time.

Data Acquisition was handled by the Common Online Data Acquisition system, CODA. At the prompting of the trigger supervisor, CODA would read out the ADC'S and TDC's from the read out controllers, the ROC's. This data was then handled by the event builder, EB, which would package the data into a event, i.e. a pre-specified format. From here events were passed to the Event Transport system where EPICS data, Compton Polarimeter and scalers events were included, but at a much lower rate. By taking advantage of Event Transfer ability for event spying, a set of online monitoring programs were written that could observe ADC and TDC histograms and other calculated quantities such as vertex reconstruction in real time. In this way, real-time results could be seen and corrected before data analysis. Finally Coda's Event Recorder was used to store the data onto disk for later analysis.

Chapter 4

Analysis

4.1 Introduction

The BLAST experiment ran during two different periods in consecutive years, 2004 and 2005. The differences between the two data sets are as follows:

1.) In 2005 the average beam current was higher due to improved understanding of the ring properties. 2.) 2005 had lower target polarization possibly due to a new target cell with poorer performance. 3.) The direction of the target polarization vector was nominally 32° for 2004 and 47° for 2005. The target spin angle was in the plane of the detector and with its vector pointing into the left sector with respect to the beam line. The angles were chosen to maximize statistics for different Q^2 ranges in the extraction of G_E^n.

4.2 Event Selection

4.2.1 Introduction

The process of cuts and event selection was done in stages. The first stage was to select out e-p events from the data using a series of charge, timing, and vertex cuts. Once e-p events were determined, each track's kinematic variables, $(p_e, \theta_e, \phi_e, z_e)$ for the electron and $(p_p, \theta_p, \phi_p, z_p)$ for the proton, were used to determine the global

variables of $(Q^2, p_m, m_M, \theta_{cms}, \theta^*, \phi^*)$. The next stage was to select out of quasi-elastic events by placing a 2 σ cut around the missing mass peak. Since there was a slight systematic reconstruction error of $\sim$ 12 MeV/c in the (assumed) electron's momentum, a kinematic correction was made. This led to a correction to (p_e, θ_e) that necessitated a recalculation of the global variables. It was these values that were used in the analysis.

4.2.2 PID cuts

To select e-p events, events were chosen with two charged tracks with opposite signs that passed through opposite sectors. The charge was determined from the curvature of the tracks in the wire chamber; the BLAST magnetic field ran clockwise around the beam while looking down on it, so that the electrons (protons) were inbending (outbending). Likewise, to minimize the contamination of π^-'s, Cerenkovs were used to separate them from electrons. It is important to note that events where the proton was not detected but a π^+ was would still make it through; however timing cuts and missing mass cuts (See sections 4.2.3 and 4.2.5) helped eliminate this.

4.2.3 Timing cuts

Timing cuts were performed by using the offset-subtracted tdcs from the TOFs to further select out protons and eliminate unwanted deuterons and pions from the data sample. To ensure their validity, the tdcs were explicitly correlated to a wire chamber track. The fastest particle, assumed to be the electron, is "self-timed" *i.e.* its tdc value gives no information on that particle's time of flight; therefore, the timing of this arm was determined by the path length the electron traversed divided by the velocity of the electron. For example, if the electron was emitted into the left sector, its timing information, T_l, was determined by

$$T_l = \frac{L_l}{v_l} \tag{4.1}$$

$$= \frac{L_l}{p/\gamma m} \tag{4.2}$$

where L_l is the path length of the left paricle, v_l is its velocity, p its momentum and m is the mass. Subsequently, the TOF tdc values are used in conjunction with this timing value to determine the right-sector particles time of flight,

$$T_r = tdc_r - tdc_l + T_l. \tag{4.3}$$

For timing cuts a parameter ΔT was created, which when plotted for different choices of mass in the non-self-triggering arm, was used to select out different events. It represents the difference between the time for the non-triggering track taken from the TDC value to it's timing value determined by using its path length divided by its velocity. If we assume an electron in the left sector, the definition for ΔT is

$$\Delta T \equiv tdc_l - \frac{L_l}{v_l} - tdc_r + \frac{L_r}{v_r}. \tag{4.4}$$

Figure 4-1, shows the value for ΔT when the second particle chosen was the proton. It clearly shows a massive peak at $\Delta T = 0$ along with much smaller peaks away from t=0, showing deuteron and pion contamination. Cuts were placed around the central peak. Similarly, plots were done where deuteron and π^+ masses were chosen,

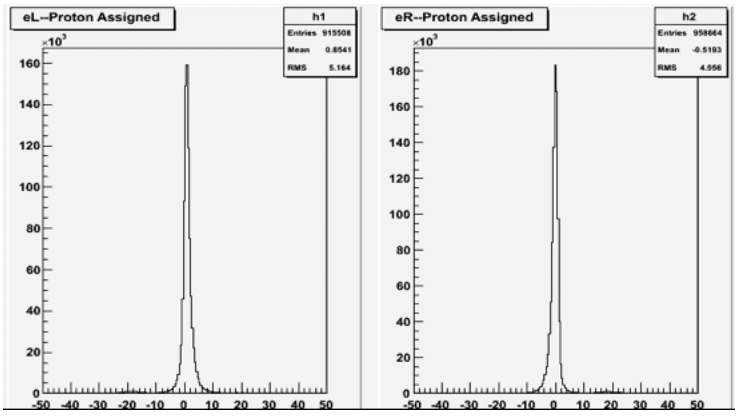

Figure 4-1: ΔT where mass chosen is that of the proton for both parallel and perpendicular kinematics. Figure shows large primary peak of protons with small (barely visible) peaks of faster pions and slower deuterons. Increasing time runs backwards for electron left and forwards for electron right events.

resulting in small peaks around $t = 0$ which were removed from the data sample. The

effects of these cuts led to a much reduced dependence of hP_z on Q^2, an example that showed that a majority of pion contamination was eliminated.

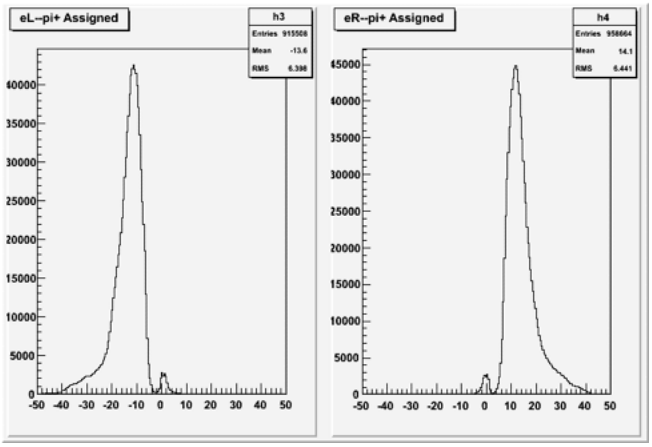

(a) ΔT where mass chosen is a π^+

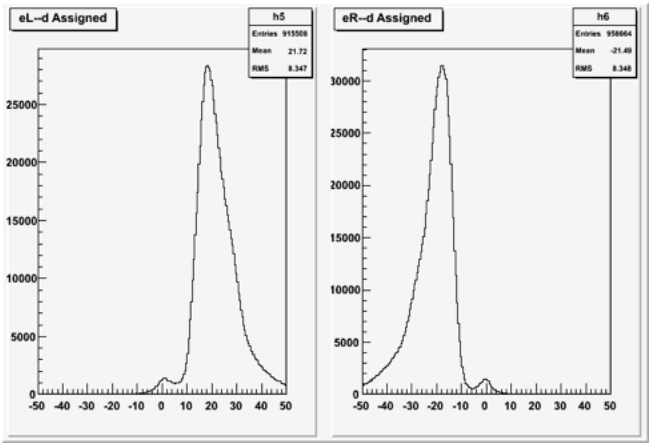

(b) ΔT where mass chosen is that of deuteron

Figure 4-2: Timing selection for pions and deuterons

4.2.4 Vertex Cuts

A source of background events originated from the beam halo striking the collimator located upstream from the target. Therefore, a cut was placed on the vertex (z component) of the particles passing through the left and right sectors of BLAST to ensure that they originated from the target. Since the target cell used was 60 cm but the holding field was 40 cm, a cut of ± 20 cm was placed on the reconstructed z coordinate from the wire chamber information. Figure 4-3(a) shows the z-distribution

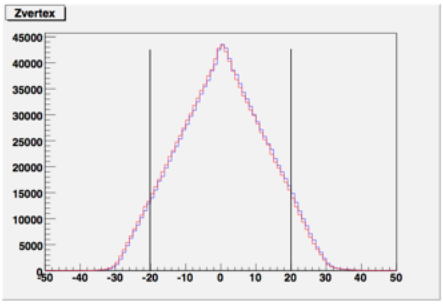

(a) Vertex cut for particles traversing the left sector (blue) and the right sector (red)

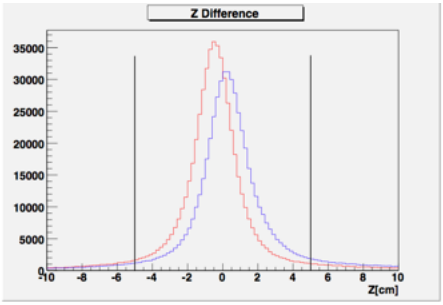

(b) The difference in vertex position for electron left-proton right (blue) and electron right-proton left (red)

Figure 4-3: Z Cuts

with cuts for both combinations of parallel and perpendicular kinematics. In addition to ensure that the two particles came from the same event, a cut was placed on the relative separation of the two particles of $|z_p - z_e| < 5$ cm as shown in figure 4-3(b) figure, much larger than the reconstructed z resolution achieved by the wire chamber of 1 μm.

4.2.5 Missing Mass Cut

Since in this experiment the neutron was left undetected, a kinematic constraint was imposed on the reaction to help ensure that the undetected particle was a neutron. The constraint made required the "missing mass" of the particle to be that of the neutron. The missing mass is defined as

$$m_M^2 \equiv E_M^2 - p_M^2 \tag{4.5}$$

where in terms of measured quantites we have

$$E_m \equiv \omega + M_d - E_p \tag{4.6}$$

and

$$p_m \equiv p_p - q \tag{4.7}$$

Figure 4-5 shows the missing mass spectrum after vertex, particle ID cuts, and

timing cuts for parallel and perpendicular kinematics. The peak values for the two spectra are nearly the value for the neutron mass with relatively smaller distribution of higher missing momentum events, showing that the even selection process is relatively sound. The slight offset from the neutron mass peak is due to imperfections in the kinematic reconstruction of BLAST by either misalignment of the detector components, detector noise, etc. and the spread in distribution is due to the Fermi motion of the neutron within the nucleus. The higher missing momentum distibution is the result of events of higher excited states or additional particles created. The biggest source of data contamination came from the reaction

$$e + d \Rightarrow e + p + n + \pi^0 \tag{4.8}$$

This reaction would have a missing mass of 1.075 GeV/c^2. Therefore a cut was placed around the peak of 2 σ of the missing mass spread of 25 MeV/c^2 extending the data acceptance to roughly 63 MeV/c^2, or roughly half of the pion mass. If the detector resolution were perfect this should ensure no pion contamination; however imperfect resolutions may leave some small pion contamination even with this and the previously discussed cuts.

4.3 Kinematic Corrections

The wire chamber was able to reconstruct the origin and the angles of the tracks, and the momentum of the the electron (k_e,θ_e,ϕ_e,z_e) and proton (p_p,θ_p,ϕ_p,z_p) for each event. However, due to errors inherent to the reconstruction, lack of information on the location of the wires, particle energy loss, an overall compensating correction to the kinematics was applied. For the usable Q^2 range, the size of correction was on the order of 12 MeV/c^2, estimated by examining the missing mass spectra and determining offset of the centroid from the mass of the neutron. It was necessary to correct for errors in reconstruction because, not only did it effect data selection, but it also caused a shift in the reconstructed value of Q^2 since $Q^2 = f(E, E', \theta_e)$.

Errors in reconstruction were assumed greater for protons than for electrons. Protons passing through the wire chamber had a much higher curvature, giving a better track resolution than for electrons, which were mainly relativistic and whose tracks were nearly straight. In addition, calibration from elastic scattering indicated that the angles for both the proton and the electron were known to within 0.5°. These results led to the decision to ascribe all the error to the electron's momentum, k', and correct for it in the way described below. From kinematics we have four-momentum conservation,

$$K + P_d = K' + P_p + P_n \tag{4.9}$$

where K is the four-momentum of the incoming electron, K' is the four-momentum of the outgoing electron, P_d is the on-shell, initial state deuteron four-momentum and P_p and P_n are the outgoing four-momentum of the nucleons. P_n is not measured but its square is set equal to the missing mass and required from quasi-elastic kinematics to be the mass of the neutron, $P_n^2 = M_m = M_n$, so that

$$M_n^2 = (K - K' - P_p)^2. \tag{4.10}$$

Multiplying this out and substituting the measured kinematic quantities in BLAST, there is one equation and one unknown, the momentum of the electron. The momentum of the electron can be solved for in the following equation,

$$\begin{aligned} M_n^2 \;=\; & 2kM_d + M_d + M_p - 2(k - k' + M_d)E_p \\ & +2k_p P_p \cos\theta_p \\ & +2k'[k(\cos\theta_e - 1) - M_d - P_d(\cos\theta_e cos\theta_p + \cos(\phi_e - \phi_p)\sin\theta_e sin\theta_p)] \end{aligned} \tag{4.11}$$

The correction could have been done on an event by event basis, but this would have placed the missing mass exactly equal to the mass of the neutron for all cases approximating a delta function. Instead, a parameterization was made of the difference between the electron momentum from equation 4.12 and the measured value vs. θ_e. This was done for each sector, for each year of data. For each data set, one

equation was obtained that gave a corrected value of the electron momentum for each measured k' and θ_e value. Because this correction changed an important kinematic variable, a new set of kinematic variables had to be recalculated after the correction was applied.

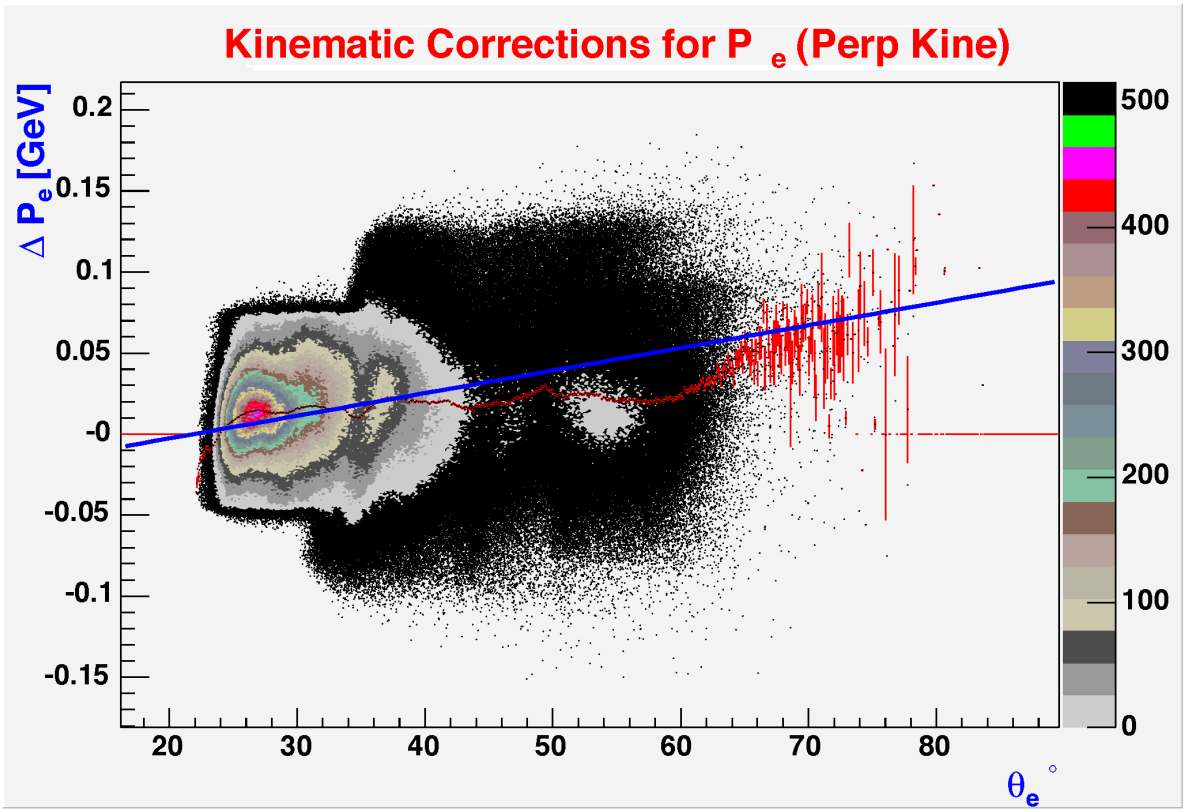

Figure 4-4: Plot of difference between corrected momentum and measured momentum vs. electron angle for perpendicular kinematics and the 2005 data set. Results show an average of roughly 12 Mev in the difference between the two values.

4.4 Formulae for determining Asymmetries

Experimentally, each asymmetry can be in written in terms of the measured rates:

$$a_j A^j = \frac{\sum_i g_i^j r_i^T}{\sum_i r_i^T} \tag{4.12}$$

where a_j contains the polarization factors plus any numerical factors used in Arenhoevel's definitions, A^j is the measured asymmetry, g_i^j is the matrix element needed to combine rates to arrive at the correct asymmetries, r_i^T is the true rate after background subtraction, and the denominator, $\sum_i r_i^T$ is the average rates of the six spin states. To write out explicitly in terms of the asymmetries, A_e, A_d^V, A_{ed}^V, A_d^T and A_{ed}^T and polarizations h, P_z and P_{zz} we have,

$$\begin{pmatrix} 6h\overline{r}A_e \\ \sqrt{\frac{2}{3}}P_z\overline{r}A_d^V \\ \sqrt{\frac{2}{3}}hP_z\overline{r}A_{ed}^V \\ \sqrt{2}P_{zz}\overline{r}A_d^T \\ \sqrt{2}h\overline{r}A_{ed}^T \end{pmatrix} = \begin{pmatrix} +1 & -1 & +1 & -1 & +1 & -1 \\ +1 & +1 & -1 & -1 & 0 & 0 \\ +1 & -1 & -1 & +1 & 0 & 0 \\ +1 & +1 & +1 & +1 & -2 & -2 \\ +1 & -1 & +1 & -1 & -2 & +2 \end{pmatrix} \begin{pmatrix} r(+1,+1,+1) \\ r(-1,+1,+1) \\ r(+1,-1,+1) \\ r(-1,-1,+1) \\ r(+1,\ 0,-2) \\ r(-1,\ 0,-2) \end{pmatrix} \tag{4.13}$$

The right hand column shows the six rates r(h,P_z, P_{zz}) corresponding to the six possible combinations of h, P_z and P_{zz}. In general, background rates lower the true rates, r_i^T, and must be subtracted.

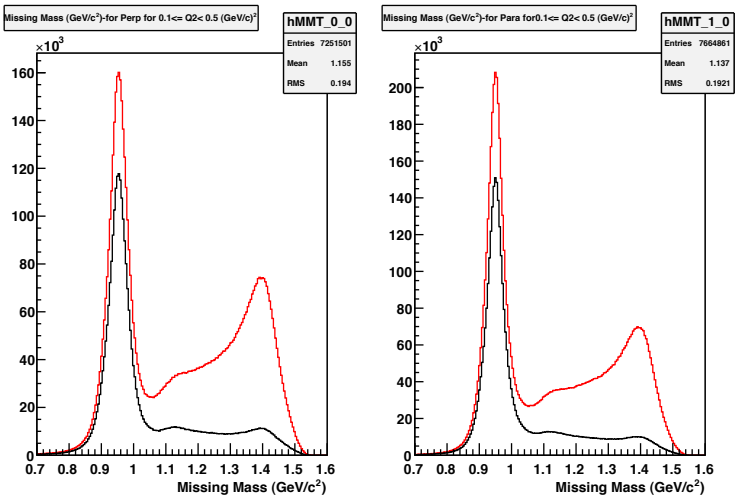

(a) 32°–Perpendicular Kinematics and Parallel Kinematics

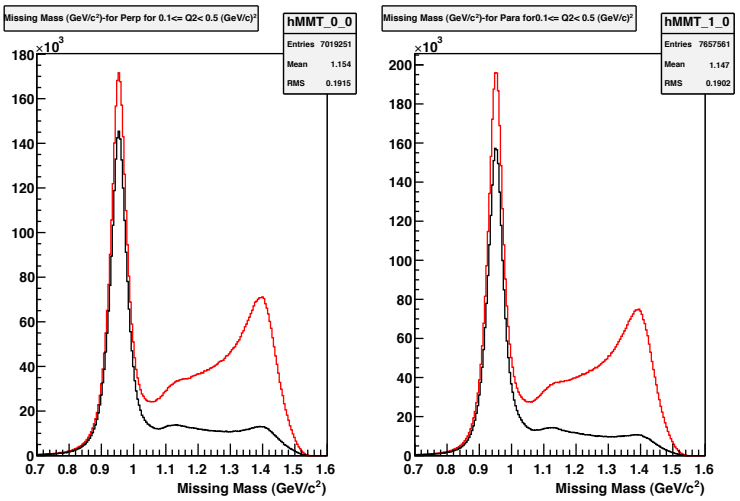

(b) 47°–Perpendicular and Parallel Kinematics

Figure 4-5: Plots of Missing Mass for 32° and 47° data without Cerenkov Cuts (red histogram) and with Cerenkov Cuts (black histogram) for 0.1 $(GeV/c)^2 < Q^2 <$ 0.5 $(GeV/c)^2$ and both sets of kinematics. Results from individulal Q^2 bins can be found in Appendix A.1.3. Plots are made before kinematic corrections and thus missing mass peaks differ from that of the neutron by 10 MeV/c^2.

Missing Mass			
Q2 Bin	Missing Mass(centroid) (GeV/c^2)	$\sigma(GeV/c^2)$	Size of Cut
32°–Perpendicular Kinematics			
$0.1\ GeV/c^2 < Q^2 < 0.2\ GeV/c^2$	0.9528	0.0208	2.5 σ
$0.2\ GeV/c^2 < Q^2 < 0.3\ GeV/c^2$	0.9558	0.0277	2.5 σ
$0.3\ GeV/c^2 < Q^2 < 0.4\ GeV/c^2$	0.9569	0.0299	2.5 σ
$0.4\ GeV/c^2 < Q^2 < 0.5\ GeV/c^2$	0.9542	0.0292	2.5 σ
32°–Parallel Kinematics			
$0.1\ GeV/c^2 < Q^2 < 0.2\ GeV/c^2$	0.9518	0.0194	2.5 σ
$0.2\ GeV/c^2 < Q^2 < 0.3\ GeV/c^2$	0.9478	0.0284	2.5 σ
$0.3\ GeV/c^2 < Q^2 < 0.4\ GeV/c^2$	0.9514	0.0307	2.5 σ
$0.4\ GeV/c^2 < Q^2 < 0.5\ GeV/c^2$	0.9454	0.0361	2.5 σ
47°–Perpendicular Kinematics			
$0.1\ GeV/c^2 < Q^2 < 0.2\ GeV/c^2$	0.9528	0.02016	2.5 σ
$0.2\ GeV/c^2 < Q^2 < 0.3\ GeV/c^2$	0.9563	0.0347	2.5 σ
$0.3\ GeV/c^2 < Q^2 < 0.4\ GeV/c^2$	0.9556	0.0371	2.5 σ
$0.4\ GeV/c^2 < Q^2 < 0.5\ GeV/c^2$	0.9500	0.0282	2.5 σ
47°–Parallel Kinematics			
$0.1\ GeV/c^2 < Q^2 < 0.2\ GeV/c^2$	0.9505	0.0185	2.5 σ
$0.2\ GeV/c^2 < Q^2 < 0.3\ GeV/c^2$	0.9464	0.0196	2.5 σ
$0.3\ GeV/c^2 < Q^2 < 0.4\ GeV/c^2$	0.9465	0.0306	2.5 σ
$0.4\ GeV/c^2 < Q^2 < 0.5\ GeV/c^2$	0.9410	0.0361	2.5 σ

Table 4.1: Table showing missing Mass peaks, width of peak, and size of cut for each set of kinematics.

4.5 Comparison of Reconstructed Events with Monte Carlo

After the quasi-elastic ep events were selected, a comparison was made between the reconstructed kinematic variables and the one generated by Monte Carlo. Following are plots of these variables with Monte Carlo data scaled to match the measured values.

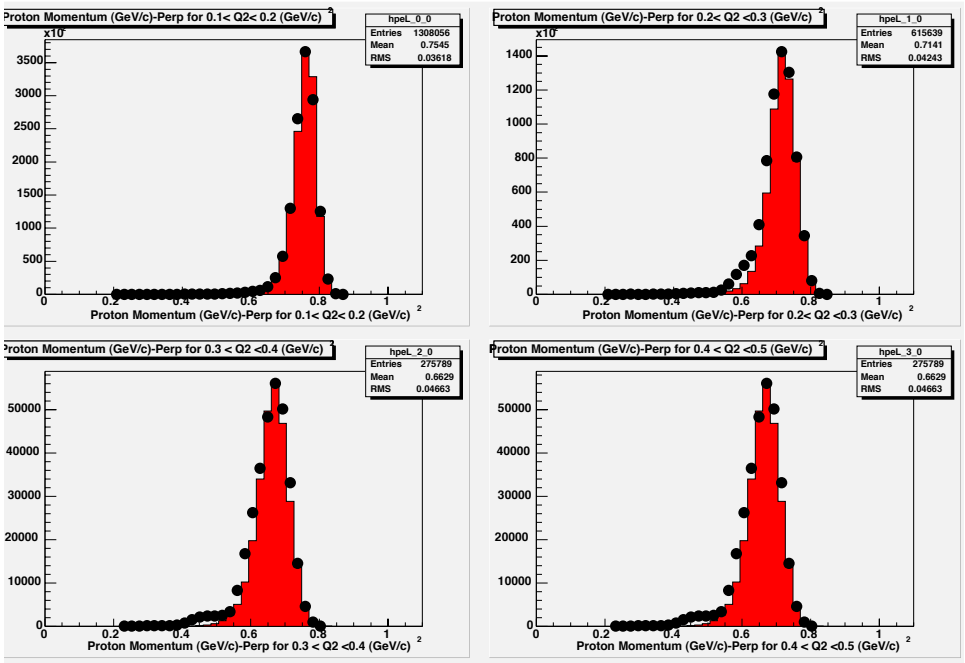

(a) 2004

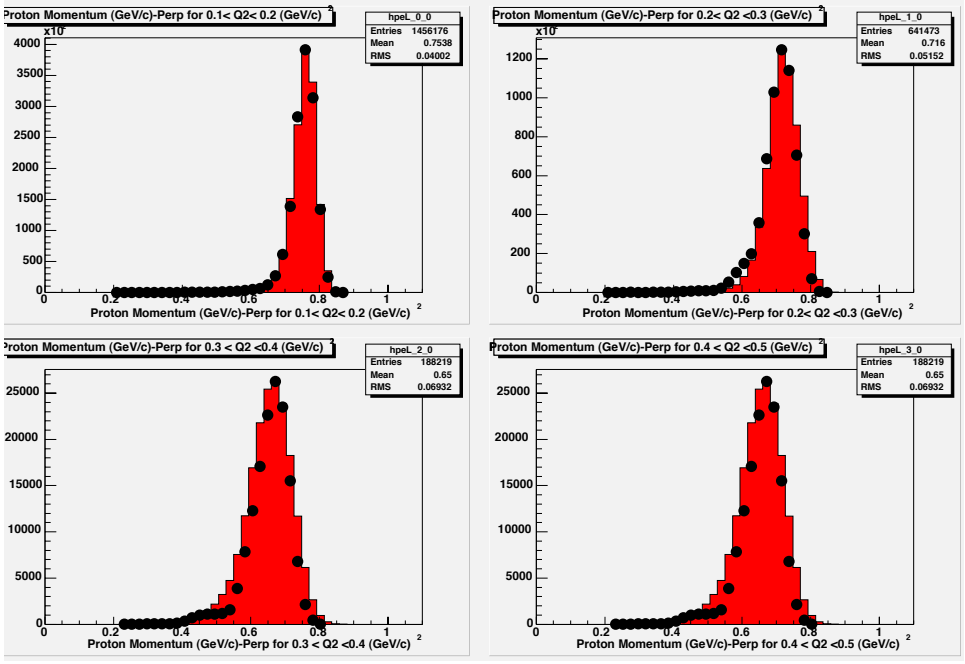

(b) 2005

Figure 4-6: Reconstructed electron momentum for parallel kinematics (Red Histogram) compared to that generated Monte Carlo (black dots) for both sets of data for all Q^2 bins

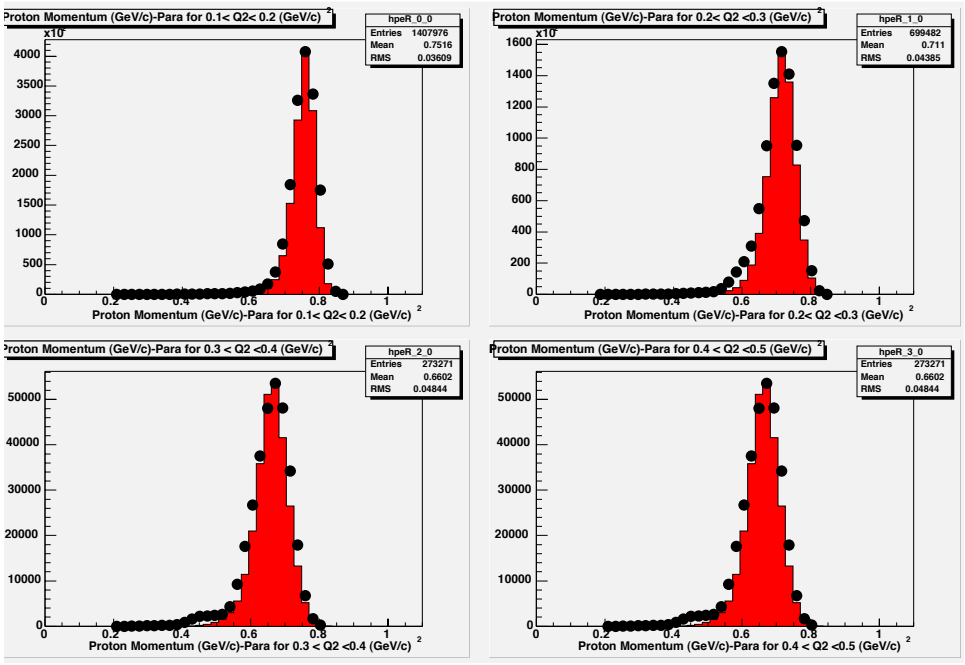

(a) 2004

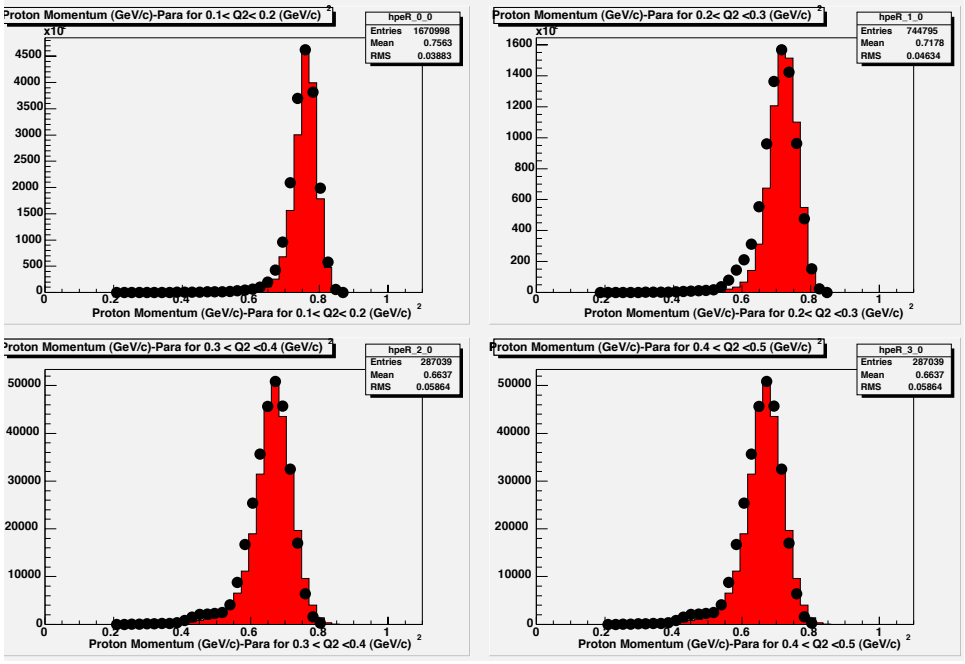

(b) 2005

Figure 4-7: Reconstructed electron momentum for perpendicular kinematics (Red Histogram) compared to that generated Monte Carlo (black dots) for both sets of data for all Q^2 bins

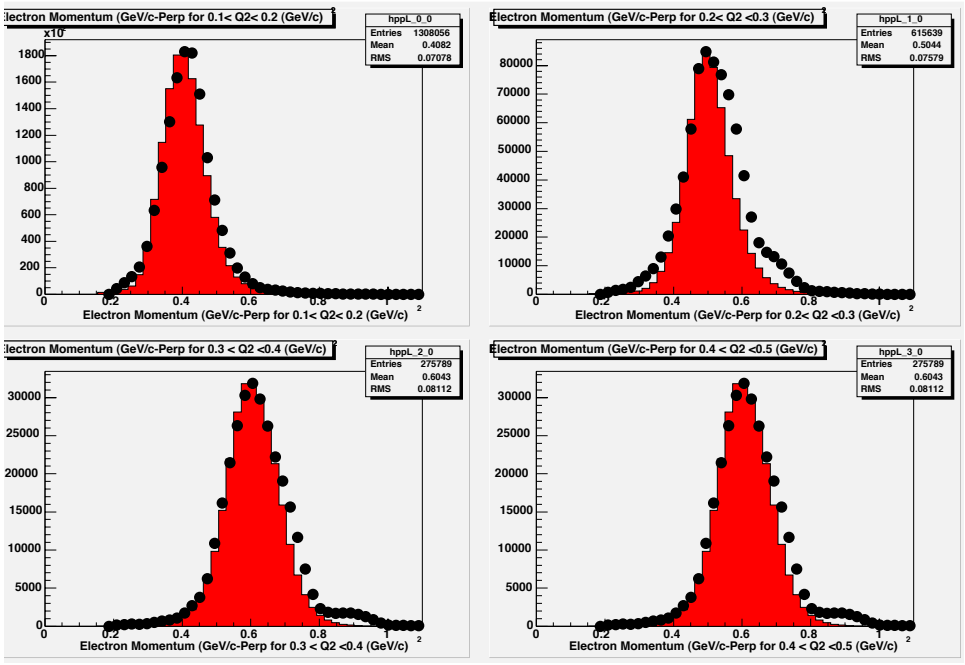

(a) 2004

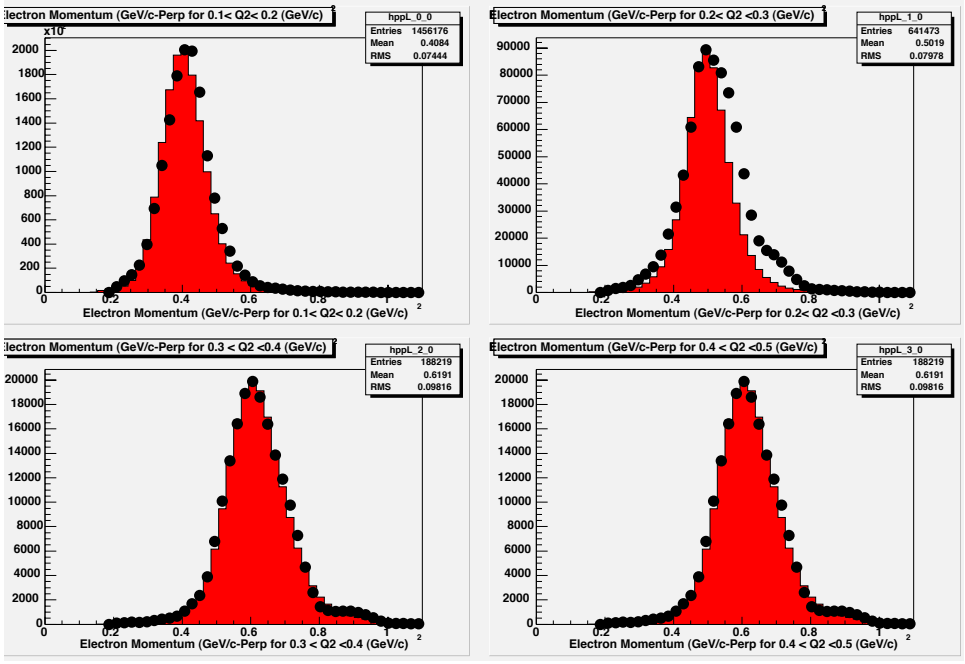

(b) 2005

Figure 4-8: Reconstructed proton momentum for perpendicular kinematics (Red Histogram) compared to that generated Monte Carlo (black dots) for both sets of data for all Q^2 bins

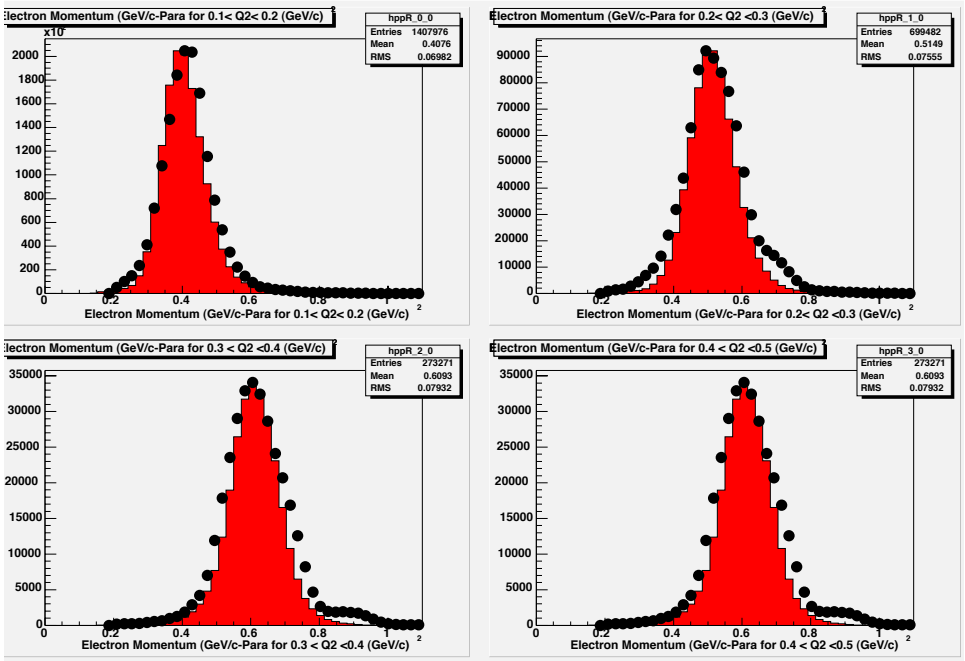

(a) 2004

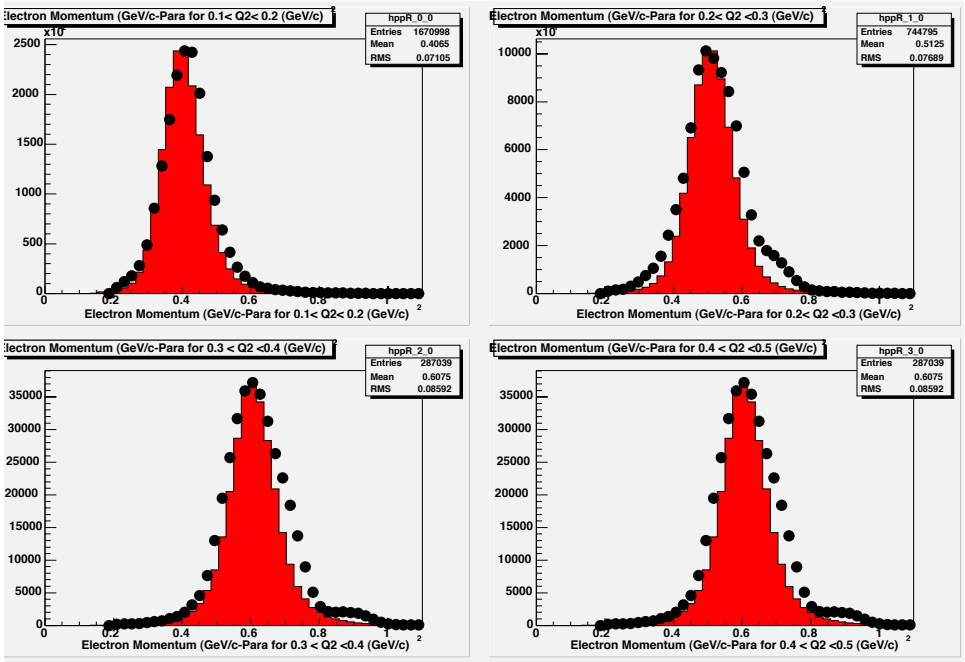

(b) 2005

Figure 4-9: Reconstructed proton momentum for parallel kinematics (Red Histogram) compared to that generated Monte Carlo (black dots) for both sets of data for all Q^2 bins

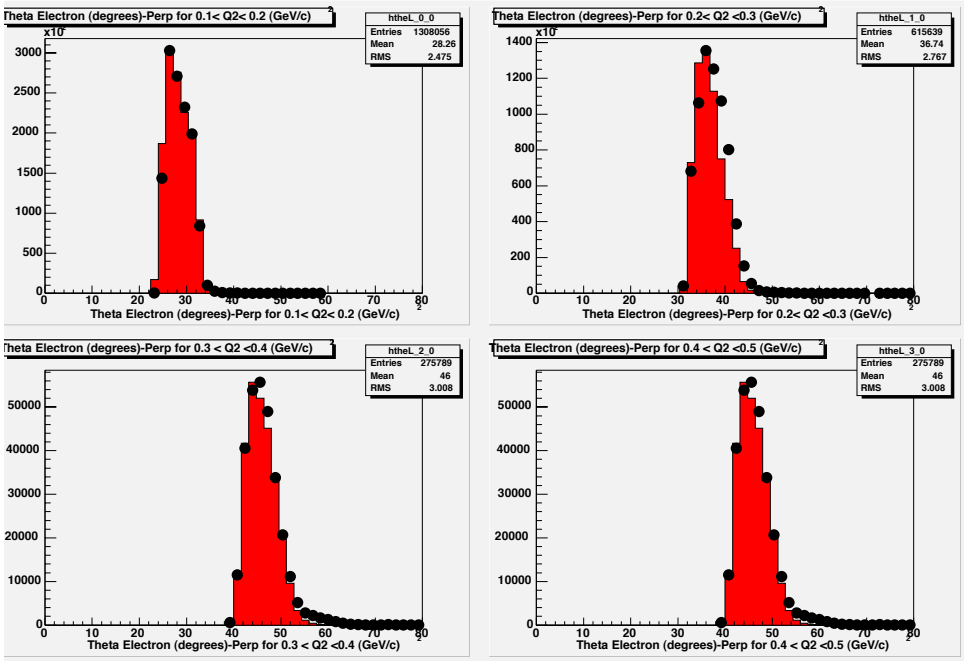

(a) 2004

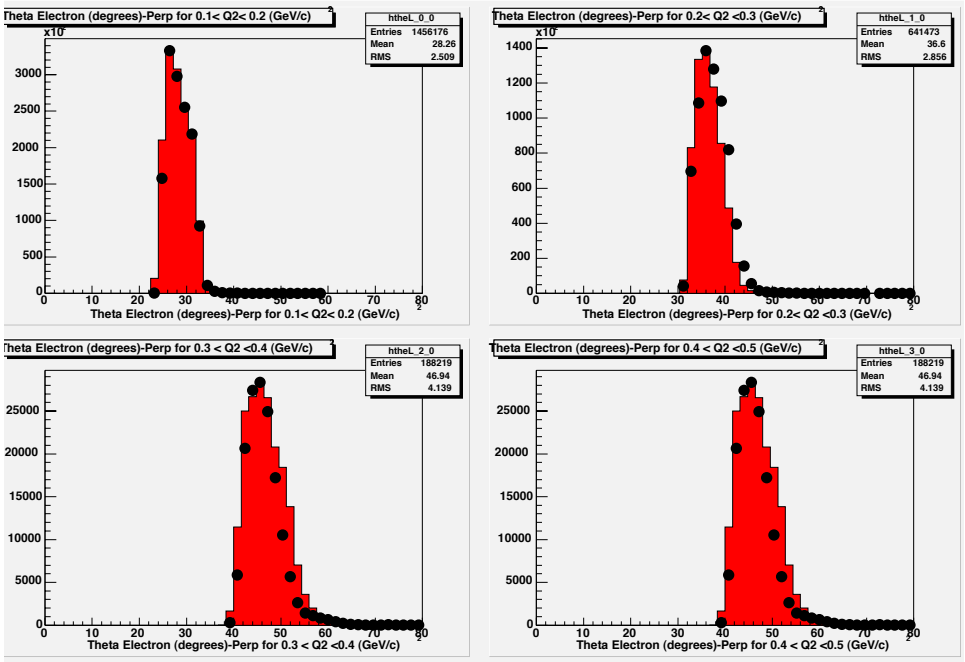

(b) 2005

Figure 4-10: Reconstructed theta angle for the electron for perpendicular kinematics (Red Histogram) compared to that generated Monte Carlo (black dots) for both sets of data for all Q^2 bins

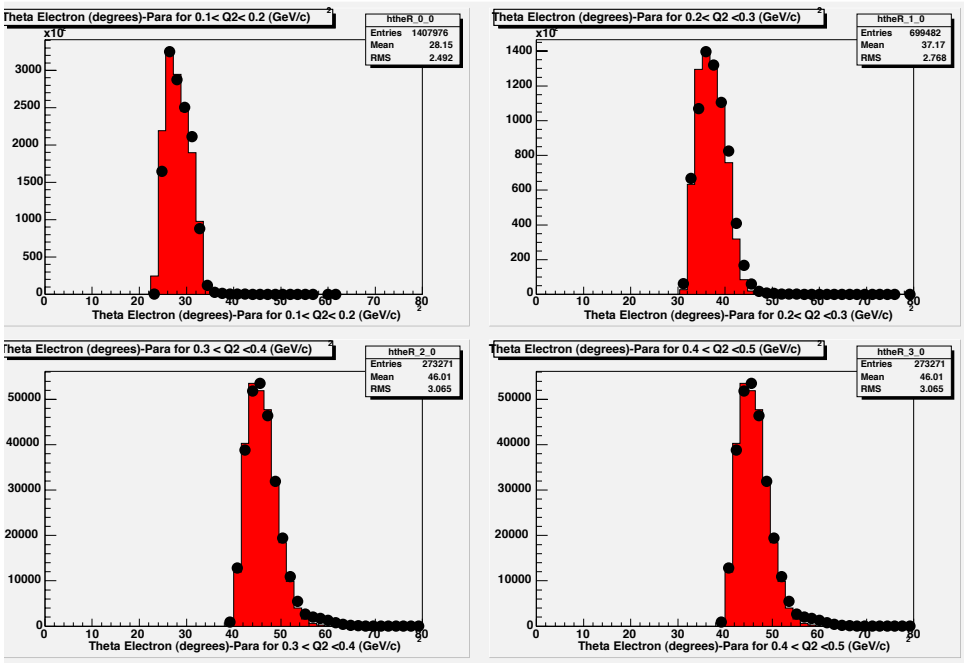

(a) 2004

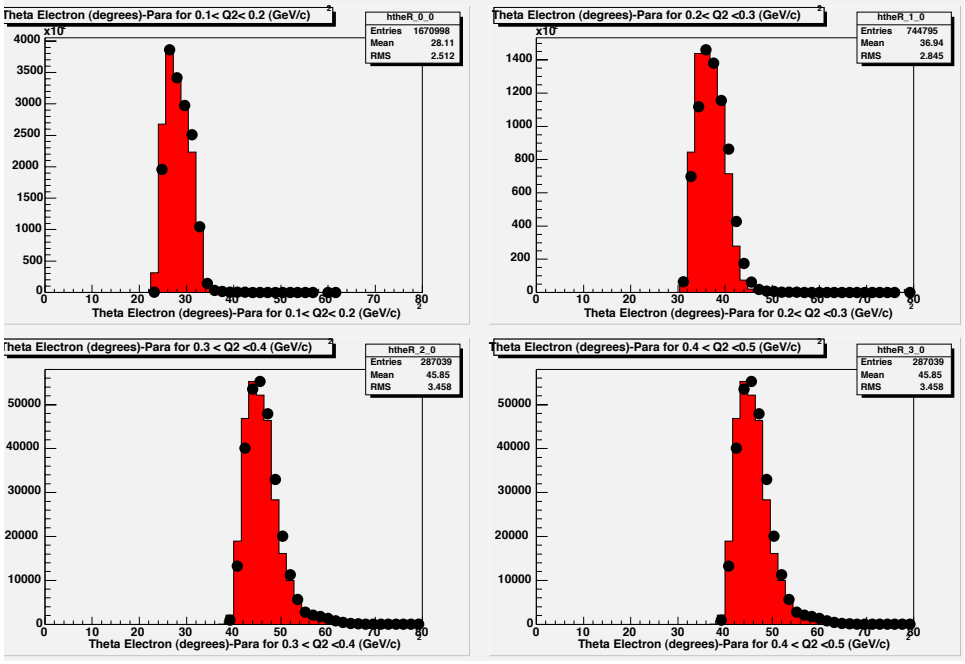

(b) 2005

Figure 4-11: Reconstructed theta angle for the electron for parallel kinematics (Red Histogram) compared to that generated Monte Carlo (black dots) for both sets of data for all Q^2 bins

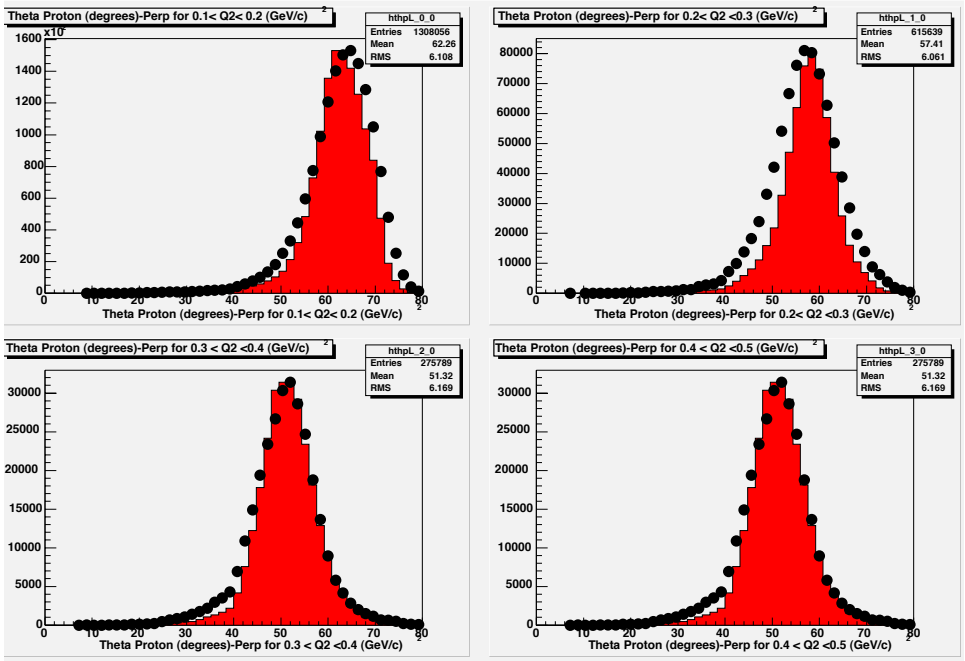

(a) 2004

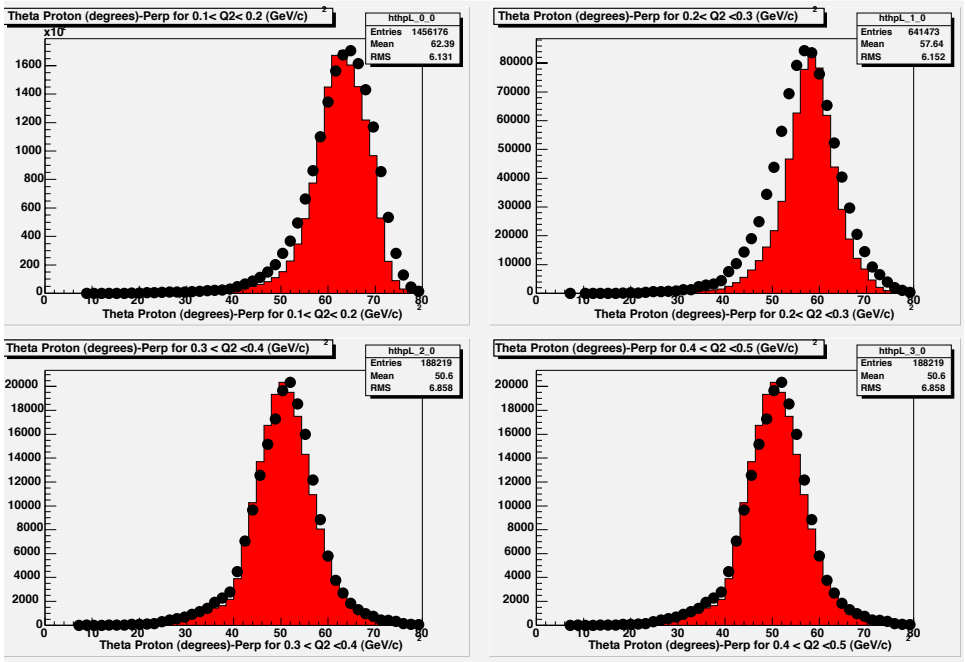

(b) 2005

Figure 4-12: Reconstructed theta angle for the proton for perpendicular kinematics (Red Histogram) compared to that generated Monte Carlo (black dots) for both sets of data for all Q^2 bins

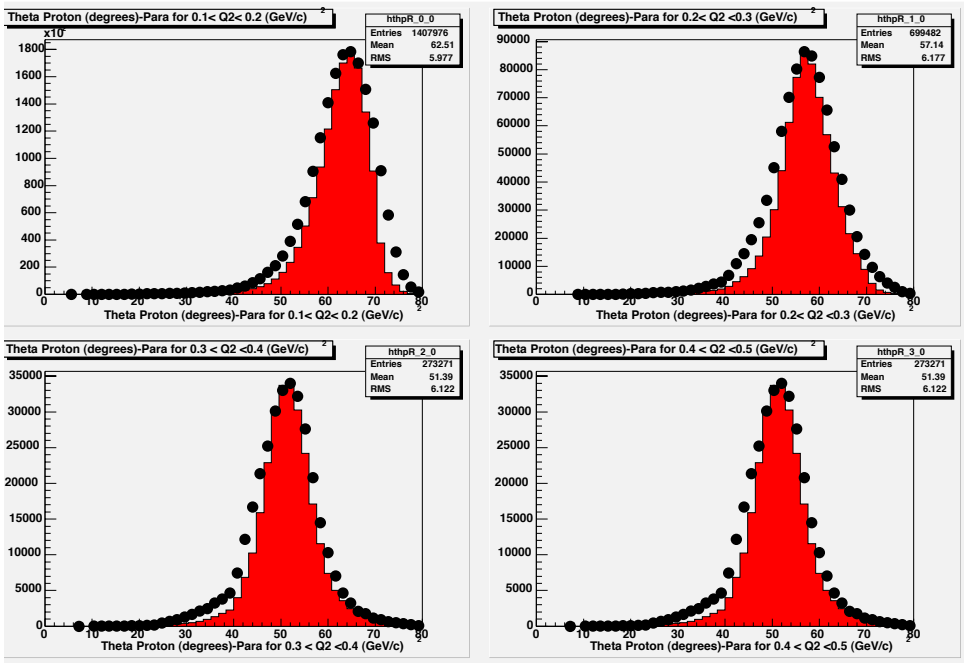

(a) 2004

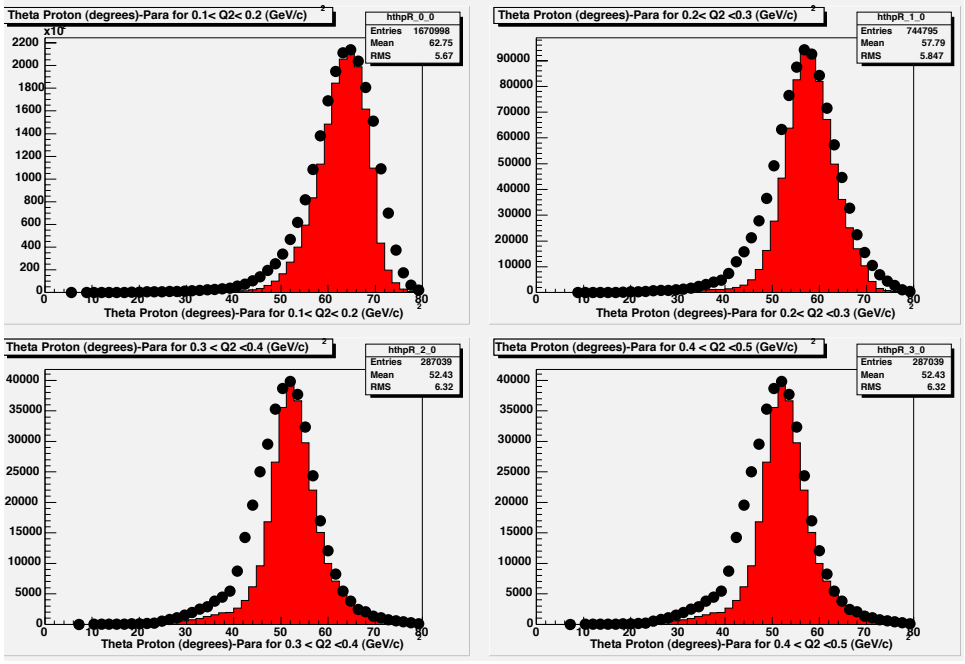

(b) 2005

Figure 4-13: Reconstructed theta angle for the proton for parallel kinematics (Red Histogram) compared to that generated Monte Carlo (black dots) for both sets of data for all Q^2 bins

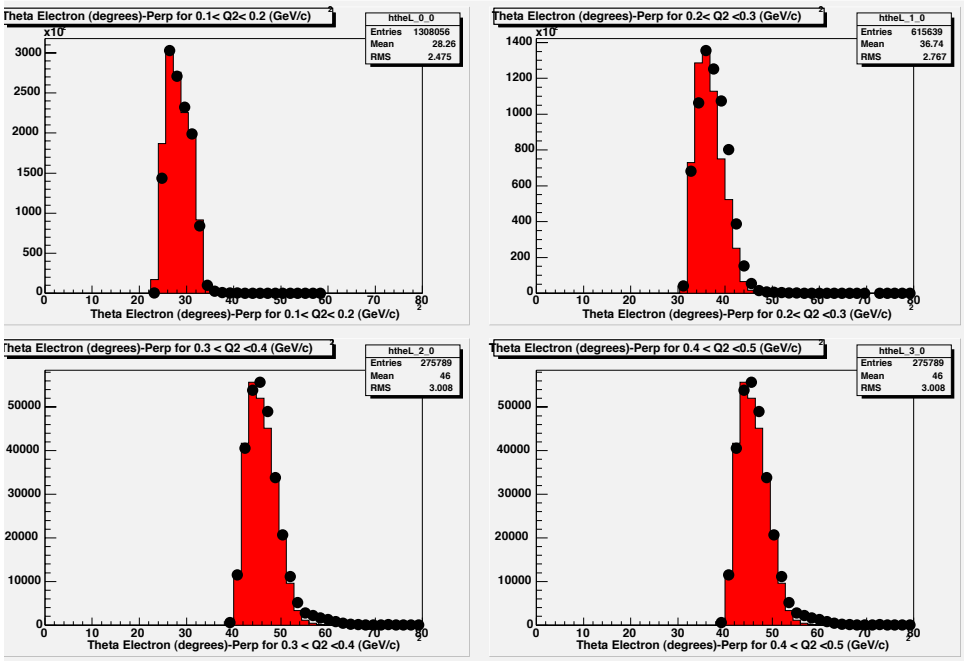

(a) 2004

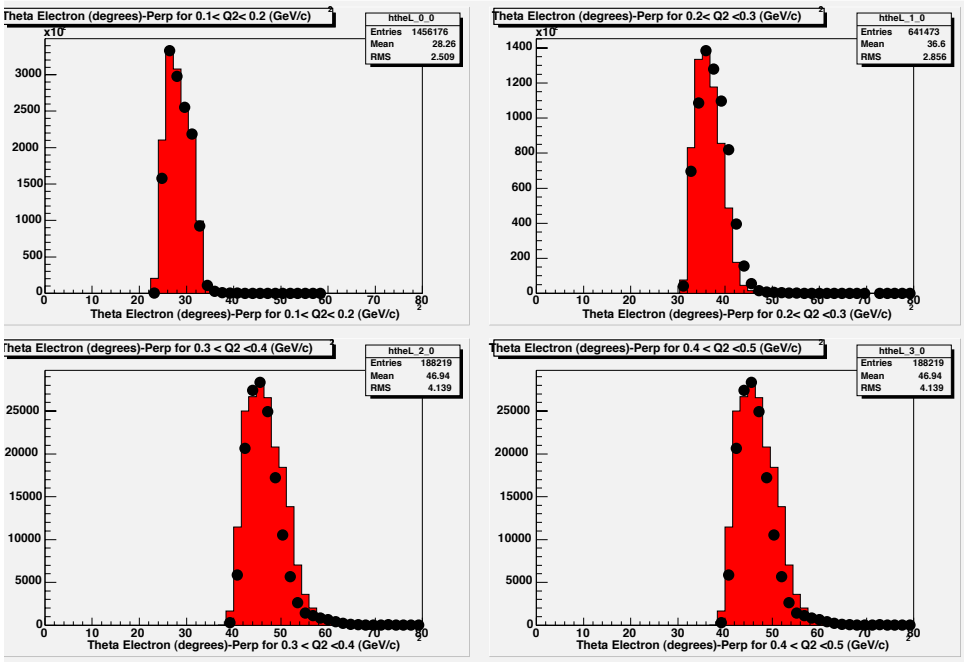

(b) 2005

Figure 4-14: Reconstructed theta angle for the electron for perpendicular kinematics (Red Histogram) compared to that generated Monte Carlo (black dots) for both sets of data for all Q^2 bins

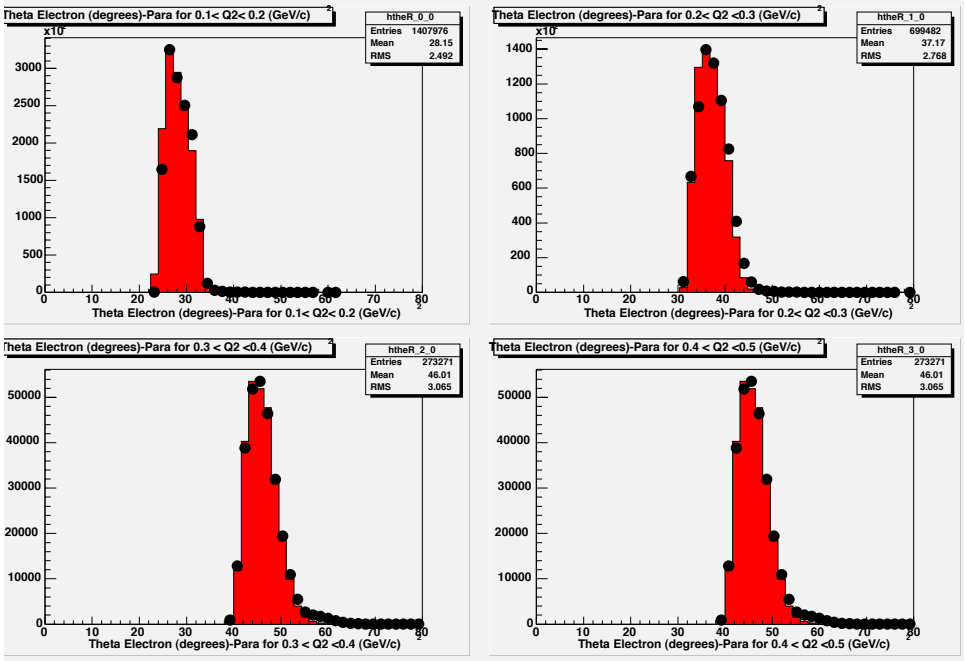

(a) 2004

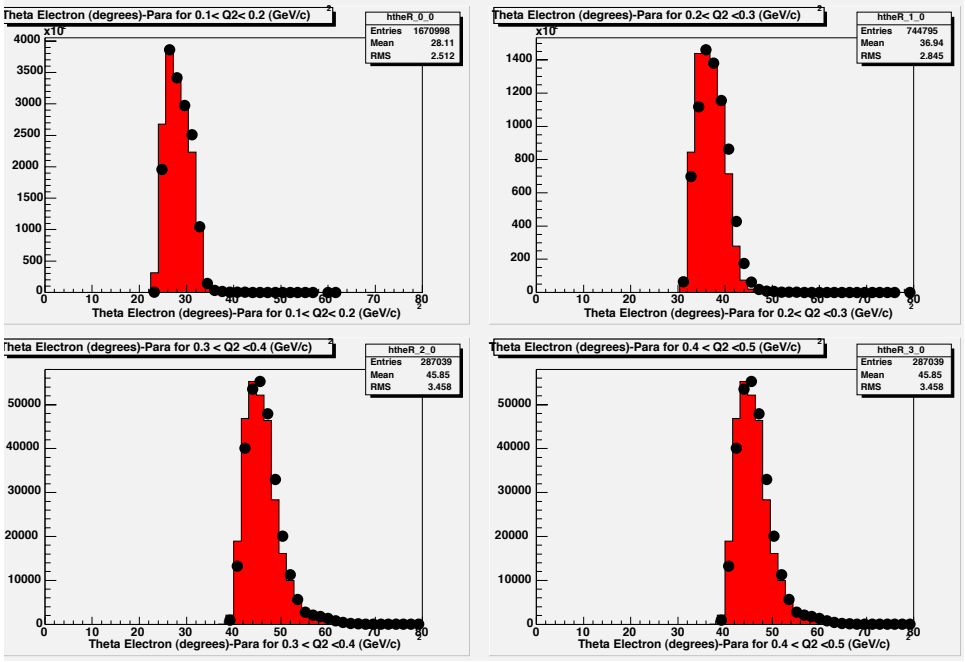

(b) 2005

Figure 4-15: Reconstructed theta angle for the electron for parallel kinematics (Red Histogram) compared to that generated Monte Carlo (black dots) for both sets of data for all Q^2 bins

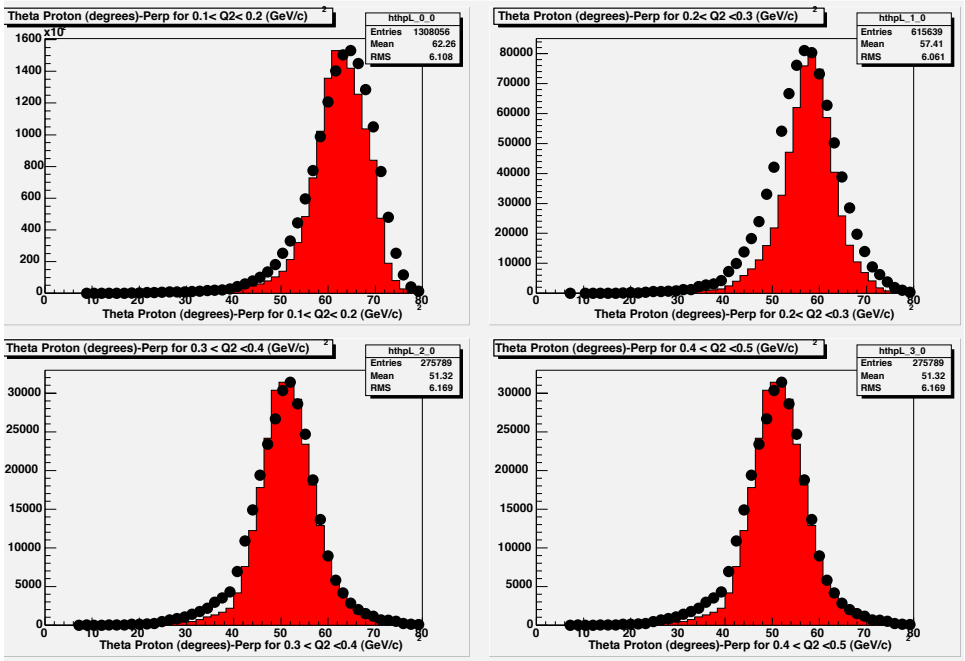

(a) 2004

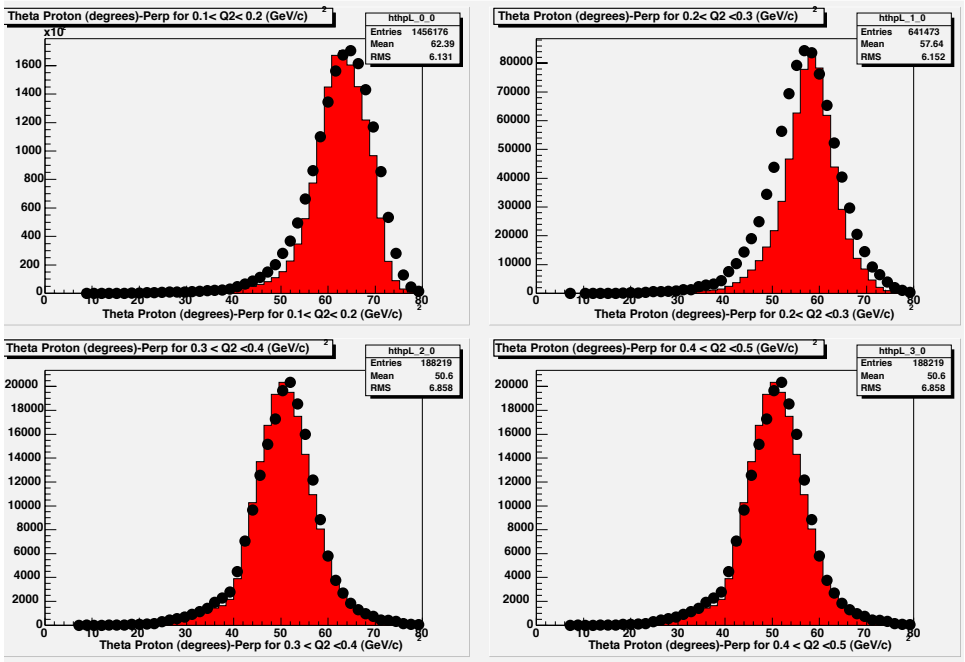

(b) 2005

Figure 4-16: Reconstructed theta angle for the proton for perpendicular kinematics (Red Histogram) compared to that generated Monte Carlo (black dots) for both sets of data for all Q^2 bins

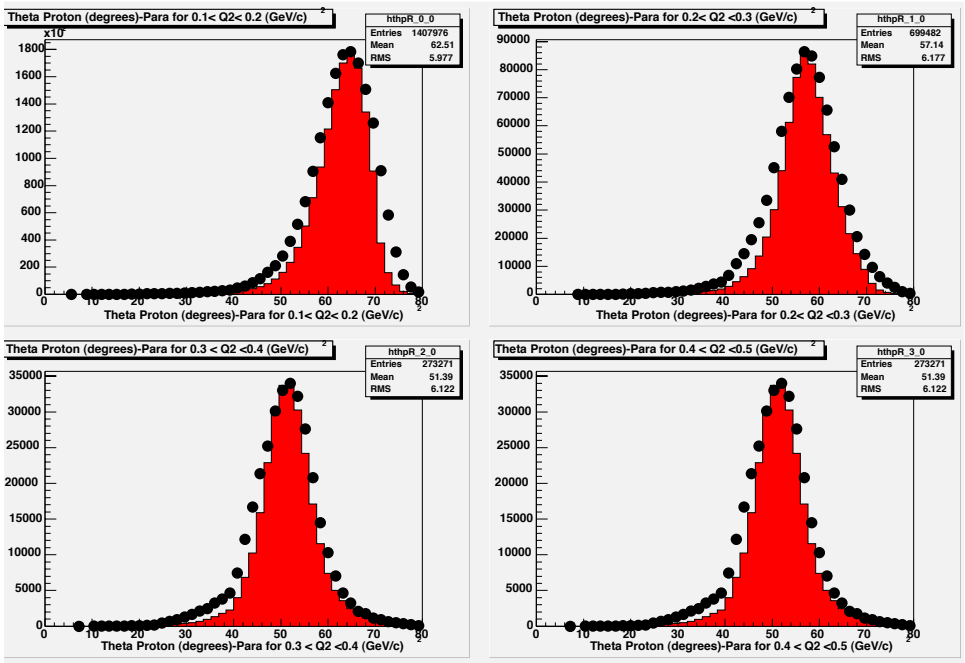

(a) 2004

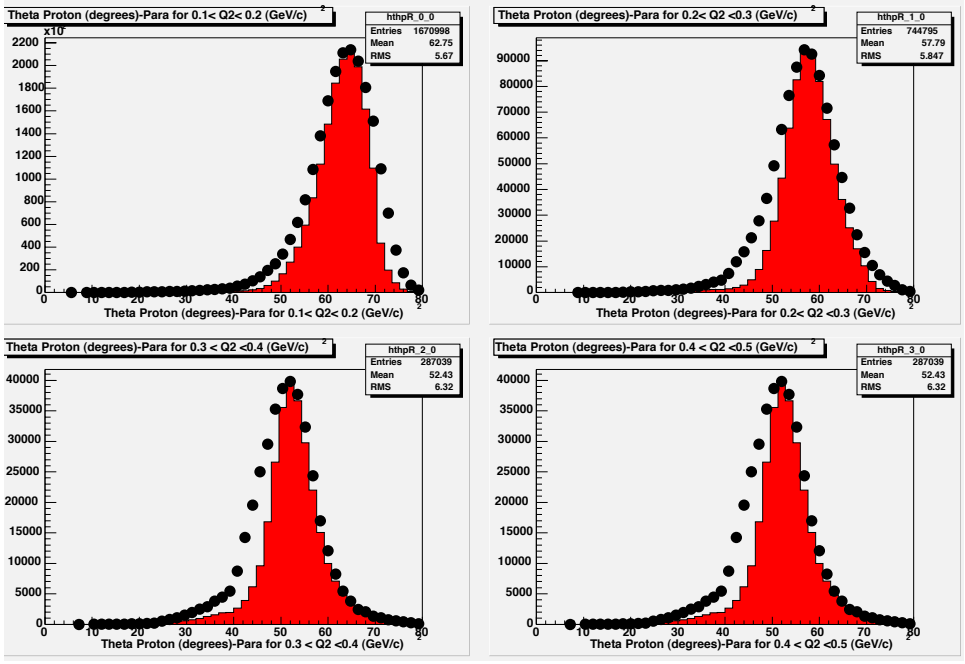

(b) 2005

Figure 4-17: Reconstructed theta angle for the proton for parallel kinematics (Red Histogram) compared to that generated Monte Carlo (black dots) for both sets of data for all Q^2 bins

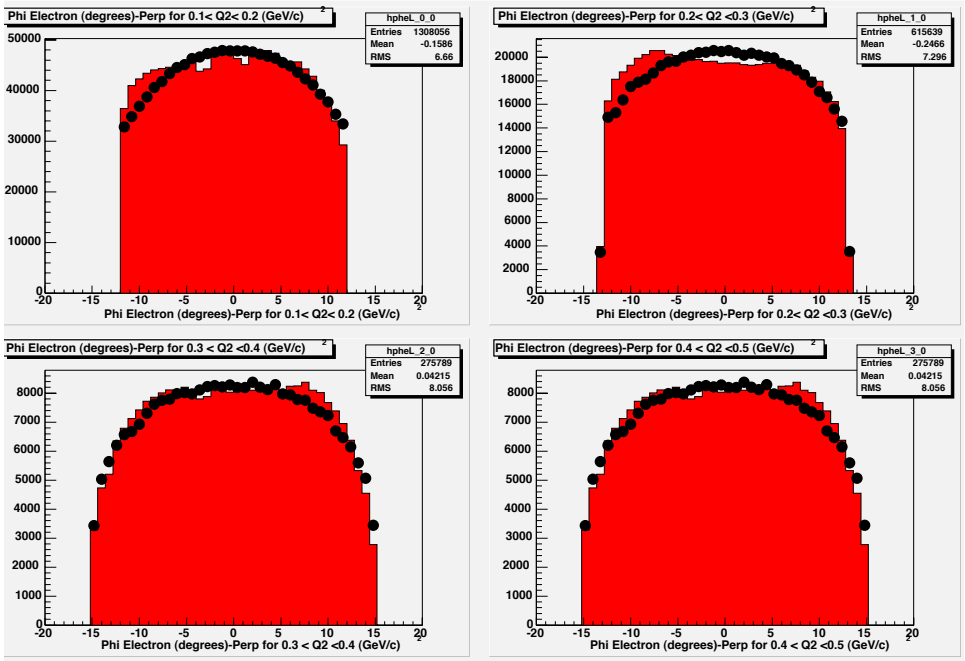

(a) 2004

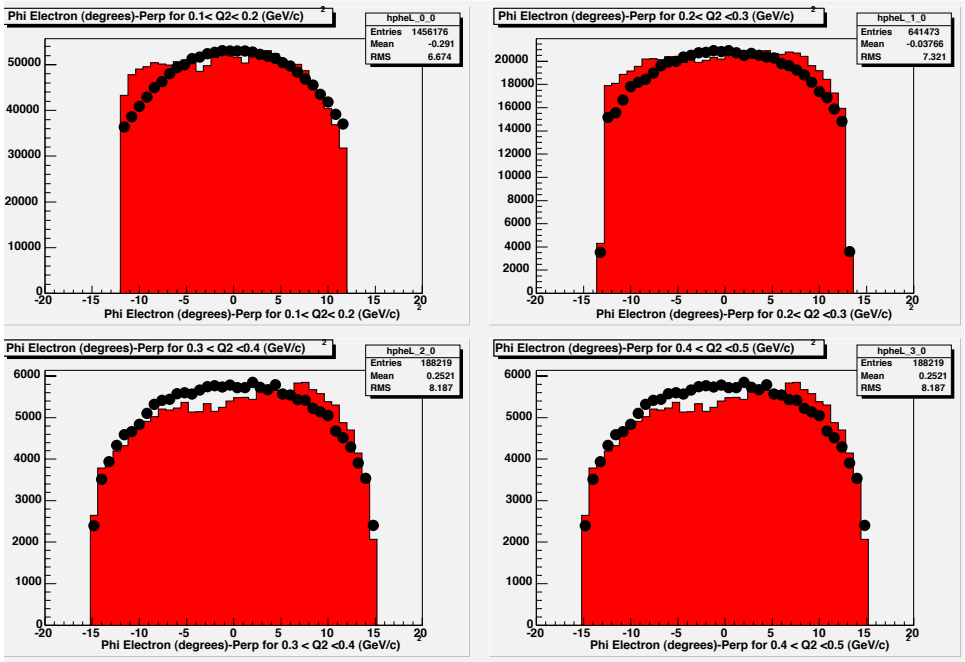

(b) 2005

Figure 4-18: Reconstructed phi angle for the electron for perpendicular kinematics (Red Histogram) compared to that generated Monte Carlo (black dots) for both sets of data for all Q^2 bins

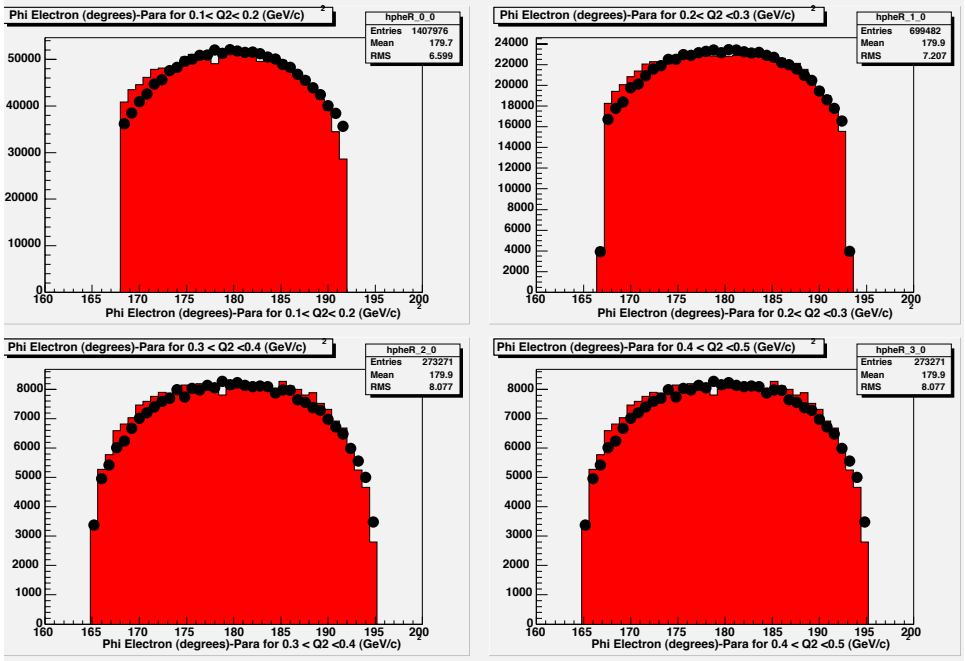

(a) 2004

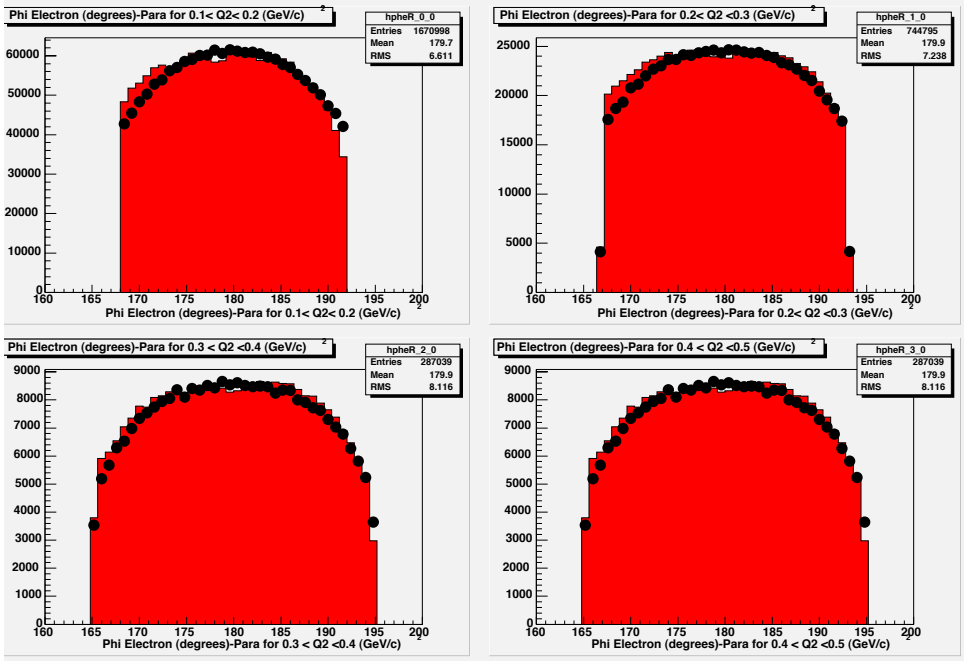

(b) 2005

Figure 4-19: Reconstructed phi angle for the electron for parallel kinematics (Red Histogram) compared to that generated Monte Carlo (black dots) for both sets of data for all Q^2 bins

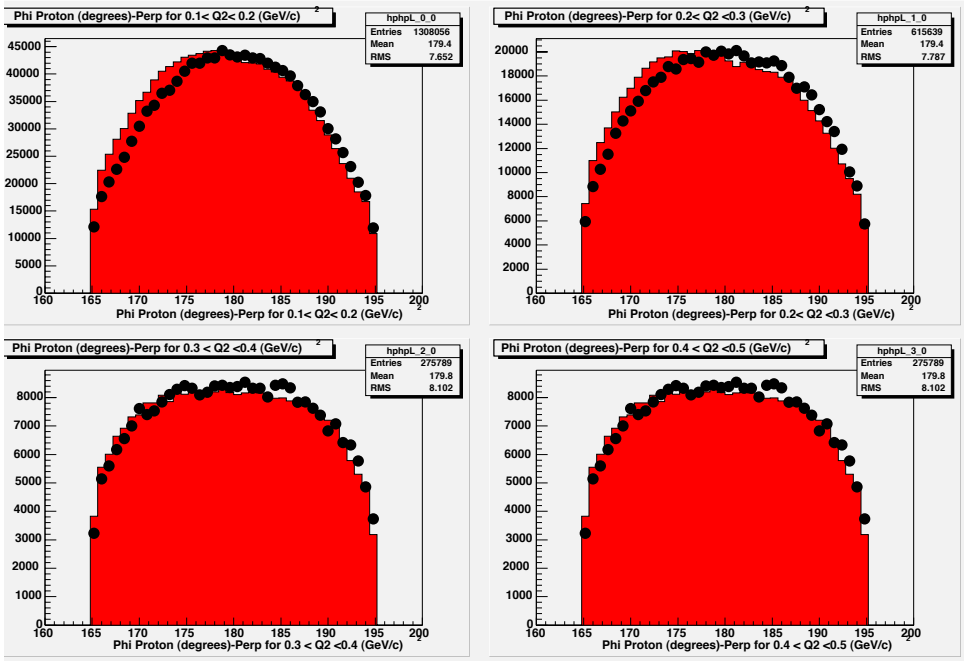

(a) 2004

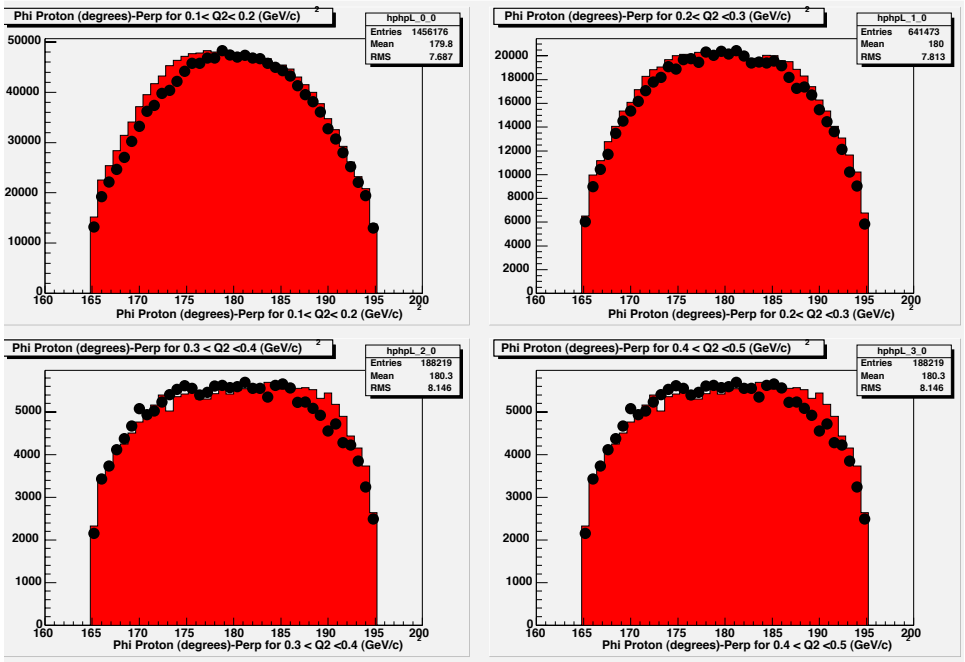

(b) 2005

Figure 4-20: Reconstructed phi angle for the proton for perpendicular kinematics (Red Histogram) compared to that generated Monte Carlo (black dots) for both sets of data for all Q^2 bins

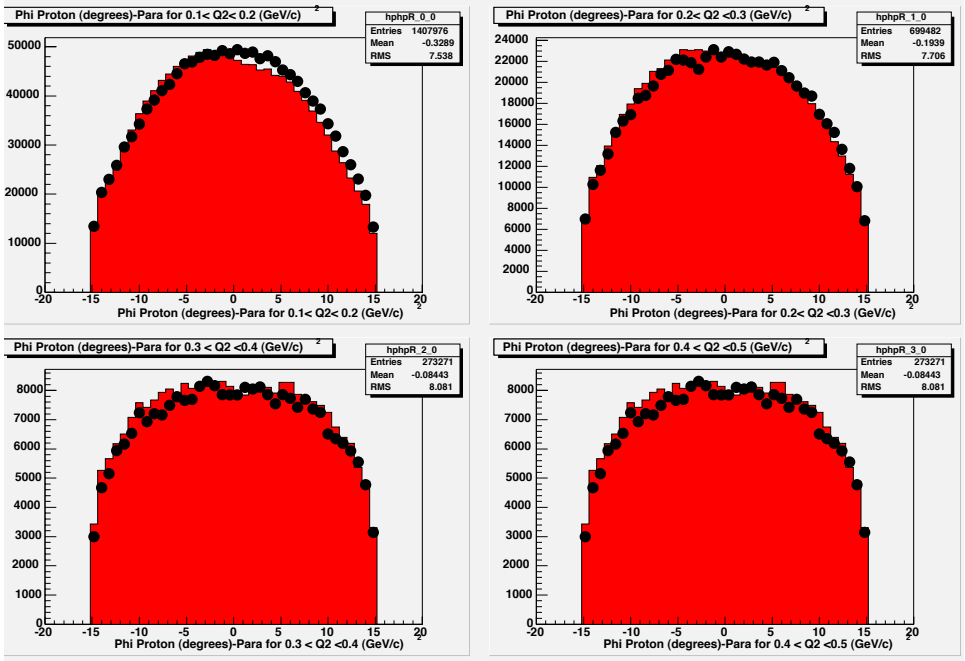

(a) 2004

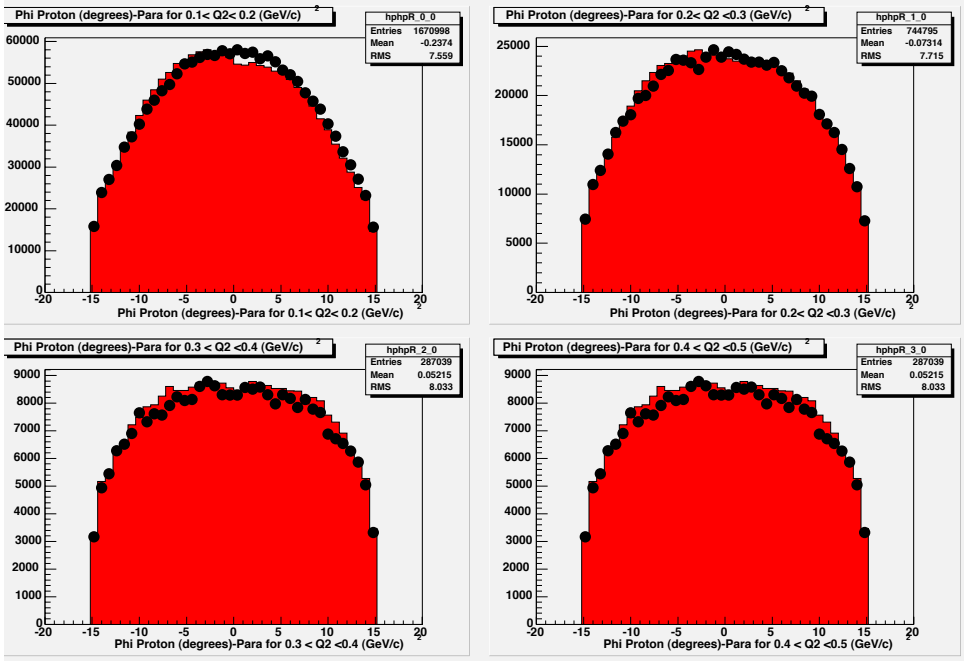

(b) 2005

Figure 4-21: Reconstructed phi angle for the proton for parallel kinematics (Red Histogram) compared to that generated Monte Carlo (black dots) for both sets of data for all Q^2 bins

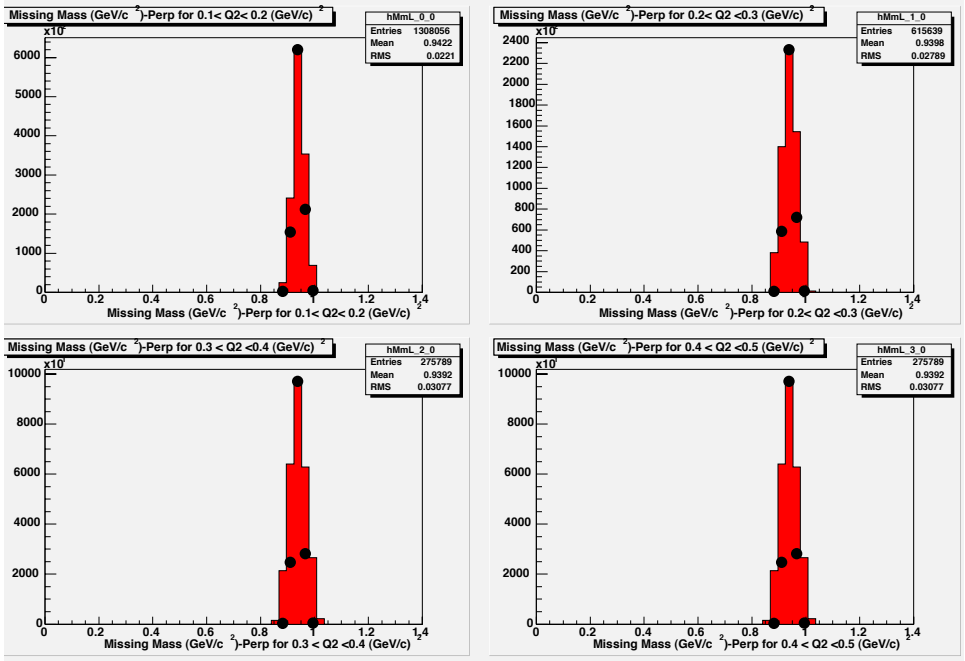

(a) 2004

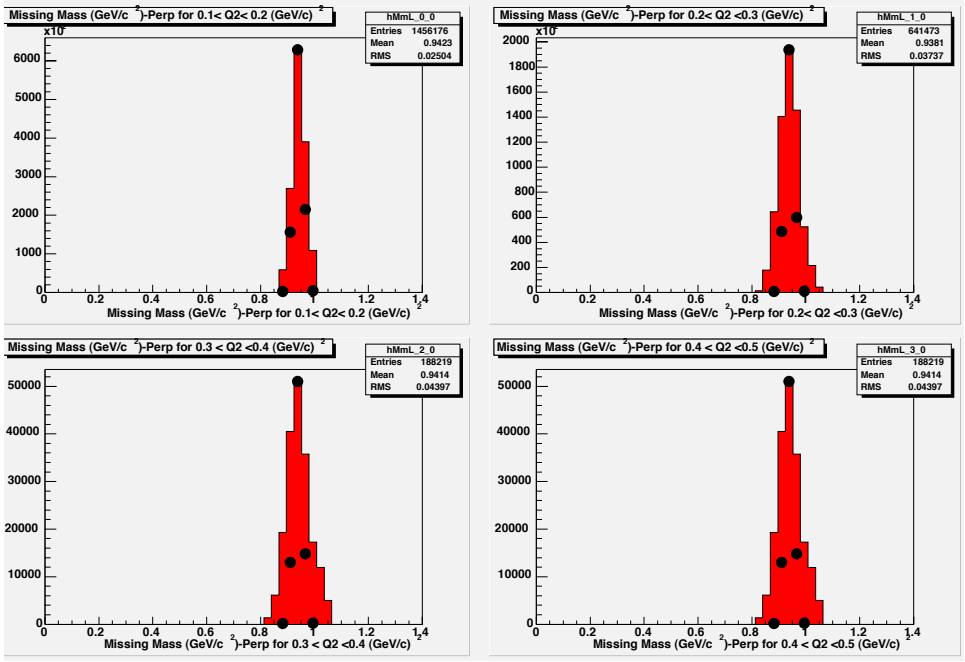

(b) 2005

Figure 4-22: Reconstructed Missing Mass for perpendicular kinematics (Red Histogram) compared to that generated Monte Carlo (black dots) for both sets of data for all Q^2 bins

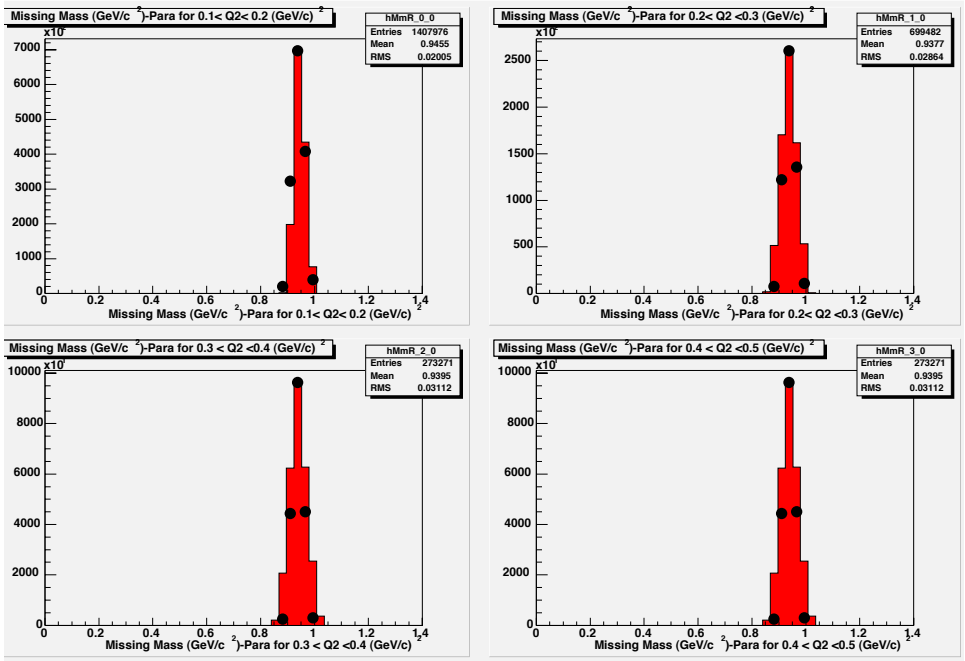

(a) 2004

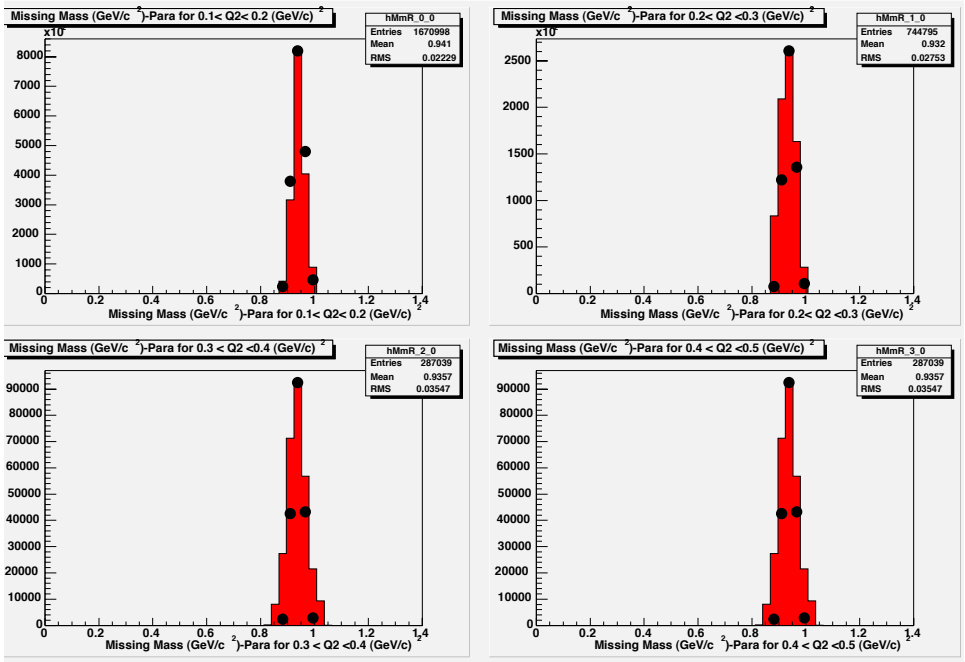

(b) 2005

Figure 4-23: 22Reconstructed Missing Mass for parallel kinematics (Red Histogram) compared to that generated Monte Carlo (black dots) for both sets of data for all Q^2 bins

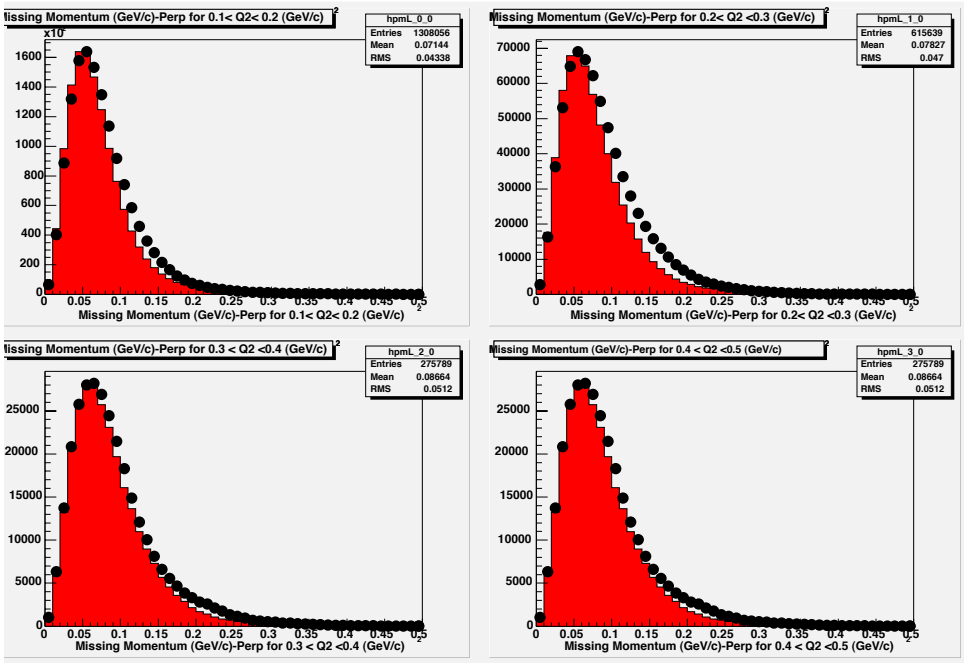

(a) 2004

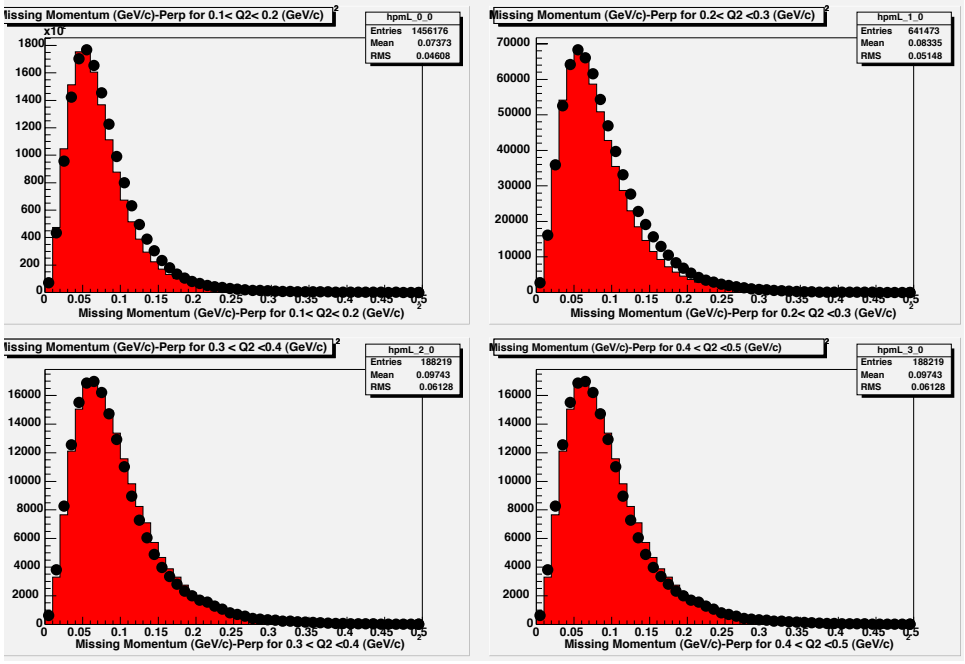

(b) 2005

Figure 4-24: 23Reconstructed Missing Momentum for perpendicular kinematics (Red Histogram) compared to that generated Monte Carlo (black dots) for both sets of data for all Q^2 bins

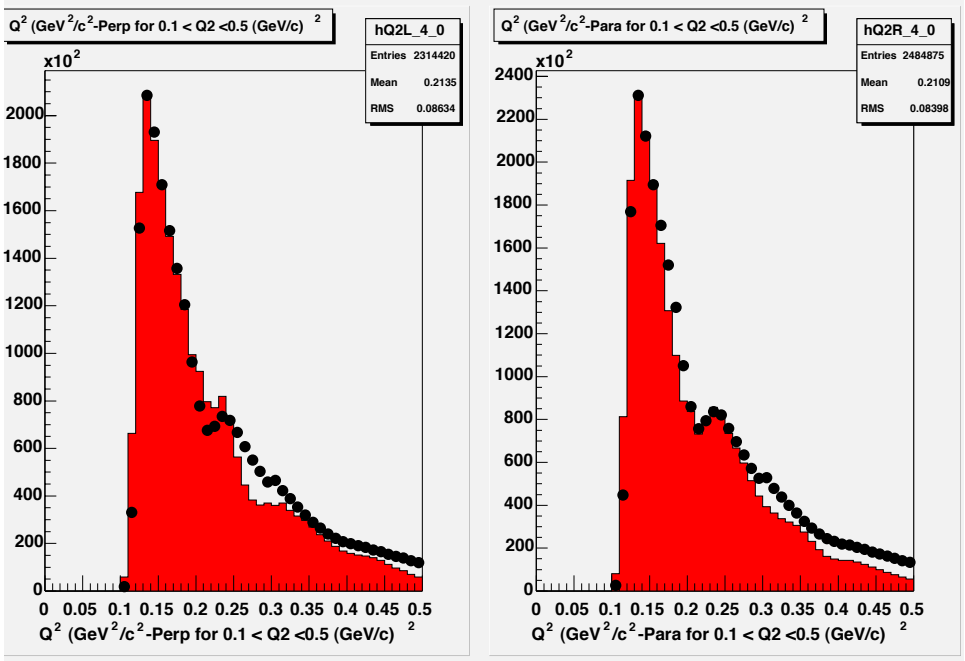

(a) 2004

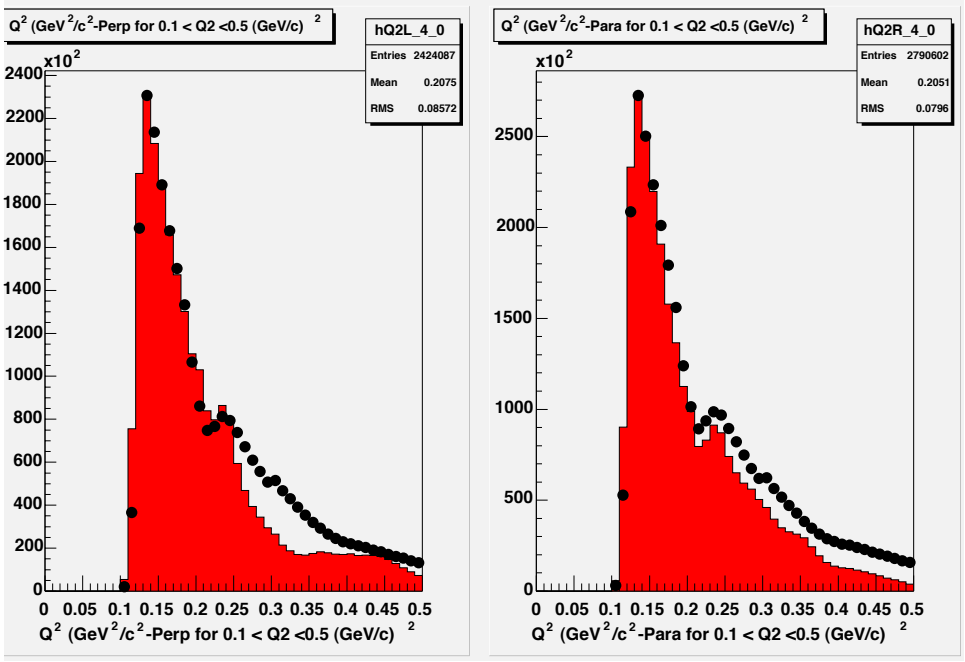

(b) 2004

Figure 4-25: Reconstructed Q2 for perpendicular kinematics (Red Histogram-Left) and parallel kinematics (right) compared to that generated Monte Carlo (black dots) for all Q^2 bins

4.6 Corrections to Asymmetries Due to Background Rates

Background rates arose predominately from beam collisions with the cell wall and entered into the measured asymmetries as a dilution from their true values. The dominant source was believed to be quasi-elastic electron-proton scattering from the aluminum walls in the target region, since other reactions would have been eliminated by vertex and missing mass cuts. Estimates for the background rates were made by running the BLAST detector with beam but without gas in the target cell. The magnetic fields for ABS operation were switched at their normal rate to investigate any spin dependence in the background rates and to simulate data taking as closely as possible. The rates were found to be independent of ABS magnetic fields and were assumed be constant with respect to any spin state in the correction. The empty cell runs ran in 2004 and 2005 and accumulated a total of 37.33 kC and 54.54 kC of charge respectively. It should be noted that only rates from the 2004 empty cell run were used for background subtraction due to an anomaly found in the 2005 data where rates for the very highest p_m bins had empty target rates greater than rates with gas in the cell. Background rates were estimated from empty cell data vs. Q^2 and p_m for A_{ED}^V and A_d^T extraction. Following the notation used in the previous section, the general equation for the measured asymmetry is written,

$$a_j A^j = \frac{\sum_i g_i^j r_i^T}{\sum_i r_i^T} \tag{4.14}$$

where a_j is the polarization product, A^j is the true asymmetry, r_i^R are the measured rates and the quantities g_j^i are multiplication factors used to combine rates. The real rates can be written in terms of measured true rates as $r_i^T = r_i^M - r^B$ with $r_i^B = r^B$ (assuming the background spin-independent), leading to the equation,

$$a_j A^{j,R} = \frac{\sum_i g_i^j (r_i^M - r^B)}{\sum_i (r_i^M - r^B)}, \tag{4.15}$$

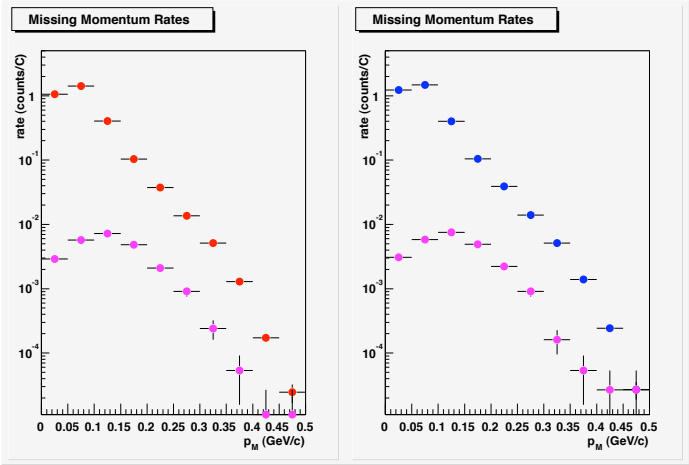

(a) Measured rates (red/blue) and background rates (pink) for parallel kinematics (left) and perpendicular kinematics (right) vs p_m

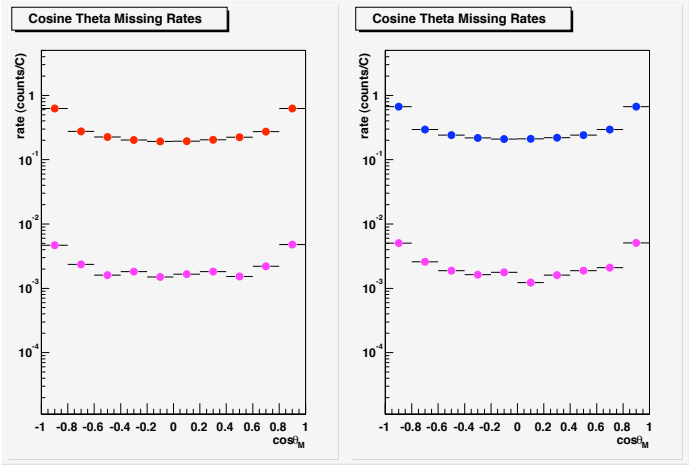

(b) Measured rates (red/blue) and background rates (pink) for parallel kinematics (left) and perpendicular kinematics (right) vs $\cos\theta_m$

Figure 4-26: Representative plots of total and background rates for the 2004 data run showing both sets of kinematics for 0.1 $(GeV/c)^2 < Q^2 < 0.2$ $(GeV/c)^2$. The top graphs are vs p_m and the bottom graphs are vs $\cos\theta_m$.

Figures 4-26(a) and 4-26(b) show representative plots of background rates vs p_m and $\cos\theta_m$ for the 2004 data. The event sample was generated by running the same code that applies the cuts and corrections to select out quasi-elastic ep data. The statistical error is given by 4.16 where the error in the beam charge was small enough so that the first term was negligable. Since data rates decrease dramatically at high missing momentum, certain bins, especially as the Q^2 bin increased, had no counts. For these cases it was decided to leave the background for this bin as zero and assign an error to the bin calculated from adding a count of one event to that bin. To arrive at the true measured rate background, subtraction was done on a bin by bin basis with the uncertainty in the measured rates given by,

$$\begin{aligned}\delta(r_i^T)^2 &= \left(\frac{n_i^M}{(C_i^M)^2}\right)^2\delta(C_i^T)^2+\left(\frac{n_B}{C_B^2}\right)^2\delta(C_B)^2 \\ &\quad +\left(\frac{1}{C_i^M}\right)^2\delta(n_i^T)^2+\left(\frac{1}{C_B}^2\right)\delta(n_B)^2 \\ &\approx \left(\frac{1}{C_i^M}\right)^2 n_i^T+\left(\frac{1}{C_B}\right)^2 n_B \end{aligned} \tag{4.16}$$

where the C_i is the total charge for the i^{th} spin-state, C_B is the background charge and the n's are the number of events in that bin.

4.7 Statistical errors in the measured asymmetry

The rates used in measuring the asymmetries were the background subtracted, true rates whose statistical errors, δr_i, were calculated in the previous section. Therefore, to obtain the statistical error associated with the measured asymmetries, one starts again with its general form where the measured rates are replaced with the true rates,

$$a_j A^j = \frac{\sum_i g_i^j r_i^R}{\sum_i r_i^R} \tag{4.17}$$

Here a_j is either $a_{hP_z} * h \cdot P_z$ for the beam-vector asymmetry or $a_{zz} * P_{zz}$ for the tensor asymmetry and the a's are numerical factors defined by the formalism. The

statistical error is calculated starting with the equation,

$$\delta(A^j)^2 = \left(\frac{1}{a_j}\right)^2 \cdot \sum_k \left[\delta_{ik}\partial_{r_k}\left(\frac{\sum_i g_i^j r_i^R}{\sum_i r_i^R}\right)\right]^2 \cdot (\delta r_j)^2 + \left(\frac{\sum_i g_i^j r_i^R}{\sum_i r_i^R}\right)^2 \cdot \frac{1}{a_j^2} \cdot (\delta a_j)^2 \quad (4.18)$$

The second term was included as a systematic error in hP_z since it affects the asymmetries approximately the same for all bins, and has the tendency to raise or lower each individual asymmetry measurement by the same amount. Also note that for the determination of hP_z, the above equation is valid provided it is calculated for an undiluted beam-vector asymmetry. The equation can be simplified by introducing the symbols N_1 and N_2^j into the equation for the statistical error of the asymmetry,

$$\delta(A^j)^2 = \left(\frac{1}{a_j}\right)^2 \sum_k \left(\frac{(g_k^j)^2(N_1^j)^2 + (N_2)^2 - 2g_k^j N_1^j \cdot N_2}{N_2^4}\right) \cdot (\delta r_k)^2 + \left(\frac{N_1^j}{N_2}\right)^2 \cdot \frac{1}{a_j^2} \cdot (\delta a_j)^2. \quad (4.19)$$

Here, N_1 and N_2 are defined as

$$N_1^j = \sum_i g_i^j r_i \quad (4.20)$$

and

$$N_2 = \sum_i r_i \ . \quad (4.21)$$

4.8 Statistical errors in the generated asymmetry from Monte Carlo

The statistical uncertainty can be written in a form similar to that for the data provided that instead of count rates, the cross section weighted variable is used. This can be summarized is a similar matrix to the one for the data. The second term is not present since there is no dilution. The statistical error was calculated on a bin-by-bin basis to be,

$$(\delta A^j)^2 = \sum_k \left(\frac{(g_k^j)^2(N_1^j)^2 + (N_2)^2 - 2g_k^j N_1^j \cdot N_2}{N_2^4}\right) \cdot (\delta r_k)^2 \quad (4.22)$$

where now a_j is either a_{hP_z} or $a_{P_{zz}}$ and σ_i is the cross section weighted variable for the i$^t h$ state.

$$N_1^j = \sum_i g_i^j \sigma_i \tag{4.23}$$

and

$$N_2 = \sum_i \sigma_i \ . \tag{4.24}$$

4.9 Beam-Vector Polarization

There primary method to extract the beam-vector polarization, hP_z, relied on comparing the measured beam-vector asymmetry to the one generated by Monte Carlo in the kinematic region where model dependence and subnuclear effects were small. In this regime of low Q^2 (high statistics) and low missing momentum (minimal model dependence), we have to a good approximation the asymmetry in the quasi-elastic limit. In this limit, the beam-vector asymmetry's value is well understood, and hP_z can be determined by the ratio,

$$hP_z = \frac{A^V_{ed,MEAS}}{A^V_{ed,MC}}. \tag{4.25}$$

where $A^V_{ed,MEAS}$ is the measured asymmetry and $A^V_{ed,MC}$ was generated by Monte Carlo. The BLAST detector covered a missing momentum range of 0.0 GeV/c to 0.5 GeV/c which were divided into 10 bins of equal size. The beam-vector asymmetry was limited for this extraction to less than 0.1 GeV/c in Q^2 giving two bins of data. To extract hP_z, a weighted average of the two points were taken where,

$$hP_{z,1} = \frac{A^V_{ed,MEAS,1}/A^V_{ed,MC,1}}{\sigma_1^2} \tag{4.26}$$

and

$$hP_{z,2} = \frac{A^V_{ed,MEAS,2}/A^V_{ed,MC,2}}{\sigma_2^2} \tag{4.27}$$

hP_z				
Year	Kine	hP_z	stat	sys
2004	Perp	0.619	0.05648	0.0121
2004	Para	0.606	0.01168	0.0885
2005	Perp	0.396	0.0147	0.0290
2005	Para	0.412	0.0121	0.0276

Table 4.2: Dilution factors for the beam-vector asymmetries

so that $hP_z = \frac{1}{2}(hP_{z,1} + hP_{z,2})$, and the sample variance squared is thus,

$$s^2 = \frac{1}{N-1}\sum_i (hP_{z,i} - hP_z)^2. \tag{4.28}$$

The σ_is were the uncertainties of the measured asymmetries (the uncertainties in the Monte Carlo were small and, therefore, could be neglected). For the final results quoted in the Table 4.9, the bonn potential was used, and the difference in results due to model choice was added on as a systematic error. In addition a value was measured for each year's data and for each sector since each sector provided an independent measurement.

4.10 Polarizations and Spin Angle

As stated previously the total differential cross section for the reaction ${}^2\overleftrightarrow{H}(\vec{e}, ep)n$ can be written as the sum of products of asymmetries and polarizations multiplied by an overall factor of the unpolarized cross section,

$$\frac{d\sigma}{d\omega d\Omega_e d\Omega_{pn}^{CM}} = S_o\left[1 + \tilde{P}_z A_d^V + P_{zz} A_d^T + h\left(A_e + \tilde{P}_z A_{ed}^V + P_{zz} A_{ed}^T\right)\right]. \tag{4.29}$$

For an experiment with perfect polarization, the true asymmetries would be equal to the measured asymmetry. In BLAST electron beam polarization was $\approx 65\%$ and target polarizations were $\tilde{P}_z \approx 86\%$ ($\approx 79\%$) and $\tilde{P_{zz}} \approx 86\%$ ($\approx 55\%$) for deuterium for 2004 (2005), thus the measured asymmetry was diminished from the true values by these amounts.

However, even for an experiment that had perfect polarization, the cross section would still depend on the direction of the polarization vector of the target. This can be seen in the general form of the asymmetries as described by Arenhoevel in [11],

$$A(\phi, \tilde{\phi}, \theta_d) = \sum_{M=0}^{I} \alpha_{IM}(\phi, \tilde{\phi}) d^I_{M0}(\theta_d), \tag{4.30}$$

where the sum runs to $I = 0$ for no target polarization, $I = 1$ for vector polarization, and $I = 2$ for tensor. The functions $\alpha_{IM}(\phi, \tilde{\phi})$ are coefficients that depend on the azimuthal angle between the reaction plane and the scattering plane, and $\tilde{\phi}$ defined as the difference between the azimuthal angle of the outgoing np system and the target angle, $\phi - \phi_d$. These functions separate out as functions that depend on ϕ multiplied by sine or cosine that contain $\tilde{\phi}$,

$$\alpha_{IM}(\phi, \tilde{\phi}) = c_{IM}(\phi) \cos(M\tilde{\phi}_) + s_{IM}(\phi) \sin(M\tilde{\phi}). \tag{4.31}$$

and, $d^I_{M0}(\theta_d)$ are Wigner functions defined here..

In general the target angle was not a single value over the length of the cell, but varied along it's length by up to $\sim 25\%$ near the ends of the usable target length. The shape was repeatedly measured by a series of hall probe surveys and compass measurement of varying needle sizes. The measurements showed a target spin profile with a characteristic shape (see Figure 4-27), but the absolute value varied from between measurements. A seventh order polynomial was fit to the data with the average value, $\theta_d^{BLAST}|_{z_{BLAST}=0}$, being determined by the measurement of the spin angle from e-d elastic scattering discussed in the next section.

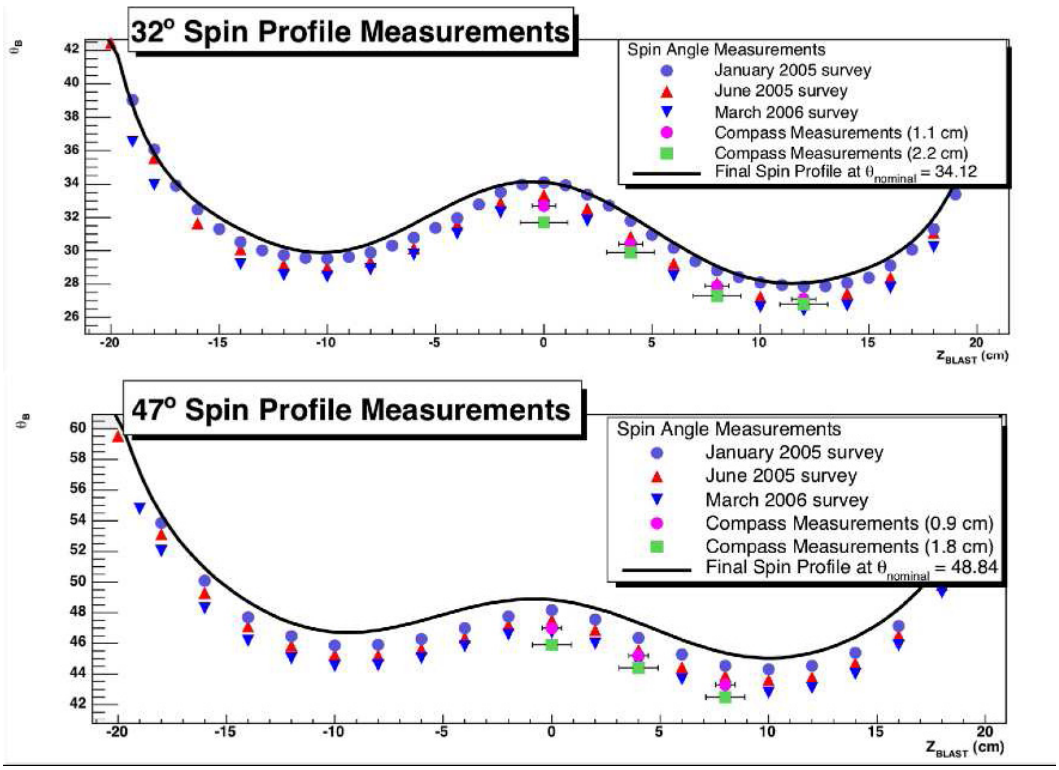

Figure 4-27: Polarization direction as a function of position along the target cell for different data runs

4.11 Tensor Polarization

In extracting the tensor asymmetry the true value, A_d^T, is obtained by dividing the measured value by the tensor polarization [1],

$$A_{d,true}^T = \frac{A_{exp}}{P_{zz}}. \tag{4.32}$$

It was important to have an accurate and precise measurement of P_{zz} since the uncertainty in the true asymmetry will be dominated when by the fractional error in P_{zz} if it is greater than that for the measured asymmetry.

The value of P_{zz} used in this thesis was determined from the analysis of elastic e-d scattering as part of the BLAST experiment [40] . This reaction was chosen because it provided the highest sensitivity to P_{zz} as well as simultaneously having the capability of determining the nominal value of the target spin angle. Starting with the total cross section for elastic e-d scattering written in terms of asymmetry observables and polarization factors, we have

$$\frac{d\sigma}{d\Omega_e}(h, \tilde{P}_z, P_{zz}) = S_0(1 + P_{zz}\Gamma + h\tilde{P}_z\Delta) \tag{4.33}$$

where S_0 is the unpolarized differential cross section, Γ is the tensor cross section, and Δ is the beam-vector cross section. Since we are interested in the extraction of P_{zz}, consider only the part of the cross section that depends on tensor polarization, Γ. In terms of its tensor analyzing powers, T_{ij}, Γ can be expanded as,

$$\Gamma = \frac{1}{\sqrt{2}}\left[\left(\frac{3}{2}\cos^2\theta_d - \frac{1}{2}\right)T_{20} - \sqrt{\frac{3}{2}}\sin 2\theta_d \cos\phi_d T_{21} + \sqrt{\frac{3}{2}}\sin^2\theta_d \cos 2\phi_d T_{22}\right] \tag{4.34}$$

Since the tensor + state contains either vector - or vector + the two states must be combined to cancel the vector state leaving a combination of pure tensor + state, called Y_+. The tensor minus state is assumed to be a pure state leaving the equation

[1] The asymmetries that are compared to theoretical ones are referred here as the 'true' asymmetries and the 'measured' asymmetries are the asymmetries directly measured and are not corrected for the fact the target and beam did not have perfect polarizations.

for the measured asymmetry to [2],

$$A_{exp} = \sqrt{2}\frac{Y_+ - Y_-}{P_{zz}^+ Y^- - P_{zz}^- Y^+} \tag{4.35}$$

Assuming equally mixed states for the tensor + and pure state for the tensor -, there is the following relation,

$$P_{zz}^- = -2P_{zz}^+ = -2\overline{P}_{zz}. \tag{4.36}$$

By putting this into eq 4.35 and following the formalism of Arenhovel that introduces a factor of $\sqrt{2}$ a relation can be made between the true asymmetry and the one measured.

$$A_{true}^T = -\sqrt{2}\overline{P_{zz}} A_{measured}^T. \tag{4.37}$$

To extract the spin angle and the tensor polarization, the first two Q^2 bins out of the entire Q^2 range (11 bins) were compared to Monte Carlo. The Abbot Parameterization 3 for the form factors was used since it was based on the world data at the time of the analysis and lies approximately in the middle of the range of models.

Because BLAST was a large acceptance and symmetric detector, it allowed for two independent $P_{zz}(\theta_S)$ curves to be extracted simultaneously, corresponded to roughly perpendicular and parallel kinematics. Since P_{zz} and θ_S must be the same for both, where the curves cross yields P_{zz} and θ_S, specifically

$$P_{zz}^{\parallel}(\theta_S) = \frac{A_{raw}^{\parallel}}{A_{MC}^{\parallel}(\theta_S)} \tag{4.38}$$

and

$$P_{zz}^{\perp}(\theta_S) = \frac{A_{raw}^{\perp}}{A_{MC}^{\perp}(\theta_S)}. \tag{4.39}$$

[2] In the analysis performed by Zhang [40] the arrival at the measured asymmetry being equal to $A_{measured}^T$ is a non trivial process. In the analysis he shows that three terms that are the result of having a mixture of states introduce a very small error ($\sim 0.01\%$) and therefore to a very good approximation the two are equal.

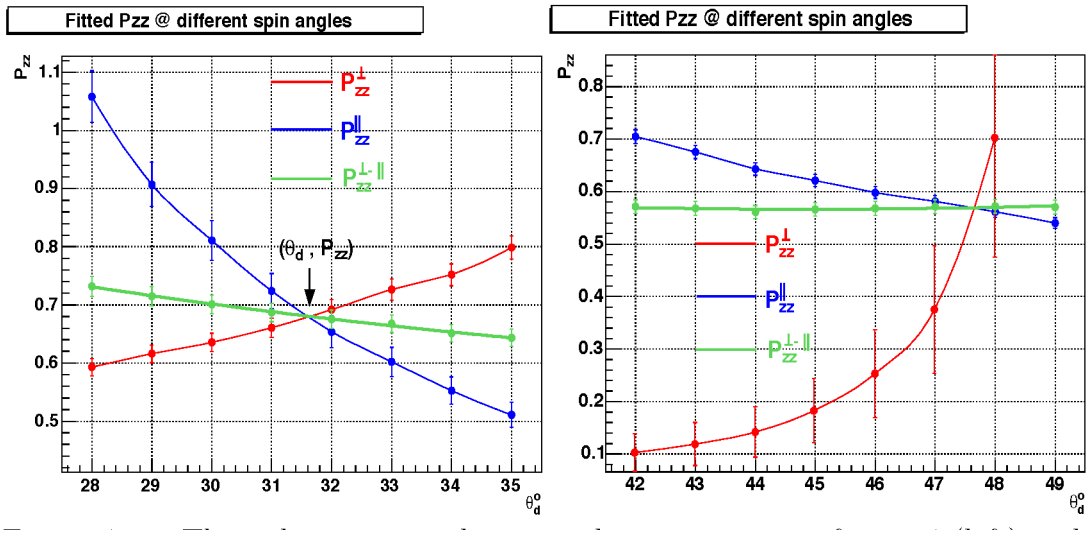

Figure 4-28: Tensor polarization measurements from 2004 and 2005 data sets. The crossing point of the plots was used to determine the nominal spin angle. In addition it was the parameter $P_z^{\perp-\parallel}z$ that was used to determine the tensor polarization because it is less sensitive to θ_S.

The two figures in 4-28 show the plots of P_{zz} vs spin angle for the two sets of data. Note that the crossing point where $P^{\parallel}_{zz}(\theta_S) = P^{\perp}_{zz}(\theta_S)$ defines the value of $\overline{\theta}_S$ and $\overline{P}_{zz}$. The parallel and perpendicular components have strong dependences on $\overline{\theta}_S$, which allowed for a precise determination of the spin agle. These same curves however would be poor choices for determining the average spin polarization since any error in $\overline{\theta}_S$ would be strongly propagated into $\overline{P}_{zz}$. As a consequence, another quantity was chosen, $P^{\parallel-\perp}$ that minimized the correlation between these two parameters yet had the same crossing value as $P^{\parallel}_{zz}(\theta_S)$ and $P^{\perp}_{zz}(\theta_S)$. Defined as

$$P^{\parallel-\perp} = \frac{A^{\parallel}_{raw} - A^{\perp}_{raw}}{A^{\parallel}_{MC} - A^{\perp}_{MC}}, \tag{4.40}$$

one sees from Figures in 4-28 it had a smaller slope and hence less dependence on θ_S. It can be shown to be equal to $\overline{P}_{zz}$ by dividing by the numerator and denominator

by $A^{\parallel}_{MC} \cdot A^{\perp}_{MC}$ and using the relations above,

$$P^{\parallel-\perp}|_{\theta=\bar{\theta}_S} = \frac{A^{\parallel}/(A^{\parallel}_{MC} \cdot A^{\perp}_{MC}) - A^{\perp}/(A^{\parallel}_{MC} \cdot A^{\perp}_{MC})}{1/A^{\perp}_{MC} - 1/A^{\parallel}_{MC}}\Bigg|_{\theta=\bar{\theta}_S} \tag{4.41}$$

$$= \frac{1/A^{\perp}_{MC} - 1/A^{\parallel}_{MC}}{1/A^{\perp}_{MC} - 1/A^{\parallel}_{MC}}\Bigg|_{\theta=\bar{\theta}_S} \cdot \overline{P}_{zz} \tag{4.42}$$

$$= \overline{P}_{zz} \tag{4.43}$$

The final results for P_{zz} with the statistical and systematic error added in quadrature, quoted from [40], were $P_{zz} = 0.683 \pm 0.015$ in 2004 and$P_{zz} = 0.563 \pm 0.042$ in 2005. The nominal spin angles were 31.72 ± 0.035 in 2004 and 47.74 ± 0.042 in 2005. The largest error was the error due to the comparison made between the measured asymmetry and the one obtained from theory, specifically it was found that at the two lowest Q^2 bins used, the predominate error was attributed to the theoretical value of T_{20} which had an overall uncertainty of $\approx 15\%$.

There were certain qualifications that need to be made to this method. As discussed previously, the target had an angular distribution vs z due to variations in the magnetic field across the z-axis of the beam line most likely due to the presence of nearby magnetic materials; this distribution was not determined at the time of this analysis and therefore the Monte Carlo and the data had assumed a single value for the spin angle. This was, however, included as a systematic error and is discussed in the next section. A reanalysis is underway [72] where the shape of the target spin angle vs Z will be included in the both the analysis of the data and the Monte Carlo so that a new value of $\tilde{P_{zz}}$ will be generated.

4.12 Systematic and Statistical Errors in the Tensor Polarization

Table 4.3 shows the sources for the statistical and systematic errors from the extraction of P_{zz} as well as from θ_S. As stated the largest source of systematical error was the dependence on theory in the Monte Carlo asymmetry. Since the measured asym-

	2004		2005	
source	ΔP_{zz}	$\Delta\theta_S$	ΔP_{zz}	$\Delta\theta_S$
Statistics	0.015	0.35°	0.013	0.42°
$\Delta\theta_e$	0.015	0.20°	0.018	0.12°
$\Delta\theta_S$	0.004		0.002	
ΔR	0.002	0.10°	0.019	0.01°
theory	0.034	0.10°	0.028	0.10°
total	0.040	0.43°	0.040	0.45°

Table 4.3: Systematic errors in P_{zz} and θ_S from various sources (taken from [40]. The statistical errors are also listed for comparison.

metry is in fact the result of the sums of tensor polarization observables containing different kinematic variables as coefficients, the predominate theoretical uncertainty was found to be the theoretical uncertainty in T_{20}. There was an approximately $\pm 5-7\%$ difference in the theory curves for this observable in the lowest bins chosen.

Zhang:2005phd it was shown that a correlated reconstruction error was about half of an uncorrelated error for the case of low Q^2 which is the region used to determine P_{zz}. If the former source is ignored when considering, the size of error is 1/5 that of statistical error, the error estimate was limited to uncorrelated errors. Therefore the error in $\Delta A_{exp}(\Delta\theta_e)$ is simply estimated by,

4.12.1 Correction of Dipole Form Factor and Related Systematic Errors

Historically the value of $G_E^n(Q^2)$ was measured from elastic scattering and was severely limited by model dependencies. The results were described by the Galster parameterization which used a dipole fit to the form factors and are given by

$$G_E^p(Q^2) = \frac{1}{\mu_p} G_M^p(Q^2) = G_D \equiv \frac{1}{(1+Q^2/\Lambda^2)}, \tag{4.44}$$

with $\Lambda^2 = 0.71(GeV/c)^2$ with the dipole form multiplied an appropriate function such that $G_E^n(0) = 0$ *i.e.* $G_E^n(Q^2) = \frac{a_G\tau}{1+b_G\tau} \cdot G_D Q^2)$. However recent polarization measurements have provided methods of extracting the form factors that are nearly

free of model assumptions. This has led to the work of Friedrich and Walcher who have attempted to provide a versions of the form factors to match the new data. Their work modified the fitting function for G_n^E and putting forth a phenomenological ansatz for the form factors where the "smooth" part is described by two dipole-like terms

$$G_s(Q^2)\frac{a_{10}}{(1+Q^2/a_{11})^2} + \frac{a_{20}}{(1+Q^2/a_{11})^2} \tag{4.45}$$

where the bump seen in G_E^n is given by two exponentials

$$G_b(Q^2) = e^{\frac{1}{2}\frac{(Q-Q_b)^2}{\sigma_b}} + e^{\frac{1}{2}\frac{(Q+Q_b)^2}{\sigma_b}} \tag{4.46}$$

so that the nucleon form factor is

$$G_N(Q^2) = G_s(Q^2) + a_b \cdot Q^2 G_b(Q^2) \tag{4.47}$$

Since the Monte Carlo of BLAST incorporating work done by Arenhoevel used the dipole form factors a correction was made to the measurement of hP_z in light of the most recent information. The correction relies on the fact that the value taken for hPz was for low missing momentum where the particle is struck quasielastically with behavior similar to elastic-ep, ignoring the fermi momentum and exchange effects. The asymmetry for this reaction is given by

$$A_{ep}^V = \frac{\cos\theta^* \alpha(Q^2) \sin\theta^* \cos\phi^* R(Q^2)}{\beta(Q^2) + \gamma(Q^2) R(Q^2)^2} \tag{4.48}$$

where θ^* and ϕ^* are the target polarization angles of the proton in the direction of the q-vector. The difference between the two results for the vector asymmetry enters in explicitly in R, the form factor ratio where $R(Q^2) \equiv \mu_p \frac{G_E(Q^2)}{G_M(Q^2)}$. In the dipole form, R is equal to 1 for all Q^2 values with deviations from this value, a property of Friedrich and Walcher's fit. From figure 4-29, it is apparent that the overall effect of recent data on the fit to the form factor results in a deviation from 1 on the order of a couple percent. To correct for this difference in the results of hP_z, a factor was formed that

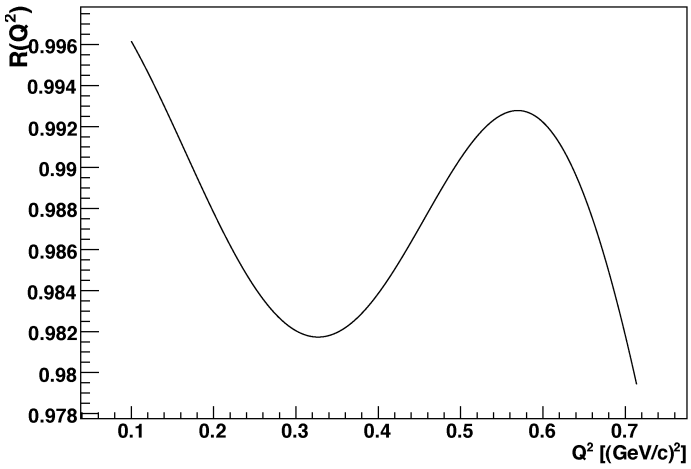

Figure 4-29: Deviations of the Friedrich and Walcher parameterization of the the ratio of electric to magnitic form factor, $R(Q^2) \equiv \mu_p \frac{G_E(Q^2)}{G_M(Q^2)}$ to that from the dipole form factors where $R(Q^2) = 1$.

related the difference between the asymmetries using these two parameterizations in the Q^2 range used by BLAST to determine hPz, *i.e.*, $0.1\ G_eV/c^2 < Q^2 < 0.2\ G_eV/c^2$. The correction is given by the relation

$$hP_{z,FW} = \frac{A^V_{ed,Meas}}{A^V_{ed,MC,Dipole}} \cdot \frac{A^V_{ep,Dipole}}{A^V_{ep,FW}} \tag{4.49}$$

$$= hP_{z,Meas} \cdot f \tag{4.50}$$

$$\tag{4.51}$$

The correction f is the ratio of the elastic asymmetry using the dipole form factors to that of Friedrich and Walcher. Figure 4.12.1 shows the corrections assuming that θ^* equals $\pi/2$ and 0 for perpendicular and parallel kinematics, respectively. The resulting correction factor was weighted by the event distribution for the Q^2 range used in determining hP_z (see figure 4-31 and figure 4-32). For parallel kinematics this was 0.997, and for perpendicular kinematic, it was 0.985, with these values under the assumptions made independent target spin angle.

The systematic errors to this correction are inherently small due to the size of the correction itself. An estimate of the systematic errors was obtained by varying θ^* by

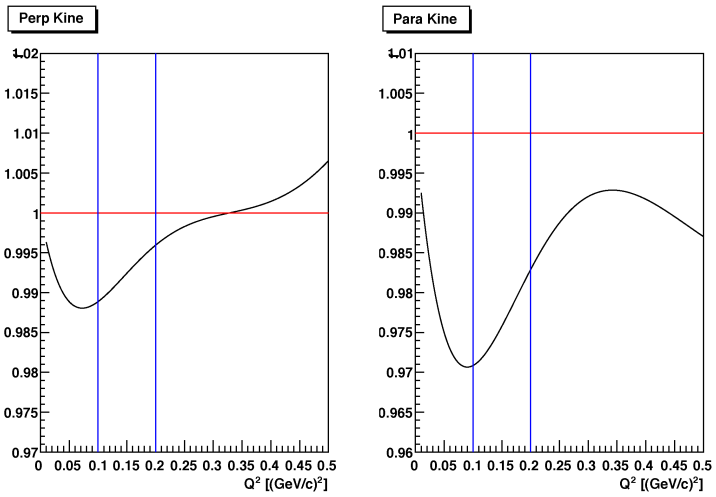

Figure 4-30: Ratio of electric and proton form factor from the fit of Friedrich and Walcher. Deviations from unity show effects of recent polarizations measurements since unity corresponds to the dipole fit.

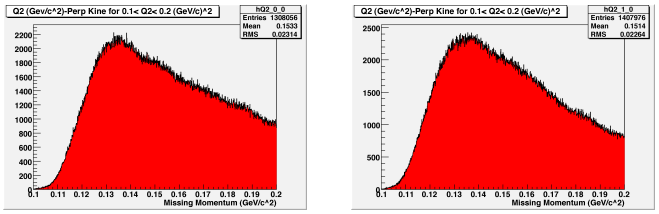

(a) Perpendicular Kinematics

(b) Parallel Kinematics

Figure 4-31: Q^2 distribution used to event weight the factor to the correction of the dipole form factor in h_{Pz} for 32 degree target angle data

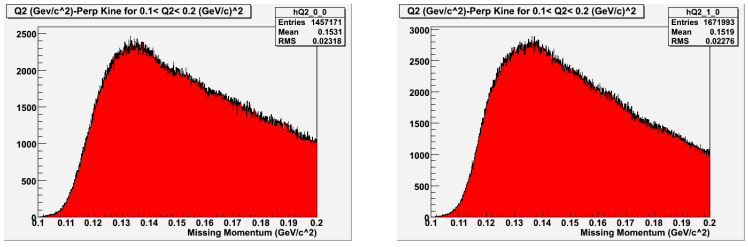

(a) Perpendicular Kinematics-2005

(b) Parallel Kinematics-2005

Figure 4-32: Q^2 distribution used to event weight the factor to the correction of the dipole form factor in h_{Pz} for 47 degree target angle data

roughly 15° in and watching how the correction changed. It was found that this value changed at most by 10 % of the size of the correction; therefore this statistical error is on the order of 0.1 and, therefore, negligible.

4.12.2 Systematic Error of hP_z due to model dependence

It was found that in the quasielastic regime of low p_m, the regime where hP_z was extracted there was little dependence in A_{ed}^V on the model used. The difference between the Bonn, ArgonneV18, ArgonneV14 and Paris potentialor missing momentum values less than $0.1(GeV/c)$ is seen to be vary small. A value of hPz was calculated for each of these potentials. As stated previously, the final value quoted was chosen to be the Bonn potential due to its strong hadronic nature. The systematic error due to model dependence was then estimated as the largest difference between the Bonn potential and the others.

4.13 Radiative Corrections

Radiative corrections were not explicitly included in the formalism given by Arenhoevel and thus were added as a systematic uncertainty to the asymmetries. Radiative corrections occur when the incident or scattered electron loses energy by radiating a real or virtual photon. Following the procedure put forth by Afansevos *et al.* [73], the radiated cross section, σ_R, can be written to explicitly in terms of the unradiated cross section, σ_0, as,

$$\sigma_R = (1-\delta)\sigma_0 + \sigma_1, \tag{4.52}$$

where δ is the factorized correction and σ_1 is the unfactorized contribution from bremsstrahlung radiation.

The relative difference between the asymmetry including radiation and the one without is characterized by $\Delta_R \equiv \frac{A_R - A_0}{A_0}$ is relatively independent of the factorization quantity, δ, and can be shown to be equal to the following,

$$\Delta_R \equiv \frac{\Delta A_R}{A_0} = \frac{A_R - A_0}{A_0} = \frac{r^p - r^u}{1 + \delta^p + r^u}. \tag{4.53}$$

Here the superscripts"u" and "p" stand for unpolarized and polarized respectively,

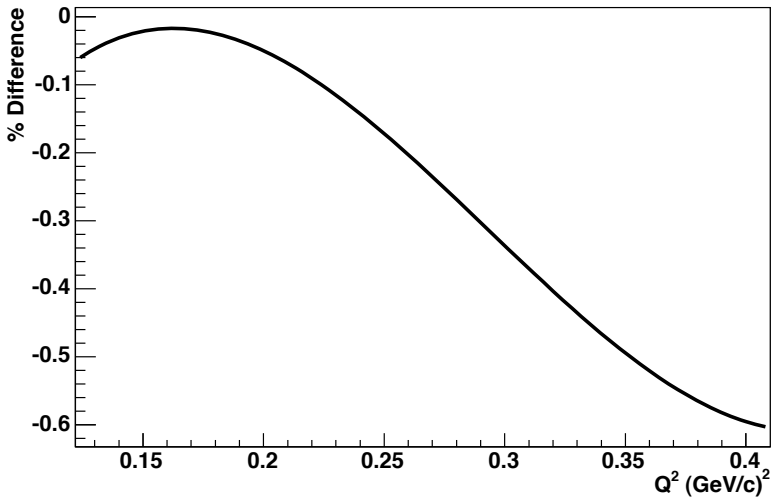

Figure 4-33: Plot of relative difference between the radiated corrected asymmetry and the unradiated asymmetry vs Q^2. Taken from [14].

and the rs are the ratio cross sections so that, for example, $r^u \equiv \sigma_1^u/_0^u$. Figure 4-33 shows the size of Δ_R vs. Q^2 generated for elastic electron proton scattering using MASCARAD code developed by [73]. To the extent quasielastic scattering approximates ep scattering, the results shown that the % difference is $< 1\%$. However since the data sample includes non-quasielastic reactions the conservative value of 1% was used.

Chapter 5

Results

5.1 Introduction

The results of the beam-vector and tensor asymmetries for the electrodisintegration of the deuteron with the proton detected in the final state are presented. The results were plotted for BLAST's Q^2 range of 0.1 (GeV/c)^2 to 0.5 (GeV/c)^2 in bins of 0.1 (GeV/c)^2. A_{ed}^V and A_d^T are expected to be non-zero in the Born approximation and are plotted vs missing momentum (for A_{ed}^V and A_d^T) for values of P_m=0.0 GeV/c^2 to 0.5 GeV/c^2 in divisions of 10 for the entire range. The results are compared to theory curves where different nucleon-nucleon potentials are used in the formalism and separately to curves where the Bonn potential is used and various subnuclear effects are included. The appendix contain the values for the theory values along with measurement data and their total errors; the errors in the Monte Carlo are negligible and not included in the tables.

5.2 The Beam-Vector Asymmetry vs. Missing Momentum for 2005 and 2004 Data Including Contributions From Subnuclear Effects

In the PWIA, the beam-vector asymmetry is highly sensitive to the polarization of the proton in the deuteron, as well as dependent on the proton form factors and the kinematics of the reaction $^2\vec{H}(e,e\vec{p})n$. Since the form factors are well known, in regions where subnuclear effects are small, the beam-vector asymmetry is well determined. However, these results must be modified to include the Plane Wave Born Approximation and subnuclear effects for regions of high Q^2 and high P_m.

The bottom graphs in Figures show the beam-vector asymmetry results for the BLAST data plotted versus p_m for the Q^2 range of $0.1(GeV/c)^2 < Q^2 < (0.5GeV/c)^2$ for perpendicular and parallel kinematics. Measurements of the reaction $^2\vec{H}(\vec{e},e\vec{p})n$ and are compared to results derived from the Bonn potential where the formalism of Arenhoevel *et. al.* was used as input for Monte Carlo simulations. Curves generated to include various subnuclear effects were also plotted on graphs to show the relative size of each contribution and to test how well these effects agree with data.

Calculations start with the plane wave born approximation and have as contributions included in the formalism whose source is the following subnuclear effects:

FSI = Final State Interactions

MEC = Meson Exchange Currents

IC = Isobar Currents

RC = Relativistic Corrections

Therefore, for example, a plot labeled "BONN PWBA + FSI + MEC" would be a calculation where the Bonn potential was used in the Plane Wave Born Approximation along with corrections due to Final State Interactions and Meson Exchange Currents. In addition, the plot labeled Bonn "PWBA + Total" would have all the above contributions.

5.3 The Beam-Vector Asymmetry vs. Missing Momentum for 2005 and 2004 Data for Different Potentials

Figures were made with the BLAST data and included curves from Monte Carlo calculations where different potentials were used as input. In each case the contributions from all the subnuclear effects were included. The following potentials used were: Bonn, Argonne V18 (labeled 'v18'), Argonne V14 (labeled 'v14') and the Paris potential. The label "T" Means that the full effects were included in the Monte Carlo calculation

Again results from these simulations along with comparison to data are tabulated in the appendix.

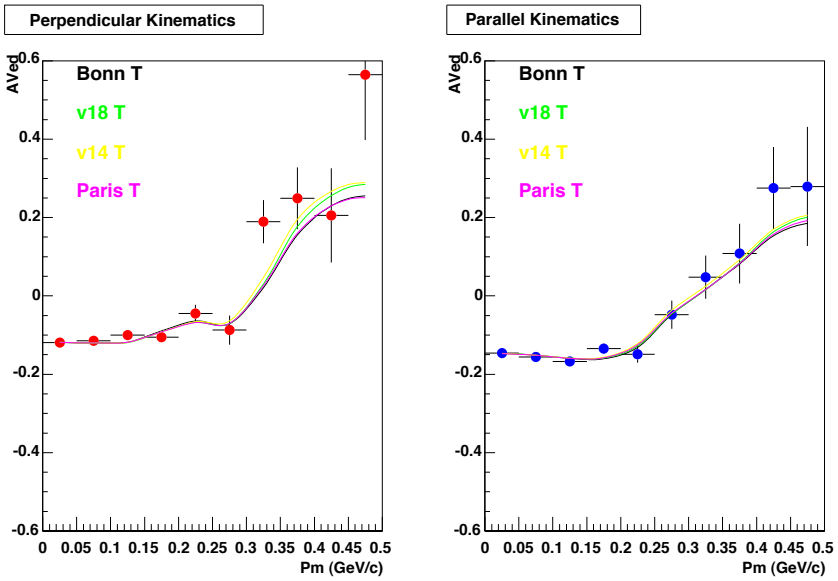

(a) Plots of reconstructed beam-vector asymmetries versus P_m with theoretical curves obtained using various potentials.

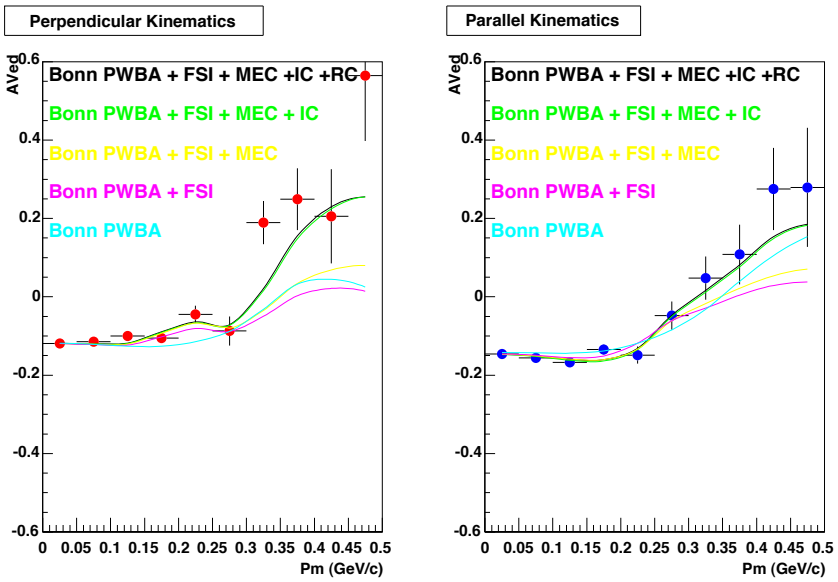

(b) Plots of reconstructed beam-vector asymmetries versus P_m with theoretical curves obtained including subnuclear effects.

Figure 5-1: Plots of reconstructed beam-vector asymmetries for $0.1(GeV/c)^2 < Q^2 < 0.2(GeV/c)^2$ versus missing momentum for the 2005 data run.

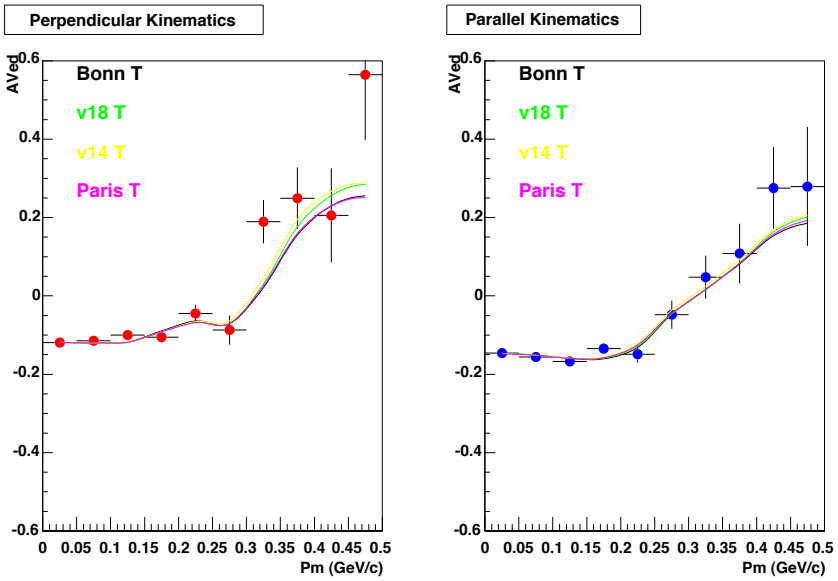

(a) Plots of reconstructed beam-vector asymmetries versus P_m with theoretical curves obtained using various potentials.

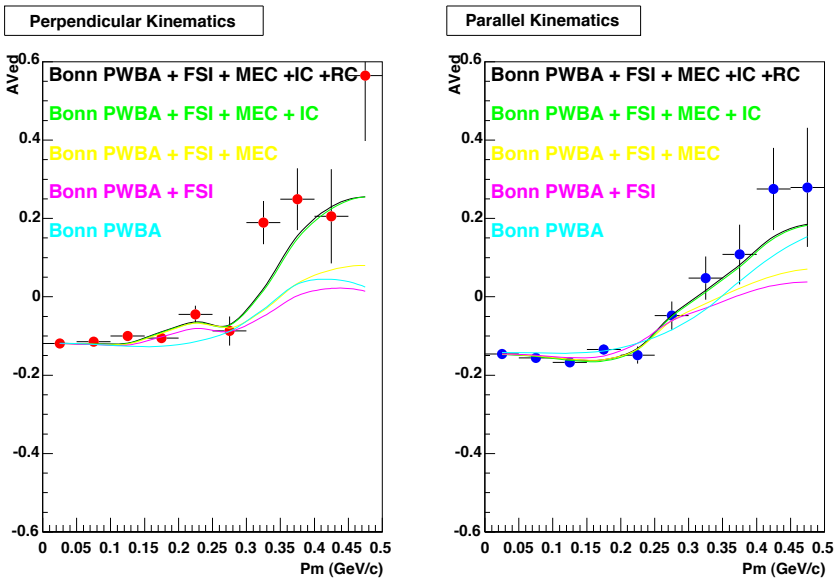

(b) Plots of reconstructed beam-vector asymmetries versus P_m with theoretical curves obtained including subnuclear effects.

Figure 5-2: Plots of reconstructed beam-vector asymmetries for $0.2(GeV/c)^2 < Q^2 < 0.3(GeV/c)^2$ versus missing momentum for the 2005 data run.

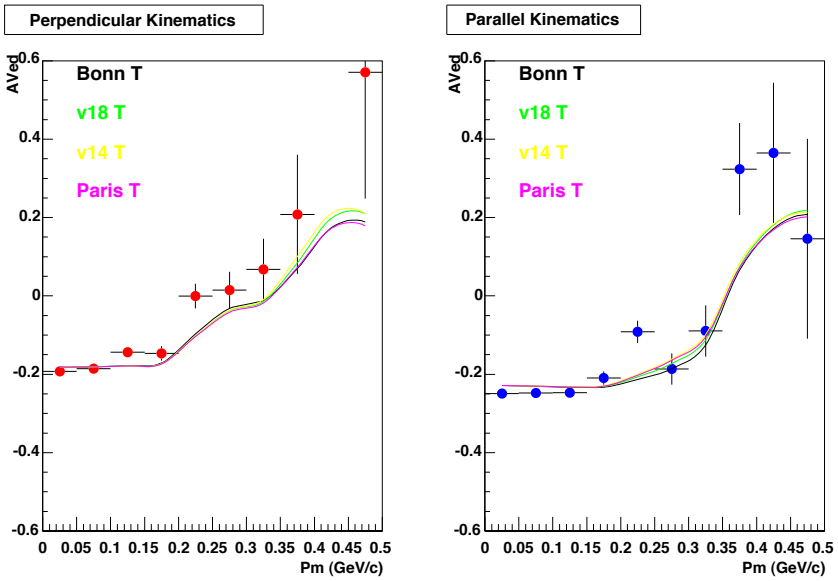

(a) Plots of reconstructed beam-vector asymmetries versus P_m with theoretical curves obtained using various potentials.

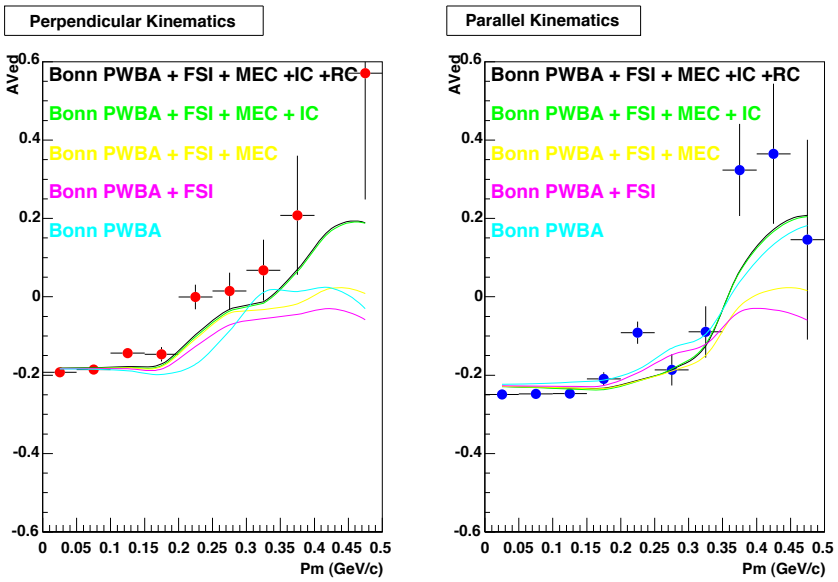

(b) Plots of reconstructed beam-vector asymmetries versus P_m with theoretical curves obtained including subnuclear effects.

Figure 5-3: Plots of reconstructed beam-vector asymmetries for $0.3(GeV/c)^2 < Q^2 < 0.4(GeV/c)^2$ versus missing momentum for the 2005 data run.

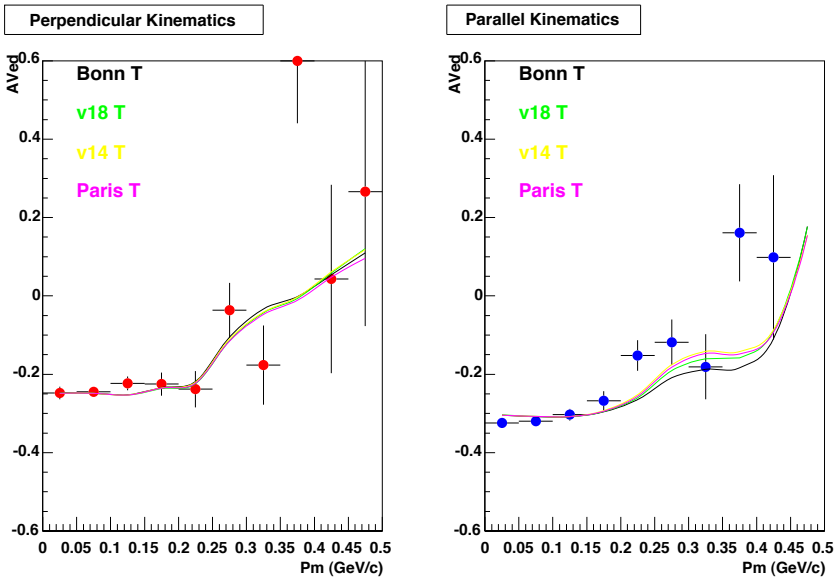

(a) Plots of reconstructed beam-vector asymmetries versus P_m with theoretical curves obtained using various potentials.

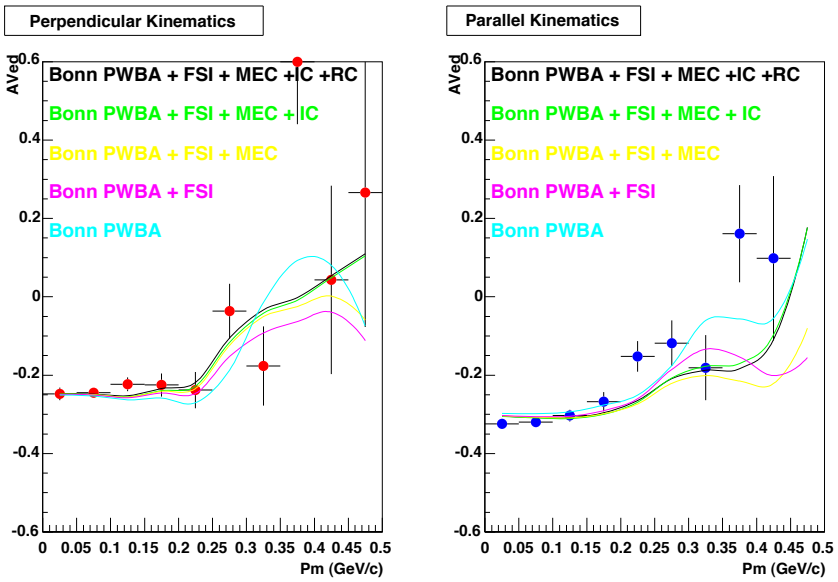

(b) Plots of reconstructed beam-vector asymmetries versus P_m with theoretical curves obtained including subnuclear effects.

Figure 5-4: Plots of reconstructed beam-vector asymmetries for $0.4(GeV/c)^2 < Q^2 < 0.5(GeV/c)^2$ versus missing momentum for the 2005 data run.

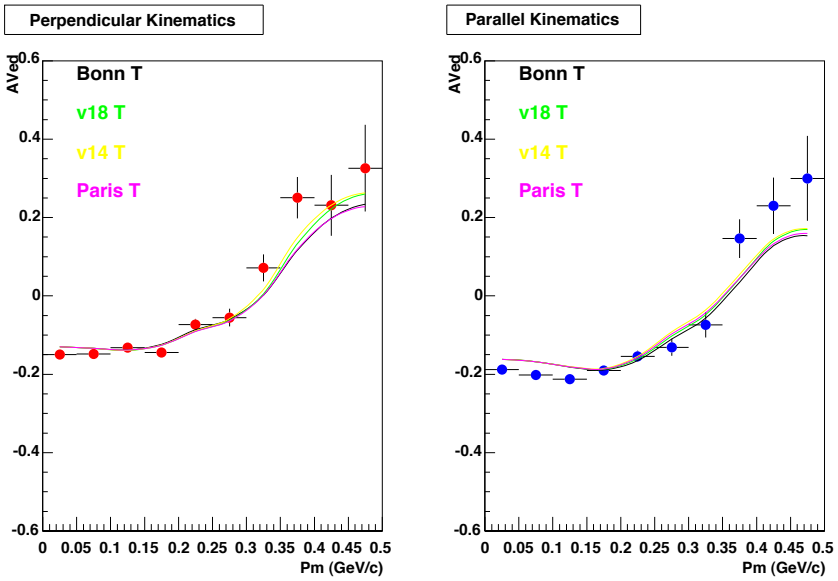

(a) Plots of reconstructed beam-vector asymmetries versus P_m with theoretical curves obtained using various potentials.

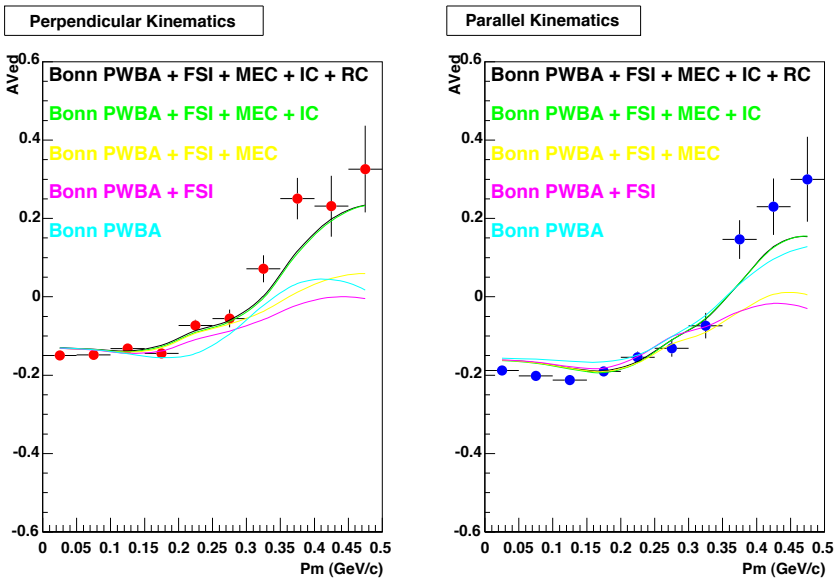

(b) Plots of reconstructed beam-vector asymmetries versus P_m with theoretical curves obtained including subnuclear effects.

Figure 5-5: Plots of reconstructed beam-vector asymmetries for $0.1(GeV/c)^2 < Q^2 < 0.5(GeV/c)^2$ versus missing momentum for the 2005 data run.

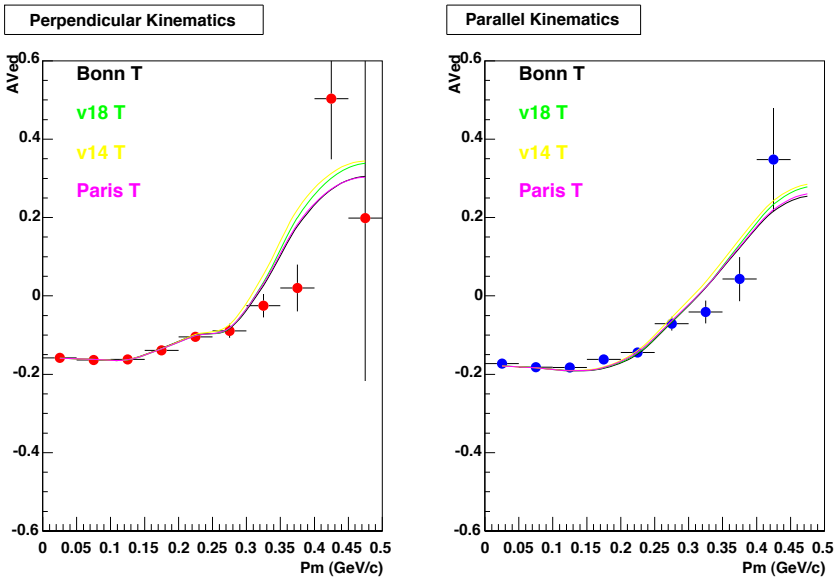

(a) Plots of reconstructed beam-vector asymmetries versus P_m with theoretical curves obtained using various potentials.

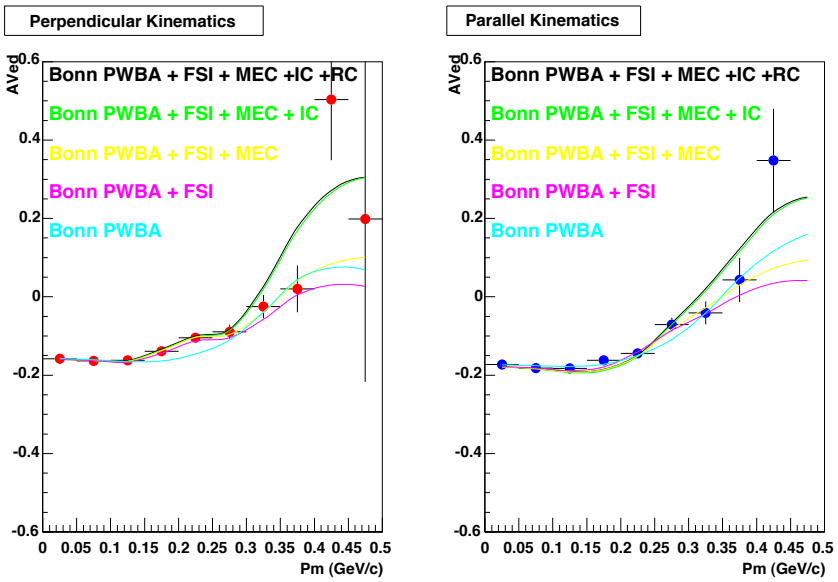

(b) Plots of reconstructed beam-vector asymmetries versus P_m with theoretical curves obtained including subnuclear effects.

Figure 5-6: Plots of reconstructed beam-vector asymmetries for $0.1(GeV/c)^2 < Q^2 < 0.2(GeV/c)^2$ versus missing momentum for the 2004 data run.

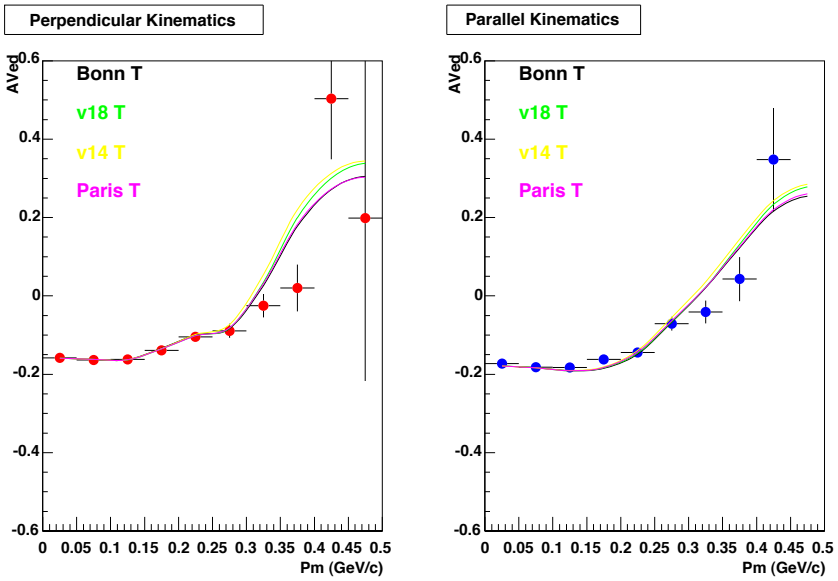

(a) Plots of reconstructed beam-vector asymmetries versus P_m with theoretical curves obtained using various potentials.

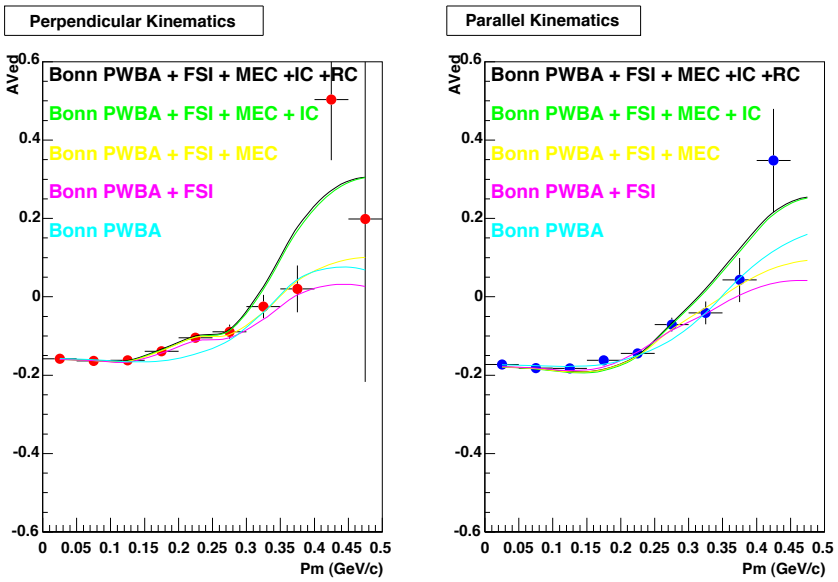

(b) Plots of reconstructed beam-vector asymmetries versus P_m with theoretical curves obtained including subnuclear effects.

Figure 5-7: Plots of reconstructed beam-vector asymmetries for $0.2(GeV/c)^2 < Q^2 < 0.3(GeV/c)^2$ versus missing momentum for the 2004 data run.

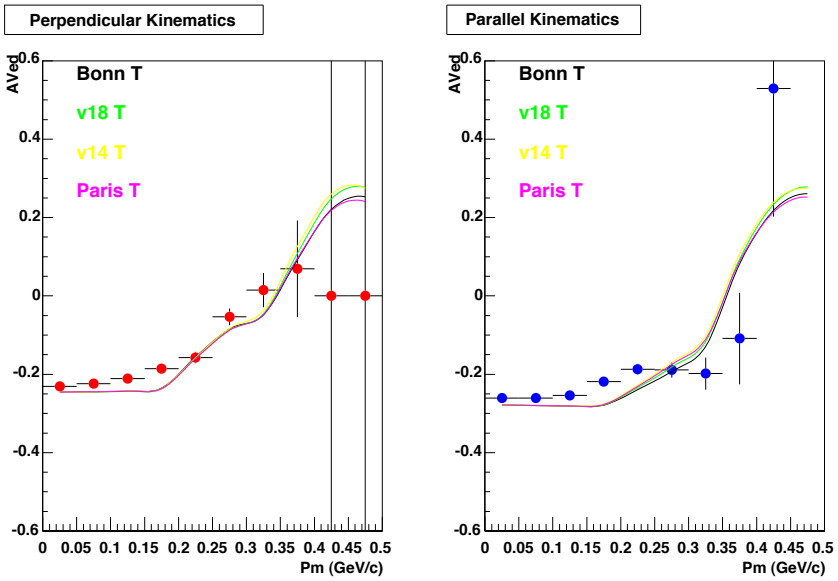

(a) Plots of reconstructed beam-vector asymmetries versus P_m with theoretical curves obtained using various potentials.

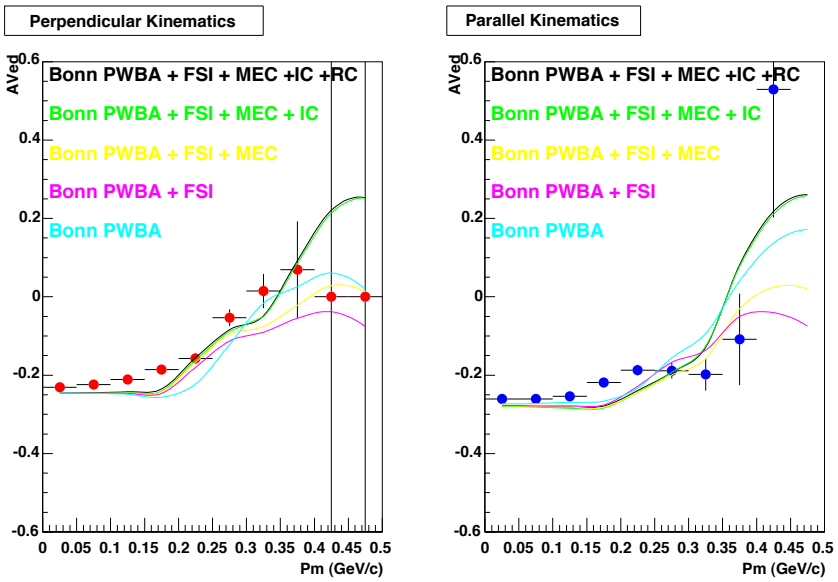

(b) Plots of reconstructed beam-vector asymmetries versus P_m with theoretical curves obtained including subnuclear effects.

Figure 5-8: Plots of reconstructed beam-vector asymmetries for $0.3(GeV/c)^2 < Q^2 < 0.4(GeV/c)^2$ versus missing momentum for the 2004 data run.

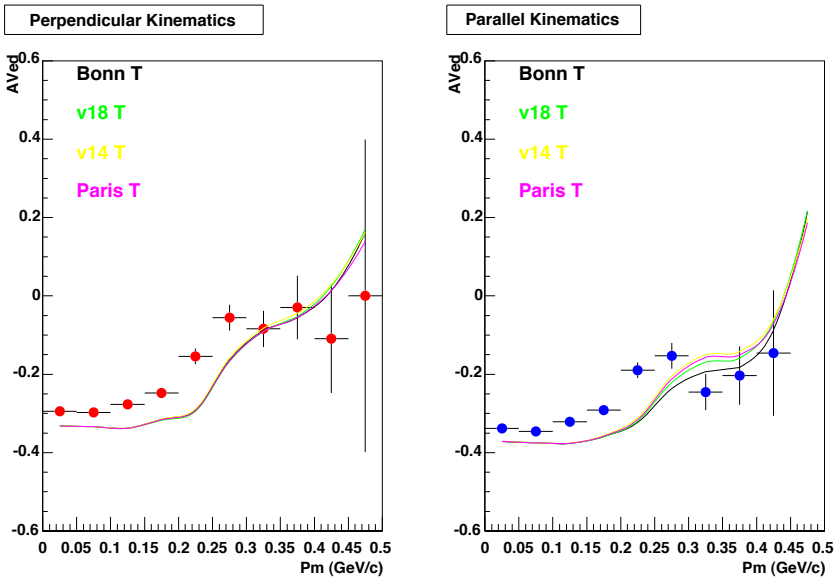

(a) Plots of reconstructed beam-vector asymmetries versus P_m with theoretical curves obtained using various potentials.

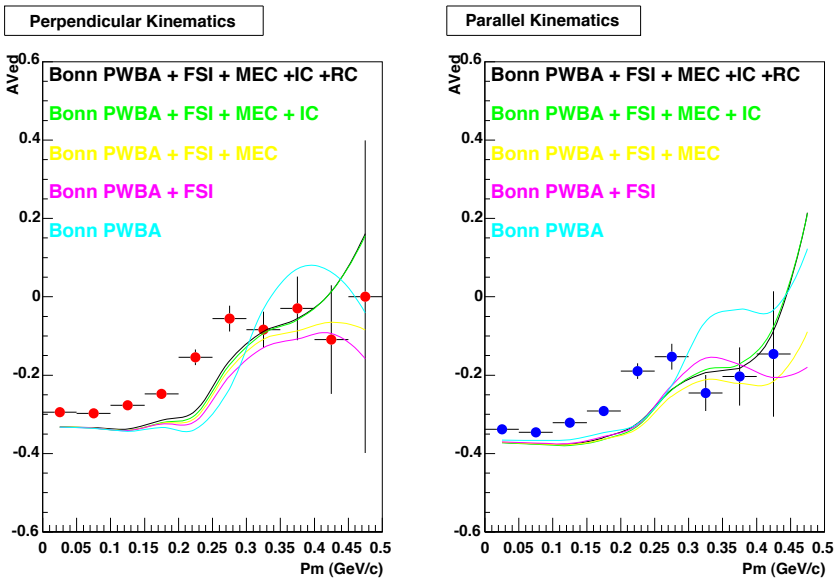

(b) Plots of reconstructed beam-vector asymmetries versus P_m with theoretical curves obtained including subnuclear effects.

Figure 5-9: Plots of reconstructed beam-vector asymmetries for $0.4(GeV/c)^2 < Q^2 < 0.5(GeV/c)^2$ versus missing momentum for the 2004 data run.

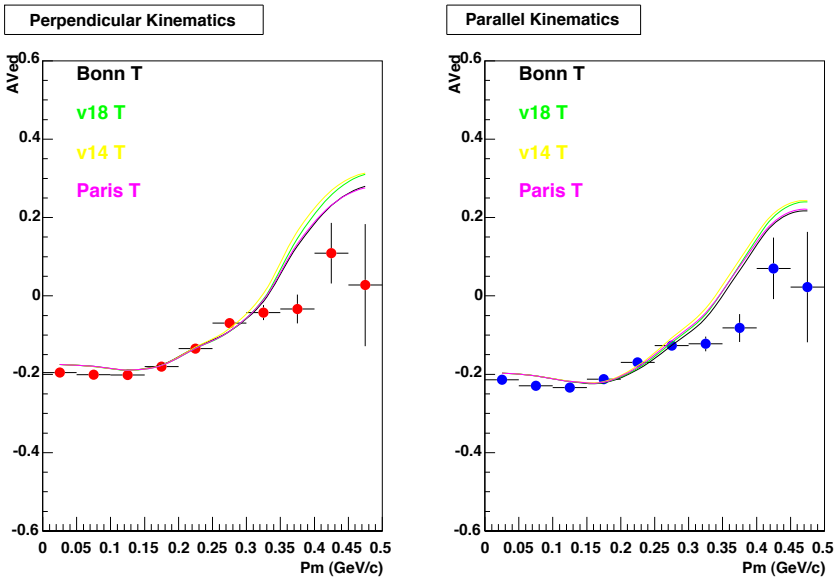

(a) Plots of reconstructed beam-vector asymmetries versus P_m with theoretical curves obtained using various potentials.

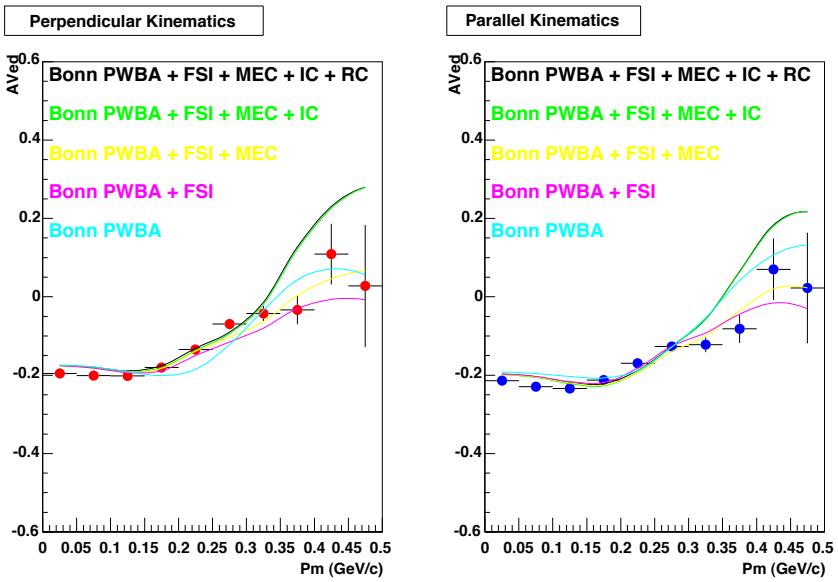

(b) Plots of reconstructed beam-vector asymmetries versus P_m with theoretical curves obtained including subnuclear effects.

Figure 5-10: Plots of reconstructed beam-vector asymmetries for $0.1(GeV/c)^2 < Q^2 < 0.5(GeV/c)^2$ versus missing momentum for the 2004 data run.

5.4 The Tensor Asymmetry vs. Missing Momentum Including Contributions from Subnuclear Effects

Results are plotted with the same kinematic parameters and subnuclear effects as those for the beam-vector asymmetry. As discussed in the analysis section, the tensor polarization was taken from the analysis of e-d elastic scattering and used to dilute the asymmetries by the same amount throughout the data. The figures show the results of the tensor asymmetry vs P_m for the BLAST's Q^2 range. The labeling is done exactly as described in section 5.2 with subnuclear effects added onto the PWBA in succession.

5.5 The Tensor Asymmetry vs. Missing Momentum Including Contributions from Various Potential Contributions

The bottom figures (Figures (b) of Figures show the beam-tensor asymmetries vs. P_m for the same nucleon-nucleon potentials as in **??**; the labeling of the curves is also the same.

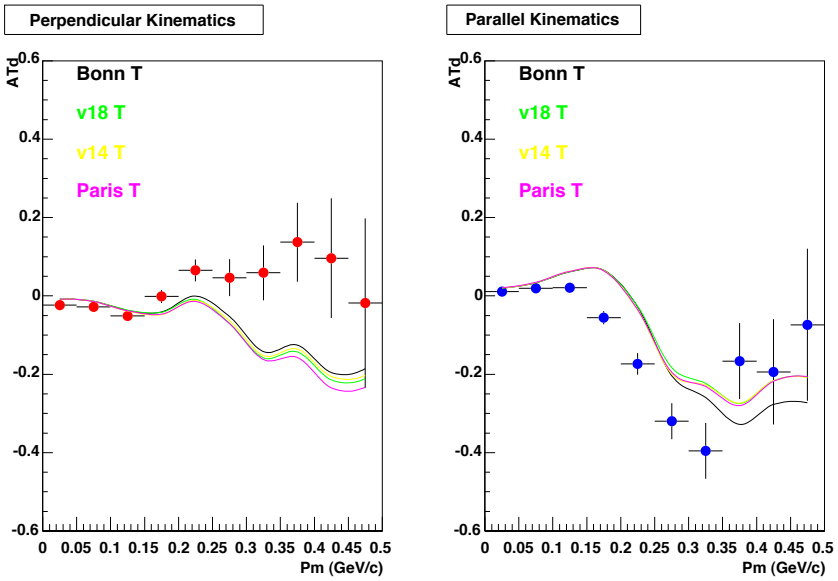

(a) Plots of reconstructed tensor asymmetries versus P_m with theoretical curves obtained using various potentials.

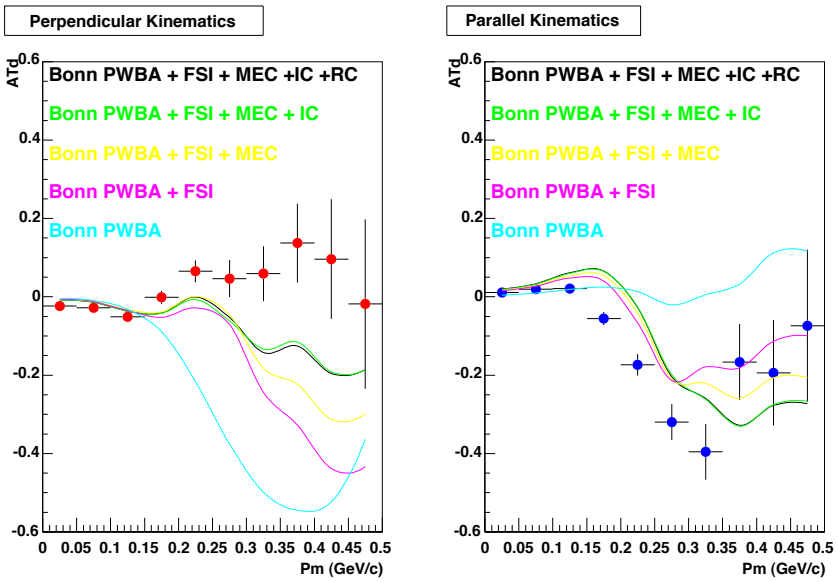

(b) Plots of reconstructed tensor asymmetries versus P_m with theoretical curves obtained including subnuclear effects.

Figure 5-11: Plots of reconstructed tensor asymmetries for $0.1(GeV/c)^2 < Q^2 < 0.2(GeV/c)^2$ versus missing momentum for the 2005 data run.

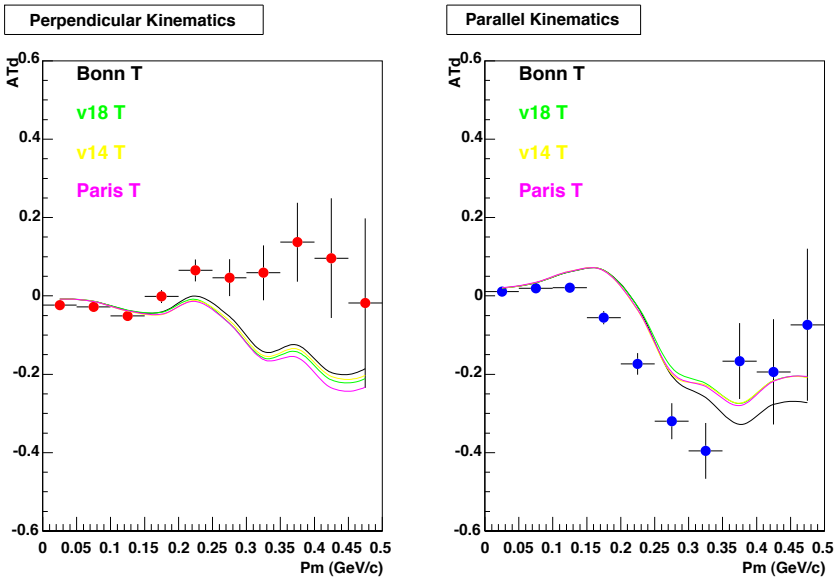

(a) Plots of reconstructed tensor asymmetries versus P_m with theoretical curves obtained using various potentials.

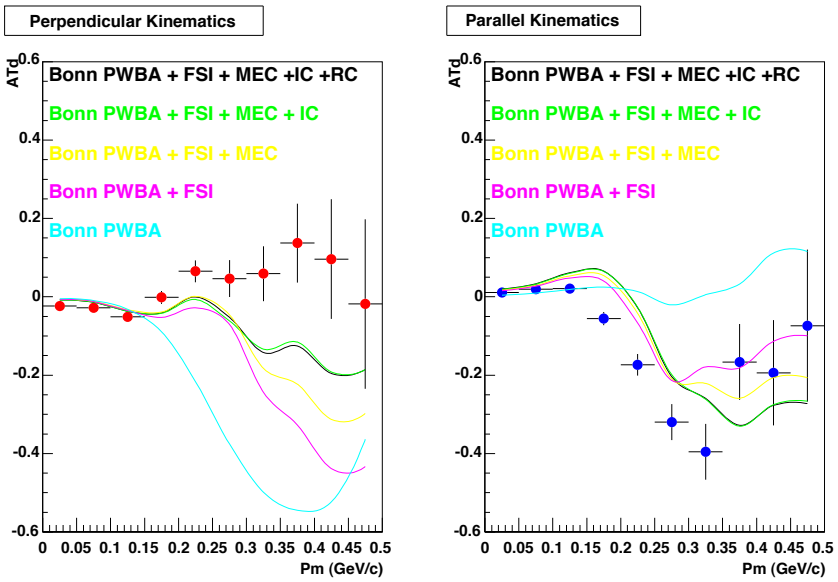

(b) Plots of reconstructed tensor asymmetries versus P_m with theoretical curves obtained including subnuclear effects.

Figure 5-12: Plots of reconstructed beam-vector asymmetries for $0.2(GeV/c)^2 < Q^2 < 0.3(GeV/c)^2$ versus missing momentum for the 2005 data run.

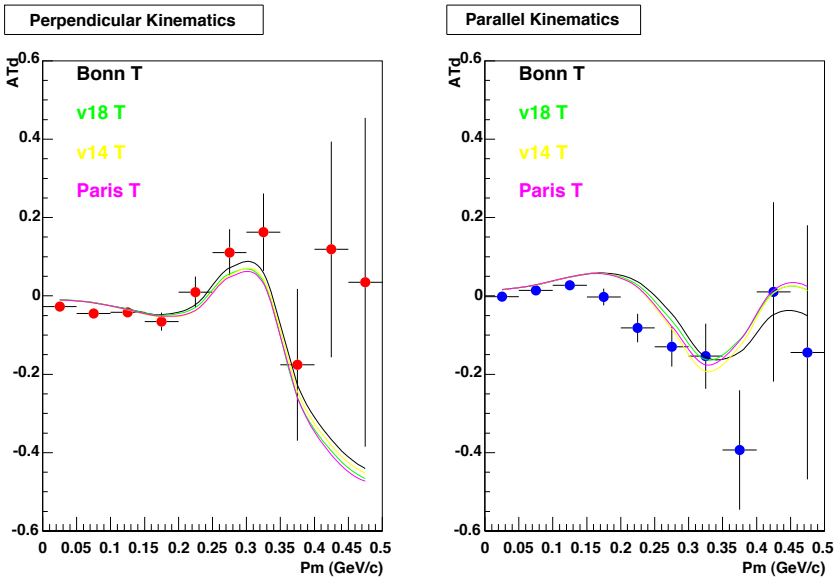

(a) Plots of reconstructed tensor asymmetries versus P_m with theoretical curves obtained using various potentials.

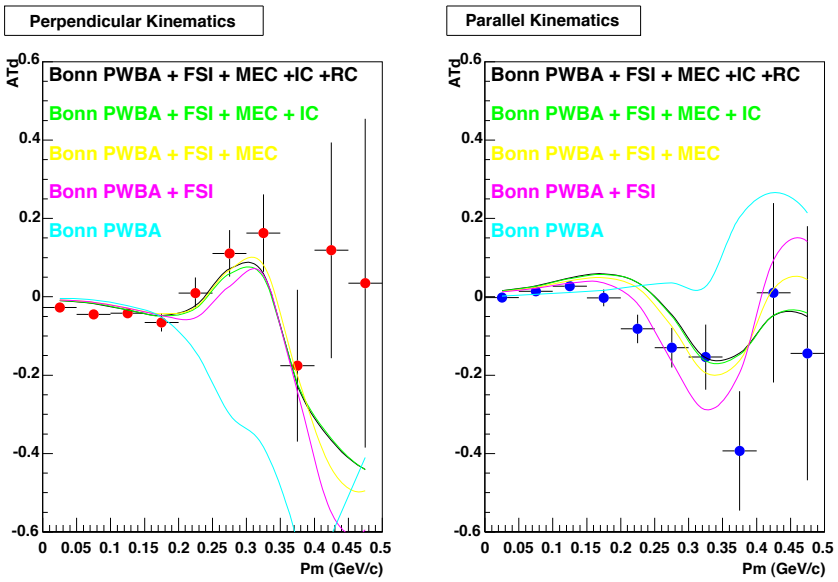

(b) Plots of reconstructed tensor asymmetries versus P_m with theoretical curves obtained including subnuclear effects.

Figure 5-13: Plots of reconstructed tensor asymmetries for $0.3(GeV/c)^2 < Q^2 < 0.4(GeV/c)^2$ versus missing momentum for the 2005 data run.

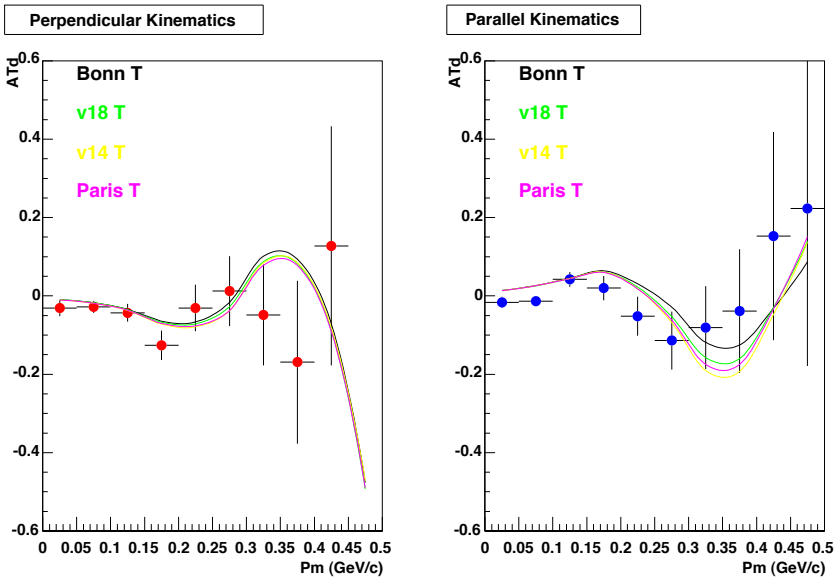

(a) Plots of reconstructed tensor asymmetries versus P_m with theoretical curves obtained using various potentials.

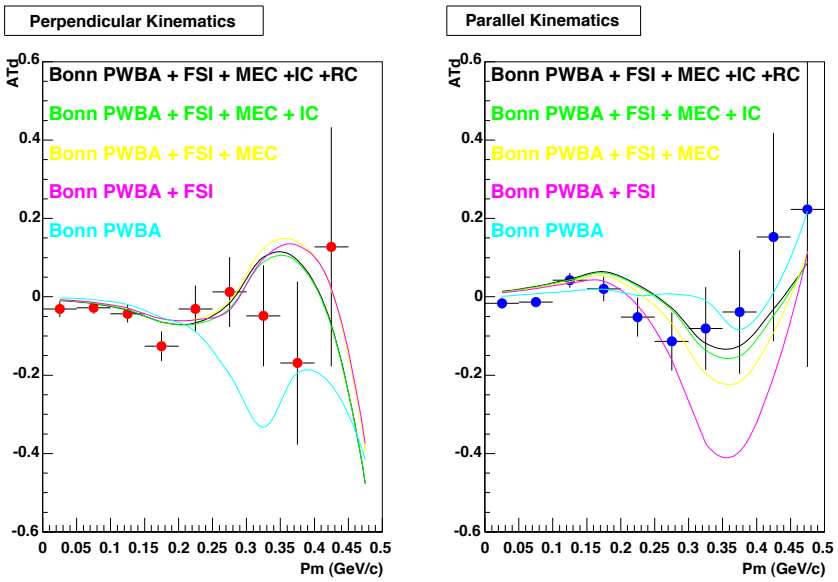

(b) Plots of reconstructed tensor asymmetries versus P_m with theoretical curves obtained including subnuclear effects.

Figure 5-14: Plots of reconstructed tensor asymmetries for $0.4(GeV/c)^2 < Q^2 < 0.5(GeV/c)^2$ versus missing momentum for the 2005 data run.

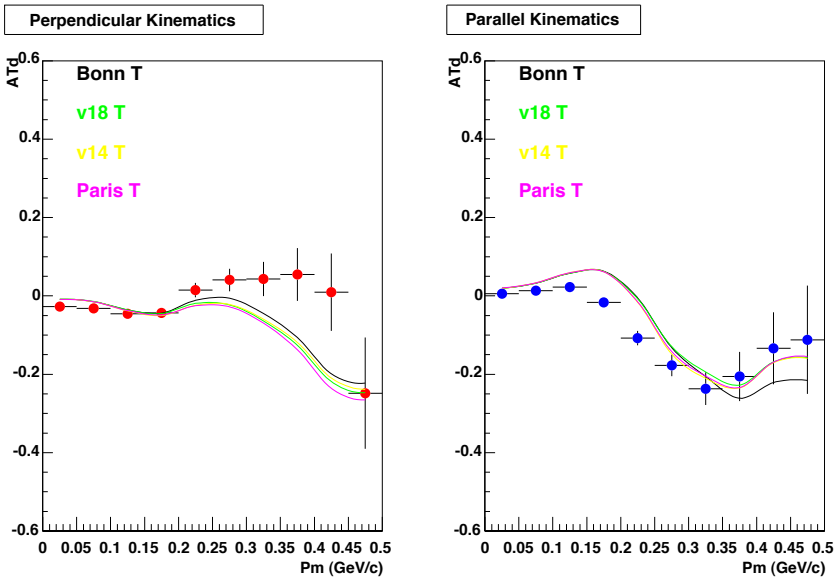

(a) Plots of reconstructed tensor asymmetries versus P_m with theoretical curves obtained using various potentials.

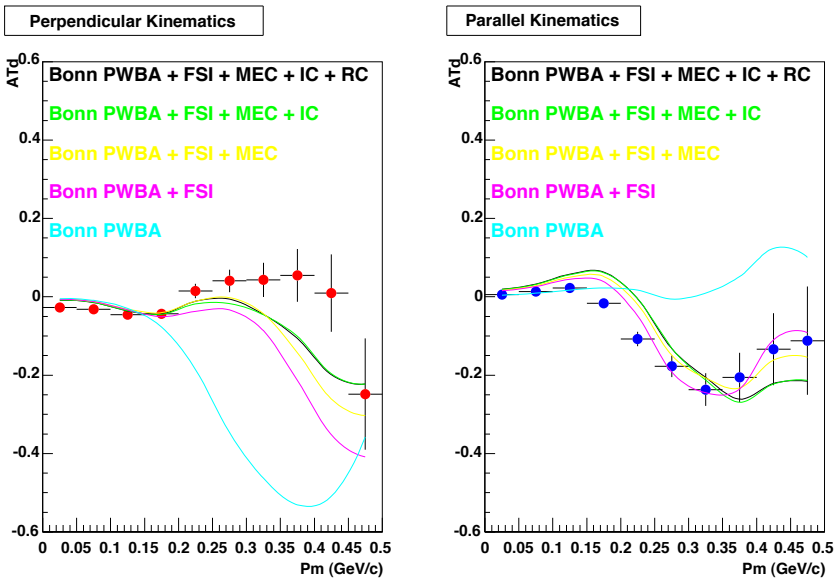

(b) Plots of reconstructed tensor asymmetries versus P_m with theoretical curves obtained including subnuclear effects.

Figure 5-15: Plots of reconstructed tensor asymmetries for $0.1(GeV/c)^2 < Q^2 < 0.5(GeV/c)^2$ versus missing momentum for the 2005 data run.

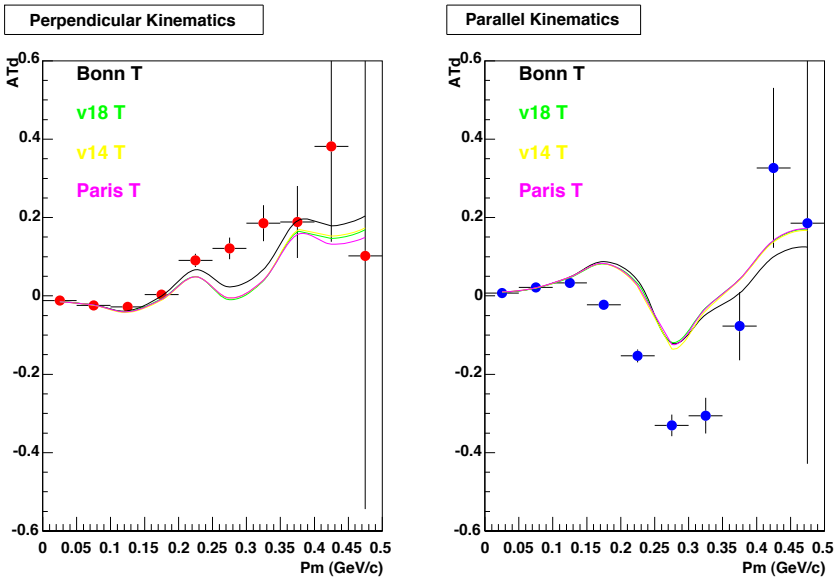

(a) Plots of reconstructed tensor asymmetries versus P_m with theoretical curves obtained using various potentials.

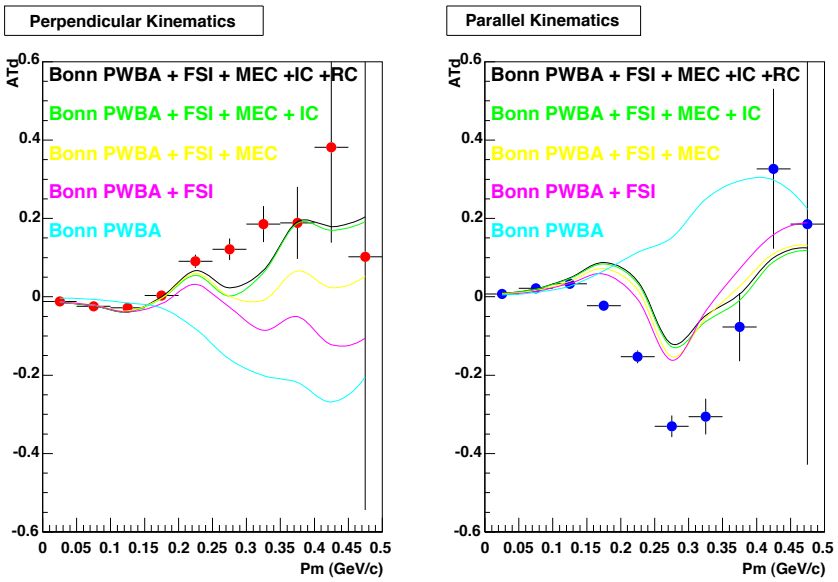

(b) Plots of reconstructed tensor asymmetries versus P_m with theoretical curves obtained including subnuclear effects.

Figure 5-16: Plots of reconstructed tensor asymmetries for $0.1(GeV/c)^2 < Q^2 < 0.2(GeV/c)^2$ versus missing momentum for the 2004 data run.

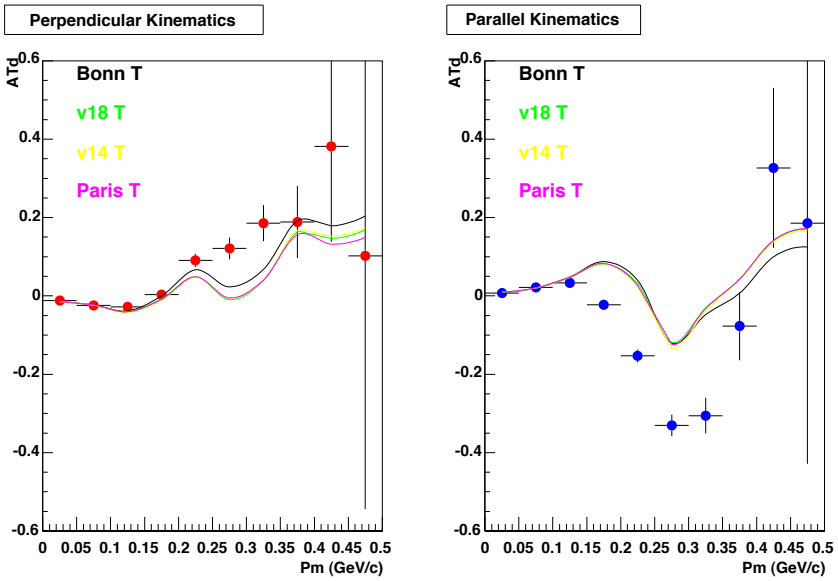

(a) Plots of reconstructed tensor asymmetries versus P_m with theoretical curves obtained using various potentials.

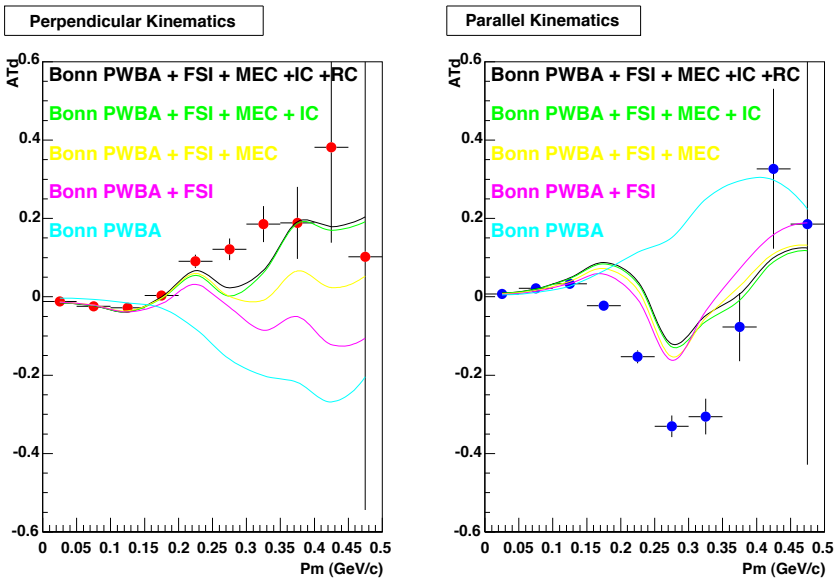

(b) Plots of reconstructed tensor asymmetries versus P_m with theoretical curves obtained including subnuclear effects.

Figure 5-17: Plots of reconstructed tensor asymmetries for $0.2(GeV/c)^2 < Q^2 < 0.3(GeV/c)^2$ versus missing momentum for the 2004 data run.

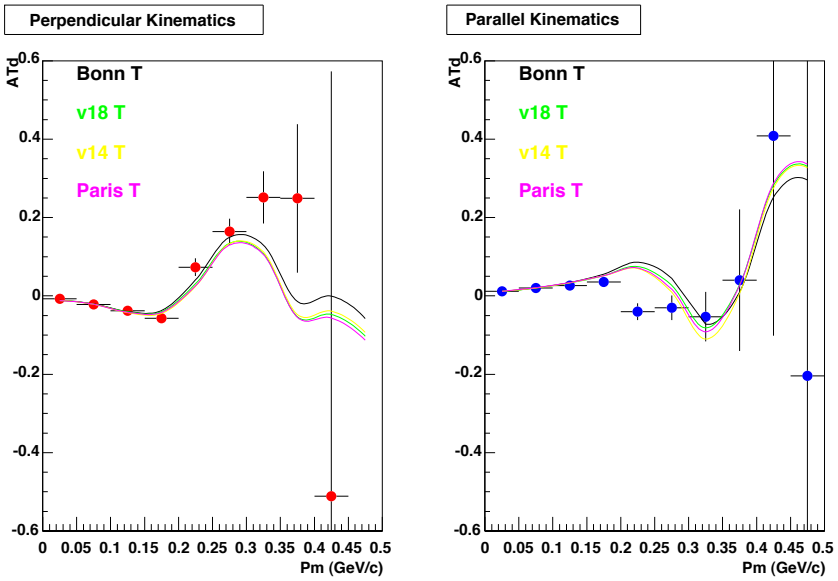

(a) Plots of reconstructed tensor asymmetries versus P_m with theoretical curves obtained using various potentials.

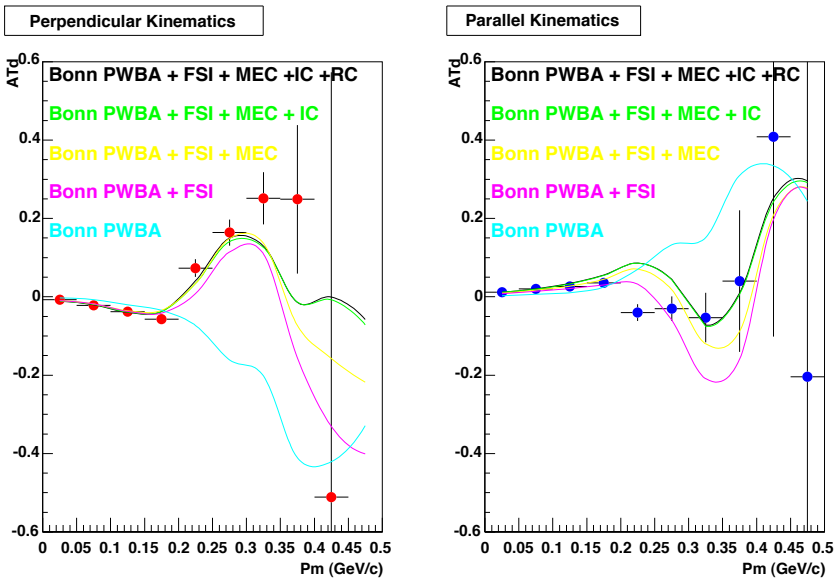

(b) Plots of reconstructed tensor asymmetries versus P_m with theoretical curves obtained including subnuclear effects.

Figure 5-18: Plots of reconstructed tensor asymmetries for $0.3(GeV/c)^2 < Q^2 < 0.4(GeV/c)^2$ versus missing momentum for the 2004 data run.

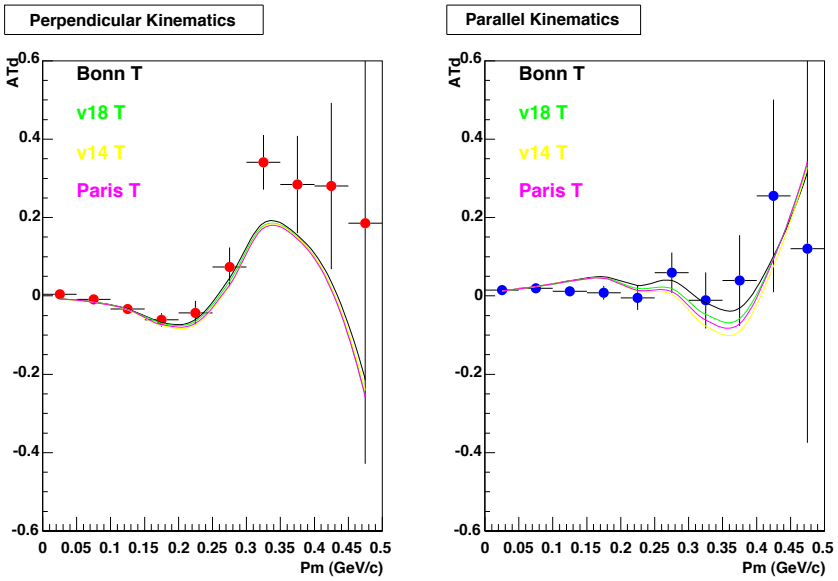

(a) Plots of reconstructed tensor asymmetries versus P_m with theoretical curves obtained using various potentials.

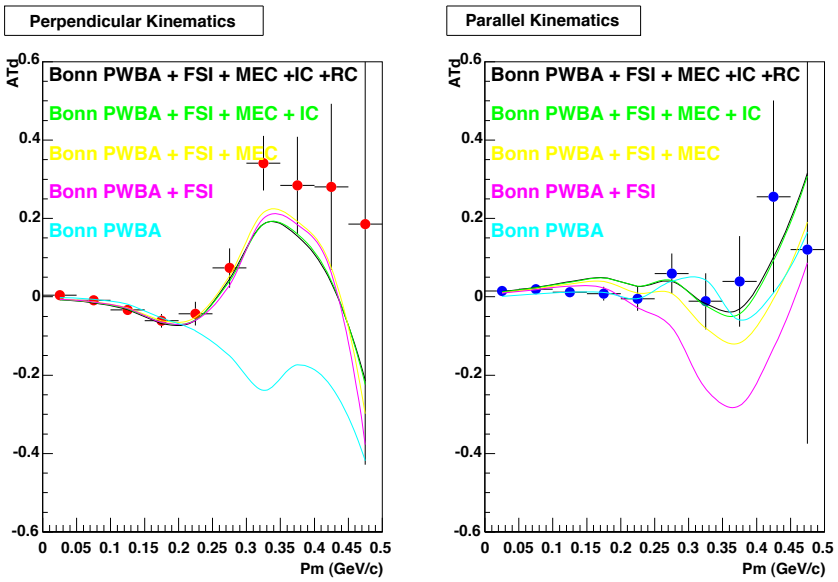

(b) Plots of reconstructed tensor asymmetries versus P_m with theoretical curves obtained including subnuclear effects.

Figure 5-19: Plots of reconstructed tensor asymmetries for $0.4(GeV/c)^2 < Q^2 < 0.5(GeV/c)^2$ versus missing momentum for the 2004 data run.

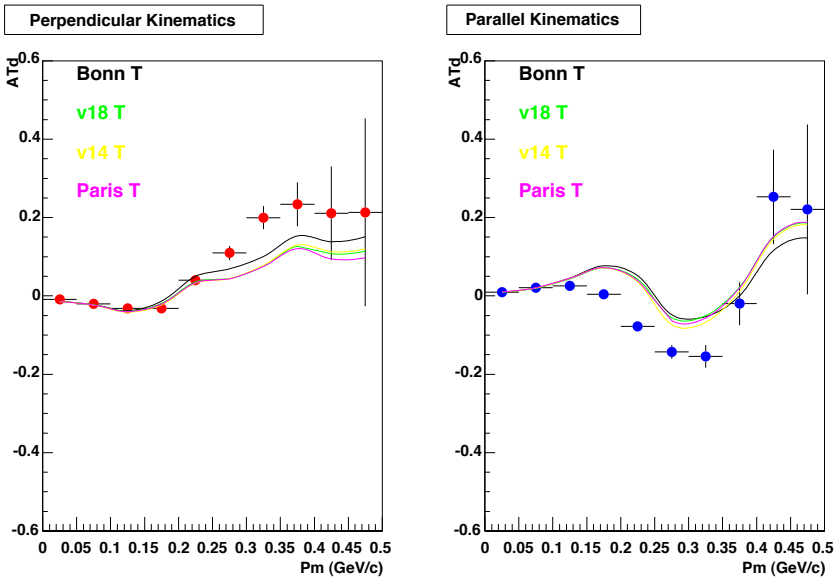

(a) Plots of reconstructed tensor asymmetries versus P_m with theoretical curves obtained using various potentials.

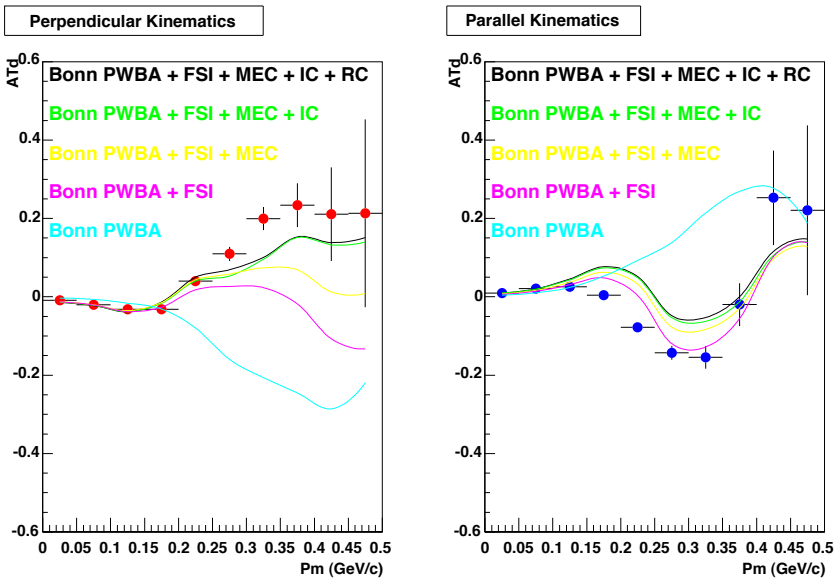

(b) Plots of reconstructed tensor asymmetries versus P_m with theoretical curves obtained including subnuclear effects.

Figure 5-20: Plots of reconstructed tensor asymmetries for $0.1(GeV/c)^2 < Q^2 < 0.5(GeV/c)^2$ versus missing momentum for the 2004 data run.

Chapter 6

Conclusions and Outlook

6.1 Results of Beam-Vector Asymmetries vs. Missing Momentum

In general the data was in overall good agreement to the theory although some important points need to be made. There was negligible difference for the Monte Carlo results using different potentials for values of Q^2 below (0.25 GeV/c)^2. For values greater than this there was a slight variation; however this was the regime of high P_m and hence lower statistics which therefore had large statistical errors. For these cases it was not possible to state preferences of one nucleon-nucleon potential over another in terms of agreement to data.

An important statement can be made that in general the full effects were needed to obtain good agreement with the data especially at higher P_m values of greater than (0.25 GeV/c)^2. Here Isobar Currents have a significant contribution to the beam-vector asymmetry and are an important contribution to the spin dependent cross section.

The existence of a notable dependence of hP_z on Q^2 as seen in the data especially for the 2004 data set. This appears as an increasing mismatch between the data and the first P_m bin as one increases in Q^2 bin. This mismatch peaks at the highest Q^2 bin and is roughly a 15% effect for Q^2 = [0.4,0.5] (GeV/c)^2. This Q^2 dependence

is believed to be due pion contaminations that in uncorrected in the data set. This mismatch also has the appearance of causing a greater disagreement between data and theory for these high Q^2 points; however, if one notices this shift as solely a product of hP_z Q2 dependence one can bring the data sample back into agreement with the curves especially seen in the intermediary range of $Q^2 = [0.1, 0.3]$ $(GeV/c)^2$.

6.2 Discussion of Tensor Asymmetries vs. Missing Momentum Results

The reconstructed beam-vector results follow a similar shape when compared to the theory curves, a value of ~ 0 for values of $Q^2 < 0.15$ $(GeV/c)^2$, generally followed by a dip in values between 0.2 $(GeV/c)^2 < Q^2 < 0.3$ $(GeV/c)^2$, then followed by a rise at values above 0.35 $(GeV/c)^2$. Similar to the beam-vector results, there the difference in theory curves is not distinguishable by reconstructed values, with any deviations occurring at high values of P_m. This allowed one to choose confidently a single potential when examining the results of various subnuclear effects. When examining the effects of subnuclear contributions, it is clear that the full calculation is needed for the best agreement, although some discrepancy still exists. One regime where there is a noticeable difference between data and theory is in the P_m regime of 0.2 to 0.4 GeV/c. In this regime, the reconstructed value in general overshoots the peak (or valley) as seen in the Monte Carlo results. This is most clearly seen in the curves for $Q^2 < 0.3$ $(Gev/c)^2$. A possible explanation would have been unaccounted-for background rates vs. P_m, since this would have diluted the asymmetry further; however, the deviations seen are on the order of 10-15%, as seen in Figure 5-17. At this Q^2 range, background rates were shown to be only of the order of 1-3%. It believed, therefore, that background rates are not the source for this mismatch. Another possible source could be the modification of the individual form factors when bound within the deuteron. As stated in the theoretical calculation, the free dipole form of the form factors are used in the calculation. Since the deuteron is still a

bound system it might be necessary to modify the form factors due to this fact. In addition there may be some effects of using more realistic form factor for the individual nucleons that may modify the results. These effects are difficult to account for in this analysis and hence are not included.

6.3 General Conclusions and Outlook

There are two main points of comparison between data and theory: the agreement between the extracted asymmetries and the theoretical results using different potentials with full subnuclear and isobaric effects included, and the level of agreement between these data and the Bonn potential with different curves corresponding to the increasing number of effects added. From the results section we see an overall qualitative agreement with the data, but there are some key trends where discrepancies are noticeable. In the comparison between data and the curves using the Bonn potential with various subnuclear and isobaric effects, one can confidently state that, for the best agreement, the full effects are needed for all Q^2 and all missing-momentum bins. In comparing data to theory with different potentials, the difference between curves is too small to make any distinction in terms of better agreement with one over another.

If one examines the results on a bin-by-bin basis, some general qualitative statements can be made. Generally, for A_{ed}^V there is better agreement between data and theory at low Q^2 where the statistics are the largest. This is especially true for the first two bins of $0.1(GeV/c)^2 < Q^2 < 0.2(GeV/c)^2$ and $0.2(GeV/c)^2 < Q^2 < 0.3(GeV/c)^2$. As Q^2 increases the statistical uncertainties increase dramatically, as does the apparent agreement. From these results it would be apparent that the best way to improve the results would be to increase statistics by longer data runs. This region of high Q^2 also shows the most differentiation between the inclusion or exclusion of individual subnuclear effects. Therefore by reducing the error bars it may be possible to select out which contributions have greater impact in obtaining agreement with the results.

This leads to an element of the theory that could have improved the discriminating power of the experiment: the ability to turn on or off–or even change the size of–

individual subnuclear or isobaric effects. By having strong control over the individual theoretical curves, one may be able to not only say which ones are necessary to provide the greatest agreement but also indicate the size of the affect needed for this agreement in regions where the affect can be isolated.

For the extractions of A_d^T, similar statements can be made although with some important exceptions. For the best agreement, one must look again at the region of high statistics (low Q^2). However even in this regime, when one speaks of A_d^T as a direct measurement of the contribution of the D-state of the deuteron, one sees that the data deviate from a non-zero value at a lower missing momentum value than is represented by the theory. This may indicate that the crossing-over point from s-wave dominance to d-wave dominance in the p-space wave function of the deuteron occurs previously than is earlier expected. Since this occurs for regions of low statistical error this result is significant. It should also be noted that this qualitative statement can be made for both sets of runs and is therefore on more solid experimental ground. Again, statements comparing results with theory for higher Q^2 are less persuasive since these regions have low statistics and hence higher uncertainties and more data would be needed to determine discrepancies definitively.

Appendix A

Background Rates

A.1 Rates vs p_m (GeV/c) for 32°

Total and Background Rates vs p_m (GeV/c) for 32°, Perp Kine, and $Q^2 = [0.1, 0.2]$ $(GeV/c)^2$		
p_m (GeV/c) (bin center)	Empty Target	Full Target
0.025	0.00289±0.000278	1.06±0.00161
0.075	0.00571±0.000391	1.42±0.00186
0.125	0.00721±0.000439	0.405±0.000997
0.175	0.00485±0.00036	0.104±0.000505
0.225	0.00209±0.000237	0.0376±0.000304
0.275	0.000911±0.000156	0.0137±0.000183
0.325	0.000241±8e-05	0.0051±0.000112
0.375	5.4e-05±3.8e-05	0.00129±5.6e-05
0.425	0±2.7e-05	0.000172±2.1e-05
0.475	0±2.7e-05	2.5e-05±8e-06

Total and Background Rates vs p_m (GeV/c) **for** 32°**, Para Kine, and** $Q^2 = [0.1, 0.2]$ $(GeV/c)^2$		
p_m (GeV/c) (bin center)	Empty Target	Full Target
0.025	0.00308±0.000287	1.23±0.00174
0.075	0.00581±0.000395	1.47±0.0019
0.125	0.00755±0.00045	0.403±0.000995
0.175	0.0049±0.000362	0.105±0.000507
0.225	0.00222±0.000244	0.0389±0.000309
0.275	0.000911±0.000156	0.014±0.000185
0.325	0.000161±6.6e-05	0.00513±0.000112
0.375	5.4e-05±3.8e-05	0.0014±5.9e-05
0.425	2.7e-05±2.7e-05	0.000243±2.4e-05
0.475	2.7e-05±2.7e-05	2.7e-05±8e-06

Total and Background Rates vs p_m (GeV/c) **for** 32°**, Perp Kine, and** $Q^2 = [0.2, 0.3]$ $(GeV/c)^2$		
p_m (GeV/c) (bin center)	Empty Target	Full Target
0.025	0.00134±0.000189	0.43±0.00103
0.075	0.00289±0.000278	0.648±0.00126
0.125	0.00469±0.000354	0.245±0.000776
0.175	0.00346±0.000304	0.0703±0.000416
0.225	0.00147±0.000199	0.0232±0.000239
0.275	0.000482±0.000114	0.0106±0.000161
0.325	0.000134±6e-05	0.00272±8.2e-05
0.375	0±2.7e-05	0.000342±2.9e-05
0.425	0±2.7e-05	1.2e-05±5e-06
0.475	0±2.7e-05	2e-06±2e-06
Total and Background Rates vs p_m (GeV/c) **for** 32°**, Para Kine, and** $Q^2 = [0.2, 0.3]$ $(GeV/c)^2$		
p_m (GeV/c) (bin center)	Empty Target	Full Target
0.025	0.00153±0.000202	0.469±0.00107
0.075	0.00289±0.000278	0.742±0.00135
0.125	0.00525±0.000375	0.289±0.000843
0.175	0.00399±0.000327	0.082±0.000449
0.225	0.00212±0.000238	0.0268±0.000257
0.275	0.000697±0.000137	0.012±0.000172
0.325	8e-05±4.6e-05	0.0031±8.7e-05
0.375	2.7e-05±2.7e-05	0.000396±3.1e-05
0.425	0±2.7e-05	3.9e-05±1e-05
0.475	0±2.7e-05	1.5e-05±6e-06

Total and Background Rates vs p_m (GeV/c) **for** 32°**, Perp Kine, and** $Q^2 = [0.3, 0.4]$ $(GeV/c)^2$		
p_m (GeV/c) (bin center)	Empty Target	Full Target
0.025	0.000429±0.000107	0.153±0.000614
0.075	0.00126±0.000184	0.289±0.000842
0.125	0.0026±0.000264	0.133±0.000571
0.175	0.00185±0.000223	0.044±0.000329
0.225	0.00115±0.000176	0.0134±0.000181
0.275	0.000429±0.000107	0.00497±0.00011
0.325	0.000241±8e-05	0.00239±7.7e-05
0.375	0.000107±5.4e-05	0.000826±4.5e-05
0.425	5.4e-05±3.8e-05	0.000268±2.6e-05
0.475	0±2.7e-05	3.9e-05±1e-05

Total and Background Rates vs p_m (GeV/c) **for** 32°**, Para Kine, and** $Q^2 = [0.3, 0.4]$ $(GeV/c)^2$		
p_m (GeV/c) (bin center)	Empty Target	Full Target
0.025	0.000375±0.0001	0.164±0.000635
0.075	0.00134±0.000189	0.286±0.000838
0.125	0.00249±0.000258	0.122±0.000548
0.175	0.0022±0.000243	0.0401±0.000314
0.225	0.00126±0.000184	0.0135±0.000182
0.275	0.000402±0.000104	0.00488±0.00011
0.325	0.000188±7.1e-05	0.00251±7.9e-05
0.375	2.7e-05±2.7e-05	0.000941±4.8e-05
0.425	0±2.7e-05	0.000197±2.2e-05
0.475	2.7e-05±2.7e-05	4.9e-05±1.1e-05

Total and Background Rates vs p_m (GeV/c) **for** 32°**, Perp Kine, and** $Q^2 = [0.4, 0.5]$ $(GeV/c)^2$		
p_m (GeV/c) (bin center)	Empty Target	Full Target
0.025	0.000241±8e-05	0.071±0.000418
0.075	0.000348±9.7e-05	0.117±0.000537
0.125	0.00112±0.000174	0.0496±0.000349
0.175	0.000697±0.000137	0.0178±0.000209
0.225	0.000455±0.00011	0.00644±0.000126
0.275	0.000107±5.4e-05	0.00234±7.6e-05
0.325	8e-05±4.6e-05	0.00137±5.8e-05
0.375	2.7e-05±2.7e-05	0.000759±4.3e-05
0.425	0±2.7e-05	0.000263±2.5e-05
0.475	0±2.7e-05	0.000111±1.6e-05

Total and Background Rates vs p_m (GeV/c) **for** 32°**, Para Kine, and** $Q^2 = [0.4, 0.5]$ $(GeV/c)^2$		
p_m (GeV/c) (bin center)	Empty Target	Full Target
0.025	8e-05±4.6e-05	0.0599±0.000384
0.075	0.000777±0.000144	0.108±0.000515
0.125	0.00067±0.000134	0.0472±0.000341
0.175	0.000643±0.000131	0.0159±0.000197
0.225	0.000348±9.7e-05	0.00601±0.000122
0.275	0.000295±8.9e-05	0.00247±7.8e-05
0.325	2.7e-05±2.7e-05	0.00134±5.7e-05
0.375	5.4e-05±3.8e-05	0.000666±4e-05
0.425	5.4e-05±3.8e-05	0.000216±2.3e-05
0.475	0±2.7e-05	0.000125±1.8e-05

A.1.1 Rates vs p_m (GeV/c) for 47°

Total and Background Rates vs p_m (GeV/c) for 47°, Perp Kine, and $Q^2 = [0.1, 0.2]$ $(GeV/c)^2$		
p_m (GeV/c) (bin center)	Empty Target	Full Target
0.025	0.00438±0.000283	0.916±0.00134
0.075	0.00774±0.000377	1.27±0.00158
0.125	0.00974±0.000423	0.398±0.000885
0.175	0.00706±0.00036	0.105±0.000454
0.225	0.00394±0.000269	0.0365±0.000268
0.275	0.00271±0.000223	0.0132±0.000161
0.325	0.00202±0.000192	0.00582±0.000107
0.375	0.00178±0.000181	0.00285±7.5e-05
0.425	0.0018±0.000182	0.00128±5e-05
0.475	0.0015±0.000166	0.000594±3.4e-05
Total and Background Rates vs p_m (GeV/c) for 47°, Para Kine, and $Q^2 = [0.1, 0.2]$ $(GeV/c)^2$		
p_m (GeV/c) (bin center)	Empty Target	Full Target
0.025	0.00589±0.000329	1.18±0.00152
0.075	0.00858±0.000397	1.42±0.00167
0.125	0.00988±0.000426	0.389±0.000874
0.175	0.00713±0.000362	0.0962±0.000435
0.225	0.00458±0.00029	0.0356±0.000265
0.275	0.00326±0.000245	0.0133±0.000162
0.325	0.00222±0.000202	0.00593±0.000108
0.375	0.00211±0.000197	0.00297±7.6e-05
0.425	0.00202±0.000192	0.00155±5.5e-05
0.475	0.00154±0.000168	0.000746±3.8e-05

Total and Background Rates vs p_m (GeV/c) **for** $47°$**, Perp Kine, and** $Q^2 = [0.2, 0.3]$ $(GeV/c)^2$		
p_m (GeV/c) (bin center)	Empty Target	Full Target
0.025	0.0015±0.000166	0.312±0.000784
0.075	0.00281±0.000227	0.522±0.00101
0.125	0.00416±0.000276	0.223±0.000663
0.175	0.00361±0.000257	0.0723±0.000377
0.225	0.00264±0.00022	0.0242±0.000218
0.275	0.00136±0.000158	0.0106±0.000144
0.325	0.00145±0.000163	0.00389±8.7e-05
0.375	0.00137±0.000159	0.0012±4.9e-05
0.425	0.00143±0.000162	0.000523±3.2e-05
0.475	0.00139±0.00016	0.000319±2.5e-05
Total and Background Rates vs p_m (GeV/c) **for** $47°$**, Para Kine, and** $Q^2 = [0.2, 0.3]$ $(GeV/c)^2$		
p_m (GeV/c) (bin center)	Empty Target	Full Target
0.025	0.00181±0.000182	0.423±0.000913
0.075	0.00376±0.000263	0.62±0.0011
0.125	0.00563±0.000321	0.215±0.000651
0.175	0.00449±0.000287	0.0624±0.00035
0.225	0.00354±0.000255	0.0223±0.000209
0.275	0.00246±0.000212	0.0116±0.000151
0.325	0.00147±0.000164	0.00435±9.2e-05
0.375	0.00156±0.000169	0.00141±5.3e-05
0.425	0.00128±0.000153	0.000675±3.6e-05
0.475	0.00125±0.000151	0.000309±2.5e-05

Total and Background Rates vs p_m (GeV/c) **for** $47°$**, Perp Kine, and** $Q^2 = [0.3, 0.4]$ $(GeV/c)^2$		
p_m (GeV/c) (bin center)	Empty Target	Full Target
0.025	0.000367±8.2e-05	0.0692±0.000369
0.075	0.00101±0.000136	0.139±0.000524
0.125	0.00183±0.000183	0.0767±0.000388
0.175	0.00158±0.00017	0.0305±0.000245
0.225	0.00161±0.000172	0.0122±0.000155
0.275	0.00115±0.000146	0.00538±0.000103
0.325	0.000972±0.000133	0.00264±7.2e-05
0.375	0.000623±0.000107	0.0011±4.7e-05
0.425	0.000642±0.000108	0.000498±3.1e-05
0.475	0.000458±9.2e-05	0.000234±2.1e-05

Total and Background Rates vs p_m (GeV/c) **for** $47°$**, Para Kine, and** $Q^2 = [0.3, 0.4]$ $(GeV/c)^2$		
p_m (GeV/c) (bin center)	Empty Target	Full Target
0.025	0.000788±0.00012	0.134±0.000514
0.075	0.0013±0.000155	0.218±0.000655
0.125	0.00216±0.000199	0.0948±0.000432
0.175	0.00218±0.0002	0.0358±0.000265
0.225	0.00196±0.00019	0.0146±0.000169
0.275	0.00121±0.000149	0.00675±0.000115
0.325	0.000917±0.00013	0.0033±8.1e-05
0.375	0.00077±0.000119	0.00146±5.4e-05
0.425	0.000825±0.000123	0.000502±3.1e-05
0.475	0.00055±0.0001	0.000199±2e-05

Total and Background Rates vs p_m (GeV/c) **for** $47°$**, Perp Kine, and** $Q^2 = [0.4, 0.5]$ $(GeV/c)^2$		
p_m (GeV/c) (bin center)	Empty Target	Full Target
0.025	0.000238±6.6e-05	0.0647±0.000357
0.075	0.000367±8.2e-05	0.106±0.000457
0.125	0.00134±0.000157	0.0481±0.000308
0.175	0.000935±0.000131	0.0183±0.00019
0.225	0.000403±8.6e-05	0.00652±0.000113
0.275	0.00055±0.0001	0.00254±7.1e-05
0.325	0.000458±9.2e-05	0.00115±4.8e-05
0.375	0.000238±6.6e-05	0.000661±3.6e-05
0.425	0.000165±5.5e-05	0.000307±2.5e-05
0.475	9.2e-05±4.1e-05	0.000124±1.6e-05

Total and Background Rates vs p_m (GeV/c) **for** $47°$**, Para Kine, and** $Q^2 = [0.4, 0.5]$ $(GeV/c)^2$		
p_m (GeV/c) (bin center)	Empty Target	Full Target
0.025	0.000183±5.8e-05	0.0342±0.000259
0.075	0.000403±8.6e-05	0.0664±0.000361
0.125	0.000532±9.9e-05	0.0362±0.000267
0.175	0.000972±0.000133	0.0154±0.000174
0.225	0.000678±0.000112	0.00634±0.000112
0.275	0.000348±8e-05	0.00284±7.5e-05
0.325	0.000458±9.2e-05	0.00151±5.5e-05
0.375	0.000202±6.1e-05	0.000738±3.8e-05
0.425	0.000128±4.9e-05	0.00036±2.7e-05
0.475	0.000183±5.8e-05	0.000138±1.6e-05

Rates vs $\cos\theta_m$ for 32°

Total and Background Rates vs $\cos\theta_m$ for 32°, Perp Kine, and $Q^2 = [0.1, 0.2]$ $(GeV/c)^2$		
$\cos\theta_m$ (bin center)	Empty Target	Full Target
-0.95	0.00346±0.000304	0.436±0.00103
-0.85	0.00121±0.00018	0.187±0.000678
-0.75	0.00155±0.000204	0.147±0.000602
-0.65	0.000804±0.000147	0.128±0.000561
-0.55	0.00083±0.000149	0.116±0.000535
-0.45	0.000777±0.000144	0.109±0.000517
-0.35	0.00107±0.000169	0.104±0.000505
-0.25	0.00075±0.000142	0.0992±0.000494
-0.15	0.000723±0.000139	0.0971±0.000489
-0.05	0.000777±0.000144	0.0957±0.000485
0.05	0.00067±0.000134	0.0964±0.000487
0.15	0.000991±0.000163	0.0978±0.00049
0.25	0.000777±0.000144	0.1±0.000496
0.35	0.00105±0.000167	0.104±0.000505
0.45	0.000616±0.000128	0.108±0.000516
0.55	0.000911±0.000156	0.115±0.000532
0.65	0.0011±0.000172	0.128±0.00056
0.75	0.0011±0.000172	0.147±0.0006
0.85	0.00139±0.000193	0.187±0.000677
0.95	0.0034±0.000302	0.436±0.00104

Total and Background Rates vs $\cos\theta_m$ for 32°, Para Kine, and $Q^2 = [0.1, 0.2]$ $(GeV/c)^2$		
$\cos\theta_m$ (bin center)	Empty Target	Full Target
-0.95	0.00343±0.000303	0.469±0.00107
-0.85	0.00161±0.000208	0.2±0.000702
-0.75	0.00139±0.000193	0.158±0.000624
-0.65	0.00118±0.000178	0.137±0.00058
-0.55	0.000991±0.000163	0.125±0.000554
-0.45	0.000884±0.000154	0.117±0.000536
-0.35	0.00083±0.000149	0.111±0.000522
-0.25	0.000804±0.000147	0.108±0.000515
-0.15	0.000804±0.000147	0.106±0.000509
-0.05	0.000964±0.000161	0.104±0.000505
0.05	0.000777±0.000144	0.105±0.000508
0.15	0.000455±0.00011	0.105±0.000509
0.25	0.000697±0.000137	0.108±0.000516
0.35	0.000911±0.000156	0.111±0.000523
0.45	0.000911±0.000156	0.117±0.000535
0.55	0.000964±0.000161	0.125±0.000554
0.65	0.00083±0.000149	0.137±0.00058
0.75	0.00126±0.000184	0.157±0.000622
0.85	0.00155±0.000204	0.2±0.000702
0.95	0.00351±0.000307	0.468±0.00107

Total and Background Rates vs $\cos\theta_m$ for 32°, Perp Kine, and $Q^2 = [0.2, 0.3]$ $(GeV/c)^2$		
$\cos\theta_m$ (bin center)	Empty Target	Full Target
-0.95	0.00196±0.000229	0.206±0.000712
-0.85	0.000938±0.000158	0.0871±0.000463
-0.75	0.000589±0.000126	0.0694±0.000413
-0.65	0.000509±0.000117	0.0604±0.000385
-0.55	0.000321±9.3e-05	0.0545±0.000366
-0.45	0.000536±0.00012	0.0504±0.000352
-0.35	0.000589±0.000126	0.0483±0.000345
-0.25	0.000589±0.000126	0.0474±0.000341
-0.15	0.000295±8.9e-05	0.0456±0.000335
-0.05	0.000509±0.000117	0.0453±0.000334
0.05	0.000295±8.9e-05	0.0449±0.000332
0.15	0.000616±0.000128	0.0462±0.000337
0.25	0.00067±0.000134	0.0477±0.000342
0.35	0.000482±0.000114	0.0489±0.000347
0.45	0.000455±0.00011	0.051±0.000354
0.55	0.000643±0.000131	0.0547±0.000367
0.65	0.00075±0.000142	0.0606±0.000386
0.75	0.000616±0.000128	0.0691±0.000412
0.85	0.000777±0.000144	0.0877±0.000464
0.95	0.00233±0.00025	0.205±0.00071

Total and Background Rates vs $\cos\theta_m$ **for** 32°**, Para Kine, and** $Q^2 = [0.2, 0.3]$ $(GeV/c)^2$		
$\cos\theta_m$ (bin center)	Empty Target	Full Target
-0.95	0.00233±0.00025	0.233±0.000757
-0.85	0.00131±0.000188	0.0989±0.000493
-0.75	0.000911±0.000156	0.078±0.000438
-0.65	0.000563±0.000123	0.0688±0.000411
-0.55	0.000429±0.000107	0.0624±0.000392
-0.45	0.00083±0.000149	0.0581±0.000378
-0.35	0.000375±0.0001	0.0549±0.000367
-0.25	0.000536±0.00012	0.054±0.000364
-0.15	0.000536±0.00012	0.0519±0.000357
-0.05	0.000321±9.3e-05	0.0514±0.000355
0.05	0.000563±0.000123	0.0523±0.000358
0.15	0.000482±0.000114	0.0521±0.000358
0.25	0.000589±0.000126	0.0537±0.000363
0.35	0.000643±0.000131	0.0555±0.000369
0.45	0.000616±0.000128	0.0575±0.000376
0.55	0.000643±0.000131	0.0623±0.000391
0.65	0.000697±0.000137	0.0684±0.00041
0.75	0.00067±0.000134	0.0784±0.000439
0.85	0.000991±0.000163	0.0998±0.000495
0.95	0.00255±0.000261	0.233±0.000758

Total and Background Rates vs $\cos\theta_m$ **for** 32°**, Perp Kine, and** $Q^2 = [0.3, 0.4]$ $(GeV/c)^2$		
$\cos\theta_m$ (bin center)	Empty Target	Full Target
-0.95	0.00134±0.000189	0.092±0.000476
-0.85	0.000295±8.9e-05	0.0393±0.000311
-0.75	0.000429±0.000107	0.0307±0.000275
-0.65	0.000536±0.00012	0.0273±0.000259
-0.55	0.000214±7.6e-05	0.0248±0.000247
-0.45	0.000348±9.7e-05	0.023±0.000238
-0.35	0.000402±0.000104	0.0215±0.00023
-0.25	0.000268±8.5e-05	0.0212±0.000228
-0.15	0.000188±7.1e-05	0.0206±0.000225
-0.05	0.000214±7.6e-05	0.02±0.000222
0.05	0.000134±6e-05	0.0206±0.000225
0.15	0.000321±9.3e-05	0.0204±0.000224
0.25	0.000241±8e-05	0.0214±0.000229
0.35	0.000268±8.5e-05	0.0222±0.000233
0.45	0.000214±7.6e-05	0.023±0.000238
0.55	0.000241±8e-05	0.0244±0.000245
0.65	0.000482±0.000114	0.0266±0.000256
0.75	0.000295±8.9e-05	0.031±0.000276
0.85	0.000348±9.7e-05	0.0391±0.00031
0.95	0.00134±0.000189	0.0916±0.000474

Total and Background Rates vs $\cos\theta_m$ for 32°, Para Kine, and $Q^2 = [0.3, 0.4]$ $(GeV/c)^2$		
$\cos\theta_m$ (bin center)	Empty Target	Full Target
-0.95	0.00107±0.000169	0.0917±0.000475
-0.85	0.000455±0.00011	0.0389±0.000309
-0.75	0.000509±0.000117	0.0307±0.000275
-0.65	0.000375±0.0001	0.0265±0.000255
-0.55	0.000321±9.3e-05	0.0242±0.000244
-0.45	0.000134±6e-05	0.0225±0.000235
-0.35	0.000321±9.3e-05	0.0218±0.000231
-0.25	0.000134±6e-05	0.0207±0.000225
-0.15	0.000375±0.0001	0.0206±0.000225
-0.05	0.000429±0.000107	0.0202±0.000223
0.05	0.000188±7.1e-05	0.0203±0.000223
0.15	0.000188±7.1e-05	0.0206±0.000225
0.25	0.000375±0.0001	0.0209±0.000226
0.35	0.000295±8.9e-05	0.0213±0.000229
0.45	0.000214±7.6e-05	0.023±0.000238
0.55	0.000188±7.1e-05	0.0239±0.000243
0.65	0.000402±0.000104	0.0265±0.000255
0.75	0.000429±0.000107	0.0303±0.000273
0.85	0.000402±0.000104	0.0392±0.00031
0.95	0.0015±0.0002	0.0906±0.000472

Total and Background Rates vs $\cos\theta_m$ **for** 32°**, Perp Kine, and** $Q^2 = [0.4, 0.5]$ $(GeV/c)^2$		
$\cos\theta_m$ (bin center)	Empty Target	Full Target
-0.95	0.000402±0.000104	0.0382±0.000306
-0.85	0.000161±6.6e-05	0.0166±0.000202
-0.75	8e-05±4.6e-05	0.0128±0.000177
-0.65	0.000188±7.1e-05	0.0111±0.000165
-0.55	0.000214±7.6e-05	0.0099±0.000156
-0.45	0.000134±6e-05	0.00997±0.000157
-0.35	0.000161±6.6e-05	0.00902±0.000149
-0.25	0.000107±5.4e-05	0.0088±0.000147
-0.15	0.000161±6.6e-05	0.00857±0.000145
-0.05	0.000134±6e-05	0.00845±0.000144
0.05	2.7e-05±2.7e-05	0.00857±0.000145
0.15	8e-05±4.6e-05	0.00854±0.000145
0.25	0.000188±7.1e-05	0.00878±0.000147
0.35	0.000134±6e-05	0.00875±0.000147
0.45	0.000134±6e-05	0.00974±0.000155
0.55	0.000134±6e-05	0.0103±0.000159
0.65	0.000107±5.4e-05	0.0112±0.000166
0.75	0.000107±5.4e-05	0.0132±0.00018
0.85	0.000134±6e-05	0.0163±0.0002
0.95	0.000295±8.9e-05	0.0382±0.000306

Total and Background Rates vs $\cos\theta_m$ **for** 32°**, Para Kine, and** $Q^2 = [0.4, 0.5]$ $(GeV/c)^2$		
$\cos\theta_m$ (bin center)	Empty Target	Full Target
-0.95	0.000348±9.7e-05	0.035±0.000293
-0.85	0.000214±7.6e-05	0.0144±0.000188
-0.75	0.000241±8e-05	0.0119±0.000171
-0.65	0.000107±5.4e-05	0.0104±0.00016
-0.55	5.4e-05±3.8e-05	0.00897±0.000149
-0.45	0.000134±6e-05	0.00845±0.000144
-0.35	8e-05±4.6e-05	0.00825±0.000142
-0.25	0.000134±6e-05	0.00799±0.00014
-0.15	5.4e-05±3.8e-05	0.00768±0.000137
-0.05	0.000107±5.4e-05	0.00785±0.000139
0.05	8e-05±4.6e-05	0.00772±0.000138
0.15	8e-05±4.6e-05	0.00778±0.000138
0.25	0.000107±5.4e-05	0.00768±0.000137
0.35	5.4e-05±3.8e-05	0.00802±0.00014
0.45	5.4e-05±3.8e-05	0.00857±0.000145
0.55	8e-05±4.6e-05	0.00944±0.000152
0.65	0.000134±6e-05	0.0102±0.000158
0.75	8e-05±4.6e-05	0.0118±0.00017
0.85	0.000241±8e-05	0.0149±0.000191
0.95	0.000563±0.000123	0.0347±0.000292

Rates vs $\cos\theta_m$ for 47°

Total and Background Rates vs $\cos\theta_m$ for 47°, Perp Kine, and $Q^2 = [0.1, 0.2]$ $(GeV/c)^2$		
$\cos\theta_m$ (bin center)	Empty Target	Full Target
-0.95	0.00722±0.000364	0.396±0.000882
-0.85	0.0027±0.000222	0.169±0.000577
-0.75	0.00229±0.000205	0.134±0.000514
-0.65	0.0022±0.000201	0.116±0.000477
-0.55	0.0016±0.000171	0.105±0.000454
-0.45	0.00178±0.000181	0.0982±0.000439
-0.35	0.00154±0.000168	0.0938±0.00043
-0.25	0.00114±0.000144	0.0913±0.000424
-0.15	0.0016±0.000171	0.0888±0.000418
-0.05	0.00137±0.000159	0.0882±0.000417
0.05	0.00139±0.00016	0.0874±0.000415
0.15	0.00143±0.000162	0.0885±0.000417
0.25	0.00161±0.000172	0.0899±0.000421
0.35	0.00169±0.000176	0.0932±0.000428
0.45	0.00172±0.000178	0.0986±0.000441
0.55	0.00202±0.000192	0.105±0.000454
0.65	0.00209±0.000196	0.115±0.000476
0.75	0.00238±0.000209	0.133±0.000511
0.85	0.00251±0.000215	0.168±0.000575
0.95	0.0069±0.000356	0.396±0.000883

Total and Background Rates vs $\cos\theta_m$ **for** 47°**, Para Kine, and** $Q^2 = [0.1, 0.2]$ $(GeV/c)^2$		
$\cos\theta_m$ (bin center)	Empty Target	Full Target
-0.95	0.0079±0.000381	0.452±0.000943
-0.85	0.00328±0.000245	0.193±0.000616
-0.75	0.00275±0.000225	0.153±0.000548
-0.65	0.00211±0.000197	0.132±0.000509
-0.55	0.00183±0.000183	0.12±0.000486
-0.45	0.00194±0.000189	0.112±0.000469
-0.35	0.00205±0.000194	0.107±0.000459
-0.25	0.00165±0.000174	0.103±0.00045
-0.15	0.00154±0.000168	0.102±0.000447
-0.05	0.00167±0.000175	0.1±0.000445
0.05	0.0016±0.000171	0.1±0.000443
0.15	0.00181±0.000182	0.101±0.000445
0.25	0.00176±0.00018	0.103±0.000451
0.35	0.00176±0.00018	0.107±0.000459
0.45	0.00176±0.00018	0.112±0.00047
0.55	0.00196±0.00019	0.12±0.000486
0.65	0.002±0.000191	0.132±0.000509
0.75	0.00281±0.000227	0.152±0.000546
0.85	0.00337±0.000249	0.193±0.000617
0.95	0.00673±0.000351	0.451±0.000942

Total and Background Rates vs $\cos\theta_m$ **for** 47°**, Perp Kine, and** $Q^2 = [0.2, 0.3]$ $(GeV/c)^2$		
$\cos\theta_m$ (bin center)	Empty Target	Full Target
-0.95	0.00358±0.000256	0.168±0.000575
-0.85	0.0013±0.000155	0.0715±0.000375
-0.75	0.00103±0.000137	0.0562±0.000332
-0.65	0.00103±0.000137	0.049±0.00031
-0.55	0.00103±0.000137	0.0444±0.000296
-0.45	0.00099±0.000135	0.042±0.000287
-0.35	0.000898±0.000128	0.0406±0.000283
-0.25	0.000917±0.00013	0.0384±0.000275
-0.15	0.000935±0.000131	0.0378±0.000273
-0.05	0.00077±0.000119	0.0378±0.000273
0.05	0.000788±0.00012	0.0375±0.000272
0.15	0.000843±0.000124	0.0379±0.000273
0.25	0.000898±0.000128	0.0384±0.000275
0.35	0.000898±0.000128	0.04±0.000281
0.45	0.00114±0.000144	0.0419±0.000287
0.55	0.0011±0.000142	0.0444±0.000296
0.65	0.00105±0.000138	0.0489±0.00031
0.75	0.00156±0.000169	0.0565±0.000333
0.85	0.00156±0.000169	0.0725±0.000378
0.95	0.00341±0.00025	0.168±0.000574

Total and Background Rates vs $\cos\theta_m$ **for** 47°**, Para Kine, and** $Q^2 = [0.2, 0.3]$ $(GeV/c)^2$		
$\cos\theta_m$ (bin center)	Empty Target	Full Target
-0.95	0.00416±0.000276	0.196±0.000622
-0.85	0.00163±0.000173	0.083±0.000404
-0.75	0.00158±0.00017	0.0661±0.00036
-0.65	0.00112±0.000143	0.057±0.000335
-0.55	0.00125±0.000151	0.052±0.00032
-0.45	0.00123±0.00015	0.0486±0.000309
-0.35	0.00114±0.000144	0.0469±0.000304
-0.25	0.00136±0.000158	0.0449±0.000297
-0.15	0.00105±0.000138	0.0438±0.000294
-0.05	0.00101±0.000136	0.0431±0.000291
0.05	0.00088±0.000127	0.0428±0.00029
0.15	0.00114±0.000144	0.0439±0.000294
0.25	0.000898±0.000128	0.0446±0.000296
0.35	0.00123±0.00015	0.0461±0.000301
0.45	0.00121±0.000149	0.0485±0.000309
0.55	0.00125±0.000151	0.0518±0.000319
0.65	0.00136±0.000158	0.057±0.000335
0.75	0.00149±0.000165	0.0652±0.000358
0.85	0.00196±0.00019	0.0835±0.000405
0.95	0.00414±0.000276	0.197±0.000622

Total and Background Rates vs $\cos\theta_m$ **for** 47°**, Perp Kine, and** $Q^2 = [0.3, 0.4]$ $(GeV/c)^2$		
$\cos\theta_m$ (bin center)	Empty Target	Full Target
-0.95	0.00143±0.000162	0.0483±0.000308
-0.85	0.000605±0.000105	0.0206±0.000201
-0.75	0.00055±0.0001	0.0164±0.00018
-0.65	0.000403±8.6e-05	0.0141±0.000166
-0.55	0.000403±8.6e-05	0.0129±0.00016
-0.45	0.000458±9.2e-05	0.012±0.000154
-0.35	0.000202±6.1e-05	0.0114±0.00015
-0.25	0.000385±8.4e-05	0.0114±0.000149
-0.15	0.00044±9e-05	0.011±0.000147
-0.05	0.000367±8.2e-05	0.0111±0.000148
0.05	0.000367±8.2e-05	0.0106±0.000144
0.15	0.000422±8.8e-05	0.0107±0.000145
0.25	0.000513±9.7e-05	0.0112±0.000148
0.35	0.000403±8.6e-05	0.0116±0.000151
0.45	0.00033±7.8e-05	0.012±0.000154
0.55	0.000385±8.4e-05	0.0128±0.000158
0.65	0.000385±8.4e-05	0.0142±0.000167
0.75	0.000605±0.000105	0.0164±0.00018
0.85	0.000788±0.00012	0.021±0.000203
0.95	0.00161±0.000172	0.0484±0.000309

Total and Background Rates vs $\cos\theta_m$ for 47°, Para Kine, and $Q^2 = [0.3, 0.4]$ $(GeV/c)^2$		
$\cos\theta_m$ (bin center)	Empty Target	Full Target
-0.95	0.00174±0.000179	0.0733±0.00038
-0.85	0.000752±0.000117	0.0314±0.000249
-0.75	0.000495±9.5e-05	0.0249±0.000221
-0.65	0.000587±0.000104	0.0214±0.000205
-0.55	0.00055±0.0001	0.0194±0.000195
-0.45	0.000458±9.2e-05	0.0184±0.00019
-0.35	0.000568±0.000102	0.0175±0.000185
-0.25	0.000587±0.000104	0.0171±0.000183
-0.15	0.000348±8e-05	0.0164±0.00018
-0.05	0.000532±9.9e-05	0.0163±0.000179
0.05	0.000367±8.2e-05	0.0162±0.000179
0.15	0.000367±8.2e-05	0.0166±0.000181
0.25	0.000312±7.6e-05	0.0168±0.000182
0.35	0.000422±8.8e-05	0.0175±0.000185
0.45	0.000587±0.000104	0.0181±0.000189
0.55	0.000587±0.000104	0.0198±0.000197
0.65	0.000587±0.000104	0.0212±0.000204
0.75	0.000605±0.000105	0.0243±0.000219
0.85	0.000568±0.000102	0.0306±0.000246
0.95	0.0024±0.00021	0.0732±0.000379

Total and Background Rates vs $\cos\theta_m$ **for** 47°**, Perp Kine, and** $Q^2 = [0.4, 0.5]$ $(GeV/c)^2$		
$\cos\theta_m$ (bin center)	Empty Target	Full Target
-0.95	0.000587±0.000104	0.0357±0.000265
-0.85	0.000202±6.1e-05	0.0152±0.000173
-0.75	0.000385±8.4e-05	0.0119±0.000153
-0.65	0.000275±7.1e-05	0.0104±0.000143
-0.55	0.000312±7.6e-05	0.00961±0.000137
-0.45	0.00022±6.4e-05	0.00887±0.000132
-0.35	0.00011±4.5e-05	0.00852±0.000129
-0.25	0.00011±4.5e-05	0.00832±0.000128
-0.15	0.000238±6.6e-05	0.00775±0.000123
-0.05	0.000165±5.5e-05	0.00788±0.000125
0.05	0.000147±5.2e-05	0.00789±0.000125
0.15	0.000147±5.2e-05	0.00813±0.000126
0.25	7.3e-05±3.7e-05	0.00819±0.000127
0.35	0.00011±4.5e-05	0.00843±0.000129
0.45	0.000183±5.8e-05	0.00886±0.000132
0.55	0.00022±6.4e-05	0.00959±0.000137
0.65	0.000183±5.8e-05	0.0102±0.000142
0.75	0.000385±8.4e-05	0.0119±0.000153
0.85	0.000275±7.1e-05	0.0153±0.000173
0.95	0.000568±0.000102	0.0358±0.000265

A.1.2 AV_{ed} vs P_m

AV_{ed} vs P_m for 2005 data

Beam-Vector Asymmetries Versus Missing Momentum for 2005 Data for Different Potentials						
Perpendicular Kinematics–$0.1 < Q^2 < 0.2(GeV/c)^2$						
P_m (bin center)	Reconstructed Value	Total Error	Bonn	v18	v14	Paris
0.025	-0.119174	0.0042677	-0.118493	-0.118491	-0.118482	-0.118378
0.075	-0.114667	0.00369987	-0.120067	-0.120149	-0.120089	-0.119935
0.125	-0.100071	0.00672023	-0.118265	-0.118878	-0.118689	-0.11849
0.175	-0.10558	0.0130185	-0.0894856	-0.0916579	-0.0915015	-0.0917548
0.225	-0.0448469	0.0220192	-0.06414	-0.0671307	-0.0659304	-0.0680137
0.275	-0.0872668	0.0370839	-0.0711936	-0.0705727	-0.0637681	-0.0700487
0.325	0.189583	0.0552002	0.0213224	0.0298518	0.0470879	0.0261584
0.375	0.249096	0.0790367	0.155349	0.176516	0.195148	0.159856
0.425	0.205482	0.120061	0.229819	0.256026	0.266889	0.229667
0.475	0.564397	0.166573	0.255233	0.284622	0.28871	0.250915

Beam-Vector Asymmetries Versus Missing Momentum for 2005 Data for Different Potentials						
Parallel Kinematics–$0.1(GeV/c)^2 < Q^2 < 0.2(GeV/c)^2$						
P_m (bin center)	Reconstructed Value	Total Error	Bonn	v18	v14	Paris
0.025	-0.14578	0.00374032	-0.146831	-0.147037	-0.14708	-0.14721
0.075	-0.156232	0.00345324	-0.150984	-0.151111	-0.151112	-0.151344
0.125	-0.167493	0.00662983	-0.159758	-0.159335	-0.158877	-0.159544
0.175	-0.134799	0.0132426	-0.160422	-0.158704	-0.156437	-0.158004
0.225	-0.148809	0.0217865	-0.131234	-0.127724	-0.12161	-0.124727
0.275	-0.0480782	0.0359021	-0.0472946	-0.045944	-0.0367717	-0.043509
0.325	0.0475347	0.0550849	0.0162974	0.015663	0.0244675	0.0162932
0.375	0.108071	0.07607	0.0816345	0.0843477	0.0923568	0.0830299
0.425	0.275062	0.105114	0.153528	0.163319	0.169966	0.157495
0.475	0.279061	0.152046	0.184941	0.20084	0.20588	0.192346

Beam-Vector Asymmetries Versus Missing Momentum for 2005 Data for Different Potentials						
Perpendicular Kinematics–$0.2 < Q^2 < 0.3(GeV/c)^2$						
P_m (bin center)	Reconstructed Value	Total Error	Bonn	v18	v14	Paris
0.025	-0.192556	0.00743385	-0.181947	-0.182118	-0.182136	-0.182066
0.075	-0.185787	0.00610242	-0.181047	-0.181429	-0.181362	-0.181266
0.125	-0.143865	0.0100771	-0.177996	-0.17905	-0.178605	-0.1786
0.175	-0.146769	0.0182505	-0.171313	-0.173924	-0.173027	-0.173416
0.225	-0.000736193	0.0314071	-0.0969877	-0.1026	-0.102066	-0.10403
0.275	0.0146309	0.0466906	-0.03164	-0.038054	-0.037591	-0.041599
0.325	0.0678559	0.0778611	-0.0128104	-0.0138391	-0.00909183	-0.0179546
0.375	0.208093	0.151992	0.0698641	0.0845305	0.100529	0.0732303
0.425	0.842053	0.205614	0.173792	0.198117	0.209959	0.172224
0.475	0.570851	0.32276	0.188818	0.210095	0.210086	0.17904

Beam-Vector Asymmetries Versus Missing Momentum for 2005 Data for Different Potentials						
Parallel Kinematics–$0.2(GeV/c)^2 < Q^2 < 0.3(GeV/c)^2$						
P_m (bin center)	Reconstructed Value	Total Error	Bonn	v18	v14	Paris
0.025	-0.24962	0.00626181	-0.228884	-0.228497	-0.228678	-0.228738
0.075	-0.2478	0.00528527	-0.230698	-0.230206	-0.230338	-0.230498
0.125	-0.246771	0.00907783	-0.232924	-0.232328	-0.231932	-0.232412
0.175	-0.209672	0.0168407	-0.232932	-0.231331	-0.22917	-0.230536
0.225	-0.0916749	0.0285151	-0.2131	-0.206393	-0.199938	-0.202684
0.275	-0.186447	0.0396756	-0.185842	-0.172379	-0.160976	-0.164612
0.325	-0.0894038	0.0653954	-0.125359	-0.112148	-0.0987453	-0.105191
0.375	0.323661	0.117343	0.0654873	0.0744717	0.0845206	0.071971
0.425	0.365002	0.178873	0.172015	0.181184	0.183448	0.168627
0.475	0.146001	0.255053	0.207586	0.218485	0.213057	0.201776

Beam-Vector Asymmetries Versus Missing Momentum for 2005 Data for Different Potentials						
Perpendicular Kinematics–$0.3 < Q^2 < 0.4 (GeV/c)^2$						
P_m (bin center)	Reconstructed Value	Total Error	Bonn	v18	v14	Paris
0.025	-0.247987	0.0159458	-0.248022	-0.248195	-0.248238	-0.248195
0.075	-0.244873	0.0120594	-0.248477	-0.248836	-0.248772	-0.248753
0.125	-0.223313	0.0178781	-0.252377	-0.253311	-0.252829	-0.252951
0.175	-0.224962	0.0295006	-0.233987	-0.236593	-0.234437	-0.235475
0.225	-0.238085	0.0464085	-0.218503	-0.224116	-0.220389	-0.22293
0.275	-0.0367528	0.0701957	-0.105092	-0.114509	-0.109892	-0.115544
0.325	-0.176589	0.101234	-0.03338	-0.0431858	-0.041427	-0.0474865
0.375	0.599474	0.159183	-0.00175426	-0.00653712	-0.00315164	-0.0115375
0.425	0.0431045	0.240391	0.0536495	0.0585197	0.0613064	0.0476282
0.475	0.266237	0.342953	0.109587	0.120825	0.118343	0.096283

Beam-Vector Asymmetries Versus Missing Momentum for 2005 Data for Different Potentials						
Parallel Kinematics–$0.3 (GeV/c)^2 < Q^2 < 0.4 (GeV/c)^2$						
P_m (bin center)	Reconstructed Value	Total Error	Bonn	v18	v14	Paris
0.025	-0.324547	0.0112725	-0.304435	-0.303849	-0.304051	-0.304198
0.075	-0.319709	0.00930813	-0.308146	-0.307337	-0.307558	-0.307769
0.125	-0.303094	0.0147992	-0.308599	-0.307983	-0.307807	-0.308237
0.175	-0.267949	0.0244657	-0.295806	-0.295179	-0.292597	-0.294089
0.225	-0.151962	0.0392237	-0.264806	-0.259783	-0.252155	-0.256133
0.275	-0.118378	0.0580551	-0.208959	-0.190719	-0.175801	-0.181962
0.325	-0.180835	0.0830347	-0.187617	-0.160401	-0.141548	-0.146713
0.375	0.161232	0.124034	-0.183738	-0.158094	-0.142412	-0.148173
0.425	0.0983915	0.209572	-0.109063	-0.0898915	-0.0861191	-0.0933388
0.475	0.829772	0.302328	0.177394	0.176193	0.155955	0.153976

Beam-Vector Asymmetries Versus Missing Momentum for 2005 Data for Different Potentials						
Perpendicular Kinematics–$0.4 < Q^2 < 0.5 (GeV/c)^2$						
P_m (bin center)	Reconstructed Value	Total Error	Bonn	v18	v14	Paris
0.025	-0.326523	0.0161911	-0.319621	-0.31988	-0.319982	-0.319936
0.075	-0.30323	0.01334	-0.312523	-0.313005	-0.313005	-0.313009
0.125	-0.282034	0.021144	-0.321782	-0.322726	-0.322406	-0.322579
0.175	-0.24622	0.0352711	-0.360837	-0.362398	-0.361671	-0.361936
0.225	-0.1639	0.0599046	-0.311221	-0.31517	-0.311115	-0.313099
0.275	0.162147	0.097032	-0.132355	-0.140537	-0.126569	-0.136005
0.325	-0.0469026	0.144769	-0.0557143	-0.0698613	-0.0567393	-0.0671812
0.375	-4.83615e-07	0.184396	-0.029363	-0.0443404	-0.0366389	-0.0462748
0.425	-0.264681	0.265044	0.00267175	0.000342825	0.00312161	-0.00767788
0.475	0.158808	0.460566	0.0538504	0.0588268	0.0558015	0.0466314

Beam-Vector Asymmetries Versus Missing Momentum for 2005 Data for Different Potentials						
Parallel Kinematics–$0.4 (GeV/c)^2 < Q^2 < 0.5 (GeV/c)^2$						
P_m (bin center)	Reconstructed Value	Total Error	Bonn	v18	v14	Paris
0.025	-0.38402	0.0232518	-0.378142	-0.377684	-0.377861	-0.378099
0.075	-0.385598	0.0178364	-0.378698	-0.378118	-0.378323	-0.378648
0.125	-0.334706	0.0257077	-0.382598	-0.381847	-0.381422	-0.382191
0.175	-0.320081	0.0408803	-0.382604	-0.381404	-0.379584	-0.381094
0.225	-0.0711064	0.0643636	-0.339635	-0.336793	-0.330683	-0.334234
0.275	-0.36858	0.090611	-0.19054	-0.172976	-0.154632	-0.164558
0.325	-0.271091	0.125031	-0.0997186	-0.0639855	-0.0428551	-0.0519521
0.375	-0.0935619	0.176987	-0.107595	-0.0679129	-0.0497856	-0.0561719
0.425	-0.167631	0.273162	-0.144745	-0.118165	-0.112124	-0.115946
0.475	0.603471	0.389551	-0.319362	-0.30343	-0.300518	-0.304064

Beam-Vector Asymmetries Versus Missing Momentum for 2005 Data for Different Potentials						
Perpendicular Kinematics–$0.1 < Q^2 < 0.5(GeV/c)^2$						
P_m (bin center)	Reconstructed Value	Total Error	Bonn	v18	v14	Paris
0.025	-0.150087	0.00533015	-0.130139	-0.130195	-0.130202	-0.130083
0.075	-0.14829	0.00281253	-0.133484	-0.133651	-0.133572	-0.133434
0.125	-0.132016	0.00465635	-0.138224	-0.138929	-0.138672	-0.138513
0.175	-0.144168	0.00845194	-0.123447	-0.12576	-0.125488	-0.125724
0.225	-0.07318	0.0142631	-0.0861769	-0.0900668	-0.0890326	-0.0910432
0.275	-0.0552339	0.0227535	-0.0597934	-0.0625962	-0.0582517	-0.0637033
0.325	0.0713796	0.0343635	0.00210832	0.00520034	0.0166398	0.00165757
0.375	0.250743	0.0529135	0.116564	0.133129	0.149095	0.119313
0.425	0.231406	0.0776976	0.198205	0.221994	0.231626	0.197383
0.475	0.325948	0.110836	0.233448	0.260238	0.262805	0.227814

Beam-Vector Asymmetries Versus Missing Momentum for 2005 Data for Different Potentials						
Parallel Kinematics–$0.1(GeV/c)^2 < Q^2 < 0.5(GeV/c)^2$						
P_m (bin center)	Reconstructed Value	Total Error	Bonn	v18	v14	Paris
0.025	-0.188021	0.00302423	-0.161735	-0.161884	-0.161941	-0.162061
0.075	-0.201874	0.0026383	-0.167781	-0.167833	-0.167823	-0.168054
0.125	-0.212623	0.00468672	-0.181637	-0.181172	-0.18073	-0.181343
0.175	-0.190194	0.00875465	-0.189023	-0.187401	-0.185268	-0.186724
0.225	-0.154109	0.0143932	-0.164899	-0.160448	-0.154301	-0.157296
0.275	-0.131098	0.0217398	-0.110228	-0.102485	-0.0914026	-0.0971172
0.325	-0.0736337	0.0327472	-0.056544	-0.0479839	-0.0359505	-0.0430523
0.375	0.146207	0.0494246	0.0349374	0.0443622	0.0542768	0.0450983
0.425	0.230005	0.0720147	0.127776	0.139396	0.14482	0.132772
0.475	0.29997	0.108036	0.153784	0.169814	0.171616	0.159608

Beam-Vector Asymmetries Versus Missing Momentum for 2005 Data for Various Subnuclear Effects							
Perpendicular Kinematics–$0.1 < Q^2 < 0.2(GeV/c)^2$							
P_m (bin center)	Reconstructed	Total Error	PWBA	PWBA+FSI	PWBA+FSI+MEC	PWBA+FSI+MEC+IC	TOTAL
0.025	-0.119174	0.0042677	-0.118664	-0.119382	-0.119031	-0.118816	-0.118493
0.075	-0.114667	0.00369987	-0.121238	-0.121703	-0.120974	-0.120574	-0.120067
0.125	-0.100071	0.00672023	-0.126335	-0.123086	-0.120402	-0.11913	-0.118265
0.175	-0.10558	0.0130185	-0.126025	-0.102369	-0.093345	-0.0909898	-0.0894856
0.225	-0.0448469	0.0220192	-0.114576	-0.0810915	-0.0669994	-0.0663193	-0.06414
0.275	-0.0872668	0.0370839	-0.0882177	-0.088396	-0.0799616	-0.0727194	-0.0711936
0.325	0.189583	0.0552002	-0.0315839	-0.0498399	-0.034909	0.0157281	0.0213224
0.375	0.249096	0.0790367	0.0323817	0.00251386	0.0339679	0.148033	0.155349
0.425	0.205482	0.120061	0.0445026	0.0214698	0.068684	0.224546	0.229819
0.475	0.564397	0.166573	0.0248776	0.0144144	0.0800929	0.255247	0.255233

Beam-Vector Asymmetries Versus Missing Momentum for 2005 Data for Various Subnuclear Effects							
Parallel Kinematics–$0.1(GeV/c)^2 < Q^2 < 0.2(GeV/c)^2$							
P_m (bin center)	Reconstructed	Total Error	PWBA	PWBA+FSI	PWBA+FSI+MEC	PWBA+FSI+MEC+IC	TOTAL
0.025	-0.14578	0.00374032	-0.141743	-0.145691	-0.146692	-0.147338	-0.146831
0.075	-0.156232	0.00345324	-0.143011	-0.149136	-0.150797	-0.151878	-0.150984
0.125	-0.167493	0.00662983	-0.143834	-0.15547	-0.159307	-0.161705	-0.159758
0.175	-0.134799	0.0132426	-0.138104	-0.150955	-0.160345	-0.163745	-0.160422
0.225	-0.148809	0.0217865	-0.118296	-0.118376	-0.133301	-0.134186	-0.131234
0.275	-0.0480782	0.0359021	-0.0843605	-0.0611573	-0.0609735	-0.0501916	-0.0472946
0.325	0.0475347	0.0550849	-0.0320632	-0.0290488	-0.0175365	0.0119479	0.0162974
0.375	0.108071	0.07607	0.0397116	0.00430323	0.021346	0.0762713	0.0816345
0.425	0.275062	0.105114	0.105186	0.0289567	0.0537964	0.148793	0.153528
0.475	0.279061	0.152046	0.153682	0.0377167	0.0709955	0.182648	0.184941

Beam-Vector Asymmetries Versus Missing Momentum for 2005 Data for Various Subnuclear Effects							
Perpendicular Kinematics–$0.2 < Q^2 < 0.3(GeV/c)^2$							
P_m (bin center)	Reconstructed	Total Error	PWBA	PWBA+FSI	PWBA+FSI+MEC	PWBA+FSI+MEC+IC	TOTAL
0.025	-0.192556	0.00743385	-0.184176	-0.183293	-0.182855	-0.182592	-0.181947
0.075	-0.185787	0.00610242	-0.185157	-0.183476	-0.182669	-0.182201	-0.181047
0.125	-0.143865	0.0100771	-0.188559	-0.183554	-0.181422	-0.18036	-0.177996
0.175	-0.146769	0.0182505	-0.198349	-0.184347	-0.178141	-0.175466	-0.171313
0.225	-0.000736193	0.0314071	-0.172123	-0.126938	-0.107523	-0.102425	-0.0969877
0.275	0.0146309	0.0466906	-0.0870793	-0.0718051	-0.0420294	-0.0366143	-0.03164
0.325	0.0678559	0.0778611	0.0113482	-0.0559256	-0.0329427	-0.0169131	-0.0128104
0.375	0.208093	0.151992	0.0135862	-0.044697	-0.0178255	0.0645367	0.0698641
0.425	0.842053	0.205614	0.0223835	-0.0303774	0.0216811	0.168496	0.173792
0.475	0.570851	0.32276	-0.0300617	-0.0583788	0.00831844	0.187914	0.188818

Beam-Vector Asymmetries Versus Missing Momentum for 2005 Data for Various Subnuclear Effects							
Parallel Kinematics–$0.2(GeV/c)^2 < Q^2 < 0.3(GeV/c)^2$							
P_m (bin center)	Reconstructed	Total Error	PWBA	PWBA+FSI	PWBA+FSI+MEC	PWBA+FSI+MEC+IC	TOTAL
0.025	-0.24962	0.00626181	-0.223153	-0.227285	-0.228498	-0.229754	-0.228884
0.075	-0.2478	0.00528527	-0.221952	-0.228204	-0.230186	-0.232028	-0.230698
0.125	-0.246771	0.00907783	-0.21793	-0.228453	-0.232575	-0.235354	-0.232924
0.175	-0.209672	0.0168407	-0.212429	-0.226298	-0.234037	-0.236669	-0.232932
0.225	-0.0916749	0.0285151	-0.185882	-0.193902	-0.215107	-0.215826	-0.2131
0.275	-0.186447	0.0396756	-0.131062	-0.148313	-0.189597	-0.184261	-0.185842
0.325	-0.0894038	0.0653954	-0.0950403	-0.120802	-0.149534	-0.121274	-0.125359
0.375	0.323661	0.117343	0.0375548	-0.0386359	-0.0244886	0.0628121	0.0654873
0.425	0.365002	0.178873	0.13364	-0.0332698	0.0188506	0.166304	0.172015
0.475	0.146001	0.255053	0.181849	-0.0596395	0.0159761	0.204999	0.207586

Beam-Vector Asymmetries Versus Missing Momentum for 2005 Data for Various Subnuclear Effects							
Perpendicular Kinematics–$0.3 < Q^2 < 0.4(GeV/c)^2$							
P_m (bin center)	Reconstructed	Total Error	PWBA	PWBA+FSI	PWBA+FSI+MEC	PWBA+FSI+MEC+IC	TOTAL
0.025	-0.247987	0.0159458	-0.250896	-0.249114	-0.248661	-0.248554	-0.248022
0.075	-0.244873	0.0120594	-0.253471	-0.250611	-0.249824	-0.249633	-0.248477
0.125	-0.223313	0.0178781	-0.262977	-0.257541	-0.255915	-0.255361	-0.252377
0.175	-0.224962	0.0295006	-0.258334	-0.245484	-0.241151	-0.23936	-0.233987
0.225	-0.238085	0.0464085	-0.270219	-0.246569	-0.234267	-0.227723	-0.218503
0.275	-0.0367528	0.0701957	-0.187603	-0.152333	-0.123858	-0.116356	-0.105092
0.325	-0.176589	0.101234	-0.0141337	-0.0924504	-0.0504962	-0.0418134	-0.03338
0.375	0.599474	0.159183	0.0927065	-0.0633816	-0.0247203	-0.00872591	-0.00175426
0.425	0.0431045	0.240391	0.0801991	-0.0391467	0.00152416	0.0488618	0.0536495
0.475	0.266237	0.342953	-0.0750963	-0.112218	-0.0593447	0.104382	0.109587

Beam-Vector Asymmetries Versus Missing Momentum for 2005 Data for Various Subnuclear Effects							
Parallel Kinematics–$0.3(GeV/c)^2 < Q^2 < 0.4(GeV/c)^2$							
P_m (bin center)	Reconstructed	Total Error	PWBA	PWBA+FSI	PWBA+FSI+MEC	PWBA+FSI+MEC+IC	TOTAL
0.025	-0.324547	0.0112725	-0.297497	-0.302642	-0.303889	-0.30503	-0.304435
0.075	-0.319709	0.00930813	-0.298244	-0.305584	-0.307576	-0.309278	-0.308146
0.125	-0.303094	0.0147992	-0.293794	-0.304807	-0.308671	-0.3109	-0.308599
0.175	-0.267949	0.0244657	-0.276427	-0.290317	-0.298338	-0.299834	-0.295806
0.225	-0.151962	0.0392237	-0.250531	-0.260311	-0.273471	-0.269053	-0.264806
0.275	-0.118378	0.0580551	-0.175439	-0.185584	-0.221075	-0.207141	-0.208959
0.325	-0.180835	0.0830347	-0.0601246	-0.133664	-0.200957	-0.177336	-0.187617
0.375	0.161232	0.124034	-0.0566204	-0.153511	-0.214864	-0.170229	-0.183738
0.425	0.0983915	0.209572	-0.0545549	-0.201066	-0.221339	-0.0967386	-0.109063
0.475	0.829772	0.302328	0.147309	-0.154994	-0.0797603	0.1762	0.177394

Beam-Vector Asymmetries Versus Missing Momentum for 2005 Data for Various Subnuclear Effects							
Perpendicular Kinematics–$0.4 < Q^2 < 0.5(GeV/c)^2$							
P_m (bin center)	Reconstructed	Total Error	PWBA	PWBA+FSI	PWBA+FSI+MEC	PWBA+FSI+MEC+IC	TOTAL
0.025	-0.326523	0.0161911	-0.323053	-0.321063	-0.320601	-0.320536	-0.319621
0.075	-0.30323	0.01334	-0.318264	-0.314956	-0.314228	-0.314133	-0.312523
0.125	-0.282034	0.021144	-0.332302	-0.327042	-0.325669	-0.325253	-0.321782
0.175	-0.24622	0.0352711	-0.377239	-0.371562	-0.369098	-0.36729	-0.360837
0.225	-0.1639	0.0599046	-0.347791	-0.335844	-0.330624	-0.324479	-0.311221
0.275	0.162147	0.097032	-0.165854	-0.155454	-0.146976	-0.143503	-0.132355
0.325	-0.0469026	0.144769	-0.0459066	-0.101891	-0.0766278	-0.0676538	-0.0557143
0.375	-4.83615e-07	0.184396	0.0448436	-0.108393	-0.063455	-0.0410908	-0.029363
0.425	-0.264681	0.265044	0.0693491	-0.0882191	-0.0399244	-0.006012	0.00267175
0.475	0.158808	0.460566	0.0669504	-0.0326553	0.00727698	0.0468698	0.0538504

Beam-Vector Asymmetries Versus Missing Momentum for 2005 Data for Various Subnuclear Effects							
Parallel Kinematics–$0.4(GeV/c)^2 < Q^2 < 0.5(GeV/c)^2$							
P_m (bin center)	Reconstructed	Total Error	PWBA	PWBA+FSI	PWBA+FSI+MEC	PWBA+FSI+MEC+IC	TOTAL
0.025	-0.38402	0.0232518	-0.371289	-0.377246	-0.378387	-0.378981	-0.378142
0.075	-0.385598	0.0178364	-0.368954	-0.377247	-0.379057	-0.379955	-0.378698
0.125	-0.334706	0.0257077	-0.369146	-0.380556	-0.383524	-0.384786	-0.382598
0.175	-0.320081	0.0408803	-0.369817	-0.382161	-0.385785	-0.386191	-0.382604
0.225	-0.0711064	0.0643636	-0.334978	-0.343727	-0.350913	-0.346347	-0.339635
0.275	-0.36858	0.090611	-0.181021	-0.180467	-0.205776	-0.187157	-0.19054
0.325	-0.271091	0.125031	-0.0401832	-0.0844998	-0.123424	-0.0820296	-0.0997186
0.375	-0.0935619	0.176987	0.0303118	-0.0943404	-0.15565	-0.0819418	-0.107595
0.425	-0.167631	0.273162	-0.100518	-0.180676	-0.224369	-0.121423	-0.144745
0.475	0.603471	0.389551	-0.301035	-0.304534	-0.366369	-0.292899	-0.319362

Beam-Vector Asymmetries Versus Missing Momentum for 2005 Data for Various Subnuclear Effects							
Perpendicular Kinematics–$0.1 < Q^2 < 0.5(GeV/c)^2$							
P_m (bin center)	Reconstructed	Total Error	PWBA	PWBA+FSI	PWBA+FSI+MEC	PWBA+FSI+MEC+IC	TOTAL
0.025	-0.150087	0.00533015	-0.130769	-0.131682	-0.131325	-0.131087	-0.130139
0.075	-0.14829	0.00281253	-0.134871	-0.135767	-0.13503	-0.134603	-0.133484
0.125	-0.132016	0.00465635	-0.145485	-0.14402	-0.141492	-0.140262	-0.138224
0.175	-0.144168	0.00845194	-0.15534	-0.138249	-0.130015	-0.127079	-0.123447
0.225	-0.07318	0.0142631	-0.144747	-0.108956	-0.0933326	-0.0904828	-0.0861769
0.275	-0.0552339	0.0227535	-0.0950529	-0.0874524	-0.0697264	-0.0635118	-0.0597934
0.325	0.0713796	0.0343635	-0.0216918	-0.0582687	-0.0369408	-0.00309316	0.00210832
0.375	0.250743	0.0529135	0.0337082	-0.0209579	0.0118296	0.110474	0.116564
0.425	0.231406	0.0776976	0.0440764	-0.00115004	0.046938	0.19368	0.198205
0.475	0.325948	0.110836	0.0169943	-0.00464885	0.0594898	0.233189	0.233448

Beam-Vector Asymmetries Versus Missing Momentum for 2005 Data for Various Subnuclear Effects							
Parallel Kinematics–$0.1(GeV/c)^2 < Q^2 < 0.5(GeV/c)^2$							
P_m (bin center)	Reconstructed	Total Error	PWBA	PWBA+FSI	PWBA+FSI+MEC	PWBA+FSI+MEC+IC	TOTAL
0.025	-0.188021	0.00302423	-0.156677	-0.161258	-0.162308	-0.163022	-0.161735
0.075	-0.201874	0.0026383	-0.159312	-0.166435	-0.16817	-0.169364	-0.167781
0.125	-0.212623	0.00468672	-0.164533	-0.178148	-0.182036	-0.184472	-0.181637
0.175	-0.190194	0.00875465	-0.166006	-0.182178	-0.19072	-0.193393	-0.189023
0.225	-0.154109	0.0143932	-0.148623	-0.152406	-0.168608	-0.168488	-0.164899
0.275	-0.131098	0.0217398	-0.101763	-0.101906	-0.120794	-0.110432	-0.110228
0.325	-0.0736337	0.0327472	-0.0470575	-0.0762586	-0.0906072	-0.0549684	-0.056544
0.375	0.146207	0.0494246	0.0326295	-0.0373191	-0.0379571	0.0351443	0.0349374
0.425	0.230005	0.0720147	0.0959225	-0.0169073	0.00614632	0.12598	0.127776
0.475	0.29997	0.108036	0.127812	-0.0303076	0.00517869	0.155262	0.153784

AV_{ed} vs P_m for 2004 data

Beam-Vector Asymmetries Versus Missing Momentum for 2004 Data for Different Potentials						
Perpendicular Kinematics–$0.1 < Q^2 < 0.5(GeV/c)^2$						
P_m (bin center)	Reconstructed Value	Total Error	Bonn	v18	v14	Paris
0.025	-0.158488	0.00201592	-0.158999	-0.159047	-0.159008	-0.158973
0.075	-0.163361	0.00174928	-0.161809	-0.161913	-0.161852	-0.161771
0.125	-0.162138	0.00328162	-0.162858	-0.163308	-0.162969	-0.162971
0.175	-0.138728	0.00648975	-0.133731	-0.135341	-0.134452	-0.135182
0.225	-0.104915	0.0108025	-0.099842	-0.101717	-0.0986932	-0.101661
0.275	-0.0891098	0.017997	-0.0835221	-0.0824871	-0.0730803	-0.0812663
0.325	-0.0250675	0.0297341	0.0264847	0.0347586	0.0542762	0.0312427
0.375	0.0201254	0.0595758	0.177708	0.199464	0.220146	0.182594
0.425	0.503494	0.155199	0.271651	0.300339	0.31299	0.272589
0.475	0.198436	0.415605	0.30468	0.338258	0.343853	0.302607

Beam-Vector Asymmetries Versus Missing Momentum for 2004 Data for Different Potentials						
Parallel Kinematics–$0.1(GeV/c)^2 < Q^2 < 0.5(GeV/c)^2$						
P_m (bin center)	Reconstructed Value	Total Error	Bonn	v18	v14	Paris
0.025	-0.173044	0.00186622	-0.178862	-0.179048	-0.179036	-0.179175
0.075	-0.182216	0.0017094	-0.183302	-0.183444	-0.183405	-0.183614
0.125	-0.182934	0.00327056	-0.191432	-0.19115	-0.190661	-0.191249
0.175	-0.162129	0.00641911	-0.184704	-0.183581	-0.181271	-0.182881
0.225	-0.144068	0.0105185	-0.148364	-0.145742	-0.13931	-0.142974
0.275	-0.0705547	0.0176224	-0.067347	-0.0657947	-0.0548573	-0.063256
0.325	-0.0412407	0.0290742	0.0206496	0.0223458	0.0357534	0.0219771
0.375	0.0429051	0.0561355	0.122624	0.13117	0.144544	0.125386
0.425	0.347773	0.131763	0.216277	0.233462	0.243257	0.220224
0.475	0.721574	0.363751	0.254525	0.278528	0.28476	0.26069

Beam-Vector Asymmetries Versus Missing Momentum for 2004 Data for Different Potentials						
Perpendicular Kinematics–$0.1 < Q^2 < 0.5(GeV/c)^2$						
P_m (bin center)	Reconstructed Value	Total Error	Bonn	v18	v14	Paris
0.025	-0.230594	0.00318392	-0.245245	-0.245323	-0.245371	-0.245329
0.075	-0.224224	0.00266545	-0.244842	-0.245087	-0.245056	-0.245019
0.125	-0.21123	0.00446199	-0.242368	-0.243247	-0.242666	-0.242807
0.175	-0.185944	0.00844326	-0.235459	-0.237549	-0.235986	-0.236795
0.225	-0.157492	0.0145912	-0.15604	-0.159587	-0.157158	-0.159893
0.275	-0.0531997	0.0216505	-0.0840724	-0.0865582	-0.082878	-0.0878089
0.325	0.0149201	0.0433542	-0.0484567	-0.0456226	-0.0371936	-0.0476799
0.375	0.0690212	0.123266	0.0920345	0.108562	0.126986	0.0961973
0.425	1.77413e-07	0.661442	0.221003	0.247608	0.26015	0.218482
0.475	0	1.32288	0.253179	0.276896	0.274685	0.240967

Beam-Vector Asymmetries Versus Missing Momentum for 2004 Data for Different Potentials						
Parallel Kinematics–$0.1(GeV/c)^2 < Q^2 < 0.5(GeV/c)^2$						
P_m (bin center)	Reconstructed Value	Total Error	Bonn	v18	v14	Paris
0.025	-0.260704	0.00305357	-0.278236	-0.27791	-0.278077	-0.278129
0.075	-0.260619	0.00250011	-0.279891	-0.279505	-0.279627	-0.279755
0.125	-0.25427	0.00411862	-0.281164	-0.280862	-0.280347	-0.280825
0.175	-0.218412	0.00784457	-0.279031	-0.278155	-0.275743	-0.277214
0.225	-0.187268	0.0136794	-0.239094	-0.234051	-0.227519	-0.230755
0.275	-0.188719	0.0201732	-0.193032	-0.181521	-0.170094	-0.174822
0.325	-0.198245	0.0407239	-0.128856	-0.116155	-0.101708	-0.110391
0.375	-0.108519	0.116696	0.0814086	0.0937881	0.107371	0.088234
0.425	0.529162	0.326669	0.218033	0.233676	0.238948	0.213985
0.475	1.19061	0.416656	0.260801	0.278525	0.273452	0.25219

Beam-Vector Asymmetries Versus Missing Momentum for 2004 Data for Different Potentials						
Perpendicular Kinematics–$0.1 < Q^2 < 0.5 (GeV/c)^2$						
P_m (bin center)	Reconstructed Value	Total Error	Bonn	v18	v14	Paris
0.025	-0.294542	0.00535702	-0.332066	-0.332074	-0.332167	-0.332168
0.075	-0.297687	0.00403732	-0.333647	-0.333766	-0.333764	-0.33381
0.125	-0.276674	0.00619535	-0.337353	-0.338102	-0.337574	-0.33782
0.175	-0.247685	0.0108632	-0.314798	-0.317202	-0.314265	-0.31575
0.225	-0.154309	0.0196661	-0.290757	-0.294816	-0.288885	-0.292587
0.275	-0.0555908	0.0326296	-0.16314	-0.167275	-0.158354	-0.165746
0.325	-0.0842867	0.046034	-0.0882332	-0.0898752	-0.0826744	-0.0901741
0.375	-0.0298397	0.0810997	-0.0558162	-0.0529956	-0.0452055	-0.0551399
0.425	-0.10903	0.138415	0.0132889	0.0245523	0.0291458	0.0136828
0.475	1.72037e-07	0.398865	0.161231	0.170737	0.161615	0.139677

Beam-Vector Asymmetries Versus Missing Momentum for 2004 Data for Different Potentials						
Parallel Kinematics–$0.1 (GeV/c)^2 < Q^2 < 0.5 (GeV/c)^2$						
P_m (bin center)	Reconstructed Value	Total Error	Bonn	v18	v14	Paris
0.025	-0.338451	0.00516508	-0.371408	-0.370881	-0.371079	-0.371224
0.075	-0.345521	0.00406154	-0.375232	-0.37452	-0.374732	-0.374928
0.125	-0.321622	0.00643135	-0.376574	-0.37621	-0.375911	-0.376372
0.175	-0.291515	0.0112757	-0.359155	-0.359231	-0.35612	-0.35786
0.225	-0.189562	0.0197586	-0.323136	-0.319719	-0.311186	-0.315804
0.275	-0.152642	0.0330883	-0.236496	-0.221154	-0.205129	-0.212732
0.325	-0.245612	0.0458334	-0.193507	-0.169278	-0.149968	-0.156881
0.375	-0.203524	0.0743716	-0.183019	-0.158606	-0.142285	-0.15059
0.425	-0.145908	0.15988	-0.0862676	-0.0647686	-0.0593682	-0.0720365
0.475	-0.700354	0.293847	0.214741	0.217866	0.19712	0.187027

Beam-Vector Asymmetries Versus Missing Momentum for 2004 Data for Different Potentials						
Perpendicular Kinematics–$0.1 < Q^2 < 0.5 (GeV/c)^2$						
P_m (bin center)	Reconstructed Value	Total Error	Bonn	v18	v14	Paris
0.025	-0.349959	0.00782307	-0.423802	-0.42392	-0.424078	-0.424095
0.075	-0.337391	0.00634981	-0.41696	-0.417271	-0.417328	-0.417425
0.125	-0.314151	0.0100621	-0.427336	-0.42804	-0.427581	-0.427984
0.175	-0.28667	0.0169006	-0.465657	-0.466842	-0.465571	-0.46629
0.225	-0.179208	0.0285306	-0.40289	-0.405991	-0.400317	-0.403241
0.275	-0.0739668	0.0473843	-0.182401	-0.185472	-0.166203	-0.178661
0.325	-0.0461476	0.0608051	-0.0850268	-0.088681	-0.0695276	-0.0825533
0.375	-0.186499	0.0806696	-0.0568723	-0.0584244	-0.0451755	-0.0564546
0.425	0.0218063	0.138665	-0.0403256	-0.034116	-0.0285659	-0.0404021
0.475	0.152643	0.211074	-0.0180099	-0.00859205	-0.0122393	-0.0219877

Beam-Vector Asymmetries Versus Missing Momentum for 2004 Data for Different Potentials						
Parallel Kinematics–$0.1 (GeV/c)^2 < Q^2 < 0.5 (GeV/c)^2$						
P_m (bin center)	Reconstructed Value	Total Error	Bonn	v18	v14	Paris
0.025	-0.406079	0.00859522	-0.464653	-0.464267	-0.464471	-0.464692
0.075	-0.409829	0.00679605	-0.46339	-0.462946	-0.463155	-0.46348
0.125	-0.375465	0.0109056	-0.469325	-0.468843	-0.468341	-0.469145
0.175	-0.322066	0.0191183	-0.479695	-0.47895	-0.476946	-0.478512
0.225	-0.197772	0.0310085	-0.422652	-0.420944	-0.413831	-0.417877
0.275	-0.124187	0.048146	-0.227056	-0.212189	-0.190278	-0.202715
0.325	-0.155028	0.0672297	-0.117651	-0.0864362	-0.0622167	-0.0737041
0.375	0.0586509	0.092793	-0.117932	-0.0822188	-0.0628033	-0.0711915
0.425	0.034213	0.17367	-0.138752	-0.113277	-0.10625	-0.113096
0.475	0.28348	0.220787	-0.30253	-0.286399	-0.283737	-0.288508

Beam-Vector Asymmetries Versus Missing Momentum for 2004 Data for Different Potentials						
Perpendicular Kinematics–$3.36312e-44 < Q^2 < 3.36312e-44 (GeV/c)^2$						
P_m (bin center)	Reconstructed Value	Total Error	Bonn	v18	v14	Paris
0.025	-0.195705	0.00285244	-0.17479	-0.174879	-0.174855	-0.174808
0.075	-0.201156	0.00131068	-0.179961	-0.18012	-0.18004	-0.179973
0.125	-0.202141	0.00225827	-0.189187	-0.189708	-0.189323	-0.189351
0.175	-0.180727	0.00424652	-0.175901	-0.177688	-0.17675	-0.177416
0.225	-0.134724	0.00728524	-0.131284	-0.133776	-0.13092	-0.133785
0.275	-0.0692682	0.011668	-0.090136	-0.090668	-0.0831767	-0.0902091
0.325	-0.0425247	0.019264	-0.0140719	-0.00843868	0.00629401	-0.0105141
0.375	-0.0332994	0.0365294	0.127338	0.146307	0.16482	0.132736
0.425	0.109105	0.0774003	0.230409	0.257544	0.268744	0.231449
0.475	0.0275607	0.155884	0.279744	0.310445	0.313514	0.275466

Beam-Vector Asymmetries Versus Missing Momentum for 2004 Data for Different Potentials						
Parallel Kinematics–$3.36312e-44 (GeV/c)^2 < Q^2 < 3.36312e-44 (GeV/c)^2$						
P_m (bin center)	Reconstructed Value	Total Error	Bonn	v18	v14	Paris
0.025	-0.214278	0.00148446	-0.197044	-0.197189	-0.19719	-0.19732
0.075	-0.229384	0.0012727	-0.203793	-0.203875	-0.203822	-0.204034
0.125	-0.233862	0.00221358	-0.218459	-0.21815	-0.217654	-0.218212
0.175	-0.212706	0.00417821	-0.221958	-0.220942	-0.218754	-0.220252
0.225	-0.169765	0.00706936	-0.187953	-0.184642	-0.178247	-0.18176
0.275	-0.12714	0.0113269	-0.126265	-0.119375	-0.107228	-0.114389
0.325	-0.122331	0.0188198	-0.0563484	-0.0470597	-0.0320599	-0.0431433
0.375	-0.0817845	0.0355317	0.0643196	0.078088	0.092272	0.0751121
0.425	0.0701185	0.0785756	0.183337	0.201673	0.209948	0.18803
0.475	0.0225495	0.141007	0.216639	0.240074	0.242665	0.220919

Beam-Vector Asymmetries Versus Missing Momentum for 2004 Data for Various Subnuclear Effects							
Perpendicular Kinematics–$0.1 < Q^2 < 0.2 (GeV/c)^2$							
P_m (bin center)	Reconstructed	Total Error	PWBA	PWBA+FSI	PWBA+FSI+MEC	PWBA+FSI+MEC+IC	TOTAL
0.025	-0.158488	0.00201592	-0.157704	-0.159504	-0.159449	-0.159414	-0.158999
0.075	-0.163361	0.00174928	-0.16064	-0.162913	-0.162674	-0.162594	-0.161809
0.125	-0.162138	0.00328162	-0.165896	-0.166272	-0.164832	-0.164335	-0.162858
0.175	-0.138728	0.00648975	-0.163563	-0.143611	-0.137544	-0.136197	-0.133731
0.225	-0.104915	0.0108025	-0.146294	-0.112761	-0.103228	-0.102772	-0.099842
0.275	-0.0891098	0.017997	-0.110406	-0.104586	-0.0962781	-0.0858313	-0.0835221
0.325	-0.0250675	0.0297341	-0.0394491	-0.0574498	-0.0392462	0.0196913	0.0264847
0.375	0.0201254	0.0595758	0.0442041	0.00460574	0.0404888	0.169027	0.177708
0.425	0.503494	0.155199	0.0740001	0.0299977	0.0838141	0.265123	0.271651
0.475	0.198436	0.415605	0.0683063	0.026146	0.100254	0.304085	0.30468

Beam-Vector Asymmetries Versus Missing Momentum for 2004 Data for Various Subnuclear Effects							
Parallel Kinematics–$0.1 (GeV/c)^2 < Q^2 < 0.2 (GeV/c)^2$							
P_m (bin center)	Reconstructed	Total Error	PWBA	PWBA+FSI	PWBA+FSI+MEC	PWBA+FSI+MEC+IC	TOTAL
0.025	-0.173044	0.00186622	-0.173831	-0.177938	-0.178842	-0.179407	-0.178862
0.075	-0.182216	0.0017094	-0.1757	-0.181893	-0.183328	-0.184283	-0.183302
0.125	-0.182934	0.00327056	-0.177647	-0.188396	-0.191523	-0.193594	-0.191432
0.175	-0.162129	0.00641911	-0.171944	-0.178718	-0.185688	-0.188396	-0.184704
0.225	-0.144068	0.0105185	-0.149414	-0.140359	-0.151265	-0.151891	-0.148364
0.275	-0.0705547	0.0176224	-0.108967	-0.0856397	-0.0832736	-0.0706377	-0.067347
0.325	-0.0412407	0.0290742	-0.0411294	-0.0434919	-0.0281559	0.0148901	0.0206496
0.375	0.0429051	0.0561355	0.0479312	0.00440348	0.0300184	0.115289	0.122624
0.425	0.347773	0.131763	0.116775	0.0347619	0.0726837	0.210199	0.216277
0.475	0.721574	0.363751	0.159222	0.0414109	0.092921	0.252274	0.254525

Beam-Vector Asymmetries Versus Missing Momentum for 2004 Data for Various Subnuclear Effects							
Perpendicular Kinematics–$0.2 < Q^2 < 0.3 (GeV/c)^2$							
P_m (bin center)	Reconstructed	Total Error	PWBA	PWBA+FSI	PWBA+FSI+MEC	PWBA+FSI+MEC+IC	TOTAL
0.025	-0.230594	0.00318392	-0.245831	-0.246123	-0.246023	-0.246107	-0.245245
0.075	-0.224224	0.00266545	-0.246354	-0.246504	-0.246299	-0.246357	-0.244842
0.125	-0.21123	0.00446199	-0.248412	-0.246557	-0.245688	-0.245452	-0.242368
0.175	-0.185944	0.00844326	-0.256361	-0.246447	-0.24259	-0.240671	-0.235459
0.225	-0.157492	0.0145912	-0.222528	-0.180054	-0.167087	-0.162175	-0.15604
0.275	-0.0531997	0.0216505	-0.122399	-0.112901	-0.0953384	-0.0884859	-0.0840724
0.325	0.0149201	0.0433542	-0.0162843	-0.0906005	-0.0757303	-0.0513501	-0.0484567
0.375	0.0690212	0.123266	0.0256839	-0.0546377	-0.0215671	0.085615	0.0920345
0.425	1.77413e-07	0.661442	0.0608427	-0.0383212	0.0284994	0.213958	0.221003
0.475	0	1.32288	0.0181619	-0.0759821	0.0128067	0.25163	0.253179

Beam-Vector Asymmetries Versus Missing Momentum for 2004 Data for Various Subnuclear Effects							
Parallel Kinematics–$0.2 (GeV/c)^2 < Q^2 < 0.3 (GeV/c)^2$							
P_m (bin center)	Reconstructed	Total Error	PWBA	PWBA+FSI	PWBA+FSI+MEC	PWBA+FSI+MEC+IC	TOTAL
0.025	-0.260704	0.00305357	-0.273204	-0.277064	-0.278131	-0.279296	-0.278236
0.075	-0.260619	0.00250011	-0.272358	-0.278092	-0.279823	-0.281504	-0.279891
0.125	-0.25427	0.00411862	-0.269087	-0.278186	-0.281701	-0.284167	-0.281164
0.175	-0.218412	0.00784457	-0.265912	-0.275913	-0.281921	-0.283825	-0.279031
0.225	-0.187268	0.0136794	-0.232867	-0.228417	-0.244027	-0.243301	-0.239094
0.275	-0.188719	0.0201732	-0.155605	-0.167339	-0.199737	-0.19291	-0.193032
0.325	-0.198245	0.0407239	-0.093279	-0.13602	-0.157975	-0.125905	-0.128856
0.375	-0.108519	0.116696	0.0408519	-0.0506011	-0.0300899	0.0774456	0.0814086
0.425	0.529162	0.326669	0.137349	-0.0406471	0.0246612	0.211123	0.218033
0.475	1.19061	0.416656	0.171813	-0.0749812	0.0192023	0.258029	0.260801

Beam-Vector Asymmetries Versus Missing Momentum for 2004 Data for Various Subnuclear Effects							
Perpendicular Kinematics–$0.3 < Q^2 < 0.4 (GeV/c)^2$							
P_m (bin center)	Reconstructed	Total Error	PWBA	PWBA+FSI	PWBA+FSI+MEC	PWBA+FSI+MEC+IC	TOTAL
0.025	-0.294542	0.00535702	-0.332937	-0.332636	-0.332526	-0.332746	-0.332066
0.075	-0.297687	0.00403732	-0.335703	-0.33502	-0.334826	-0.335121	-0.333647
0.125	-0.276674	0.00619535	-0.34357	-0.341395	-0.340918	-0.341001	-0.337353
0.175	-0.247685	0.0108632	-0.333436	-0.324649	-0.32269	-0.321289	-0.314798
0.225	-0.154309	0.0196661	-0.337928	-0.317398	-0.308874	-0.300999	-0.290757
0.275	-0.0555908	0.0326296	-0.234539	-0.202746	-0.185092	-0.173679	-0.16314
0.325	-0.0842867	0.046034	-0.0311209	-0.130088	-0.10818	-0.0934566	-0.0882332
0.375	-0.0298397	0.0810997	0.0714051	-0.107955	-0.0868742	-0.0586684	-0.0558162
0.425	-0.10903	0.138415	0.0632277	-0.0935443	-0.0649503	0.0131477	0.0132889
0.475	1.72037e-07	0.398865	-0.0414245	-0.15831	-0.0843085	0.155523	0.161231

Beam-Vector Asymmetries Versus Missing Momentum for 2004 Data for Various Subnuclear Effects							
Parallel Kinematics–$0.3 (GeV/c)^2 < Q^2 < 0.4 (GeV/c)^2$							
P_m (bin center)	Reconstructed	Total Error	PWBA	PWBA+FSI	PWBA+FSI+MEC	PWBA+FSI+MEC+IC	TOTAL
0.025	-0.338451	0.00516508	-0.365394	-0.369981	-0.37108	-0.372185	-0.371408
0.075	-0.345521	0.00406154	-0.366804	-0.373275	-0.375024	-0.376662	-0.375232
0.125	-0.321622	0.00643135	-0.364755	-0.374156	-0.377519	-0.379567	-0.376574
0.175	-0.291515	0.0112757	-0.346611	-0.356858	-0.363536	-0.364506	-0.359155
0.225	-0.189562	0.0197586	-0.323496	-0.326519	-0.336093	-0.329906	-0.323136
0.275	-0.152642	0.0330883	-0.225794	-0.226275	-0.25372	-0.237886	-0.236496
0.325	-0.245612	0.0458334	-0.062918	-0.156429	-0.211567	-0.185655	-0.193507
0.375	-0.203524	0.0743716	-0.0318354	-0.172875	-0.221302	-0.171504	-0.183019
0.425	-0.145908	0.15988	-0.0335919	-0.205909	-0.21534	-0.0753321	-0.0862676
0.475	-0.700354	0.293847	0.122854	-0.179618	-0.0895654	0.21282	0.214741

Beam-Vector Asymmetries Versus Missing Momentum for 2004 Data for Various Subnuclear Effects							
Perpendicular Kinematics–$0.4 < Q^2 < 0.5(GeV/c)^2$							
P_m (bin center)	Reconstructed	Total Error	PWBA	PWBA+FSI	PWBA+FSI+MEC	PWBA+FSI+MEC+IC	TOTAL
0.025	-0.349959	0.00782307	-0.425234	-0.424953	-0.424818	-0.424921	-0.423802
0.075	-0.337391	0.00634981	-0.419814	-0.418939	-0.418742	-0.418915	-0.41696
0.125	-0.314151	0.0100621	-0.43389	-0.431985	-0.431475	-0.431419	-0.427336
0.175	-0.28667	0.0169006	-0.478335	-0.476216	-0.47476	-0.473067	-0.465657
0.225	-0.179208	0.0285306	-0.438597	-0.429134	-0.425633	-0.418044	-0.40289
0.275	-0.0739668	0.0473843	-0.213741	-0.202896	-0.201279	-0.192194	-0.182401
0.325	-0.0461476	0.0608051	-0.0551256	-0.124408	-0.112592	-0.0916431	-0.0850268
0.375	-0.186499	0.0806696	0.0570704	-0.132526	-0.104096	-0.0613721	-0.0568723
0.425	0.0218063	0.138665	0.0464782	-0.133505	-0.101868	-0.041921	-0.0403256
0.475	0.152643	0.211074	-0.00775276	-0.117641	-0.0898708	-0.017582	-0.0180099

Beam-Vector Asymmetries Versus Missing Momentum for 2004 Data for Various Subnuclear Effects							
Parallel Kinematics–$0.4(GeV/c)^2 < Q^2 < 0.5(GeV/c)^2$							
P_m (bin center)	Reconstructed	Total Error	PWBA	PWBA+FSI	PWBA+FSI+MEC	PWBA+FSI+MEC+IC	TOTAL
0.025	-0.406079	0.00859522	-0.458885	-0.464211	-0.465216	-0.465785	-0.464653
0.075	-0.409829	0.00679605	-0.45535	-0.462642	-0.464225	-0.465089	-0.46339
0.125	-0.375465	0.0109056	-0.458881	-0.4687	-0.471251	-0.472385	-0.469325
0.175	-0.322066	0.0191183	-0.471733	-0.482285	-0.485169	-0.485065	-0.479695
0.225	-0.197772	0.0310085	-0.428465	-0.433536	-0.43891	-0.432716	-0.422652
0.275	-0.124187	0.048146	-0.228649	-0.224367	-0.24667	-0.227044	-0.227056
0.325	-0.155028	0.0672297	-0.0524427	-0.113419	-0.14636	-0.103132	-0.117651
0.375	0.0586509	0.092793	0.0408914	-0.127724	-0.174651	-0.0956745	-0.117932
0.425	0.034213	0.17367	-0.0766627	-0.198822	-0.229872	-0.118432	-0.138752
0.475	0.28348	0.220787	-0.263659	-0.301675	-0.354065	-0.278558	-0.30253

Beam-Vector Asymmetries Versus Missing Momentum for 2004 Data for Various Subnuclear Effects							
Perpendicular Kinematics–$0.1 < Q^2 < 0.5(GeV/c)^2$							
P_m (bin center)	Reconstructed	Total Error	PWBA	PWBA+FSI	PWBA+FSI+MEC	PWBA+FSI+MEC+IC	TOTAL
0.025	-0.195705	0.00285244	-0.173917	-0.176137	-0.176067	-0.176036	-0.17479
0.075	-0.201156	0.00131068	-0.178956	-0.181887	-0.181661	-0.181593	-0.179961
0.125	-0.202141	0.00225827	-0.191091	-0.193834	-0.192542	-0.192056	-0.189187
0.175	-0.180727	0.00424652	-0.200992	-0.188546	-0.182961	-0.180792	-0.175901
0.225	-0.134724	0.00728524	-0.184975	-0.15014	-0.139424	-0.136498	-0.131284
0.275	-0.0692682	0.011668	-0.121964	-0.115151	-0.103086	-0.0937979	-0.090136
0.325	-0.0425247	0.019264	-0.0342765	-0.0798411	-0.0628615	-0.0187067	-0.0140719
0.375	-0.0332994	0.0365294	0.0434789	-0.0301271	0.00289367	0.121329	0.127338
0.425	0.109105	0.0774003	0.0708639	-0.0068533	0.0458861	0.225764	0.230409
0.475	0.0275607	0.155884	0.055831	-0.00755962	0.0670342	0.279362	0.279744

Beam-Vector Asymmetries Versus Missing Momentum for 2004 Data for Various Subnuclear Effects							
Parallel Kinematics–$0.1(GeV/c)^2 < Q^2 < 0.5(GeV/c)^2$							
P_m (bin center)	Reconstructed	Total Error	PWBA	PWBA+FSI	PWBA+FSI+MEC	PWBA+FSI+MEC+IC	TOTAL
0.025	-0.214278	0.00148446	-0.192106	-0.196924	-0.197859	-0.1985	-0.197044
0.075	-0.229384	0.0012727	-0.195738	-0.203076	-0.204577	-0.20563	-0.203793
0.125	-0.233862	0.00221358	-0.203328	-0.216485	-0.219681	-0.221761	-0.218459
0.175	-0.212706	0.00417821	-0.207358	-0.219051	-0.225362	-0.227228	-0.221958
0.225	-0.169765	0.00706936	-0.187757	-0.181912	-0.193644	-0.1927	-0.187953
0.275	-0.12714	0.0113269	-0.12821	-0.125723	-0.139509	-0.127523	-0.126265
0.325	-0.122331	0.0188198	-0.0535173	-0.092193	-0.100613	-0.0561638	-0.0563484
0.375	-0.0817845	0.0355317	0.0412723	-0.0444526	-0.0358106	0.0628856	0.0643196
0.425	0.0701185	0.0785756	0.10716	-0.0157319	0.0203749	0.180306	0.183337
0.475	0.0225495	0.141007	0.132508	-0.0303367	0.0222539	0.218144	0.216639

A.1.3 AT_d vs P_m

AT_d vs P_m for 2005 data

Tensor Asymmetries Versus Missing Momentum for 2005 Data for Different Potentials						
Perpendicular Kinematics–$0.1 < Q^2 < 0.2 (GeV/c)^2$						
P_m (bin center)	Reconstructed Value	Total Error	Bonn	v18	v14	Paris
0.025	-0.0235934	0.0054215	-0.00822555	-0.00794611	-0.0083273	-0.0083182
0.075	-0.0277978	0.0046998	-0.0140159	-0.0135319	-0.0142147	-0.0141022
0.125	-0.051119	0.00853473	-0.0375247	-0.0366009	-0.0388529	-0.0381463
0.175	-0.00160636	0.0165344	-0.0411308	-0.0421194	-0.047663	-0.0465394
0.225	0.0651723	0.0279451	-0.000447572	-0.00887447	-0.0117723	-0.0141857
0.275	0.0464687	0.0470852	-0.0525291	-0.0700305	-0.0630815	-0.071021
0.325	0.0589391	0.0702299	-0.142334	-0.157916	-0.152464	-0.162317
0.375	0.13718	0.100683	-0.125611	-0.142963	-0.135712	-0.157346
0.425	0.0960707	0.152792	-0.195602	-0.214392	-0.205479	-0.234583
0.475	-0.018365	0.216515	-0.185633	-0.211081	-0.202922	-0.232632

Tensor Asymmetries Versus Missing Momentum for 2005 Data for Different Potentials						
Parallel Kinematics–$0.1 (GeV/c)^2 < Q^2 < 0.2 (GeV/c)^2$						
P_m (bin center)	Reconstructed Value	Total Error	Bonn	v18	v14	Paris
0.025	0.010784	0.00475395	0.0198055	0.0202398	0.0204064	0.0207592
0.075	0.0193363	0.00439006	0.0332857	0.0336838	0.0342536	0.0345332
0.125	0.0212316	0.00843066	0.0612256	0.0615669	0.0627269	0.062672
0.175	-0.0556894	0.0168285	0.0655257	0.0653309	0.0646599	0.0641493
0.225	-0.173517	0.0277289	-0.0277177	-0.026503	-0.036773	-0.0351651
0.275	-0.319701	0.0459255	-0.203825	-0.182646	-0.199352	-0.194592
0.325	-0.395453	0.0709486	-0.25928	-0.223325	-0.227819	-0.231264
0.375	-0.166403	0.096727	-0.327812	-0.274575	-0.273693	-0.280095
0.425	-0.193923	0.134401	-0.277142	-0.216324	-0.216696	-0.217989
0.475	-0.0737782	0.194095	-0.272599	-0.207414	-0.208355	-0.205926

Tensor Asymmetries Versus Missing Momentum for 2005 Data for Different Potentials						
Perpendicular Kinematics–$0.2 < Q^2 < 0.3 (GeV/c)^2$						
P_m (bin center)	Reconstructed Value	Total Error	Bonn	v18	v14	Paris
0.025	-0.0272908	0.00945964	-0.00994606	-0.00979787	-0.0103389	-0.010352
0.075	-0.0448675	0.00776411	-0.0170504	-0.0168501	-0.0178365	-0.0177394
0.125	-0.0418985	0.0128078	-0.0335712	-0.0335486	-0.0358461	-0.0350987
0.175	-0.0656681	0.0231991	-0.0477194	-0.0490934	-0.0535758	-0.0517891
0.225	0.0096459	0.0398563	-0.0223575	-0.0292905	-0.0380237	-0.0369863
0.275	0.110719	0.0592331	0.0712247	0.0562284	0.0525404	0.0475528
0.325	0.162655	0.0987375	0.0584734	0.0359549	0.0430612	0.0314757
0.375	-0.17605	0.193771	-0.22741	-0.258162	-0.244134	-0.260434
0.425	0.118732	0.275151	-0.366386	-0.395771	-0.381429	-0.405438
0.475	0.0344964	0.419653	-0.440369	-0.466014	-0.452435	-0.473023

Tensor Asymmetries Versus Missing Momentum for 2005 Data for Different Potentials						
Parallel Kinematics–$0.2 (GeV/c)^2 < Q^2 < 0.3 (GeV/c)^2$						
P_m (bin center)	Reconstructed Value	Total Error	Bonn	v18	v14	Paris
0.025	-0.00203453	0.00798291	0.0159644	0.016124	0.0161206	0.0163592
0.075	0.0138974	0.00673741	0.0278843	0.0278813	0.0281395	0.0283307
0.125	0.0271194	0.0115714	0.0481711	0.0477407	0.0483063	0.0482213
0.175	-0.00243107	0.0214404	0.0585814	0.0568075	0.0568499	0.0560536
0.225	-0.0819235	0.0362138	0.0361259	0.0274807	0.0210552	0.0216862
0.275	-0.129783	0.0505077	-0.0455	-0.063045	-0.085015	-0.0774998
0.325	-0.153974	0.0831113	-0.155326	-0.162711	-0.192359	-0.175892
0.375	-0.393068	0.152334	-0.143891	-0.111937	-0.129033	-0.114715
0.425	0.0102933	0.229237	-0.0479006	0.00873217	0.00719043	0.0145863
0.475	-0.144106	0.324423	-0.0509661	0.0138593	0.0131045	0.0237636

Tensor Asymmetries Versus Missing Momentum for 2005 Data for Different Potentials						
Perpendicular Kinematics–$0.3 < Q^2 < 0.4 (GeV/c)^2$						
P_m (bin center)	Reconstructed Value	Total Error	Bonn	v18	v14	Paris
0.025	-0.0312432	0.0203281	-0.00961035	-0.00963239	-0.0102221	-0.0101169
0.075	-0.0281404	0.0153718	-0.0176356	-0.0176509	-0.0187274	-0.0184922
0.125	-0.0430668	0.0227722	-0.0344269	-0.0347192	-0.0369734	-0.0362961
0.175	-0.126143	0.0375981	-0.0650812	-0.0669221	-0.0719606	-0.0699568
0.225	-0.0308299	0.0591414	-0.0666354	-0.0715738	-0.0789181	-0.0761306
0.275	0.0124373	0.0890888	-0.0165979	-0.0272401	-0.037742	-0.0374222
0.325	-0.0487161	0.128769	0.101235	0.0877048	0.0841827	0.0783469
0.375	-0.169055	0.207975	0.0934971	0.0819025	0.0848354	0.0773756
0.425	0.127637	0.30495	-0.071887	-0.0886567	-0.0809808	-0.0905371
0.475	-0.638183	0.464335	-0.476891	-0.492761	-0.472548	-0.489407

Tensor Asymmetries Versus Missing Momentum for 2005 Data for Different Potentials						
Parallel Kinematics–$0.3 (GeV/c)^2 < Q^2 < 0.4 (GeV/c)^2$						
P_m (bin center)	Reconstructed Value	Total Error	Bonn	v18	v14	Paris
0.025	-0.0163667	0.0144171	0.0137293	0.0135573	0.0135542	0.0134837
0.075	-0.0135404	0.0119019	0.0264353	0.025871	0.0262115	0.0259627
0.125	0.0422236	0.0189068	0.0451552	0.0438869	0.0444256	0.043896
0.175	0.0198449	0.0312114	0.0640581	0.0608067	0.0607548	0.0597477
0.225	-0.0516194	0.0498627	0.0306593	0.0224431	0.0182773	0.0181594
0.275	-0.113999	0.073777	-0.0286004	-0.0528668	-0.0675737	-0.0616767
0.325	-0.0808655	0.105644	-0.118609	-0.157288	-0.190082	-0.174778
0.375	-0.0389729	0.157707	-0.125437	-0.160038	-0.19294	-0.174792
0.425	0.152609	0.265907	-0.0314124	-0.0293793	-0.046826	-0.0324517
0.475	0.223364	0.40253	0.0865893	0.139392	0.136329	0.150993

Tensor Asymmetries Versus Missing Momentum for 2005 Data for Different Potentials						
Perpendicular Kinematics–$0.4 < Q^2 < 0.5 (GeV/c)^2$						
P_m (bin center)	Reconstructed Value	Total Error	Bonn	v18	v14	Paris
0.025	-0.0352864	0.0207106	-0.00940156	-0.00938231	-0.0100278	-0.00976638
0.075	-0.0363064	0.0170449	-0.0168913	-0.0168371	-0.0180028	-0.0175757
0.125	-0.0542283	0.0269927	-0.0277372	-0.0280534	-0.0299293	-0.0291703
0.175	-0.101776	0.0449754	-0.0349908	-0.0363022	-0.03851	-0.0373219
0.225	-0.114793	0.0762014	-0.0731163	-0.0769096	-0.0816825	-0.0796144
0.275	-0.307163	0.124245	-0.13002	-0.13969	-0.148857	-0.148153
0.325	-0.0330664	0.183747	-0.0542977	-0.0693993	-0.0774052	-0.078858
0.375	-0.042903	0.234007	0.0642768	0.0495169	0.0492836	0.0455772
0.425	-0.0671771	0.338134	0.0355776	0.0277598	0.0318003	0.0245755
0.475	-0.335886	0.590935	-0.0850304	-0.0899975	-0.0847853	-0.0957852

Tensor Asymmetries Versus Missing Momentum for 2005 Data for Different Potentials						
Parallel Kinematics–$0.4 (GeV/c)^2 < Q^2 < 0.5 (GeV/c)^2$						
P_m (bin center)	Reconstructed Value	Total Error	Bonn	v18	v14	Paris
0.025	0.0177783	0.0298298	0.014475	0.0137305	0.0137409	0.0134568
0.075	0.00902759	0.0228849	0.0262623	0.0249363	0.0252223	0.0247352
0.125	0.000847937	0.0328946	0.0365541	0.0344696	0.0346092	0.0338452
0.175	0.0240826	0.0522696	0.0364902	0.0338451	0.0332786	0.0321532
0.225	0.0248474	0.0817087	0.05532	0.049548	0.0475183	0.0465142
0.275	-0.00792747	0.116151	0.004503	-0.0135813	-0.0240861	-0.0193596
0.325	-0.0847585	0.159565	-0.091498	-0.120985	-0.141141	-0.125005
0.375	-0.178097	0.225055	-0.119164	-0.159301	-0.186518	-0.165483
0.425	-0.0709091	0.347404	-0.087694	-0.113889	-0.135974	-0.116669
0.475	-0.867929	0.585321	-0.0300622	-0.0627258	-0.0873855	-0.0718185

Tensor Asymmetries Versus Missing Momentum for 2005 Data for Different Potentials						
Perpendicular Kinematics–$0.1 < Q^2 < 0.5(GeV/c)^2$						
P_m (bin center)	Reconstructed Value	Total Error	Bonn	v18	v14	Paris
0.025	-0.0273344	0.00442558	-0.00853078	-0.00828347	-0.00867758	-0.00867158
0.075	-0.0320709	0.00357499	-0.0146554	-0.0142254	-0.0149562	-0.0148452
0.125	-0.045983	0.00591678	-0.0365068	-0.0358266	-0.0380968	-0.0373824
0.175	-0.0430818	0.0107424	-0.0437935	-0.044916	-0.0501063	-0.0487629
0.225	0.0147714	0.0181072	-0.0114686	-0.0192121	-0.0240478	-0.025114
0.275	0.0406831	0.0288806	-0.00611346	-0.0227776	-0.0215483	-0.0277201
0.325	0.0428687	0.0436234	-0.0448944	-0.0636889	-0.0595506	-0.0696606
0.375	0.0543704	0.0674538	-0.106225	-0.125958	-0.118726	-0.137362
0.425	0.00959686	0.0989883	-0.198586	-0.219016	-0.209539	-0.235623
0.475	-0.248182	0.142335	-0.222357	-0.247228	-0.238351	-0.265457

Tensor Asymmetries Versus Missing Momentum for 2005 Data for Different Potentials						
Parallel Kinematics–$0.1(GeV/c)^2 < Q^2 < 0.5(GeV/c)^2$						
P_m (bin center)	Reconstructed Value	Total Error	Bonn	v18	v14	Paris
0.025	0.00548999	0.00384778	0.0190941	0.0194708	0.0196329	0.0199447
0.075	0.0133284	0.00335807	0.0322503	0.0325557	0.0330573	0.0333136
0.125	0.0227731	0.00596725	0.0578985	0.0580116	0.0590215	0.0589377
0.175	-0.0163336	0.0111395	0.0631424	0.0623616	0.0618853	0.0612847
0.225	-0.107555	0.0183034	-0.00544338	-0.00759641	-0.0162523	-0.0150968
0.275	-0.177426	0.0276614	-0.132049	-0.129098	-0.14808	-0.142182
0.325	-0.236991	0.0417071	-0.205591	-0.194103	-0.2105	-0.205024
0.375	-0.205641	0.0629546	-0.261125	-0.227486	-0.235044	-0.233826
0.425	-0.133573	0.0918065	-0.221314	-0.168465	-0.17051	-0.168693
0.475	-0.111962	0.138079	-0.215792	-0.157603	-0.159502	-0.154828

Tensor Asymmetries Versus Missing Momentum for 2005 Data for Various Subnuclear Effects							
Perpendicular Kinematics–$0.1 < Q^2 < 0.2(GeV/c)^2$							
P_m (bin center)	Reconstructed	Total Error	PWBA	PWBA+FSI	PWBA+FSI+MEC	PWBA+FSI+MEC+IC	TOTAL
0.025	-0.0235934	0.0054215	-0.00521349	-0.00670654	-0.00670592	-0.00804706	-0.00822555
0.075	-0.0277978	0.0046998	-0.00940152	-0.0117403	-0.0115856	-0.0137921	-0.0140159
0.125	-0.051119	0.00853473	-0.0317666	-0.0349368	-0.0330478	-0.0370793	-0.0375247
0.175	-0.00160636	0.0165344	-0.089073	-0.0527899	-0.0388669	-0.0421395	-0.0411308
0.225	0.0651723	0.0279451	-0.216473	-0.0280502	0.0011371	-0.00696945	-0.000447572
0.275	0.0464687	0.0470852	-0.37565	-0.0706336	-0.0460311	-0.0614512	-0.0525291
0.325	0.0589391	0.0702299	-0.498688	-0.243755	-0.182743	-0.133507	-0.142334
0.375	0.13718	0.100683	-0.544879	-0.327299	-0.223345	-0.115645	-0.125611
0.425	0.0960707	0.152792	-0.523064	-0.438043	-0.312637	-0.191561	-0.195602
0.475	-0.018365	0.216515	-0.363033	-0.43325	-0.297839	-0.186108	-0.185633

Tensor Asymmetries Versus Missing Momentum for 2005 Data for Various Subnuclear Effects							
Parallel Kinematics–$0.1(GeV/c)^2 < Q^2 < 0.2(GeV/c)^2$							
P_m (bin center)	Reconstructed	Total Error	PWBA	PWBA+FSI	PWBA+FSI+MEC	PWBA+FSI+MEC+IC	TOTAL
0.025	0.010784	0.00475395	0.00410463	0.0157915	0.0171419	0.0192178	0.0198055
0.075	0.0193363	0.00439006	0.00961671	0.026925	0.0291979	0.0324564	0.0332857
0.125	0.0212316	0.00843066	0.0187887	0.0479249	0.0532304	0.0597933	0.0612256
0.175	-0.0556894	0.0168285	0.0247719	0.0402918	0.0539249	0.0646959	0.0655257
0.225	-0.173517	0.0277289	0.0132195	-0.0668441	-0.0422638	-0.0267115	-0.0277177
0.275	-0.319701	0.0459255	-0.0206423	-0.213434	-0.209832	-0.198416	-0.203825
0.325	-0.395453	0.0709486	0.00529414	-0.178699	-0.220922	-0.261475	-0.25928
0.375	-0.166403	0.096727	0.0327723	-0.181407	-0.25889	-0.330215	-0.327812
0.425	-0.193923	0.134401	0.111794	-0.11342	-0.206285	-0.275166	-0.277142
0.475	-0.0737782	0.194095	0.115581	-0.0998358	-0.206801	-0.266423	-0.272599

Tensor Asymmetries Versus Missing Momentum for 2005 Data for Various Subnuclear Effects							
Perpendicular Kinematics–$0.2 < Q^2 < 0.3(GeV/c)^2$							
P_m (bin center)	Reconstructed	Total Error	PWBA	PWBA+FSI	PWBA+FSI+MEC	PWBA+FSI+MEC+IC	TOTAL
0.025	-0.0272908	0.00945964	-0.00402789	-0.00802039	-0.0080508	-0.0096283	-0.00994606
0.075	-0.0448675	0.00776411	-0.00836371	-0.0139285	-0.0139774	-0.0165569	-0.0170504
0.125	-0.0418985	0.0128078	-0.0230344	-0.0287569	-0.0285014	-0.033219	-0.0335712
0.175	-0.0656681	0.0231991	-0.0522841	-0.0475774	-0.0432866	-0.0490395	-0.0477194
0.225	0.0096459	0.0398563	-0.139688	-0.053607	-0.0273251	-0.0299385	-0.0223575
0.275	0.110719	0.0592331	-0.299834	0.0266899	0.0686474	0.058738	0.0712247
0.325	0.162655	0.0987375	-0.383061	0.0555075	0.0811334	0.0497794	0.0584734
0.375	-0.17605	0.193771	-0.62371	-0.241669	-0.20039	-0.222317	-0.22741
0.425	0.118732	0.275151	-0.607684	-0.550998	-0.437997	-0.361705	-0.366386
0.475	0.0344964	0.419653	-0.409954	-0.594749	-0.495144	-0.441218	-0.440369

Tensor Asymmetries Versus Missing Momentum for 2005 Data for Various Subnuclear Effects							
Parallel Kinematics–$0.2(GeV/c)^2 < Q^2 < 0.3(GeV/c)^2$							
P_m (bin center)	Reconstructed	Total Error	PWBA	PWBA+FSI	PWBA+FSI+MEC	PWBA+FSI+MEC+IC	TOTAL
0.025	-0.00203453	0.00798291	0.00208854	0.0121951	0.0134629	0.0153914	0.0159644
0.075	0.0138974	0.00673741	0.00631894	0.0215956	0.0238455	0.0268282	0.0278843
0.125	0.0271194	0.0115714	0.0110911	0.0350462	0.0407645	0.0463967	0.0481711
0.175	-0.00243107	0.0214404	0.0166013	0.0353832	0.0484188	0.0570415	0.0585814
0.225	-0.0819235	0.0362138	0.0279232	-0.0181215	0.0222081	0.0362336	0.0361259
0.275	-0.129783	0.0505077	0.035229	-0.165845	-0.0754354	-0.0491157	-0.0455
0.325	-0.153974	0.0831113	0.0262622	-0.288094	-0.194294	-0.163416	-0.155326
0.375	-0.393068	0.152334	0.203023	-0.194113	-0.162488	-0.147774	-0.143891
0.425	0.0102933	0.229237	0.265816	0.0938181	0.0204098	-0.047654	-0.0479006
0.475	-0.144106	0.324423	0.214043	0.141069	0.0440898	-0.0419765	-0.0509661

Tensor Asymmetries Versus Missing Momentum for 2005 Data for Various Subnuclear Effects							
Perpendicular Kinematics–$0.3 < Q^2 < 0.4(GeV/c)^2$							
P_m (bin center)	Reconstructed	Total Error	PWBA	PWBA+FSI	PWBA+FSI+MEC	PWBA+FSI+MEC+IC	TOTAL
0.025	-0.0312432	0.0203281	-0.0028645	-0.00758735	-0.00754431	-0.00901123	-0.00961035
0.075	-0.0281404	0.0153718	-0.00760489	-0.0143438	-0.0143546	-0.0166618	-0.0176356
0.125	-0.0430668	0.0227722	-0.019847	-0.0287171	-0.0289853	-0.033076	-0.0344269
0.175	-0.126143	0.0375981	-0.0522676	-0.0558955	-0.0567787	-0.0644427	-0.0650812
0.225	-0.0308299	0.0591414	-0.0884261	-0.0588688	-0.0572033	-0.0690743	-0.0666354
0.275	0.0124373	0.0890888	-0.19803	-0.0334808	-0.011487	-0.0299421	-0.0165979
0.325	-0.0487161	0.128769	-0.3328	0.0971232	0.12305	0.0889386	0.101235
0.375	-0.169055	0.207975	-0.194374	0.131492	0.140036	0.0879213	0.0934971
0.425	0.127637	0.30495	-0.225377	0.0209991	0.0174156	-0.0757683	-0.071887
0.475	-0.638183	0.464335	-0.415119	-0.374735	-0.393944	-0.47437	-0.476891

Tensor Asymmetries Versus Missing Momentum for 2005 Data for Various Subnuclear Effects							
Parallel Kinematics–$0.3(GeV/c)^2 < Q^2 < 0.4(GeV/c)^2$							
P_m (bin center)	Reconstructed	Total Error	PWBA	PWBA+FSI	PWBA+FSI+MEC	PWBA+FSI+MEC+IC	TOTAL
0.025	-0.0163667	0.0144171	0.00110629	0.0101196	0.0111631	0.0127193	0.0137293
0.075	-0.0135404	0.0119019	0.00759669	0.0206994	0.0225523	0.0248942	0.0264353
0.125	0.0422236	0.0189068	0.0142694	0.0344023	0.0389212	0.0428537	0.0451552
0.175	0.0198449	0.0312114	0.0192921	0.0397054	0.0535915	0.0611266	0.0640581
0.225	-0.0516194	0.0498627	0.00317984	-0.0225991	0.011932	0.0274586	0.0306593
0.275	-0.113999	0.073777	0.00751713	-0.160779	-0.0676803	-0.0333226	-0.0286004
0.325	-0.0808655	0.105644	-0.00969476	-0.374324	-0.195977	-0.136147	-0.118609
0.375	-0.0389729	0.157707	-0.0838067	-0.394867	-0.216466	-0.150892	-0.125437
0.425	0.152609	0.265907	0.0110161	-0.203832	-0.0916148	-0.0482398	-0.0314124
0.475	0.223364	0.40253	0.219205	0.112464	0.11477	0.0890628	0.0865893

Tensor Asymmetries Versus Missing Momentum for 2005 Data for Various Subnuclear Effects							
Perpendicular Kinematics–$0.4 < Q^2 < 0.5(GeV/c)^2$							
P_m (bin center)	Reconstructed	Total Error	PWBA	PWBA+FSI	PWBA+FSI+MEC	PWBA+FSI+MEC+IC	TOTAL
0.025	-0.0352864	0.0207106	-0.00333648	-0.00774	-0.00768423	-0.00880532	-0.00940156
0.075	-0.0363064	0.0170449	-0.00758992	-0.0141604	-0.0141138	-0.0159164	-0.0168913
0.125	-0.0542283	0.0269927	-0.014563	-0.0226901	-0.0228471	-0.0258608	-0.0277372
0.175	-0.101776	0.0449754	-0.0232774	-0.0277706	-0.0283213	-0.0324415	-0.0349908
0.225	-0.114793	0.0762014	-0.0704074	-0.0558122	-0.058911	-0.0692233	-0.0731163
0.275	-0.307163	0.124245	-0.244998	-0.0967017	-0.107507	-0.134551	-0.13002
0.325	-0.0330664	0.183747	-0.363431	0.0233828	0.00219081	-0.0578957	-0.0542977
0.375	-0.042903	0.234007	-0.330884	0.168731	0.139863	0.0595942	0.0642768
0.425	-0.0671771	0.338134	-0.171101	0.150367	0.122978	0.0360455	0.0355776
0.475	-0.335886	0.590935	-0.056899	0.023847	0.000383762	-0.0835462	-0.0850304

Tensor Asymmetries Versus Missing Momentum for 2005 Data for Various Subnuclear Effects							
Parallel Kinematics–$0.4(GeV/c)^2 < Q^2 < 0.5(GeV/c)^2$							
P_m (bin center)	Reconstructed	Total Error	PWBA	PWBA+FSI	PWBA+FSI+MEC	PWBA+FSI+MEC+IC	TOTAL
0.025	0.0177783	0.0298298	0.00353476	0.0116274	0.0124893	0.0136444	0.014475
0.075	0.00902759	0.0228849	0.00965039	0.0216657	0.0231809	0.0249247	0.0262623
0.125	0.000847937	0.0328946	0.011572	0.0279046	0.0310145	0.0338596	0.0365541
0.175	0.0240826	0.0522696	0.0106377	0.0236153	0.0289963	0.0327438	0.0364902
0.225	0.0248474	0.0817087	0.0310889	0.0227679	0.0419304	0.0511431	0.05532
0.275	-0.00792747	0.116151	0.0313632	-0.131866	-0.0450066	-0.00735587	0.004503
0.325	-0.0847585	0.159565	0.0461374	-0.35524	-0.190906	-0.114475	-0.091498
0.375	-0.178097	0.225055	0.085098	-0.481391	-0.256359	-0.151204	-0.119164
0.425	-0.0709091	0.347404	-0.0963789	-0.382753	-0.200373	-0.11583	-0.087694
0.475	-0.867929	0.585321	-0.354641	-0.323018	-0.14671	-0.0674557	-0.0300622

Tensor Asymmetries Versus Missing Momentum for 2005 Data for Various Subnuclear Effects							
Perpendicular Kinematics–$0.1 < Q^2 < 0.5(GeV/c)^2$							
P_m (bin center)	Reconstructed	Total Error	PWBA	PWBA+FSI	PWBA+FSI+MEC	PWBA+FSI+MEC+IC	TOTAL
0.025	-0.0273344	0.00442558	-0.00492643	-0.00683444	-0.00683658	-0.00821251	-0.00853078
0.075	-0.0320709	0.00357499	-0.00919568	-0.012184	-0.0120843	-0.0143434	-0.0146554
0.125	-0.045983	0.00591678	-0.0294844	-0.0332416	-0.0318179	-0.0359851	-0.0365068
0.175	-0.0430818	0.0107424	-0.0769935	-0.0508957	-0.0406059	-0.0447425	-0.0437935
0.225	0.0147714	0.0181072	-0.184848	-0.0374844	-0.0113591	-0.0180547	-0.0114686
0.275	0.0406831	0.0288806	-0.34645	-0.0337231	-0.00225088	-0.0172447	-0.00611346
0.325	0.0428687	0.0436234	-0.463145	-0.0864949	-0.0429894	-0.0459976	-0.0448944
0.375	0.0543704	0.0674538	-0.530866	-0.213396	-0.142551	-0.100882	-0.106225
0.425	0.00959686	0.0989883	-0.5091	-0.351973	-0.260882	-0.196187	-0.198586
0.475	-0.248182	0.142335	-0.357693	-0.408617	-0.303076	-0.222726	-0.222357

Tensor Asymmetries Versus Missing Momentum for 2005 Data for Various Subnuclear Effects							
Parallel Kinematics–$0.1(GeV/c)^2 < Q^2 < 0.5(GeV/c)^2$							
P_m (bin center)	Reconstructed	Total Error	PWBA	PWBA+FSI	PWBA+FSI+MEC	PWBA+FSI+MEC+IC	TOTAL
0.025	0.00548999	0.00384778	0.00385699	0.0152487	0.0165875	0.0186004	0.0190941
0.075	0.0133284	0.00335807	0.00911405	0.0259836	0.0282483	0.0314176	0.0322503
0.125	0.0227731	0.00596725	0.0171992	0.0446646	0.0500061	0.0562505	0.0578985
0.175	-0.0163336	0.0111395	0.0223454	0.0386224	0.051934	0.0618814	0.0631424
0.225	-0.107555	0.0183034	0.0168109	-0.0489152	-0.0195086	-0.00479103	-0.00544338
0.275	-0.177426	0.0276614	-0.00555793	-0.192015	-0.148866	-0.13155	-0.132049
0.325	-0.236991	0.0417071	0.00935857	-0.24503	-0.20752	-0.212614	-0.205591
0.375	-0.205641	0.0629546	0.051413	-0.235252	-0.232833	-0.269069	-0.261125
0.425	-0.133573	0.0918065	0.123566	-0.10975	-0.161577	-0.222483	-0.221314
0.475	-0.111962	0.138079	0.100927	-0.0915402	-0.154363	-0.21303	-0.215792

AT_d vs P_m for 2004 data

Tensor Asymmetries Versus Missing Momentum for 2004 Data for Different Potentials						
Perpendicular Kinematics–$0.1 < Q^2 < 0.2(GeV/c)^2$						
P_m (bin center)	Reconstructed Value	Total Error	Bonn	v18	v14	Paris
0.025	-0.0121197	0.00312762	-0.0149667	-0.0151417	-0.0154019	-0.0152856
0.075	-0.0243924	0.00271472	-0.0230033	-0.0233623	-0.0239288	-0.0236018
0.125	-0.0283806	0.00509246	-0.0382662	-0.039935	-0.0418849	-0.040487
0.175	0.00336639	0.0100584	-0.000161026	-0.0073557	-0.0109382	-0.00874562
0.225	0.0904068	0.0167127	0.0665995	0.0492705	0.0486129	0.0486997
0.275	0.121353	0.0278153	0.023209	-0.00974609	-0.00540546	-0.00533681
0.325	0.185365	0.0458014	0.067281	0.0388774	0.0405073	0.0404794
0.375	0.188614	0.0917506	0.191204	0.163197	0.166958	0.156201
0.425	0.38128	0.243097	0.178361	0.146761	0.152413	0.132218
0.475	0.102183	0.64593	0.203879	0.168521	0.173477	0.14958

Tensor Asymmetries Versus Missing Momentum for 2004 Data for Different Potentials						
Parallel Kinematics–$0.1(GeV/c)^2 < Q^2 < 0.2(GeV/c)^2$						
P_m (bin center)	Reconstructed Value	Total Error	Bonn	v18	v14	Paris
0.025	0.00724572	0.00289769	0.00987196	0.00985118	0.0100834	0.0104882
0.075	0.0214476	0.00265561	0.0201479	0.0197509	0.0203063	0.0207721
0.125	0.033093	0.00508101	0.0482762	0.0464467	0.0475231	0.0481288
0.175	-0.0224074	0.00996116	0.0875625	0.0816113	0.0819574	0.0827654
0.225	-0.15306	0.0163363	0.039547	0.0310549	0.0235183	0.0273117
0.275	-0.330255	0.0277045	-0.120153	-0.118065	-0.134911	-0.123671
0.325	-0.305709	0.0455261	-0.0478335	-0.030495	-0.0378318	-0.0318863
0.375	-0.0773277	0.0867661	0.00692345	0.0425961	0.0403084	0.0429041
0.425	0.326564	0.204084	0.099699	0.140377	0.137426	0.141953
0.475	0.185785	0.614314	0.124293	0.170223	0.16702	0.171358

Tensor Asymmetries Versus Missing Momentum for 2004 Data for Different Potentials						
Perpendicular Kinematics–$0.2 < Q^2 < 0.3(GeV/c)^2$						
P_m (bin center)	Reconstructed Value	Total Error	Bonn	v18	v14	Paris
0.025	-0.00703462	0.00496358	-0.0112292	-0.0115799	-0.011721	-0.0117028
0.075	-0.0215377	0.00415338	-0.0203984	-0.0208635	-0.0214074	-0.0212024
0.125	-0.0381067	0.00694636	-0.0396972	-0.0404941	-0.0426127	-0.0415649
0.175	-0.0569112	0.0131226	-0.0371702	-0.0403301	-0.0447436	-0.0422583
0.225	0.0730773	0.0226303	0.0404983	0.0307275	0.0240425	0.0259182
0.275	0.163821	0.0333927	0.149718	0.134334	0.133289	0.129857
0.325	0.251342	0.066477	0.129806	0.107094	0.111838	0.105278
0.375	0.248794	0.189189	-0.0145209	-0.0534071	-0.0476144	-0.0549842
0.425	-0.510916	1.0838	-0.000439514	-0.047221	-0.0387985	-0.0561919
0.475	-2.04366	6.13089	-0.0576467	-0.102966	-0.0930818	-0.113267

Tensor Asymmetries Versus Missing Momentum for 2004 Data for Different Potentials						
Parallel Kinematics–$0.2(GeV/c)^2 < Q^2 < 0.3(GeV/c)^2$						
P_m (bin center)	Reconstructed Value	Total Error	Bonn	v18	v14	Paris
0.025	0.0115792	0.00477232	0.0118097	0.0114861	0.0118385	0.0120851
0.075	0.0203192	0.0039072	0.0204263	0.0198234	0.0204174	0.0206872
0.125	0.0262436	0.00643285	0.0340883	0.0329151	0.0333976	0.0336924
0.175	0.0351284	0.0122165	0.0551256	0.0517313	0.0513135	0.0514924
0.225	-0.0404751	0.0212608	0.0859447	0.074834	0.0698082	0.0714115
0.275	-0.0303086	0.0313556	0.0447165	0.026803	0.00927933	0.0170596
0.325	-0.0530057	0.0633443	-0.0720799	-0.0817238	-0.110197	-0.0916308
0.375	0.0399151	0.180628	0.00951867	0.0290627	0.00648186	0.0265092
0.425	0.408732	0.510499	0.251908	0.282563	0.27615	0.287185
0.475	-0.204366	0.917588	0.295574	0.330585	0.326787	0.336052

Tensor Asymmetries Versus Missing Momentum for 2004 Data for Different Potentials						
Perpendicular Kinematics–$0.3 < Q^2 < 0.4 (GeV/c)^2$						
P_m (bin center)	Reconstructed Value	Total Error	Bonn	v18	v14	Paris
0.025	0.00448831	0.00839984	-0.00769984	-0.00831628	-0.00843582	-0.00821169
0.075	-0.00875294	0.00633292	-0.0154078	-0.0161692	-0.01666	-0.0162507
0.125	-0.0334834	0.00969848	-0.032966	-0.0338327	-0.0355027	-0.0345446
0.175	-0.0612381	0.0169633	-0.0686573	-0.0701882	-0.075645	-0.0729646
0.225	-0.0430316	0.0305064	-0.0602123	-0.064534	-0.0739715	-0.0696881
0.275	0.0734322	0.0504237	0.0453874	0.0368178	0.0253597	0.0277933
0.325	0.341023	0.0698574	0.185928	0.178783	0.176241	0.172741
0.375	0.284268	0.123947	0.155254	0.150069	0.149042	0.145102
0.425	0.280722	0.211997	0.0355132	0.0189862	0.0213931	0.0149376
0.475	0.185787	0.614323	-0.214689	-0.255533	-0.241872	-0.25831

Tensor Asymmetries Versus Missing Momentum for 2004 Data for Different Potentials						
Parallel Kinematics–$0.3 (GeV/c)^2 < Q^2 < 0.4 (GeV/c)^2$						
P_m (bin center)	Reconstructed Value	Total Error	Bonn	v18	v14	Paris
0.025	0.0151663	0.00813794	0.0131302	0.0123532	0.0127615	0.0128288
0.075	0.0196198	0.00640452	0.0241711	0.0229499	0.0237372	0.0237135
0.125	0.011912	0.0101135	0.0385355	0.0367853	0.0376364	0.0374947
0.175	0.00764324	0.0176747	0.0487279	0.0458624	0.0450746	0.0449628
0.225	-0.00484614	0.0307113	0.0262818	0.0191087	0.0127062	0.0142569
0.275	0.0592738	0.0513107	0.0389565	0.0184955	0.00382069	0.0108877
0.325	-0.0112702	0.0715413	-0.0175263	-0.0473448	-0.0768224	-0.0616272
0.375	0.0393011	0.115694	-0.0310604	-0.0578871	-0.0900581	-0.0709449
0.425	0.255458	0.245883	0.101074	0.0964799	0.076209	0.093372
0.475	0.120214	0.495245	0.316034	0.335665	0.328337	0.342353

Tensor Asymmetries Versus Missing Momentum for 2004 Data for Different Potentials						
Perpendicular Kinematics–$0.4 < Q^2 < 0.5 (GeV/c)^2$						
P_m (bin center)	Reconstructed Value	Total Error	Bonn	v18	v14	Paris
0.025	0.00298231	0.0123438	-0.00589217	-0.0064194	-0.00659036	-0.00619526
0.075	-0.00310994	0.0100042	-0.0118964	-0.0125186	-0.0130342	-0.0124048
0.125	-0.0440523	0.0158142	-0.0217451	-0.0227311	-0.0240453	-0.0228914
0.175	-0.0806754	0.0264936	-0.0271969	-0.0290359	-0.0311222	-0.0293235
0.225	-0.0942044	0.0443395	-0.0708114	-0.0738863	-0.0799834	-0.0767704
0.275	0.048596	0.0732637	-0.10774	-0.115087	-0.129394	-0.125028
0.325	0.140421	0.0938442	-0.0417302	-0.0552242	-0.0724065	-0.0677755
0.375	0.318842	0.123385	0.0887676	0.0785944	0.0683112	0.0714877
0.425	0.0112289	0.214231	0.0784074	0.0730032	0.06972	0.0674149
0.475	0.393012	0.317797	0.054056	0.0391663	0.0431431	0.0357988

Tensor Asymmetries Versus Missing Momentum for 2004 Data for Different Potentials						
Parallel Kinematics–$0.4 (GeV/c)^2 < Q^2 < 0.5 (GeV/c)^2$						
P_m (bin center)	Reconstructed Value	Total Error	Bonn	v18	v14	Paris
0.025	0.0172657	0.0136634	0.0152668	0.0140609	0.0144665	0.0143783
0.075	0.0140082	0.0108095	0.0268301	0.0249751	0.0257653	0.0255619
0.125	0.0231836	0.0172619	0.03654	0.0339713	0.0345404	0.0342814
0.175	0.0314001	0.0300627	0.0373773	0.0343845	0.0338743	0.0335246
0.225	0.0096721	0.0482224	0.0507321	0.0458541	0.0426039	0.0429269
0.275	-0.0149668	0.0745731	0.00492523	-0.008932	-0.0247709	-0.0169459
0.325	-0.0478984	0.104294	-0.0607758	-0.0877473	-0.113821	-0.0936868
0.375	-0.0805382	0.14347	-0.0488992	-0.0848237	-0.115315	-0.0910749
0.425	0.22903	0.266825	-0.0358781	-0.0613252	-0.0884952	-0.0658747
0.475	0.321147	0.340033	0.044089	0.00908621	-0.0152371	0.00135322

Tensor Asymmetries Versus Missing Momentum for 2004 Data for Different Potentials						
Perpendicular Kinematics–$0.1 < Q^2 < 0.5(GeV/c)^2$						
P_m (bin center)	Reconstructed Value	Total Error	Bonn	v18	v14	Paris
0.025	-0.00920213	0.0024573	-0.0143363	-0.0145528	-0.0147786	-0.0146807
0.075	-0.0200687	0.00203887	-0.0224507	-0.0228355	-0.0234076	-0.023094
0.125	-0.0321825	0.00351327	-0.0381069	-0.0395689	-0.0415354	-0.0402264
0.175	-0.0318164	0.00659712	-0.0134266	-0.0192085	-0.0230925	-0.0207902
0.225	0.0397544	0.0112885	0.0498323	0.0355433	0.0325191	0.0334363
0.275	0.109396	0.0180283	0.0691113	0.0437441	0.044205	0.0433427
0.325	0.199683	0.0296569	0.100402	0.0761365	0.0776704	0.0750788
0.375	0.233828	0.0561026	0.153008	0.126792	0.129574	0.120686
0.425	0.210686	0.119273	0.138374	0.107306	0.1124	0.0943805
0.475	0.212881	0.239753	0.150771	0.114433	0.119533	0.0974693

Tensor Asymmetries Versus Missing Momentum for 2004 Data for Different Potentials						
Parallel Kinematics–$0.1(GeV/c)^2 < Q^2 < 0.5(GeV/c)^2$						
P_m (bin center)	Reconstructed Value	Total Error	Bonn	v18	v14	Paris
0.025	0.00912778	0.00231123	0.0101393	0.0100689	0.0103213	0.0106989
0.075	0.0207742	0.00198376	0.0202147	0.0197536	0.0203144	0.0207419
0.125	0.0259027	0.00345147	0.0451375	0.0434145	0.0443639	0.0448757
0.175	0.00439942	0.00650458	0.0767705	0.0716506	0.0717033	0.0723093
0.225	-0.0778699	0.0109781	0.0516719	0.0425948	0.0358894	0.0388752
0.275	-0.142618	0.0175717	-0.04798	-0.0556146	-0.0732756	-0.0634794
0.325	-0.15447	0.0292004	-0.0527382	-0.0504052	-0.0674593	-0.0559806
0.375	-0.019949	0.0549531	0.00020708	0.0225051	0.011814	0.0204299
0.425	0.252749	0.120558	0.116103	0.150224	0.144676	0.151778
0.475	0.220621	0.216751	0.147234	0.186135	0.181294	0.187437

Tensor Asymmetries Versus Missing Momentum for 2004 Data for Various Subnuclear Effects							
Perpendicular Kinematics–$0.1 < Q^2 < 0.2(GeV/c)^2$							
P_m (bin center)	Reconstructed	Total Error	PWBA	PWBA+FSI	PWBA+FSI+MEC	PWBA+FSI+MEC+IC	TOTAL
0.025	-0.0121197	0.00312762	-0.00360201	-0.013785	-0.0135728	-0.0146844	-0.0149667
0.075	-0.0243924	0.00271472	-0.0062842	-0.0215228	-0.0210084	-0.0227343	-0.0230033
0.125	-0.0283806	0.00509246	-0.0155002	-0.038695	-0.0359452	-0.0385611	-0.0382662
0.175	0.00336639	0.0100584	-0.028549	-0.0175972	-0.00330561	-0.00425207	-0.000161026
0.225	0.0904068	0.0167127	-0.0818703	0.0317069	0.0593278	0.0545556	0.0665995
0.275	0.121353	0.0278153	-0.159292	-0.0268541	0.00105524	0.00184391	0.023209
0.325	0.185365	0.0458014	-0.201166	-0.0852131	-0.00852261	0.0615709	0.067281
0.375	0.188614	0.0917506	-0.218486	-0.0506195	0.0659361	0.187338	0.191204
0.425	0.38128	0.243097	-0.268055	-0.12187	0.0236092	0.169838	0.178361
0.475	0.102183	0.64593	-0.204238	-0.105114	0.0534796	0.191658	0.203879

Tensor Asymmetries Versus Missing Momentum for 2004 Data for Various Subnuclear Effects							
Parallel Kinematics–$0.1(GeV/c)^2 < Q^2 < 0.2(GeV/c)^2$							
P_m (bin center)	Reconstructed	Total Error	PWBA	PWBA+FSI	PWBA+FSI+MEC	PWBA+FSI+MEC+IC	TOTAL
0.025	0.00724572	0.00289769	0.0045256	0.00614738	0.00758334	0.00951889	0.00987196
0.075	0.0214476	0.00265561	0.0109648	0.0139357	0.0163542	0.0194996	0.0201479
0.125	0.033093	0.00508101	0.0274244	0.0339126	0.0396847	0.0464414	0.0482762
0.175	-0.0224074	0.00996116	0.0657977	0.0578642	0.0720588	0.0838715	0.0875625
0.225	-0.15306	0.0163363	0.113553	-0.00669848	0.0174089	0.0342148	0.039547
0.275	-0.330255	0.0277045	0.150956	-0.162006	-0.152619	-0.127525	-0.120153
0.325	-0.305709	0.0455261	0.249198	-0.0367012	-0.0538725	-0.0631533	-0.0478335
0.375	-0.0773277	0.0867661	0.295821	0.0712144	0.027016	-0.0086778	0.00692345
0.425	0.326564	0.204084	0.298017	0.158844	0.110069	0.0894002	0.099699
0.475	0.185785	0.614314	0.223258	0.188895	0.131507	0.117579	0.124293

Tensor Asymmetries Versus Missing Momentum for 2004 Data for Various Subnuclear Effects							
Perpendicular Kinematics–$0.2 < Q^2 < 0.3 (GeV/c)^2$							
P_m (bin center)	Reconstructed	Total Error	PWBA	PWBA+FSI	PWBA+FSI+MEC	PWBA+FSI+MEC+IC	TOTAL
0.025	-0.00703462	0.00496358	-0.00278572	-0.00980652	-0.00962018	-0.0108144	-0.0112292
0.075	-0.0215377	0.00415338	-0.00709015	-0.0181938	-0.0177319	-0.0196936	-0.0203984
0.125	-0.0381067	0.00694636	-0.0200377	-0.0372439	-0.0354476	-0.0387672	-0.0396972
0.175	-0.0569112	0.0131226	-0.03452	-0.0415915	-0.0346819	-0.0376881	-0.0371702
0.225	0.0730773	0.0226303	-0.0730034	0.00782172	0.0337501	0.033846	0.0404983
0.275	0.163821	0.0333927	-0.160907	0.114484	0.148648	0.140833	0.149718
0.325	0.251342	0.066477	-0.201855	0.109333	0.136529	0.126119	0.129806
0.375	0.248794	0.189189	-0.410504	-0.156198	-0.0731922	-0.0136519	-0.0145209
0.425	-0.510916	1.0838	-0.420532	-0.330564	-0.157215	-0.00763719	-0.000439514
0.475	-2.04366	6.13089	-0.328684	-0.400805	-0.217998	-0.0715031	-0.0576467

Tensor Asymmetries Versus Missing Momentum for 2004 Data for Various Subnuclear Effects							
Parallel Kinematics–$0.2 (GeV/c)^2 < Q^2 < 0.3 (GeV/c)^2$							
P_m (bin center)	Reconstructed	Total Error	PWBA	PWBA+FSI	PWBA+FSI+MEC	PWBA+FSI+MEC+IC	TOTAL
0.025	0.0115792	0.00477232	0.00253953	0.0081391	0.00952844	0.0114651	0.0118097
0.075	0.0203192	0.0039072	0.00634362	0.0142478	0.0167657	0.0197717	0.0204263
0.125	0.0262436	0.00643285	0.0104273	0.0206104	0.02714	0.0330426	0.0340883
0.175	0.0351284	0.0122165	0.0246587	0.0297994	0.0444235	0.0542663	0.0551256
0.225	-0.0404751	0.0212608	0.07001	0.0321466	0.0708475	0.085944	0.0859447
0.275	-0.0303086	0.0313556	0.132733	-0.0597441	0.0182249	0.0433796	0.0447165
0.325	-0.0530057	0.0633443	0.151076	-0.208961	-0.119933	-0.0751728	-0.0720799
0.375	0.0399151	0.180628	0.309909	-0.15922	-0.0877562	0.00617253	0.00951867
0.425	0.408732	0.510499	0.334626	0.198124	0.209273	0.242483	0.251908
0.475	-0.204366	0.917588	0.243693	0.27442	0.277252	0.290976	0.295574

Tensor Asymmetries Versus Missing Momentum for 2004 Data for Various Subnuclear Effects							
Perpendicular Kinematics–$0.3 < Q^2 < 0.4 (GeV/c)^2$							
P_m (bin center)	Reconstructed	Total Error	PWBA	PWBA+FSI	PWBA+FSI+MEC	PWBA+FSI+MEC+IC	TOTAL
0.025	0.00448831	0.00839984	-0.00216381	-0.00631508	-0.00606963	-0.00704376	-0.00769984
0.075	-0.00875294	0.00633292	-0.00675163	-0.0132323	-0.0127765	-0.0143442	-0.0154078
0.125	-0.0334834	0.00969848	-0.0189134	-0.0295996	-0.0283581	-0.0310022	-0.032966
0.175	-0.0612381	0.0169633	-0.0538891	-0.065146	-0.0614105	-0.0659057	-0.0686573
0.225	-0.0430316	0.0305064	-0.0868859	-0.0602812	-0.0520979	-0.0589452	-0.0602123
0.275	0.0734322	0.0504237	-0.150487	0.029765	0.053034	0.0398652	0.0453874
0.325	0.341023	0.0698574	-0.238801	0.199844	0.21512	0.185034	0.185928
0.375	0.284268	0.123947	-0.173782	0.18423	0.192423	0.160296	0.155254
0.425	0.280722	0.211997	-0.229282	0.0607759	0.0739457	0.0399548	0.0355132
0.475	0.185787	0.614323	-0.418772	-0.377502	-0.298069	-0.223987	-0.214689

Tensor Asymmetries Versus Missing Momentum for 2004 Data for Various Subnuclear Effects							
Parallel Kinematics–$0.3 (GeV/c)^2 < Q^2 < 0.4 (GeV/c)^2$							
P_m (bin center)	Reconstructed	Total Error	PWBA	PWBA+FSI	PWBA+FSI+MEC	PWBA+FSI+MEC+IC	TOTAL
0.025	0.0151663	0.00813794	0.00130396	0.00942755	0.0105941	0.0123286	0.0131302
0.075	0.0196198	0.00640452	0.0069668	0.0182774	0.0204061	0.0230091	0.0241711
0.125	0.011912	0.0101135	0.0116657	0.0272373	0.0326194	0.037123	0.0385355
0.175	0.00764324	0.0176747	0.011322	0.0225632	0.0390656	0.0480703	0.0487279
0.225	-0.00484614	0.0307113	-0.00450771	-0.0276645	0.00963745	0.0270877	0.0262818
0.275	0.0592738	0.0513107	0.0395699	-0.0776735	0.00842123	0.0416825	0.0389565
0.325	-0.0112702	0.0715413	0.0426873	-0.234553	-0.0798015	-0.0228465	-0.0175263
0.375	0.0393011	0.115694	-0.0591199	-0.277849	-0.117741	-0.0435177	-0.0310604
0.425	0.255458	0.245883	0.0100313	-0.131006	-0.00544671	0.0927438	0.101074
0.475	0.120214	0.495245	0.165309	0.086993	0.190618	0.308377	0.316034

Tensor Asymmetries Versus Missing Momentum for 2004 Data for Various Subnuclear Effects							
Perpendicular Kinematics–$0.4 < Q^2 < 0.5(GeV/c)^2$							
P_m (bin center)	Reconstructed	Total Error	PWBA	PWBA+FSI	PWBA+FSI+MEC	PWBA+FSI+MEC+IC	TOTAL
0.025	0.00298231	0.0123438	-0.00291127	-0.00493179	-0.00468108	-0.00530868	-0.00589217
0.075	-0.00310994	0.0100042	-0.0067391	-0.0103272	-0.00985907	-0.0108647	-0.0118964
0.125	-0.0440523	0.0158142	-0.0135558	-0.0187847	-0.0179548	-0.0196649	-0.0217451
0.175	-0.0806754	0.0264936	-0.0201591	-0.0227161	-0.0215499	-0.0239686	-0.0271969
0.225	-0.0942044	0.0443395	-0.0695092	-0.0600052	-0.056402	-0.0627838	-0.0708114
0.275	0.048596	0.0732637	-0.234742	-0.0944684	-0.0850879	-0.0992496	-0.10774
0.325	0.140421	0.0938442	-0.406268	0.00156228	0.00386318	-0.0330605	-0.0417302
0.375	0.318842	0.123385	-0.382185	0.160872	0.146492	0.093513	0.0887676
0.425	0.0112289	0.214231	-0.211606	0.147575	0.135074	0.0882386	0.0784074
0.475	0.393012	0.317797	-0.0388755	0.125125	0.104381	0.0648347	0.054056

Tensor Asymmetries Versus Missing Momentum for 2004 Data for Various Subnuclear Effects							
Parallel Kinematics–$0.4(GeV/c)^2 < Q^2 < 0.5(GeV/c)^2$							
P_m (bin center)	Reconstructed	Total Error	PWBA	PWBA+FSI	PWBA+FSI+MEC	PWBA+FSI+MEC+IC	TOTAL
0.025	0.0172657	0.0136634	0.00297336	0.0121532	0.0131516	0.014578	0.0152668
0.075	0.0140082	0.0108095	0.00880528	0.0218455	0.0236303	0.025781	0.0268301
0.125	0.0231836	0.0172619	0.0105713	0.0273199	0.0310397	0.0345658	0.03654
0.175	0.0314001	0.0300627	0.0107977	0.0238163	0.0303744	0.0350242	0.0373773
0.225	0.0096721	0.0482224	0.0257954	0.0170912	0.0401726	0.0513093	0.0507321
0.275	-0.0149668	0.0745731	0.0049323	-0.134636	-0.0372718	0.00658054	0.00492523
0.325	-0.0478984	0.104294	-0.0109183	-0.309429	-0.147131	-0.0675388	-0.0607758
0.375	-0.0805382	0.14347	0.00365364	-0.388609	-0.180123	-0.0694368	-0.0488992
0.425	0.22903	0.266825	-0.157828	-0.340301	-0.163113	-0.0534234	-0.0358781
0.475	0.321147	0.340033	-0.336069	-0.219383	-0.0684987	0.0191736	0.044089

Tensor Asymmetries Versus Missing Momentum for 2004 Data for Various Subnuclear Effects							
Perpendicular Kinematics–$0.1 < Q^2 < 0.5(GeV/c)^2$							
P_m (bin center)	Reconstructed	Total Error	PWBA	PWBA+FSI	PWBA+FSI+MEC	PWBA+FSI+MEC+IC	TOTAL
0.025	-0.00920213	0.0024573	-0.00344495	-0.0129877	-0.0127828	-0.0138989	-0.0143363
0.075	-0.0200687	0.00203887	-0.00647015	-0.0207932	-0.0203043	-0.0220557	-0.0224507
0.125	-0.0321825	0.00351327	-0.016427	-0.0377175	-0.0352508	-0.0380009	-0.0381069
0.175	-0.0318164	0.00659712	-0.0309101	-0.0263399	-0.014758	-0.0163352	-0.0134266
0.225	0.0397544	0.0112885	-0.0795935	0.0176581	0.0433229	0.0400121	0.0498323
0.275	0.109396	0.0180283	-0.160001	0.0265908	0.0578315	0.0528851	0.0691113
0.325	0.199683	0.0296569	-0.206068	0.0233829	0.0739266	0.0956196	0.100402
0.375	0.233828	0.0561026	-0.245224	-0.0181973	0.0688328	0.15135	0.153008
0.425	0.210686	0.119273	-0.285754	-0.107253	0.0123124	0.132199	0.138374
0.475	0.212881	0.239753	-0.21884	-0.133053	0.00855358	0.13972	0.150771

Tensor Asymmetries Versus Missing Momentum for 2004 Data for Various Subnuclear Effects							
Parallel Kinematics–$0.1(GeV/c)^2 < Q^2 < 0.5(GeV/c)^2$							
P_m (bin center)	Reconstructed	Total Error	PWBA	PWBA+FSI	PWBA+FSI+MEC	PWBA+FSI+MEC+IC	TOTAL
0.025	0.00912778	0.00231123	0.00424779	0.0065786	0.00799873	0.00991511	0.0101393
0.075	0.0207742	0.00198376	0.0101409	0.0140989	0.0165282	0.0196254	0.0202147
0.125	0.0259027	0.00345147	0.0236967	0.0310493	0.0369287	0.0433966	0.0451375
0.175	0.00439942	0.00650458	0.0528177	0.0482883	0.0625817	0.0737081	0.0767705
0.225	-0.0778699	0.0109781	0.0929967	0.00317382	0.032167	0.0482909	0.0516719
0.275	-0.142618	0.0175717	0.138216	-0.119521	-0.0774819	-0.0532295	-0.04798
0.325	-0.15447	0.0292004	0.213882	-0.128167	-0.0830185	-0.0627633	-0.0527382
0.375	-0.019949	0.0549531	0.269354	-0.0559045	-0.02923	-0.0127533	0.00020708
0.425	0.252749	0.120558	0.276967	0.102501	0.0972859	0.106091	0.116103
0.475	0.220621	0.216751	0.188077	0.138431	0.128411	0.13996	0.147234

Bibliography

[1] E. Rutherford, Phil. Mag. **27**, 537 (1919).

[2] J. Chadwick, Nature **129**, 312 (1932).

[3] Yukawa *et al.*, Proc. Phys. Math. Soc. Japan **17**, 48 (1935).

[4] G. P. S. Occhialini and D. C. F. Powell, Nature **160**, 453 (1947).

[5] R. Machleidt, K. Holinde, and C. Elster, Phys. Reports **149**(1) (1987).

[6] H. W. Kendall *et al.*, Phys. Rev. Lett. **23**, 930 (1969).

[7] R. Milner, Eur. Phys. J. A **28**, 1 (2006).

[8] S. M.R., G. J., and S. S., Eur. Phys. J. A **26**, 1 (2005).

[9] M. H.H., M. G.A., and T. A.W., Phys Rev C **71**, 1 (2005).

[10]

[11] H. Arenhoevel, H. Leidemann, and E. Tomusiak, Eur. Phys. J. **23**, 147 (2005).

[12] I. Passhier *et al.*, Nucl. Inst. Meth. A **414**, 446 (1998).

[13] Z. Zhou *et al.*, Phys. Rev. Lett. **82**, 687 (1999).

[14] A. Maschinot, *Analysis of Scattered Protons in Deuteron Electrodisintegration with a Polarized Electron Beam and an Internal Vector/Tensor Polarized Target at BLAST*, Ph.D. thesis, Massachusetts Institute of Technology (2005).

[15] D. Hassell, *Private communication* (2009).

[16] H. Urey, F. Brickwedde, and G. Murphy, Phys. Rev **39**, 164 (1932).

[17] I. Passchier *et al.*, Phys. Rev. Letters **88**(10) (2002).

[18] V. Dimitrev *et al.*, Phys. Lett. B **157**, 143 (1985).

[19] R. Gilman *et al.*, Phys. Rev. Lett. **65**, 1733 (1990).

[20] M. Shulze *et al.*, Phys. Rev. Lett. **52**, 597 (1990).

[21] I. The *et al.*, Phys. Rev. Lett. **67**, 173 (1991).

[22] M. Ferro-Luzzi *et al.*, Phys. Rev. Lett. **77**, 2630 (1996).

[23] M. Bouwhuis *et al.*, Phys. Rev. Lett. **82**, 3755 (1999).

[24] D. Abbot *et al.*, Phys. Rev. Lett. **84**, 5053 (2000).

[25] F. J.L., Phys Rev C **20**, 30 (1979).

[26] J. Kellog *et al.*, Phys. Rev. **55**, 318 (1939).

[27] N. Rodning and L. Knutson, Phys. Rev. C **41**, 898 (1990).

[28] G. Occhialini and C. Powell, Nature **159**, 186 (1947).

[29] T. E. O. Ericson and M. Rosa-Clot, Nucl Phys A **405**, 497 (1983).

[30] T. E. O. Ericson and M. Rosa-Clot, Ann. Rev. Nucl. Part. **35**, 271 (1985).

[31] R. Reid, Ann. Phys. **50**, 411 (1968).

[32] M. Lacombe *et al.*, Phy. Rev. C **21**, 861 (1980).

[33] I. Lagaris and V. Pandharipande, Nucl. Phys. A **359**, 331 (1981).

[34] R. R.B. Wiringa, V. Stoks, and R. Schiavilla, Phy. Rev. C **51**, 38 (1995).

[35] A. Faessler, Prog. Part. Nucl. Phy. **20**, 151 (1988).

[36] J. Carlson and R. Schiavilla, Rev. Mod. Phys. **70**, 743 (1998).

[37] J. Forest *et al.*, Phys. Rev. C **54**, 646 (1996).

[38] T. Donnelly and A. Raskin, Annals of Phys. **169** (1986).

[39] M. Bouwhuis *et al.*, Phys. Rev. Lett. **82**, 3755 (1999).

[40] C. Zhang, *A Measurement of the Tensor Analyzing Powers in the Elastic Electron Deuteron Scattering with BLAST*, Ph.D. thesis, Massachusetts Institute of Technology (2005).

[41] P. Karpius, *Vector Polarization Observables of the Deuteron*, Ph.D. thesis, University of New Hampshire (2005).

[42] H. Henning *et al.*, Phys. Rev. C **52**, 471 (1995).

[43] J. Adam and H. Arenhoevel, Nucl. Phys. A **614**, 289 (1997).

[44] H. Arenhoevel, F. Ritz, and T. Wilbois, Phys. Rev. C **61**, 034002 (2000).

[45] E. Hummel and J. A. Tjon, Phys. Rev. Lett. **63**, 1788 (1989).

[46] D. Phillips, S. Wallace, and N. Devine, Phys. Rev. C **58**, 2261 (1998).

[47] J. W. V. Orden *et al.*, Phys. Rev. Lett. **75**, 4369 (1995).

[48] D. R. Phillips, Physics Letters B **567**, 13 (2003).

[49] S. Jeschonnek and J. V. Orden, Phys. Rev. Lett. **75**, 4369 (1995).

[50] H. Arenhoevel, W. Leidmann, and E. Tomusiak, Phys. Rev. C **46**, 455 (1992).

[51] D. Riska, Physica Scripta 31 **31**, 471 (1985).

[52] A. A. Buchmann, W. Leidemann, and H. Arenhoevel, Nucl Phys A **443**, 726 (1985).

[53] F. Ritz *et al.*, Phys. Rev. C **55**, 2214 (1997).

[54] V. Ziskin, *Measurement of the Electric Form Factor of the Neutron at low Q^2 from a Vector Polarized Deuterium Target at BLAST*, Ph.D. thesis, Massachusetts Institute of Technology (2005).

[55] E. Geis, *The Electric Form Factor of the Neutron at Low Momentum Transfers as Measured at Bates Large Acceptance Spectrometer Torroid*, Ph.D. thesis, Arizona State University (2007).

[56] Geis *et al.*, Phys. Rev. Lett. **101**, 042501 (2008).

[57] D. Pierce and F. Meier, Phys. Rev. B **13**, 5484 (1976).

[58] T. Maruyama *et al.*, Phys. Rev. B **46**, 4261 (1992).

[59] M. . Farkhondeh *et al.*, in A. L. Y.I. Makdisi and W. Mackay, eds., *Spin 2002: 15^{th} International Spin Physics Symposium and Workshop on Polarized Electron Sources and Polarimeters* (AIP, 2003), vol. 675, pp. 1098–1102.

[60] G. T. Zwart, *Polarized Electrons at the Bates Accelerator Center South Hall Ring: Extracted Beam and Internal Targets*, Ph.D. thesis, Boston University (1997).

[61] T. Zwart *et al.*, in R. Milner, ed., *Physics with an Electron Polarized Light-Ion Collider* (2001).

[62] Y. Derbenev and A. Kondratenko, Sov. Phys. Dokl **20**, 562 (1976).

[63] D. Barber *et al.*, Nucl. Instrum. Meth. A **329**, 79 (1993).

[64] W. Franklin *et al.*, in *Proceedings of the SPIN-2004 Conference* (2004).

[65] V. S. Morozov *et al.*, Phys. Rev. ST Accel. Beams **4**, 104002 (2001).

[66] R. Gilman *et al.*, Nucl. Inst. Meth. **A327**, 277 (1993).

[67] Z.-L. Zhou *et al.*, Nucl. Instrum. Methods **A 378**, 40 (1996).

[68] H. Gaul and E. Steffens, Nucl. Instrum. Methods A **316**, 297 (1992).

[69] K. Dow *et al.*, *Magnetic Field Measurements of the BLAST Spectrometer* (To be published, 1999).

[70] W. Leo, *Techniques for Nuclear and Particle Physics Experiments* (Springer Verlag, 1994).

[71] D. Green, *The Physics of Particle Detectors* (Cambridge University Press, 2000).

[72] M. Kohl, *Private communication* (2009).

[73] A. Afanasev, I. Akushevich, and N. Merenkov, Phys Rev D **64**, 113009:1 (2001).